

T I N -T P O I M C
C O

by

Nicholas Ambrose Battaglia

A thesis submitted in conformity with the requirements
for the degree of Doctor of Philosophy
Graduate Department of Astronomy and Astrophysics
University of Toronto

Copyright © 2011 by Nicholas Ambrose Battaglia

Abstract

The Impact of Non-Thermal Processes in the Intracluster Medium on Cosmological Cluster
Observables

Nicholas Ambrose Battaglia

Doctor of Philosophy

Graduate Department of Astronomy and Astrophysics

University of Toronto

2011

In this thesis we describe the generation and analysis of hydrodynamical simulations of galaxy clusters and their intracluster medium (ICM), using large cosmological boxes to generate large samples, in conjunction with individual cluster computations. The main focus is the exploration of the non-thermal processes in the ICM and the effect they have on the interpretation of observations used for cosmological constraints. We provide an introduction to the cosmological structure formation framework for our computations and an overview of the numerical simulations and observations of galaxy clusters. We explore the cluster magnetic field observables through radio relics, extended entities in the ICM characterized by their diffuse radio emission. We show that statistical quantities such as radio relic luminosity functions and rotation measure power spectra are sensitive to magnetic field models. The spectral index of the radio relic emission provides information on structure formation shocks, *e.g.*, on their Mach number. We develop a coarse grained stochastic model of active galaxy nucleus (AGN) feedback in clusters and show the impact of such inhomogeneous feedback on the thermal pressure profile. We explore variations in the pressure profile as a function of cluster mass, redshift, and radius and provide a constrained fitting function for this profile. We measure the degree of the non-thermal pressure in the gas from internal cluster bulk motions and show it has an impact on the slope and scatter of the Sunyaev-Zel'dovich (SZ) scaling relation. We also find that the gross shape of the ICM, as characterized by scaled moment of inertia tensors, affects the SZ scaling relation. We demonstrate that the shape and the amplitude of the SZ angular power spectrum is sensitive to AGN feedback, and this affects the cosmological parameters determined from high resolution ACT and SPT cosmic microwave background data. We compare analytic, semi-analytic, and simulation-based methods for calculating the SZ power spectrum, and characterize their differences. All the methods must rely, one way or another, on high

resolution large-scale hydrodynamical simulations with varying assumptions for modelling the gas of the sort presented here. We show how our results can be used to interpret the latest ACT and SPT power spectrum results. We provide an outlook for the future, describing follow-up work we are undertaking to further advance the theory of cluster science.

To my family, past, present, and future

Acknowledgements

When I finished writing this thesis, I did not experience the sudden rush of happiness I had been expecting. Instead, I was relatively calm and apathetic. Actually, it took a few days contemplation to finally feel the joy that I initially expected. And that is when it hit me, it was not the thesis completion that I was happy about, but all my experiences and growth throughout these past five years. The culmination of all the work and time, and the obstacles that I overcame are really what make me proud of not just this thesis, but of myself as well. So, I would like to thank all of those who contributed and accompanied me throughout this journey.

Thank you, Dick, for influencing me early on as undergraduate summer student. Through our epically long meetings, you provided me with the necessary guidance, knowledge, and supervision to succeed. Most importantly, you instilled in me your mantra of striving for greatness and never settling for the status quo. When Dick was not around my “sub-supervisors” were. Thank you, Jon and Christoph (and Mike too), for having an open door, for the discussions we had and for suffering through the papers we wrote. To the morning coffee attendees, “business” lunch goers, influential grad students, CITA, and my office mates, thank you all for enriching my graduate school experience.

Beyond the department, thank you to my friends for being a fun and intoxicating distraction. Thank you, Mom, for all the love and care you gave me over these past 28 years. Dad, thanks for encouraging me to become anything but an architect. Thanks, Chris and Sam, for being there through it all and listening to me preach. Thank you, Nana, for being strong in Gramps’ absence: we all wish he was here to experience this.

And finally, Charlett. I could not have accomplished this without you. Thank you for putting up with me throughout this entire process; I do not know how you did it. If we grew together under these circumstances we will flourish under anything else.

Contents

1	Introduction	1
1.1	Motivation	1
1.2	The Current Cosmological Paradigm	2
1.3	Structure Formation	5
1.3.1	Galaxy Clusters as Cosmological tools	6
1.3.2	Non-Thermal Processes in Galaxy Clusters	7
1.4	Numerical Methods	8
1.5	Current and Future Observations	9
1.5.1	Brief Overview of Optical and X-ray Observations of Galaxy Clusters	10
1.5.2	The Sunyaev-Zel'dovich effect	10
1.5.3	Diffuse Radio Relic Emission	13
1.6	Thesis Outline	14
2	Exploring the magnetized cosmic web	15
2.1	Chapter Overview	15
2.2	Introduction and key questions	16
2.3	Methodology	19
2.3.1	Adopted cosmology and simulated cluster sample	20
2.3.2	Realization of magnetic fields	22
2.3.3	Cosmic ray electrons and synchrotron emission	24
2.3.4	Finding radio relics	24
	Determination of the emission threshold	26
	Removal of galaxy contamination and cool core	28
2.4	Results	28
2.4.1	Probing the intra cluster magnetic fields	28
	Luminosity functions	28
	Rotation measure	30

2.4.2	Existence and properties of the WHIM	34
	Properties of virializing shocks	34
	Predicting pre-shock properties	39
2.4.3	Dependence on dynamical state and cluster mass	40
2.5	Discussion	40
2.5.1	Comparison with previous theoretical work	40
2.5.2	Assumptions	45
2.6	Conclusions	46
2.7	Appendix: Interpolating and projecting SPH quantities	48
2.8	Appendix: Theoretical emission threshold	48
2.9	Appendix: Rankine-Hugoniot conditions	50
3	Simulations of the SZ Power Spectrum with AGN Feedback	51
3.1	Chapter Overview	51
3.2	SZ Power Templates and the Overcooling Problem	52
3.3	Modeled physics in our simulations	54
	3.3.1 Cosmological simulations	54
	3.3.2 AGN feedback model	54
3.4	Pressure Profiles	56
	3.4.1 Testing AGN feedback as resolution varies	56
	3.4.2 Stacked pressure profiles	58
3.5	SZ Power Spectra from Hydrodynamical Simulations	60
	3.5.1 Stacked SZ power spectra of translated-rotated cosmological boxes	60
	3.5.2 Current constraints on SZ template amplitudes and $\sigma_{8,SZ}$	63
3.6	Conclusions and Outlook	68
4	Scaling Relations, Non-thermal Pressure, and Shapes	71
4.1	Chapter Overview	71
4.2	Introduction	72
4.3	Cosmological simulations and cluster data set	75
4.4	Non-thermal cluster profiles	77
	4.4.1 Kinetic pressure support	78
	4.4.2 Hydrostatic Masses	82
	4.4.3 Velocity Anisotropy	83
4.5	Galaxy Cluster Shapes	84
	4.5.1 Overall shapes and dependence on modeled physics	87
	4.5.2 Projected and intrinsic shapes	93

4.5.3	Mass and redshift dependence of shape profiles	93
4.5.4	Isophotal twist of cluster structure and semi-analytical models	94
4.6	SZ Scaling Relation	96
4.6.1	Self-similar $Y - M$ scaling relation	96
4.6.2	Comparison to data	98
4.6.3	Physics dependence of the $Y - M$ relation	98
4.6.4	Toward a fundamental plane of $Y - M$	104
4.7	Discussion and Conclusions	107
4.8	Appendix: Fitting function for $P_{\text{kin}}/P_{\text{tot}}$	109
4.9	Appendix: Down-weighting the substructure in the inertial tensor	111
4.10	Appendix: Galaxy cluster in velocity space and dynamical radius definition	112
4.11	Appendix: Gaussian or Log-normal scatter?	115
5	Deconstructing the Thermal SZ Power Spectrum	117
5.1	Chapter Overview	117
5.2	Introduction	117
5.3	Cosmological simulations and cluster data set	120
5.4	The Analytic Calculations of tSZ Angular Power Spectrum	121
5.5	The Thermal Pressure Profile	122
5.5.1	Fitting Pressure Profiles from the Simulations	125
5.5.2	Constrained Thermal Pressure Profile Fits	126
5.5.3	Analytic Assumptions in the Thermal Pressure Profile	128
5.6	The tSZ power spectrum in detail	131
5.6.1	Contribution to the tSZ Power Spectrum in Cluster Mass Bins	134
5.6.2	Contribution to the tSZ Power Spectrum in Redshift Bins	134
5.6.3	Contribution to the tSZ Power Spectrum within given Cluster Radii	137
5.7	Constraints of σ_8 from Current ACT and SPT Data	137
5.8	Discussion and Conclusion	139
5.9	Appendix: Comparing the Cluster Mass Catalog to the Mass function	142
6	Conclusions and Outlook	145
6.1	Future Work	146
	Bibliography	147

List of Tables

2.1	Cluster sample considered in this paper.	21
2.2	Magnetic field parameters in various combinations	23
2.3	Parameters chosen for the relic finder.	28
2.4	Magnetic field realizations (MFR) used in RM maps.	33
3.1	Summary of periodic box simulations	53
3.2	Constraints on A_{SZ} and $\sigma_{8,SZ}$	66
4.1	Axis ratio fits for cluster as a function of mass and redshift.	89
4.2	$Y - M$ scaling relation fits for different simulated physics, subsampling in kinetic-to-thermal energy and ellipticity (of the density and pressure distribution), and along different projected axes yielding Y_{cyl}	99
5.1	Mass and redshift dependencies of the average thermal pressure profile	128
5.2	Cosmological constraints on A_{tSZ} and σ_8 from ACT and SPT using the AGN feedback tSZ power spectrum template	141

List of Figures

1.1	The CMB temperature fluctuations from the surface of last scattering are extremely uniform	3
1.2	Map of the dark matter in slices from the Hubble Volume Simulation	8
1.3	Illustration of the spectral distortion of cosmic microwave background spectrum caused by the Sunyaev-Zel'dovich effect	11
1.4	Examples of the Sunyaev-Zel'dovich effect and radio relic observations from galaxy clusters	13
2.1	Structure formation shocks triggered by a recent merger of a large galaxy cluster dissipate the associated gravitational energy	18
2.2	Surface brightness emission map for radio relics in the simulated cluster g72a	20
2.3	Simulated GMRT maps of the cluster g72a at z=0.05 and the surface emission map of the relics of g72a	25
2.4	The radio relic luminosity functions	27
2.5	The Faraday rotation measure map of the largest radio relic in g72a and the polarization angle map	29
2.6	The rotation measure power spectra	32
2.7	The spectral index map of between 150 MHz and 1.4 GHz for the largest relic in g72a	35
2.8	The spectral index distributions for our largest relic	36
2.9	The two dimensional observable parameter space for radio relics in galaxy cluster g72a	38
2.10	The radial profiles of galaxy cluster g72a restricted to the solid angle subtended by the largest radio relic	41
2.11	The median of the Mach number distribution for each relic as a function of the median of the distribution function of $\alpha_{\nu,3D}$	42
2.12	The luminosity functions for our sample of 10 clusters	43
2.13	The relation between the number of radio relics within a galaxy cluster and the cluster mass	44
2.14	The cumulative luminosity functions for different values of the emission cutoff	49

3.1	The radial profiles of the baryon and star fractions for the cluster g676 from simulations with radiative cooling and star formation and AGN feedback	57
3.2	A comparison of the thermal pressure profile from analytic calculations, simulations and observations	59
3.3	A Comparison of the predictions for the thermal Sunyaev Zel'dovich power spectrum at 30 GHz using analytical calculation, semi-analytical simulations, and simulations . . .	61
3.4	The allowed range for models of the thermal Sunyaev Zel'dovich at 150 GHz computed with $\sigma_8 = 0.8$	64
4.1	The ratio of kinetic and thermal pressure support in clusters	77
4.2	Mass and redshift dependence of thermal and kinetic pressure support	78
4.3	The kinetic pressure contribution across different simulated physics	80
4.4	Hydrostatic mass bias	81
4.5	The velocity anisotropy as a function of cluster mass and redshift	82
4.6	Rotating clusters into the principle axis frame, low redshift	85
4.7	Rotating clusters into the principle axis frame, high redshift	86
4.8	The axis ratio c/a as a function of mass and redshift	88
4.9	Stacked cluster axis ratios and ellipticities	89
4.10	Average projected 2D axis ratios compared to the 3D axis ratios	90
4.11	Mass dependence and redshift evolution of the ellipticity profile	92
4.12	The weighted median angles between the dark matter axis and gas and pressure axes .	95
4.13	The $Y - M$ scaling relation for the AGN feedback simulations compared to recent observations	97
4.14	The dependence of the normalization, slope and scatter of the $Y - M$ scaling relations on the simulated physics	100
4.15	The redshift evolution of fit parameters of the $Y - M$ scaling relations	100
4.16	The results from sub-sampling the $Y - M$ relations by the kinetic-to-thermal energy ratio	101
4.17	The results from sub-sampling the $Y - M$ relations by the gas c/a axis ratio	103
4.18	The cylindrical $Y - M$ relations	105
4.19	The ratio of kinetic and total pressure support in clusters	110
4.20	The effects of including the r^{-2} weighting in the definition of the inertial tensor on axis ratios	111
4.21	The stacked radial velocity PDF and the velocity anisotropy	112
4.22	Comparing the velocity anisotropy scaled by R_{200} and $R_{200,m}$	113
4.23	The kinetic pressure support the and ellipticity between scaled by $R_{200,m}$	113

4.24	Comparison of Gaussian and log-normal scatter relative to the best-fit $Y - M$ scaling relation	114
5.1	The individual fits to the thermal pressure profiles as functions of mass, redshift, and radius	123
5.2	The constrained fits to the thermal pressure profiles as functions of mass, redshift, and radius	124
5.3	A comparison of the projected pasted profiles to four actual clusters from the simulations	127
5.4	The thermal and total adiabatic indexes as functions of radius from simulations	129
5.5	Comparison between the current predictions for the thermal Sunyaev-Zel'dovich power spectra at 150 GHz	130
5.6	The cumulative distribution function of the thermal Sunyaev-Zel'dovich power spectrum as a function of mass and redshift at $\ell = 3000$	133
5.7	The thermal Sunyaev-Zel'dovich power spectrum sorted into bins of galaxy cluster mass	135
5.8	The thermal Sunyaev-Zel'dovich power spectrum sorted into redshift bins	136
5.9	The thermal Sunyaev-Zel'dovich power spectrum for a given radial truncation	138
5.10	The constraints on the amplitude of the thermal Sunyaev-Zel'dovich power spectrum from current ACT and SPT measurements	140
5.11	Comparison of the clusters catalog from AGN feedback simulations to the mass function from Tinker et al. (2008)	143

Chapter 1

Introduction

1.1 Motivation

How life on earth and the Universe originated are questions at the frontier of human curiosity. Astrophysics are addressing such grand questions through the cosmological, and solar/extrasolar planet fields. Cosmology is a vast field, with many sub-fields posing specific questions related to the larger one of the origin of the Universe. In that vein, this thesis describes a collection of work focusing on structure formation in the Universe, in particular on the study of giant galaxy clusters.

Galaxy clusters were first discovered by Edwin Hubble (Hubble, 1926) and later classified by Fritz Zwicky (Zwicky, 1937), who discovered that a mysterious source of additional mass (known as dark matter) was needed for the clusters to have a potential well massive enough to keep the galaxies inside from flying apart. Only after the galaxy cluster catalogs of George Abell (Abell, 1958) and early X-ray satellites began observing extended emission from the clusters (e.g., Gursky et al., 1971), did their utility as a cosmological tool become an important growing field. The interest in galaxy clusters and their potential to constrain cosmological parameters has grown over time. But why?

Simply put, galaxy clusters are the largest gravitationally bound objects in the Universe. They are found at the nodes of the cosmic web (Bond et al., 1996), where filaments intersect. They are the highest peaks of the initial matter density, the extremely massive and rare end of structure formation in the Universe. This makes them great observational tools for both cosmology and astrophysics. Just as with so many other observations in astronomy and astrophysics of collapsed objects, we wish to use cluster observations to determine their masses and their distances. There are several observational proxies for determining such quantities: for example, through dynamical measurements of the galaxies within the cluster and X-ray emission from the hot gas within the cluster. The proxies require a theory to convert such observables to a physical quantity like mass. The first attempts to model the thermodynamic properties of clusters used the fact that clusters were in deep gravitational potentials and could be modelled by virialized systems (e.g., Kaiser, 1986). For the early state of cluster observations these

theoretical models were adequate. However, the theory of clusters needs to keep pace with the increased demands on it from the higher precision of current observations, now the standard for all of cosmology. The precision of cosmological parameter measurements over the past 20 years, primarily from the cosmic microwave background (CMB), has increased dramatically, so much so that we are considered by many to be in the *golden age* of cosmology. This places pressure on we astrophysicists to develop our theoretical models of galaxy clusters to rise to these standards.

The requirements now for cosmological parameters is to achieve percent level precision. This necessitates extremely accurate modelling of the intracluster medium (ICM) if the cluster system is to contribute competitively to present standards. At this level of accuracy, there are several sub-dominant thermal and non-thermal processes that become important to model correctly. The unique environment of the ICM is also an astrophysical laboratory where, for example, one can study turbulence, pressure support from bulk motions, cosmic rays, and energetic feedback from active galactic nuclei (AGN). The overall goal of this thesis is to provide more accurate theoretical models of galaxy clusters and the ICM, quantifying and modelling the non-thermal process within the ICM, and addressing the utility of galaxy clusters as cosmology tools.

1.2 The Current Cosmological Paradigm

Understanding where galaxy clusters fit into the standard cosmology framework first requires a brief overview of the current theoretical cosmological models and the formation of structure in the Universe. Here we outline the basic cosmological framework and parameters, which are well understood, in large part due to the observations of the CMB (e.g., the Wilkinson Microwave Anisotropy Probe, WMAP). The concordance cosmological model is a Λ CDM Universe in which the Universe is roughly composed of 71% dark energy Λ^1 , 25% dark matter and 4% baryonic matter. These and other cosmological parameters are constrained to within a few percent by observations of the temperature and polarization anisotropies in the CMB, type 1a supernova, weak lensing, baryonic acoustic oscillations, the Lyman- α forest, and the large-scale structure of galaxy clusters.

The modern cosmological model is based on two underlying postulates: the Universe is homogeneous and isotropic. Observations of the CMB, from the surface of last scattering, give the strongest support for these postulates, with measurements of large-scale curvature fluctuations in the early epoch of the Universe to be on the order of 10^{-4} (cf. Fig 1.1). A nearly homogeneous and isotropic expanding Universe has an unperturbed background modelled by the Friedmann-Robertson-Walker (FRW) metric

$$ds^2 = dt^2 - \frac{a(t)^2}{c^2} \left[\frac{1}{1 - kr^2} dr^2 + r^2 d\Upsilon^2 \right] \quad (1.1)$$

where c is the speed of light, k is the spacial curvature, $a(t)$ is the scale factor, and r, θ , and ϕ form a

¹Throughout this work unless stated otherwise, we assume that dark energy is a cosmological constant.

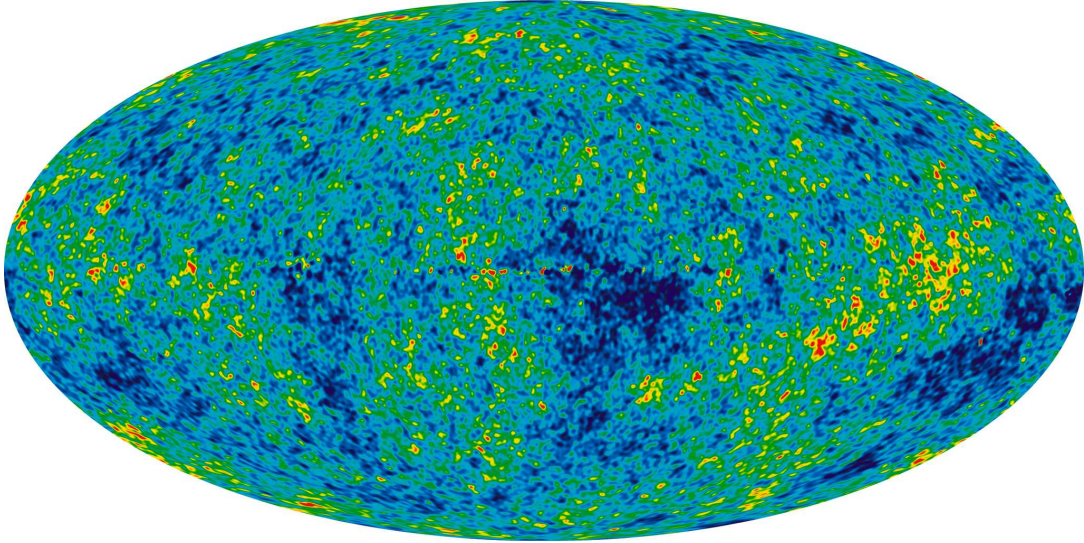


Figure 1.1: The CMB temperature fluctuations from the surface of last scattering are extremely uniform. Shown is the Internal Linear Combination Map, a weighted linear combination of the five WMAP frequency maps. The weights are computed using criteria which minimize the Galactic foreground contribution to the sky signal. The resultant map provides a low-contamination image of the CMB anisotropy. Here Galactic coordinates are used with a Mollweide projection and the scale is linear from -200 to $200 \mu\text{K}$ (-7×10^{-5} to 7×10^{-5} in relative temperature fluctuations). Credit: the WMAP Science Team.

spatial comoving coordinate system with $d\Psi^2 = d\theta^2 + \sin^2\theta d\phi^2$. Observations indicate the Universe is flat to good approximation. Hereafter the spatial curvature (k) is 0. The scale factor, $a(t)$, is conveniently normalized such that its current value is $a(t_0) = 1$. It is related to the cosmological redshift by $z = a(t_0)/a(t) - 1$: a photon is emitted at time t has its wavelength stretched by a factor of $1/a(t)$ when it reaches a present-day observer.

The FRW metric evolves according to the Friedmann equations derived from general relativity that describe the dynamics of the FRW Universe. The Friedmann equations are

$$\frac{\ddot{a}(t)}{a(t)} = -\frac{4\pi G}{3}(\rho_{\text{tot}} + 3p_{\text{tot}}), \quad (1.2)$$

$$H^2(a) \equiv \left(\frac{\dot{a}(t)}{a(t)}\right)^2 = \frac{8\pi G}{3}\rho_{\text{tot}}, \quad (1.3)$$

where ρ_{tot} and p_{tot} are the current total energy density and pressure for all components in the Universe. These energy density components consist of baryonic matter (ρ_b), dark matter (ρ_{DM}), relativistic particles (ρ_r), and dark energy (ρ_Λ). The Hubble expansion rate H , has a present-day Hubble value $H_0 = \dot{a}(t_0)/a(t_0) = 100h \text{ km Mpc}^{-1} \text{ s}^{-1}$ in terms of a dimensionless parameter h . The observational

value for h from the Hubble Space Telescope and supernova observations is 0.742 ± 0.036 (Riess et al., 2009).

One can identify a critical density by rearranging Eq. 1.3

$$\rho_{\text{crit}} = \frac{3H(t)^2}{8\pi G}, \quad (1.4)$$

where the present day values is

$$\rho_{\text{crit},0} = \frac{3H_0^2}{8\pi G}. \quad (1.5)$$

As mentioned above, in the absence of curvature ($k = 0$) the total energy density is $\rho_{\text{tot}} = \rho_{\text{b}} + \rho_{\text{DM}} + \rho_{\text{r}} + \rho_{\Lambda}$, which can be rewritten as dimensionless energy densities by normalizing to the present day critical density $\Omega_i = \rho_i/\rho_{\text{crit},0}$. These obey the simple sum rule $\Omega_{\text{b}} + \Omega_{\text{DM}} + \Omega_{\text{r}} + \Omega_{\Lambda} = 1$. The redshift evolution of these energy densities is obtained from energy conservation in the Universe. Under the influence of gravity, energy conservation is

$$\dot{\rho}c^2 = -3\frac{\dot{a}(t)}{a(t)}(\rho c^2 + p). \quad (1.6)$$

Given an equation of state, $w \equiv p/(\rho c^2)$, the equations can be integrated. For each energy density component the redshift evolution is $\rho_i \propto a^{-3(1+w_i)}$. The equation of state for non-relativistic matter is $w = 0$, so Ω_{b} and Ω_{DM} are proportional to $a^{-3} = (1+z)^3$. Radiation has a $w = 1/3$ equation of state, hence $\Omega_{\text{r}} \propto a^{-4} = (1+z)^4$. If we assume the dark energy is a cosmological constant, $w = -1$, so Ω_{Λ} is constant in time.

We can now express the Hubble parameter and critical density at any redshift (or scale factor) as,

$$H(z) = H_0 \sqrt{(\Omega_{\text{b}} + \Omega_{\text{DM}})(1+z)^3 + \Omega_{\text{r}}(1+z)^4 + \Omega_{\Lambda}}, \quad (1.7)$$

and the critical density as

$$\rho_{\text{crit}}(z) = \frac{3H_0^2}{8\pi G} \left((\Omega_{\text{b}} + \Omega_{\text{DM}})(1+z)^3 + \Omega_{\text{r}}(1+z)^4 + \Omega_{\Lambda} \right). \quad (1.8)$$

The Equation 1.7 provides the foundation to calculate cosmological distances. Integrating of the comoving line element $d\chi = c dt/a(t)$ gives the comoving distance

$$\chi(z) = c \int_0^z \frac{dz'}{H(z')}. \quad (1.9)$$

For a flat universe ($\Omega_{\text{tot}} = 1$), $\chi(z) = D_{\text{M}}(z)$, where $D_{\text{M}}(z)$ is called the transverse comoving distance. It follows that the angular diameter distance is $D_{\text{A}}(z) = D_{\text{M}}(z)/(1+z)$.

1.3 Structure Formation

With the standard cosmological framework in place for the FRW Universe from Section 1.2, we turn to the question of how structure grows in the Universe. Initially the patch of the Universe we observe must have been very smooth with tiny fluctuations in the density, at least on large-scales. Structure grows first by the gravitational collapse of small over dense regions, then it grows hierarchically through smaller structures merging into larger structures. We define the initial density fluctuations about the background density as

$$\delta(\mathbf{x}) = \frac{\rho}{\rho_0} - 1, \quad (1.10)$$

where ρ_0 is the mean background density in the Universe over a volume V and \mathbf{x} is a comoving coordinate. The model for $\delta(\mathbf{x})$ is a Gaussian random field.

The power spectrum encodes a complete description of the early Universe density fluctuations since they are Gaussian². Taking the Fourier transform of Equation 1.10 yields

$$\tilde{\delta}_{\mathbf{k}}(k) = \int \delta(\mathbf{x}) e^{i\mathbf{k}\cdot\mathbf{x}} d^3x. \quad (1.11)$$

And the power spectrum is simply $P(k) \equiv \langle |\tilde{\delta}_k|^2 \rangle$, where the angle brackets is the expectation values of the enclosed quantity. The variance can be written in terms of a smoothed mass density as a function of mass scale, M ,

$$\sigma^2(M) = \int P(k) \tilde{W}_{\text{th}}(Rk) d^3k, \quad R \equiv \left(\frac{3M}{4\pi(\rho_b + \rho_{\text{DM}})} \right)^{1/3}, \quad (1.12)$$

where $\tilde{W}_{\text{th}}(k)$ is the Fourier transform of the window function over which the field is smoothed. Here the window function is a spherical top hat, $W_{\text{th}}(\mathbf{x})$. The power spectrum is modelled locally by a simple power-law that is scale dependent (*ie* $P(k) \propto k^\alpha$). A natural choice for the matter power spectrum is the Harrison-Zel'dovich spectrum, which is scale invariant $P(k) \propto k$. This power spectrum happens to be a good approximation of the measured power spectrum $P(k) \propto k^{0.963 \pm 0.014}$ (Larson et al., 2011) and a slightly tilted index is preferred by most inflationary models.

We now briefly cover the main aspects that govern the growth of these density fluctuations using linear theory. Gravity causes the positive parts of fluctuations to grow with time, only the Hubble expansion slows the growth of $\tilde{\delta}_k$, since this collapse is extremely sub-sonic. Given the initial power spectrum one can relate the current matter power to it with a the transfer function $T(k)$ and the linear growth factor $D(a)$,

²Tiny primordial non-Gaussianity is one of the big questions in cosmology, and is being looked for in CMB and large-scale structure observations. See Dalal et al. (2008) for an example of non-Gaussian simulations.

$$P(k, a = 1) = T(k)^2 D(a)^2 P(k, a). \quad (1.13)$$

The time dependent growth of the density linear fluctuations is given by the linear growth function $D(a) \propto \frac{\delta\rho}{\rho} \propto \frac{\dot{a}}{a} \int \frac{da}{a^3}$ (for a derivation of $D(a)$ see Peebles, 1993). The transfer function describes the scale dependent evolution of the fluctuations through horizon crossing and the radiation-matter equivalents (where $\Omega_r(z) = \Omega_{DM}(z) + \Omega_b(z)$). Here we used the prior assumption that a majority of the matter in the Universe is cold (non-interacting) dark matter. Detailed transfer functions are calculated by numerical solutions to coupled Boltzmann and Einstein field equations, assuming adiabatic cold dark matter. A faster alternative is to use fitting functions provided in the literature (e.g., Bardeen et al., 1986), modified to include the effects of baryons (e.g., Eisenstein & Hu, 1998). Now one just gets the transfer function from numerical codes, such as CAMB (Lewis & Bridle, 2002).

The amplitude of the initial power spectrum is not specified by any theory of initial conditions, so it is normalized to the power spectrum measured by observations. A natural measure of the power spectrum as shown earlier is the variance within a given smoothing scale (cf. 1.12). From early observations of galaxy counts, a conventional smoothing scale of $8h^{-1}$ Mpc was chosen, since measurements then hinted that the value for σ was close to 1 upon linear extrapolation. Thus the parameter is called σ_8 and is constructed to be the *rms* variation of density fluctuations on scales of $8h^{-1}$ Mpc and is described by

$$\sigma_8^2 = \int P(k) \tilde{W}_{th}(Rk) d^3k, \quad R \equiv 8h^{-1} \text{ Mpc}. \quad (1.14)$$

The abundances of galaxy cluster, also referred to as cluster mass functions, are dependent on cosmological parameters. There are analytic theories for cluster mass functions that use overdensity thresholds to determine whether or not a region of a given mass (smoothing length) would collapse (e.g., Press & Schechter, 1974; Bond et al., 1991). They work surprisingly well. Over the past couple of decades, computation capabilities have increased roughly according to Moore's law in hardware as well as algorithmic advances. Hence, cluster mass functions have been determined through simulations, but using the underlying analytical *ansatz* that they depend on $\sigma^2(M)$. The cluster mass function is used as a foundation for theoretical predictions in cluster cosmology that focus on the growth of structure³.

1.3.1 Galaxy Clusters as Cosmological tools

Galaxy clusters are not the only probes of cosmological parameters. However, for every individual observational probe in cosmology, parameters will be correlated, and may have near-degeneracies. As well, every probe has systematic uncertainties. Degeneracies are broken with complementary measure-

³Galaxy clusters have also been hypothesized to be standard rulers through a combination of X-ray and Sunyaev-Zel'dovich observations (see Carlstrom et al., 2002, for a review), but this method is dominated by systematic uncertainties and the assumption that galaxy clusters are spherically symmetric.

ments. Thus, all measurements of cosmological parameters can play an important part in decreasing uncertainties (increasing precision).

It is apparent from the arguments and equations in sections 1.2 and 1.3 that galaxy clusters are great probes of cosmology. Section 1.3 shows how structure formation is governed by the initial matter power spectrum, transfer function, and linear growth factor. More explicitly, the normalization of the matter power spectrum, σ_8 , is sensitive to the growth of structure. Hence any measurements of structure formation, such as counts per volume or spacial correlation functions, are dependent on the underlying cosmological parameters of the Universe. And galaxy clusters are the extreme end of structure formation.

In pioneering work, galaxy clusters were modelled as simple self-similar objects whose thermodynamic properties simply scaled by the cluster mass (Kaiser, 1986; Cole & Kaiser, 1988). Another approach to galaxy clusters was to identify them in initial Lagrangian space with a point process of *peak patches*, and determine the thermodynamic quantities from the total internal energy (Bond, 1988; Bond & Myers, 1996a,b,c). The initial hypotheses were based on the hope that galaxy clusters were completely dominated by their gravitational potential, which could then be used to interpret observations with theoretical quantities like cluster mass. X-ray observations have shown that galaxy clusters are not the simple systems initially hypothesized/hoped (e.g., Voit, 2005, for a review of self-similarity and observations).

1.3.2 Non-Thermal Processes in Galaxy Clusters

As more and more observations of galaxy clusters are made with finer and finer resolution, we are finding these objects display increasing complexity, especially in their central cores and their outskirts. There are clearly different ICM properties in the cores of galaxy clusters: some are dramatically cooling their hot ICM gas and forming stars, but at a much smaller rate than simple radiative cooling models would predict; some show no signs of a cooling flow, but exhibit a morphologically disturbed ICM relative to a simple hydrostatic equilibrium; and there is a whole spectrum in between. With such variety, the consensus is that every cluster is or was once dynamically disturbed, the mechanism being the merger history inherent in hierarchical structure formation.

In the core, non-thermal processes are dominant, like the aforementioned radiative cooling and the resulting star formation. Other physical processes such as thermal instabilities, energetic feedback in the cores from AGN or massive stars etc., can act to inhibit cooling and star formation. All these processes are not understood individually, so their interactions as a whole on the ICM are still uncertain.

As one progresses from the galaxy cluster center outwards, the pressure support predominantly from internal bulk motions and turbulence becomes increasingly important. Equality is reached in the cluster outskirts (around the virial radius) between the thermal pressure and the pressure support from bulk motions. Additionally, there are magnetic fields and cosmic rays which are thought to contribute at

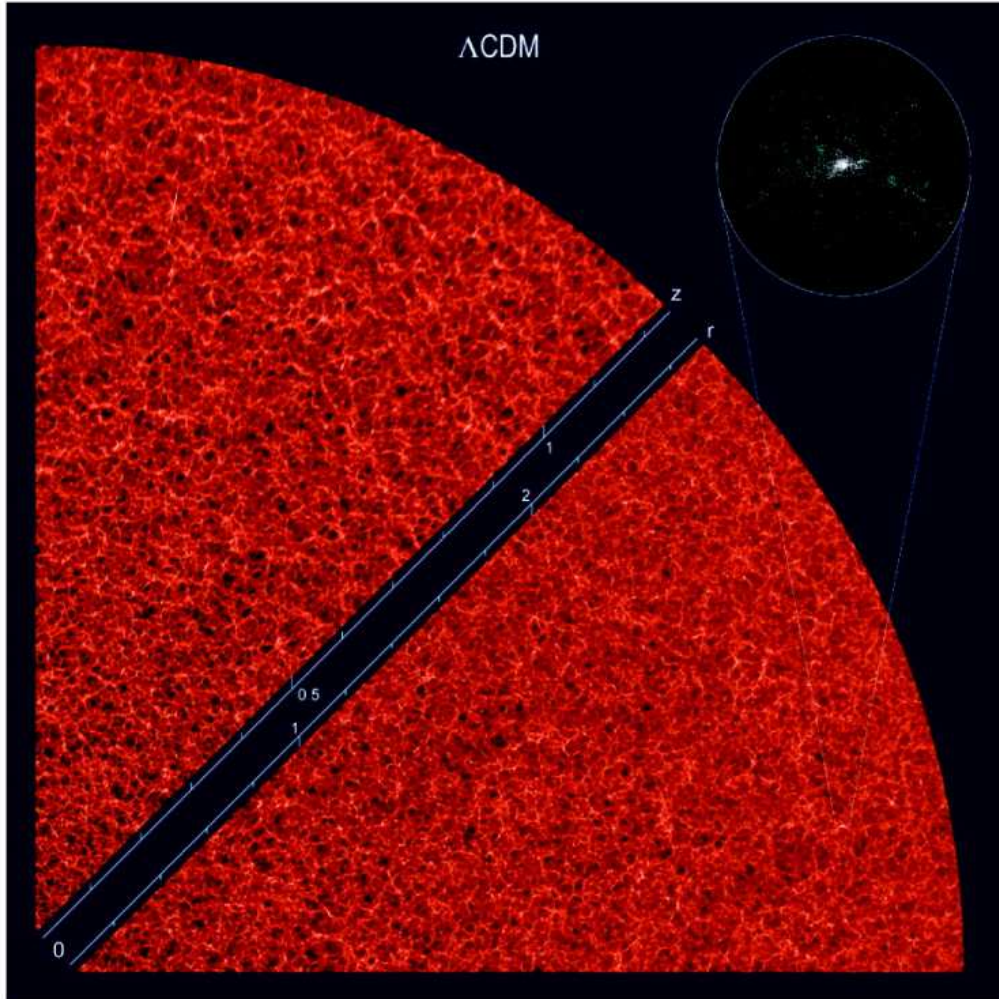


Figure 1.2: Map of the dark matter in slices from the Hubble Volume Simulation Λ CDM cosmology (Evrard et al., 2002). Regions of high density are white and regions of low density are black.

least a few percent of the total pressure support in clusters. Although observations of magnetic field and cosmic ray energy densities (volume averaged pressure) are still scarce and uncertain, measuring one often constrains the other since they are linked through the dynamical arguments (cosmic ray are confined to move along magnetic field lines).

1.4 Numerical Methods

Although the simple self-similar models for the ICM are useful as a first approach to observations, they are far too simple to meet the accuracy demanded by precision cluster cosmology. Most of the nuances in the structure formation captured by large numerical simulations are missed by self-similar models.

Furthermore, numerical simulations allow one to study individual galaxy clusters and their formation, as well as statistically-averaged quantities.

Simulations of the growth of structure start by giving a simulation's initial condition, where the equations of motion can still be well approximated by Lagrangian linear perturbation theory (Zel'dovich, 1970). Given the cosmological parameters, these initial conditions are calculated using the initial power spectrum of density fluctuations, and the transfer function. The system is then evolved numerically under gravity (and sometimes hydrodynamically). The dark matter aspects are well understood. The addition of baryonic physics, mentioned in Section 1.3.2, is the main challenge for these simulations.

Numerically simulating galaxy clusters has had a long history, beginning with the first simulations that included collision-less matter only (Peebles, 1970; White, 1976), with the addition of baryons only coming over in the late eighties (e.g., Evrard, 1988, 1990; Thomas & Couchman, 1992; Katz & White, 1993; Bryan et al., 1994; Kang et al., 1994). These simulations have laid a solid foundation in the understanding of galaxy cluster properties and large-scale structure formation on the whole (cf. Fig. 1.2). Some highlights include: The characterization of the correlations between X-ray observables and galaxy cluster masses (Evrard et al., 1996); a practically universal fitting function for the dark matter density distribution in galaxy clusters (Navarro et al., 1997); a collaborative comparison amongst the several different approaches used to simulate a galaxy cluster with the inclusion of hydrodynamics, known as the *Santa Barbara comparison cluster project* (Frenk et al., 1999); a numerical *ansatz* for the dark matter halo mass function (e.g., Jenkins et al., 2001; Warren et al., 2006; Tinker et al., 2008); large hydrodynamical simulations on the scales of the observable Universe (e.g., Evrard et al., 2002). This list is not nearly complete (see the article by Borgani & Kravtsov, 2009, for a more detailed review of status of cosmological simulations).

In this work we use a modified version of the numerical code GADGET-2 (Springel, 2005). GADGET-2 is a massively parallel Tree smoothed particle hydrodynamics (SPH) code. We chose it because we had access to a version that already included radiative cooling, star-formation, galactic winds, cosmic rays and shock statistics, the latter described in Pfrommer et al. (2006). Some of this work required us to further modify GADGET-2. Our modifications included implementing a coarse grained treatment for the energetic feedback from AGN. We do not discuss in this thesis the merits of SPH versus Eulerian grid codes. Both have played important roles in numerical simulations of clusters. However, we note that SPH codes have difficulties resolving shock fronts: an artificial viscosity is used to dissipate bulk energy into thermal energy across the fronts.

1.5 Current and Future Observations

Galaxy clusters are observed from radio waves to γ -rays. Each wavelength regime provides a valuable window into the emission processes and properties of the ICM. Large cluster surveys are mostly carried

out in the optical, Infrared, X-ray, microwave and radio wavelengths. The focus of this work is on emission in the microwave (through the Sunyaev-Zel'dovich effect) and in low frequency radio wave (through synchrotron radiation).

1.5.1 Brief Overview of Optical and X-ray Observations of Galaxy Clusters

Optical techniques use galaxy colours to identify spatial over-densities of galaxies, galaxy clusters, in large surveys, such as the *red sequence* technique (Gladders & Yee, 2000). X-ray observations search for diffuse bremsstrahlung emission from the hot ICM (Felten et al., 1966). Cosmological parameters from both optical and X-ray surveys are determined through counting galaxy clusters as a function of observable properties within a given volume (e.g., Gladders et al., 2007; Vikhlinin et al., 2009; Rozo et al., 2010). Systematics associated with their selection functions and mass proxies are the most significant uncertainties in these measurements.

Besides the clusters abundance measurements there are many other techniques used to measure cosmological parameters. Two examples are:

- In the X-rays, measurements of cosmological parameters have been made with a highly selected sample of relaxed clusters using the ratio of gas mass to total mass contained within these clusters (Allen et al., 2008). A central concern is the assumptions of universality in the evolution of the ratio of gas mass to total mass.
- Optical observations, which utilize the property that galaxy clusters act as large gravitational lenses. Weak lensing measurements of the statistical shear distortion of several background galaxies can also be used to determine cosmological parameters (e.g., Kaiser, 1992). Uncertainties in weak lensing measurements come from the modelling the lenses and from the photometric redshifts of the background galaxies.

All these measurements have been used in the determination of the current cosmological constraints.

1.5.2 The Sunyaev-Zel'dovich effect

The thermal Sunyaev-Zel'dovich (SZ) effect (Sunyaev & Zeldovich, 1970) is the Compton up-scattering of CMB photons by hot electrons. This process produces temperature distortions in the CMB with a unique spectral signature: a decrement below $\nu \sim 220$ GHz, and an excess above (see Fig. 1.3). In the non-relativistic limit, the Kompaneets (1956) equation is used to approximate this scattering process,

$$\frac{\partial n}{\partial y} = \frac{1}{x_e^2} \frac{\partial}{\partial x_e} x_e^4 \left[\frac{\partial n}{\partial x_e} + n + n^2 \right], \quad (1.15)$$

where $n(\nu)$ is the photon distribution function (occupation number). It describes a diffusion process (for a detailed derivation see Bond, 1996; Birkinshaw, 1999). Here $x_e = h_p \nu / k_b T_e$, where h_p is Planck's

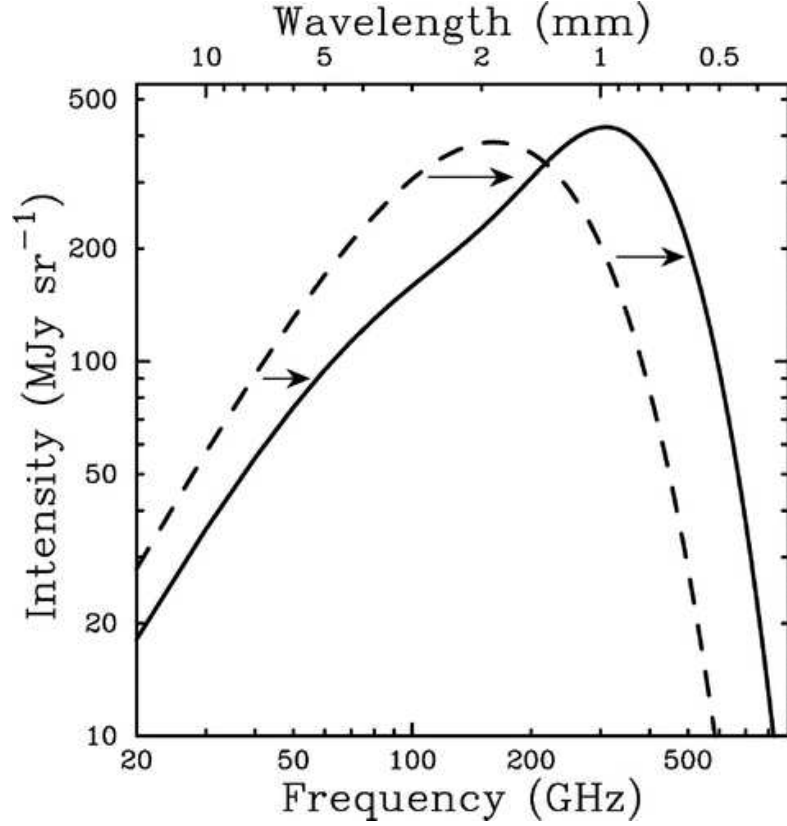


Figure 1.3: Illustration of the spectral distortion of CMB spectrum caused by the SZ effect (Carlstrom et al., 2002). Note that this distortion has been greatly exaggerated by using a fictional galaxy cluster with a mass 1000 times greater than a typical massive cluster.

constant, k_b is Boltzmann's constant, and T_e is the electron temperature. The parameter y is the Comptonization parameter

$$y = \int n_e \sigma_T \frac{k_b (T_e - T_{\text{rad}})}{m_e c^2} dl. \quad (1.16)$$

Here n_e is the electron density, σ_T is the Thomson cross-section, T_{rad} is the blackbody temperature of the CMB, and m_e electron mass. Under an isothermal assumption, the Equation 1.16 is the optical depth of electron time the fractional gain in energy from the scattering, or a more physical understanding of y is the integrated electron pressure along the sight. In the limit of small x_e , appropriate for hot electrons and CMB photons, $\partial n / \partial x_e \gg n, n^2$ so Equation 1.15 becomes

$$\frac{\partial n}{\partial y} = \frac{1}{x_e^2} \frac{\partial}{\partial x_e} x_e^4 \frac{\partial n}{\partial x_e}. \quad (1.17)$$

Making the assumption that $\frac{\partial n}{\partial y} = \frac{\Delta n}{y}$, for small y , and $n(x) = 1/(e^x - 1)$, where $x = h_p \nu / k_b T_{\text{rad}}$, Equation 1.17 is further reduced to

$$\Delta n = yx \frac{e^x}{(e^x - 1)^2} (x \coth(x/2) - 4). \quad (1.18)$$

Equation 1.18 describes the spectral change cause by scattering, with the features describe above. The temperature distortions in the CMB from this scattering are $\Delta T = x\Delta n T_{\text{rad}}$, which simplifies to

$$\frac{\Delta T}{T_{\text{rad}}} = y(x \tanh(x/2) - 4). \quad (1.19)$$

In this work, our concern is with the thermal SZ effect from inverse-Compton scattering of the ICM, the hot plasma within galaxy clusters. Galaxy clusters are the most likely extra galactic source for the thermal SZ effect and thus the most commonly referred to source for this scattering. In addition to the thermal SZ effect, there is a smaller effect which arising from the bulk motion of the scattering medium relative to the Hubble flow. This temperature distortion is referred to as the kinetic SZ effect and is described by the equation

$$\frac{\Delta T}{T_{\text{rad}}} = \frac{v_z}{c} \int n_e \sigma_T dl \quad (1.20)$$

where the v_z peculiar velocity is along the line of sight. The kinetic SZ does not have a distinct spectral signature like the thermal effect. Hence, the thermal SZ null of $\nu \sim 220$ GHz is useful ideal for digging out the kinetic SZ measurement. For relatively massive galaxy clusters, it is easy to show that in the Rayleigh jeans limit the thermal SZ effect is an order of magnitude larger than the kinetic SZ effect by just taking the ratio of Equations 1.19 and 1.20

$$\frac{\Delta T_{\text{thermal}}}{\Delta T_{\text{kinetic}}} = 2 \left(\frac{c}{v_z} \right) \left(\frac{k_b T_e}{m_e c^2} \right), \quad (1.21)$$

$$= 11.75 \left(\frac{k_b T_e}{10 \text{keV}} \right) \left(\frac{1000 \text{km s}^{-1}}{v_z} \right). \quad (1.22)$$

$$(1.23)$$

We ignore all relativistic corrections to the SZ effect in this work, since they are small except for extremely massive clusters.

An important feature of the thermal SZ effect is that it is virtually independent of redshift for clusters of the same properties. This feature of the thermal SZ effect makes it a great probe for massive clusters at high redshift that would otherwise be expensive for optical or X-ray to survey. In practice X-ray, optical, and SZ observations of galaxy clusters taken together are instrumental for determining ICM properties. For example, joint SZ and X-ray probes give insight into the n_e and T_e distributions, since it is the same hot electrons of the ICM that scatter off the ions to produce the bremsstrahlung emission in the X-rays (cf. Fig. 1.4). Optical observations are great at identifying lower mass low redshift clusters

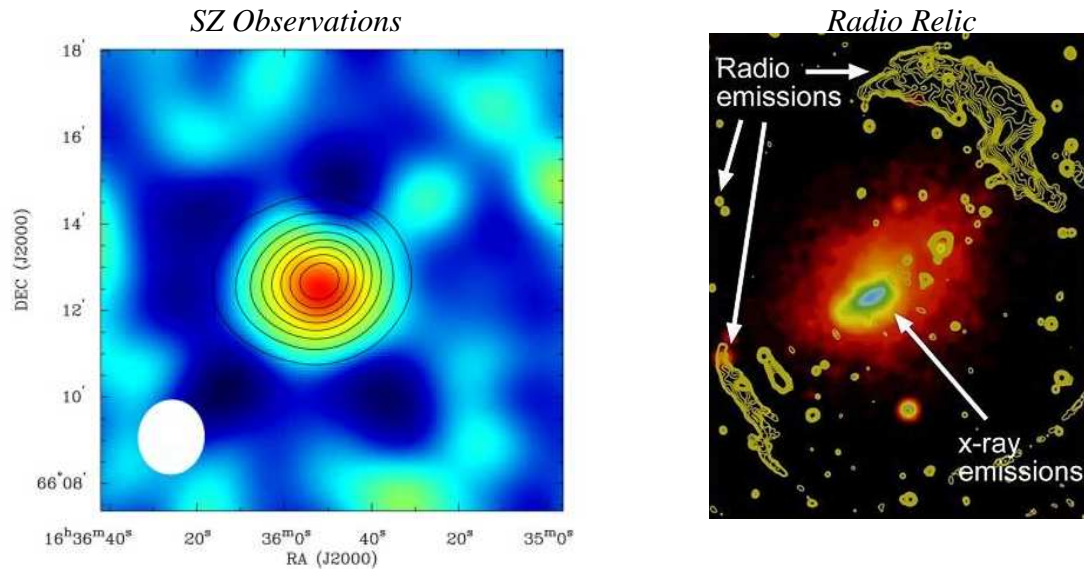


Figure 1.4: Examples of the SZ effect and radio relic observations from galaxy clusters. Left: Composite image of galaxy cluster Abell 2218. The X-ray emission measured by ROSAT is shown in colour and the SZ observations at 28.5 GHz from the Berkeley Illinois Maryland Array interferometer is illustrated by the contours. Credit: Prof. John Carlstrom. Right: Composite image of galaxy cluster Abell 3667, the X-ray emission measured by ROSAT is shown in colour and the radio emission from Australia Telescope Compact Array is illustrated by the contours. Credit: Dr. Melanie Johnston-Hollitt.

that are missed by X-ray and SZ observations, especially through the *red sequence* technique. Weak lensing observations provide independent measurements of mass.

There is currently a wave of new observations of microwave sky being made by the Atacama Cosmology Telescope (ACT), the South Pole Telescope (SPT), and the Planck satellite. They provide large SZ cluster surveys, and the goal of these surveys is to make cosmological measurements (for references to these measurements see Chapters 3, 4, and 5). These SZ observations are pushing the boundaries of the current theoretical models for the ICM.

1.5.3 Diffuse Radio Relic Emission

Diffuse radio emission from galaxy clusters was first observed in the Coma cluster of galaxies (Large et al., 1959). This emission was not associated with any galaxy. Such emission is now observed in well over 50 clusters. It has a steep power-law spectrum, which is indicative of synchrotron radiation, hence the presence of relativistic electrons, cosmic ray electrons, with large Lorentz factors, orbiting around the weak magnetic fields lines of the ICM. The origin of these electrons as well as ions are hypothesized to be from structure formations shocks, where they are accelerated through diffusive shock acceleration (also known as Fermi 1 acceleration). The two main types of diffuse radio emission in clusters have

been given working definitions based on the morphology and orientation within the cluster:

- Radio Halos are located at the centers of clusters and regular/symmetric morphologies, much like the X-ray emission from clusters.
- Radio Relics are located in the outskirts of clusters and have irregular morphologies.

There are further classifications for other less common diffuse radio emissions, such as radio Phoenix and radio mini halo. These are not discussed in this thesis.

The different morphology and orientation of radio relics and halos is hypothesized to come from separate emission mechanisms. The source of the radio relic emission is widely accepted to be relativistic electrons emitting at the location of their acceleration by a structure formation shock. The emission mechanism for radio halos is still debated. In chapter 2 we focus on only radio relic emission, since it traces structure formation in galaxy clusters, the ICM magnetic field strength and the cosmic ray electron content of the ICM. Current Radio telescopes such as the Low Frequency Array, and future telescopes such as the Square Kilometer Array should find even more radio relics.

1.6 Thesis Outline

In chapter 2 we explore the magnetic fields in the galaxy clusters and ICM through radio relic emission. We present a coarse grained self-regulating model of AGN feedback in galaxy clusters and its effects on the ICM and SZ power spectrum in chapter 3. In chapter 4 we characterize the non-thermal pressure support in clusters and the ICM shape. We also explore the impact of non-thermal pressure support and ICM shapes on the SZ scaling relations. In chapter 5 we present a detailed study of the thermal SZ power spectrum. We provide an outlook and summary in chapter 6, and present ideas for future projects.

Chapter 2

Exploring the magnetized cosmic web through low frequency radio emission

A version of this chapter has been published in the Monthly Notices of the Royal Astronomical Society as “Exploring the magnetized cosmic web through low frequency radio emission” Battaglia, N., Pfrommer, C., Sievers, J. L., Bond, J. R., & Enßlin, T. A. 2009, Volume 393, pp. 1073-1089. Reproduced by permission of MNRAS.

2.1 Chapter Overview

Recent improvements in the capabilities of low frequency radio telescopes provide a unique opportunity to study thermal and non-thermal properties of the cosmic web. We argue that the diffuse, polarized emission from giant radio relics traces structure formation shock waves and illuminates the large-scale magnetic field. To show this, we model the population of shock-accelerated relativistic electrons in high-resolution cosmological simulations of galaxy clusters and calculate the resulting radio synchrotron emission. We find that individual shock waves correspond to localized peaks in the radio surface brightness map which enables us to measure Mach numbers for these shocks. We show that the luminosities and number counts of the relics strongly depend on the magnetic field properties, the cluster mass and dynamical state. By suitably combining different cluster data, including Faraday rotation measures, we are able to constrain some macroscopic parameters of the plasma at the structure formation shocks, such as models of turbulence. We also predict upper limits for the properties of the warm-hot intergalactic medium, such as its temperature and density. We predict that the current generation of radio telescopes (LOFAR, GMRT, MWA, LWA) have the potential to discover a substantially larger sample of radio relics, with multiple relics expected for each violently merging cluster. Future experiments (SKA) should enable us to further probe the macroscopic parameters of plasma physics in clusters.

2.2 Introduction and key questions

The plasma within and between galaxies is magnetized. Despite many observational efforts to measure galactic and intergalactic magnetic fields, their properties and origins are not currently well understood. The magnetic fields influence the physics of the plasma in several important ways. They couple the collisionless charged particles to a single but complex fluid through the Lorentz force, and trace dynamical processes in the Universe. Magnetic pressure and tension mediate forces and provide the plasma with additional macroscopic degrees of freedom in terms of Alfvénic and magnetosonic waves. They cause the turbulent cascade to become anisotropic towards smaller scales and suppress transport processes such as heat conduction and cosmic ray diffusion across the mean magnetic field. They are essential for accelerating cosmic rays by providing macroscopic scattering agents which enables diffusive shock acceleration (first order Fermi process) and through magneto-hydrodynamic turbulent interactions with cosmic rays leading to second order Fermi acceleration. They illuminate distant cosmic ray electron populations by enabling synchrotron emission and tell us indirectly about violent high-energy astrophysical processes such as formation shock waves or γ -ray bursts. The magnetic fields in spiral galaxies are highly regular, showing alignment with the spiral arms. They are believed to arise from weak seed fields amplified by dynamo processes, driven by differential rotation in galactic disks. The seed fields could have been produced by many sources, ranging from stellar winds and jets of active galactic nuclei, to plasma instabilities and battery effects in shock waves, in ionization fronts, and in neutral gas-plasma interactions. More hypothetical ideas for the seed field origins invoke primordial generation in early Universe processes, such as phase transitions during the epoch of inflation. In order to understand more about magneto-genesis, we need to study the least processed plasma possible that still shows some primordial memory. This points us to the magnetized plasma in intergalactic space, in particular to the plasma in galaxy clusters. There, magnetic fields show a smaller degree of ordering compared to spiral galaxies. However, their primordial properties may be masked in clusters because of processing by turbulent gas flows, driven by galaxy cluster mergers, and the orbits of the member galaxies. For an overview on the present observational and theoretical knowledge the reader is pointed to the review articles by Rees (1987); Wiełebinski & Krause (1993); Kronberg (1994); Beck et al. (1996); Kulsrud (1999); Beck (2001); Grasso & Rubinstein (2001); Carilli & Taylor (2002); Widrow (2002). This work aims at closing a gap between theoretically motivated phenomenological models of large scale magnetic fields and actual observational non-thermal phenomena associated with them.

Diffuse radio synchrotron emission has already been observed in more than 50 galaxy clusters (Ferrari et al., 2008). The emission is associated with the entire intra-cluster medium (ICM). The synchrotron emission process demonstrates the presence of highly relativistic electrons (cosmic ray electrons, CRe) with a Lorentz factor typically up to $\gamma \sim 10^4$ and magnetic fields within the ICM. The diffuse radio emission can be classified into two categories: radio halos and radio relics. Giant radio

halos are centrally located, trace the thermal emission and show no sign of polarization, while radio relics are located at the periphery of clusters, are polarized and are elongated in appearance. There exist a number of classes of radio objects that have been referred to over the years as “radio relics” (Kempner et al., 2004, and references therein). Two of these are associated with extinct or dying active galactic nuclei (AGN). These either host a synchrotron cooling radio plasma from a past AGN outburst that created the radio lobes or are revived “radio ghosts” where an aged radio relic has been re-energized by a merger or an accretion shock (Enßlin & Gopal-Krishna, 2001).

The focus of this paper is on a third type of radio relic emission, sometimes referred to as radio “gischt”¹ (Kempner et al., 2004), that shows diffuse emission on scales up to 1 Mpc. Diffusive shock acceleration at structure formation shocks can energize a primary population of relativistic electrons that emit synchrotron radiation (Enßlin et al., 1998; Miniati et al., 2001) in a magnetic field that can be amplified by the post-shock turbulence. Prominent examples for this class of radio relics can be seen in Abell 3667 (Röttgering et al., 1997), Abell 2256 (Bridle & Fomalont, 1976; Masson & Mayer, 1978; Bridle et al., 1979; Röttgering et al., 1994; Clarke & Enßlin, 2006), Abell 3376 (Bagchi et al., 2006), and, more recently, Abell 2255 (Pizzo et al., 2008) and Abell 521 (Giacintucci et al., 2008). All galaxy clusters with observed radio relic emission are merging or show signs of ongoing dynamical activity, but not all dynamically active galaxy clusters are observed to have relics. This raises the question of whether diffuse radio emission is a property of a special subset of clusters, or a universal property, with many relics too faint to be seen by current telescopes.

From CMB measurements we know that the Universe is composed of 4.6% baryonic matter, *e.g.* Komatsu et al. (2008). However, when observing the local Universe ($z < 1$), we can account for fewer than half of these baryons (Fukugita, 2004; Danforth & Shull, 2005). This is known as the missing baryon problem. The current cosmological paradigm of large scale structure formation provides a solution to the missing baryon problem. As the Universe evolves, large scale structure grows from small density perturbations imprinted during an earlier epoch. In the hierarchical scenario of structure formation, structure grows from small to large scales, with baryons flowing in a filamentary web with clusters at the interstices. The temperature of baryons deviates from adiabatic cooling associated with the Hubble expansion by increasing multiple times in discrete steps – always corresponding to a passage through a structure formation shock. Before they are shock-heated to the virial temperatures $kT \sim 1 - 10$ keV of galaxy groups and clusters, where they can be observed through their thermal bremsstrahlung emission, they are predicted to reside in the warm-hot intergalactic medium (WHIM). Temperatures in the WHIM are in the range of $10^5 \text{ K} < T < 10^7 \text{ K}$ (Hellsten et al., 1998; Cen & Ostriker, 1999; Davé et al., 2001; Furlanetto & Loeb, 2004; Kang et al., 2005). We will investigate whether it is possible for diffuse radio emission associated with these formation shocks to be used as a tracer of the WHIM

¹The name “gischt” derives from a German word for the crest on top of waves that are breaking at the shore thus resembling the radio emission of freshly injected electrons by formation shocks.

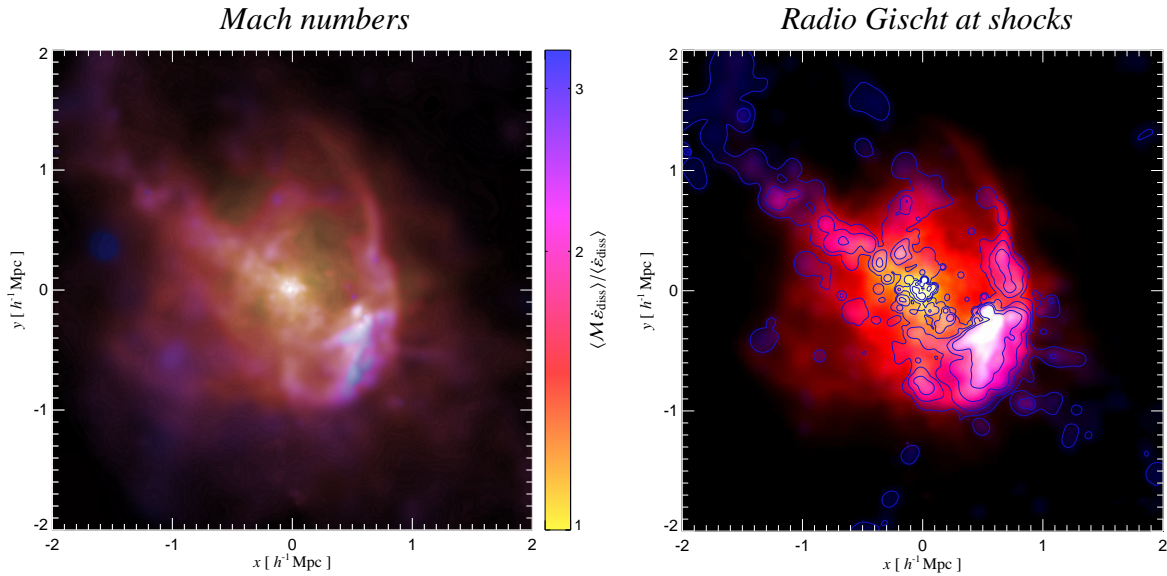


Figure 2.1: Structure formation shocks triggered by a recent merger of a large galaxy cluster ($M \simeq 10^{15} h^{-1} M_{\odot}$) dissipate the associated gravitational energy. Left: the Mach number of shocks weighted by the energy dissipation rate is shown by the colour (while the brightness displays the logarithm of the dissipation rate). Right: three-color image of energy dissipation rate at shocks (shown with a color scale ranging from black over red to yellow) and radio synchrotron emission at 150 MHz from shock-accelerated relativistic electrons (blue and contours with levels starting at 7×10^{-4} mJy arcmin $^{-2}$ and increasing with a factor of 15, respectively). This “radio gischt” emission traces structure formation shock waves, highlights the intermittent nature of mass accretion in galaxy clusters, and illuminates magnetic fields that are amplified by turbulence that can be excited by these shock waves.

boundaries and so indirectly observe the WHIM.

A larger sample size of these diffuse radio sources is required to delve deep into the details of the non-thermal processes working within galaxy clusters. However, the combination of low surface brightness, diffuseness and small dynamical range in the sensitivity of current radio telescopes makes the detection of this particular radio emission difficult. With the current capabilities of the Giant Meter Radio Telescope (GMRT, Ananthakrishnan 1995) and the imminent arrivals of the Low Frequency ARray (LOFAR, Röttgering 2003), the Murchison Wide-field Array (MWA, Morales et al. 2006) and the Long Wavelength Array (LWA, Kassim et al. 2005), and eventually the construction of the Square Kilometre Array (SKA, Keshet et al. 2004b), powerful low frequency radio telescopes are positioned to further increase our understanding of diffuse radio emission and give us insight into the following important topics:

- the strength and coherence scale of magnetic fields on scales of galaxy clusters,

- the process of diffusive shock acceleration of electrons,
- the existence and properties of the WHIM,
- the exploration of observables beyond the thermal cluster emission which are sensitive to the dynamical state of the cluster.

In the course of this work we will consider how radio relic emission can shed light on each of these topics. To do this, we adopt a simplified model for the shock-accelerated population of electrons. The key figure illustrating these considerations is shown in Fig. 2.1. In our simulations, we can visualize properties of structure formation shocks that are triggered by a recent merger of a large galaxy cluster ($M \simeq 10^{15} h^{-1} M_{\odot}$) and dissipate the associated gravitational energy. In the left panel, the shock Mach numbers, weighted by the energy dissipation rate, are encoded by the colour, while the brightness displays the logarithm of the dissipation rate. This shows that most of the energy is dissipated in weak flow shocks internal to the cluster, while the shock waves become strongest and steepest as they break at the shallower peripheral potentials of the clusters and within filaments. The right panel shows a three-color image of energy dissipation rate at shocks (shown in red and yellow) and radio synchrotron emission at 150 MHz from shock-accelerated relativistic electrons (blue and contours, modeled according to Pfrommer et al. 2008). This “radio gischt” emission traces structure formation shock waves and highlights the intermittent nature of mass accretion, in particular along the filament extending from the cluster center to the upper left of the image and for the giant radio relic to the lower-right of the cluster. This radio emission illuminates magnetic fields that are amplified by magneto-hydrodynamic instabilities that are associated with these shock waves. The paper has been structured accordingly: in Sect. 2.3 we outline our methodology; we describe our results and discuss them in Sects. 2.4 and 2.5; and present our conclusions in Sect. 2.6.

2.3 Methodology

We briefly summarize our procedure. We model the synchrotron emission by calculating the primary shock-accelerated electron population using a scheme that is based on the thermal leakage model – a model that has been developed in the context of diffusive shock acceleration at supernova remnants (Ellison et al., 1981). We use a simple parametrization for the magnetic field. This lets us quickly scan the observationally allowed parameter space associated with the mostly-unknown spatial distribution of shocks on cluster scales and beyond. In the post-processing, we search for spatially correlated synchrotron emission from formation shocks, which represent our simulated radio relics and study the properties of these relics in the clusters in our sample. Our aim is to understand how radio observables can be used to reconstruct the physical properties of radio relics, which trace structure formation

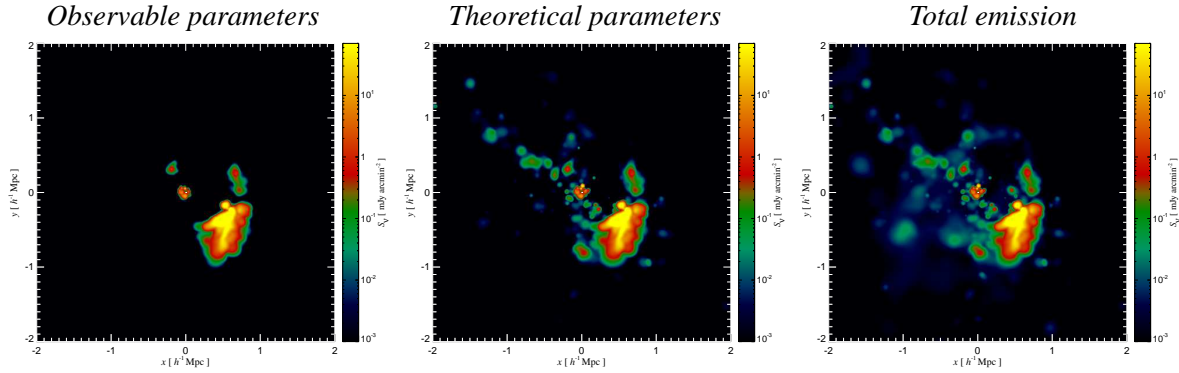


Figure 2.2: Surface brightness emission map for radio relics in the simulated cluster *g72a*. Left to right: the emission from two sets of relic finder parameters, and the total primary radio emission at 150 MHz. Our relic finder groups SPH particles using a friends-of-friends algorithm; we additionally require these particles to exceed a emissivity threshold (ET). The differences in the images illustrate the dependence on ET (left panel: *observable parameters* with $ET = 10^{-43} h^3 \text{ erg s}^{-1} \text{ Hz}^{-1} \text{ ster}^{-1} \text{ cm}^{-3}$, central panel: *theoretical parameters* $ET = 10^{-55} h^3 \text{ erg s}^{-1} \text{ Hz}^{-1} \text{ ster}^{-1} \text{ cm}^{-3}$). The central map only lacks surface brightness at the level of 10^{-3} compared to the total primary emission. Both relic emission maps to the left contain more than 99% of the total flux from the total primary emission map.

and large scale magnetic fields. In the subsequent sections there will be a detailed description of our simulations and modelling.

2.3.1 Adopted cosmology and simulated cluster sample

Our work is based on high resolution smoothed particle hydrodynamics (SPH) simulations of galaxy clusters (minimum gas mass resolution $\sim 8 \times 10^9 h^{-1} M_{\odot}$ for more details, cf. Pfrommer et al., 2007, 2008) using the ‘zoomed initial conditions’ technique (Katz & White, 1993) that were selected from a low resolution dark matter only simulation (Yoshida et al., 2001) with a box size of $479 h^{-1} \text{ Mpc}$. They were carried out using a modified version of the massively parallel tree SPH code GADGET-2 (Springel, 2005). The simulations of the galaxy clusters were performed in a “Concordance” cosmology model, Λ CDM with cosmological parameters of: $\Omega_m = \Omega_{\text{DM}} + \Omega_b = 0.3$, $\Omega_b = 0.039$, $\Omega_{\Lambda} = 0.7$, $h = 0.7$, $n_s = 1$ and $\sigma_8 = 0.9$. Here, Ω_m refers to the total matter density in units of the critical density today, $\rho_{\text{crit}} = 3H_0^2/(8\pi G)$. Ω_b and Ω_{Λ} denote the densities of baryons and the cosmological constant at the present day. The Hubble constant at the present day is parametrized as $H_0 = 100 h \text{ km s}^{-1} \text{ Mpc}^{-1}$, while n_s denotes the spectral index of the primordial power-spectrum, and σ_8 is the *rms* linear mass fluctuation within a sphere of radius $8 h^{-1} \text{ Mpc}$ extrapolated to $z = 0$.

The simulations include a prescription for radiative cooling, star formation, supernova feedback and

Table 2.1: Cluster sample considered in this paper.

Cluster name	Dynamical state ^a	M_{200}^b [$h^{-1}M_{\odot}$]	R_{200}^b [h^{-1} Mpc]	kT_{200}^c [keV]
g8a	CC	1.8×10^{15}	2.0	13.1
g1a	CC	1.3×10^{15}	1.8	10.6
g72a	PostM	1.1×10^{15}	1.7	9.4
g51	CC	1.1×10^{15}	1.7	9.4
g1b	M	3.7×10^{14}	1.2	4.7
g72b	M	1.5×10^{14}	0.87	2.4
g1c	M	1.4×10^{14}	0.84	2.3
g1d	M	9.2×10^{13}	0.73	1.7
g676	CC	8.8×10^{13}	0.72	1.7
g914	CC	8.5×10^{13}	0.71	1.6

^a The dynamical state has been classified through a combined criterion invoking a merger tree study and the visual inspection of the X-ray brightness maps. The labels for the clusters are M–merger, PostM–post merger (slightly elongated X-ray contours, weak cool core region developing), CC–cool core cluster with extended cooling region (smooth X-ray profile).

^b The virial mass and radius are related by $M_{\Delta}(z) = \frac{4}{3}\pi \Delta \rho_{\text{crit}}(z) R_{\Delta}^3$, where $\Delta = 200$ denotes a multiple of the critical overdensity $\rho_{\text{crit}}(z) = 3H(z)^2/(8\pi G)$.

^c The virial temperature is defined by $kT_{\Delta} = GM_{\Delta} \mu m_p / (2R_{\Delta})$, where μ denotes the mean molecular weight.

a formalism for detecting structure formation shocks and measuring the associated shock strengths, i.e. the Mach numbers (Pfrommer et al., 2006). Radiative cooling was computed assuming an optically thin gas of primordial composition (mass-fraction of $X_{\text{H}} = 0.76$ for hydrogen and $1 - X_{\text{H}} = 0.24$ for helium) in collisional ionisation equilibrium, following Katz et al. (1996). We also included heating by a photo-ionising, time-dependent, uniform ultraviolet (UV) background expected from a population of quasars (Haardt & Madau, 1996), which reionises the Universe at $z \simeq 6$. Star formation is treated using the hybrid multiphase model for the interstellar medium introduced by Springel & Hernquist (2003a). In short, the ISM is pictured as a two-phase fluid consisting of cold clouds that are embedded at pressure equilibrium in an ambient hot medium.

The cluster sample is displayed in Table 2.1. From this sample the cluster g72a was chosen for detailed analysis of the properties of radio relics since it is a relatively large (with a mass $M \simeq 10^{15}M_{\odot}$) post-merging cluster, similar to the Coma cluster. Additionally, it hosts the brightest radio relic in the entire sample. This relic resembles already observed ones.

2.3.2 Realization of magnetic fields

Current SPH implementations that are capable of following the magneto-hydrodynamics (MHD) of the gas are presently still fraught with numerical and physical difficulties, in particular when following dissipative gas physics (Dolag et al., 1999, 2005; Price & Monaghan, 2004, 2005). Hence we apply a parametrization in the post-processing of our completed simulations in order to determine the strength and morphology of the magnetic field (Pfrommer, 2008). Secondly, the parametrization approach provides us with the advantage of exploring the parameter space of our magnetic field description more efficiently, since we are not required to re-simulate when we alter the ab-initio unknown magnetic field parameters. We have chosen a simple scaling model for the magnetic field of

$$\varepsilon_B = \varepsilon_{B_0} \left(\frac{\varepsilon_{\text{th}}}{\varepsilon_{\text{th}_0}} \right)^{2\alpha_B}. \quad (2.1)$$

Our independent model parameters are the magnetic decline α_B , and the magnetic core energy density ε_{B_0} . The thermal energy density ε_{th} is measured in units of its central energy density $\varepsilon_{\text{th}_0} = 3P_{\text{th}_0}/2$, which we calculate by fitting a modified β -model (Eqn. 2.2) to the radial pressure profiles of our clusters. We first remove the over-cooled core (see Sect. 2.3.4),

$$P(r) = P_{\text{th}_0} \left(1 + \left(\frac{r}{r_c} \right) \right)^{-3\beta}. \quad (2.2)$$

We found that our modified β -model provides a better fit to the pressure profiles than the usually adopted spherically symmetric King profiles, i.e. a β -model (Cavaliere & Fusco-Femiano, 1978).

This parametrization (Eqn. 2.1) was motivated by non-radiative SPH MHD simulations (Dolag et al., 1999) and radiative adaptive mesh refinement MHD simulations (Dubois & Teyssier, 2008) of the formation of galaxy clusters in a cosmological setting. Rather than applying a scaling with the gas density as those simulations suggest, we chose the energy density of the thermal gas. Current cosmological radiative simulations (that do not include feedback from AGN) over-cool the centres of clusters, giving an overproduction of stars, enhanced central gas densities, and lower central temperatures than are seen in X-ray observations.² In contrast, the thermal energy density of the gas is well-behaved in simulations. Observationally, the parametrization (Eqn. 2.1) is consistent with statistical studies of Faraday rotation measure maps (Vogt & Enßlin, 2005). Theoretically, the growth of magnetic field strength is determined through turbulent dynamo processes that will saturate at a field strength determined by the strength of the magnetic back-reaction (*e.g.* Subramanian, 2003; Schekochihin & Cowley, 2006) and is typically a fraction of the turbulent energy density. The turbulent energy density should be related to the thermal energy density, thus motivating our model theoretically. The parameter ε_{B_0} is constrained by past measurements of magnetic fields within clusters and is chosen such that $B_0 = [\varepsilon_{B_0} 8\pi]^{1/2}$ to be

²Recently, Sijacki et al. (2008a) found that including cosmic rays from AGN in SPH simulations can solve the over-cooling problem while providing excellent agreement of the gas fraction and the inner temperature profile.

Table 2.2: Magnetic field parameters in various combinations.

α_B	B_0 [μG]
magnetic decline	core magnetic field strength
0.3	2.5
0.5	5.0
0.7	10.0
0.9	-

Note: We define our standard magnetic field parameters to be $\alpha_B = 0.5$, $B_0 = 5\mu\text{G}$ and $\nu = 150\text{MHz}$. These parameters are used throughout the paper unless otherwise stated.

on the order of a few μG (Govoni et al., 2006; Taylor et al., 2007; Guidetti et al., 2008). The parameters explored in our model are shown in Table 2.3.2.

To predict the polarization angle and Faraday rotation measure in our simulations, we need to model the magnetic morphology of the ICM. We follow Tribble (1991) in order to create individual components of the magnetic vector field that obey a given power spectrum. The details of the magnetic field structure within the ICM are still unknown. There have been measurements of magnetic correlations from Faraday rotation measure (RM) maps which are however limited by the finite window size of radio lobes and hence only constrain the spectrum on smaller scales. These measurements suggest that the fields are tangled with a Kolmogorov/Oboukhov-type power spectrum for coherence lengths of approximately 10 kpc scales and smaller (Vogt & Enßlin, 2003, 2005; Guidetti et al., 2008). It has been argued that shallower magnetic field power spectra allow for longer coherence lengths on the order 100 kpc (Murgia et al., 2004; Govoni et al., 2006). On the other hand, a Fourier analysis of XMM-Newton X-ray data reveals the presence of a scale-invariant pressure fluctuation spectrum in the range between 40 and 90 kpc and is found to be well described by a projected Kolmogorov/Oboukhov-type turbulence spectrum (Schuecker et al., 2004). Assuming that the growth of the magnetic field strength is determined through turbulent dynamo processes suggests a similar spectrum of magnetic and hydrodynamic turbulence (*e.g.* Subramanian, 2003).

We model the components of the magnetic field, B_i , as random Gaussian fields. We use a Kolmogorov power spectrum on scales smaller than the coherence length, and a flat (white-noise) power spectrum on larger scales. All three components of the magnetic field are treated independently, which ensures that the final distribution of $\mathbf{B}(\mathbf{r})$ has random phases. After mapping our SPH Lagrangian energy density distribution of the thermal gas onto a 3D grid (cf. Appendix Eqn. 2.23), these realizations of the magnetic field are then scaled such that the magnetic energy density obeys our assumed scaling given by Eqn. 2.1. To ensure $\nabla \cdot \mathbf{B} = 0$, we apply a divergence cleaning procedure to our fields in Fourier

space (Balsara, 1998):

$$\tilde{B}_i(\mathbf{k}) = \sum_{j=1}^3 \left(\delta_{i,j} - \frac{k_i k_j}{k^2} \right) \tilde{B}_j(\mathbf{k}). \quad (2.3)$$

Applying this procedure to our Gaussian random field removes a third of the magnetic energy. Thus, we re-normalize \mathbf{B} to conserve the magnetic energy.

2.3.3 Cosmic ray electrons and synchrotron emission

Collisionless cluster shocks are able to accelerate ions and electrons in the high-energy tail of their Maxwellian distribution functions through diffusive shock acceleration (for reviews see Drury, 1983; Blandford & Eichler, 1987; Malkov & O’C Drury, 2001). Neglecting non-linear shock acceleration and cosmic ray modified shock structure, the process of diffusive shock acceleration uniquely determines the spectrum of the freshly injected relativistic electron population in the post-shock region that cools and finally diminishes as a result of loss processes. The radio synchrotron emitting electron population cools on such a short time scale $\tau_{\text{sync}} < 10^8$ yrs (compared to the very long dynamical time scale $\tau_{\text{dyn}} \sim 1$ Gyr) that we can describe this by instantaneous cooling. In this approximation, there is no steady-state electron population and we would have to convert the energy from the electrons to inverse Compton (IC) and synchrotron radiation. Instead, we introduce a virtual electron population that lives in the SPH-broadened shock volume only; this is defined to be the volume where energy dissipation takes place. Within this volume, which is co-moving with the shock, we can use the steady-state solution for the distribution function of relativistic electrons and we assume no relativistic electrons in the post-shock volume, where no energy dissipation occurs. Thus, the cooled CR electron equilibrium spectrum can be derived from balancing the shock injection with the IC/synchrotron cooling: above a GeV it is given by

$$f_e(E) = C_e E^{-\alpha_e}, \quad C_e \propto \frac{\rho}{\varepsilon_B + \varepsilon_{\text{ph}}} \quad (2.4)$$

Here, $\alpha_e = \alpha_{\text{inj}} + 1$ is the spectral index of the equilibrium electron spectrum and ε_{ph} denotes the photon energy density, taken to be that of CMB photons. A more detailed description of our approach can be found in Pfrommer (2008). The synchrotron emissivity j_ν for a power-law spectrum of CRes scales as

$$j_\nu \propto C_e B^{\alpha_e + 1} \nu^{-\alpha_e}, \quad (2.5)$$

where $\alpha_\nu = (\alpha_e - 1)/2$. A line-of-sight summation of j_ν yields the radio surface brightness, S_ν . The surface brightness are provided in units of $h = 0.7$ to simplify comparison with observations.

2.3.4 Finding radio relics

In our search for radio relics in the simulated clusters, we have modified a friends-of-friends (FOF) (Geller & Huchra, 1983) algorithm so that it groups together connected radio synchrotron emission

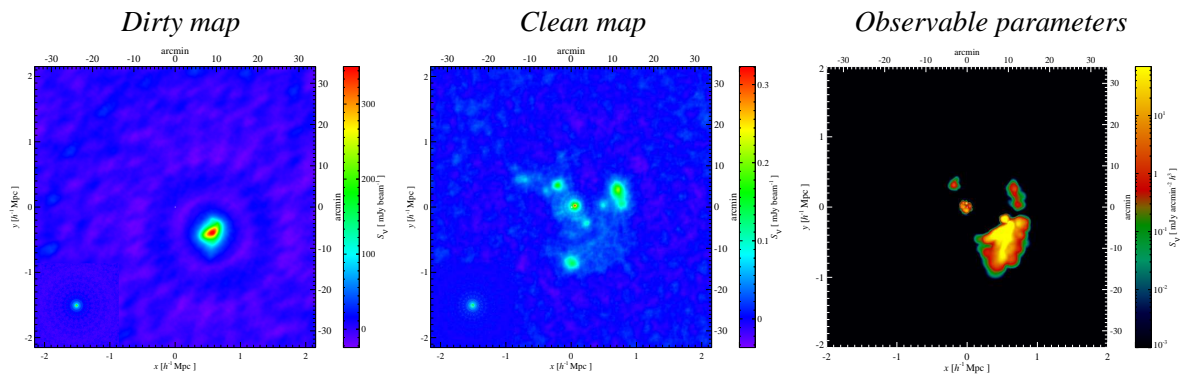


Figure 2.3: Left two panels: simulated GMRT map of the cluster g72a at $z=0.05$ (similar to the Coma cluster), with the reconstructed beam in the bottom-left corner. The left panel is the 'dirty' map and the right panel is the 'clean' map, where we removed the brightest relic found in the dirty map, mimicking the cleaning procedure of radio maps. Right panel: surface emission map of the relics of g72a using our calibrated set of *observable parameters* shown with a logarithmic colour scale. Note that we reproduce the relic emission that can principally be detected by GMRT after applying a cleaning procedure to the compact and diffuse radio emitting sources.

in 3D. This relic finder works in a manner similar to a FOF finder except we have introduced the additional criterion of an emission threshold which the SPH gas particle are required to exceed before being assigned into a group. Thus, our algorithm depends on three internal parameters which determine the groups of particles that are designated relics: the linking length, emissivity threshold, and minimum number of particles (Fig. 2.2). The linking length (LL) is the parameter which controls the maximum distance (d_{\max}) between two particles that can still be considered neighbours,

$$d_{\max} = LL \left[\frac{\langle M_{\text{DM}} \rangle}{\Omega_{\text{DM}} \rho_{\text{crit}}} \right]^{1/3}, \quad (2.6)$$

where $\rho_{\text{DM}} = \rho_{\text{crit}} \Omega_{\text{DM}}$ is the mass density of dark matter and $\langle M_{\text{DM}} \rangle^3$ is the average mass of our dark matter particles. The linking length and the emission threshold parameters have degenerate effects on the resulting groups of particles. Through inspection, we have chosen to fix the linking length value of 0.2 resulting in $d_{\max} = 50$ kpc and vary the emission threshold. A minimum particle value of 32 regulates possible SPH shot noise and allows for smaller structures to be included in the relic catalogue. The final parameter in our relic finder, which we have chosen to vary is the emission threshold. We compute the synchrotron emissivity of all the particles using Eqn. 2.5 and compare it to the emission threshold. The sets of grouped particles for each of our clusters are our relic catalogues that form the basis of our study.

³Note that the quantity in the brackets is equivalent to the ratio of $\langle M_b \rangle / \rho_b$ except that the baryonic phase consists of gas and stars.

Determination of the emission threshold

We tailored the calibration of the emission threshold in the relic finder to two cases: firstly, so that we would find relics observable by GMRT and LOFAR; secondly, so that we could study the complete picture that might be achievable with future radio telescopes such as SKA, by pushing the emission threshold back to the limit of our simulations. For this procedure, we left the magnetic field parameters unchanged. (We used our standard magnetic field parameters cf. Table 2.3.2.)

We simulate the visibilities and maps from the relics that GMRT would observe. We use the GMRT primary beam and antenna positions projected against the zenith (*i.e.* ignoring the z -component of the antenna positions). For simplicity, we approximate the continuous UV tracks for each baseline by circles in the UV plane with measurements 18 degrees apart. We observe cluster g72a surface emission at a redshift of 0.05 (cf. Fig. 2.3) and make a ‘dirty’ radio map, the Fourier transform of the visibilities. We used an integration time of 2.5 minutes with a sensitivity of $0.2 \text{ mJy } \sqrt{\text{hr}}/\text{beam}$ at the frequency $\nu = 150 \text{ MHz}$ in simulating the visibilities.

To approximate GMRT’s dynamical range, we modelled a simple cleaning procedure by removing the brightest relic in the ‘dirty’ map from the total surface emission map and re-simulated the GMRT detections – resulting in our ‘cleaned’ radio map. We compared these maps to surface brightness maps of different relic catalogues where we varied our emission threshold (cf. Fig. 2.3). The emission threshold which reproduced the simulated images most accurately was $10^{-43} h^3 \text{ erg s}^{-1} \text{ Hz}^{-1} \text{ ster}^{-1} \text{ cm}^{-3}$ with the linking length and minimum number of particles already fixed. These parameters are referred throughout this paper as *observable parameters*.

The choice of a second emission threshold is related to the peak of the emissivity distribution function which is determined by the mass resolution of the SPH particles in the simulations. We found the peak emissivity to be at $j_\nu = 10^{-55} h^3 \text{ erg s}^{-1} \text{ Hz}^{-1} \text{ ster}^{-1} \text{ cm}^{-3}$. We find that changing j_ν by six orders of magnitude does not change the number of relics in a significant way (cf. Appendix 2.8), making the difference between peak emissivity and the *observable parameters* reasonable. Together with the linking length and minimum number of particle parameters stated above, these parameters are referred to as *theoretical parameters*. Since the emissivity scales with frequency, the emission threshold must scale with frequency as well. The emission threshold (ET) scaling is fixed at our reference frequency $\nu_0 = 150 \text{ MHz}$,

$$ET = ET_0 \left(\frac{\nu}{\nu_0} \right)^{-1}, \quad (2.7)$$

and ET_0 adopts the values quoted above for both *observational* and *theoretical parameters*.

In summary, the *observable parameters* were chosen to produce relic catalogues resembling the ones obtainable from current or near future observations, whereas the *theoretical parameters* lead to hypothetical catalogues only obtainable with a perfect 3-d tomography of the medium which may find application with the future radio interferometer SKA (cf. Table 2.3.4).

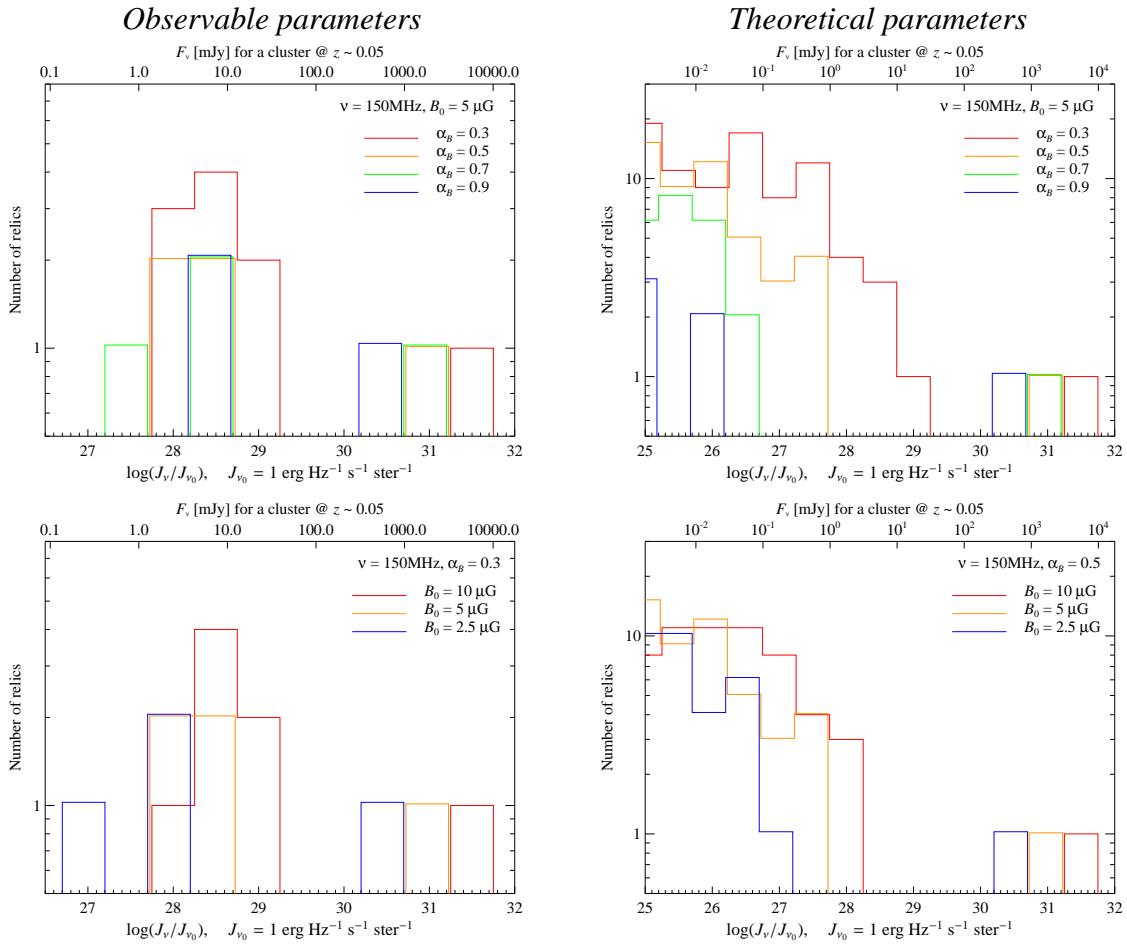


Figure 2.4: Luminosity functions with *observable parameters* (left) and *theoretical parameters* (right) of our relic finder. The top and bottom panels show how the magnetic decline α_B and the magnetic core energy density B_0 impact the luminosity functions, respectively. The choice of magnetic field parameters has a large impact on the shapes of the luminosity function which is a consequence of the inhomogeneous nature of virializing processes in cosmic structure formation. Smaller α_B values, corresponding to a shallower magnetic decline, produce many more brighter relics compared to larger values of α_B , which produce slightly more less-luminous relics. Increasing B_0 results in a greater number of more-luminous relics. Notice the loss of the less-luminous relics from the *observable* to *theoretical parameters*. This is a result of the brightest relic swallowing up smaller relics due to a decrease of the emission threshold parameter.

Table 2.3: Parameters chosen for the relic finder.

parameter name	linking length	minimum number of particles	emission threshold [erg s ⁻¹ Hz ⁻¹ ster ⁻¹ cm ⁻³]
<i>observable</i>	0.2	32	10 ⁻⁵⁵
<i>theoretical</i>	0.2	32	10 ⁻⁴³

Removal of galaxy contamination and cool core

Our radiative simulations model star formation (Hernquist & Springel, 2003) which leads to the formation of galaxies. When applying the criteria described in Sect. 2.3.4, these galaxies appear as false radio relic candidates since they are dense, compact and have enough emissivity per particle to be selected by the relic finder. To select against those objects, we impose further constraints on the SPH particles that are grouped together and require them to have a zero fraction of neutral hydrogen and to be below a very conservative threshold of number density $n_{\text{thres}} = n_{\text{SFT}}/32 = 0.004 \text{ cm}^{-3}$.

Our relic finder also picks up the over-cooled centres of galaxy clusters in our simulations, contaminating the radio emission. Since the candidate relic in the over-cooled center may be physically connected to other true relics, it cannot be removed by simply discarding the closest relic candidate to the center. We apply a very conservative cut in radius of $r = 40 \text{ kpc}$ and neglect the weak dependence on cluster mass and dynamical state. We note that smaller clusters ($M < 5 \times 10^{14} M_{\odot}$), in particular those with dynamical activity, tend to have slightly smaller cooling regions.

2.4 Results

2.4.1 Probing the intra cluster magnetic fields

In this section, we investigate how sensitive different radio synchrotron observables are with respect to the properties of the large scale magnetic field.

Luminosity functions

The magnetic fields within our simulations are parametrized by a simple scaling relation. For each cluster, we compute radio luminosity functions to aid in differentiating between different magnetic field parametrizations by employing the dependency of synchrotron emissivity on the magnetic field of the ICM. Our luminosity functions are distribution functions of the total luminosity per relic (J_{ν}), where

$$J_{\nu} = \sum_a j_{\nu,a} \frac{M_a}{\rho_a} = \sum_a J_{\nu,a}. \quad (2.8)$$

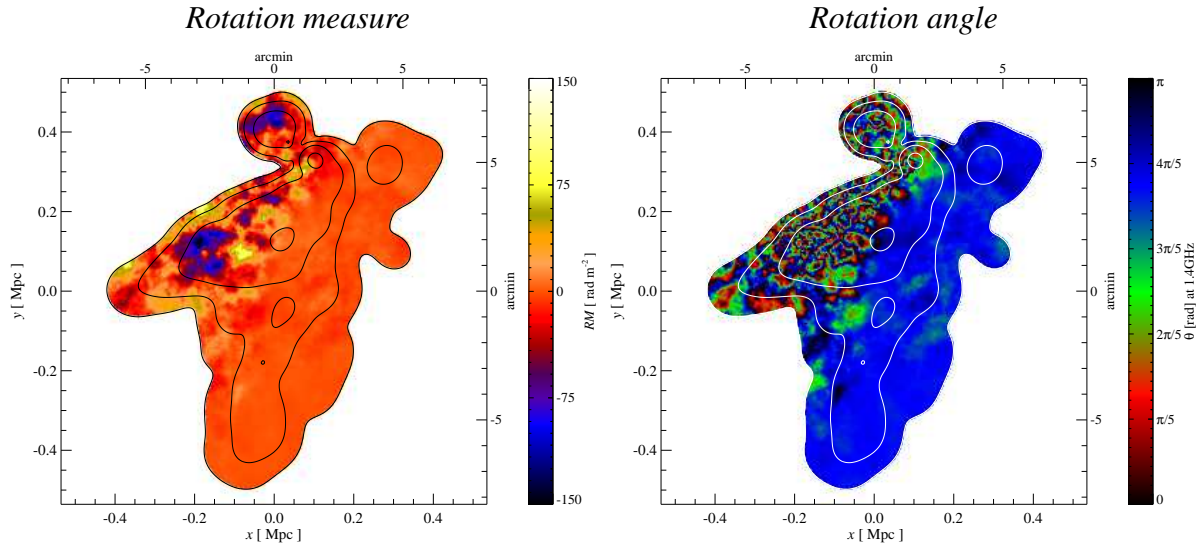


Figure 2.5: Left panel: Faraday rotation measure map of the largest relic in g72a, if the cluster were placed at $z \sim 0.05$ (mimicking A2256). Right panel: Polarization angle map at $\nu = 1.4$ GHz, assuming a uniform rotation angle at the position of the relic. The cluster center is located in the direction of the upper left corner for both the images. Regions with high RM variance correspond to high spatial variation of the polarization angle. In combination with a finite beam size, this makes it challenging to observe a high degree of polarization in such a relic. The magnetic field parameters are $\alpha_B = 0.7 B_0 = 2.5 \mu\text{G}$ and the contours represent the surface brightness increasing in decades from $5 \times 10^{-3} \text{ mJy arcmin}^{-2}$ at $\nu = 1.4$ GHz.

The units of $J_{\nu,a}$ are $\text{erg s}^{-1} \text{Hz}^{-1} \text{ster}^{-1}$, M_a and ρ_a are the SPH gas particle mass and density respectively for the set of SPH particles within the relic labelled by a .

The number of relics seen depends on the magnetic field parametrization. In Fig. 2.4, we show how the luminosity functions depend on B_0 and α_B . As expected, we find more and brighter radio relics for higher values of B_0 . However, rather than simply scaling the luminosity function to higher relic emissivities for larger B_0 (assuming a fixed slope α_B), we find that their shapes change. This is a consequence of the inhomogeneity of the virializing cosmic structure formation waves that are illuminated by the synchrotron emitting electrons. The effect of varying B_0 is analogous to the water level within a very inhomogeneous landscape that corresponds to the strength of the virializing shock waves. This level can adopt different values depending on the magnetic realization such that the resulting synchrotron emitting objects end up single connected or disjoint. So, one could consider using Minkowski functionals to characterize the different relics.

The trend for α_B is the opposite: higher values of α_B lead to a lower number of radio relics. The parameter α_B represents the slope of the magnetic scaling ($\varepsilon_{\text{th}0} > \varepsilon_{\text{th}}$), and a steeper slope will result in the magnetic field strength falling off faster with radius. We expect the effect of both B_0 and α_B on the luminosity function to be a generic effect for all the simulated clusters, since $j_\nu \propto B^{\alpha_\nu+1}/(\varepsilon_B + \varepsilon_{\text{CMB}})$ (cf. Eqns. 2.4 and 2.5) and in the peripheral cluster regions where $\varepsilon_B < \varepsilon_{\text{CMB}}$, we obtain $j_\nu \propto B^{\alpha_\nu+1}$. The luminosity functions alone are not sufficient to fully disentangle the magnetic field properties, this will require other observables.

Rotation measure

Another independent approach to constrain magnetic field models are Faraday rotation measurements. Theoretically, one expects the magnetic field in shocks to be aligned with them due to shock compression (Enßlin et al., 1998) and stretching and shearing motions induced by oblique shocks (Schekochihin & Cowley, 2006). In combination with the small synchrotron emitting volume that is caused by the small synchrotron cooling time, this yields to polarized relic emission. Indeed, radio relics have been observed to be polarized up to the 40 per cent level (Feretti et al., 2004; Clarke & Enßlin, 2006). When polarized radio emission propagates through a magnetized medium, its plane of polarization rotates for a nonzero line-of-sight component of the magnetic field B_z due to the birefringent property of the plasma – Faraday rotation. The Faraday rotation angle is given by

$$\Phi_{\text{obs}} = \lambda^2 RM + \Phi_{\text{init}}, \quad (2.9)$$

where

$$RM(\mathbf{x}_\perp) = a_0 \int_0^L B_z(\mathbf{x}) n_e(\mathbf{x}) dz \quad (2.10)$$

$$\simeq 812 \frac{\text{rad}}{\text{m}^2} \frac{B}{\mu\text{G}} \frac{n_e}{10^{-3} \text{cm}^{-3}} \frac{L}{\text{Mpc}}, \quad (2.11)$$

where $a_0 = e^3/(2\pi m_e^2 c^4)$, $\mathbf{x} = (\mathbf{x}_\perp, l)$, and n_e is the number density of electrons. In Eqn. 2.11, we have assumed constant values and a homogeneous magnetic field along the line-of-sight to give an order of magnitude estimate for RM values. Assuming statistically homogeneous and isotropic magnetic fields, the RM dispersion $\langle RM^2 \rangle$ reads as follows,

$$\langle RM^2 \rangle = a_0^2 \left\langle \left[\int_0^L n_e(\mathbf{x}) B_z(\mathbf{x}) dz \right]^2 \right\rangle \quad (2.12)$$

$$= a_0^2 \frac{3\lambda_B}{2} L \langle n_e(\mathbf{x})^2 B_z(\mathbf{x})^2 \rangle \quad (2.13)$$

$$= a_0^2 \frac{3\lambda_B}{2} L C_{n_e B_z} \langle n_e(\mathbf{x})^2 \rangle \langle B_z(\mathbf{x})^2 \rangle, \quad (2.14)$$

where

$$C_{n_e B_z} = \frac{\langle B_z^2 n_e^2 \rangle}{\langle B_z^2 \rangle \langle n_e^2 \rangle}, \quad (2.15)$$

is defined as the correlation factor and $\lambda_B = 2/3 \times \lambda_z$ is the 3D magnetic auto-correlation scale (Enßlin & Vogt, 2003) which can be estimated from the measured RM power spectrum.

We studied the Faraday rotation of the largest relic in cluster g72a (Fig. 2.5). The aim is to recover intrinsic statistical properties of the ICM magnetic field by studying RM statistics. We produce the RM map by projecting the line-of-sight component of our tangled magnetic field (Sect. 2.3.2) and the thermal electron density that has also been mapped from its Lagrangian distribution onto a 3D grid.⁴ Firstly, we are concerned about the observability of polarized emission. The RM scales with B_\parallel and n_e according to Eqn. 2.10 such that we expect RM values to increase across the relic towards the projected cluster center. However, large RM values leads to confusion when trying to observe the polarization angle. Beam width depolarization (Gardner & Whiteoak, 1966) takes place if the polarization angle changes by a radian on scales shorter than the beam. To avoid this, one can go to shorter wavelengths and smaller beams at the expense of radio luminosity. Secondly, we are concerned with RM contamination from the galaxy. Even at moderately high galactic latitudes the galactic RM contribution (Simard-Normandin et al., 1981) can be approximately the same order as the RM we calculate. However, the strength of our RM depends on the relic location with respect to the cluster and observer, as well as our magnetic field parameters. Therefore, a different location or parametrization will lead to stronger or weaker RM. Also, the galactic RM in principle can be modelled and removed from the RM map.

High-quality rotation measure maps enable one to measure the RM power spectra. The large angular extent of giant radio relics provides a powerful tool of probing the maximum coherence scales of the magnetic field in clusters; in contrast RM maps from radio lobes are typically much smaller. We calculate power spectra from our RM maps and magnetic field realizations for each model separately (Fig. 2.6 and Table 2.4.1). For consistency reasons, we only consider the volume subtended by the radio

⁴Note that we neglect gas above the very conservative threshold of number density $n_{\text{thres}} = n_{\text{SFT}}/32$ to be consistent with our proceeding in Sect. 2.3.4.

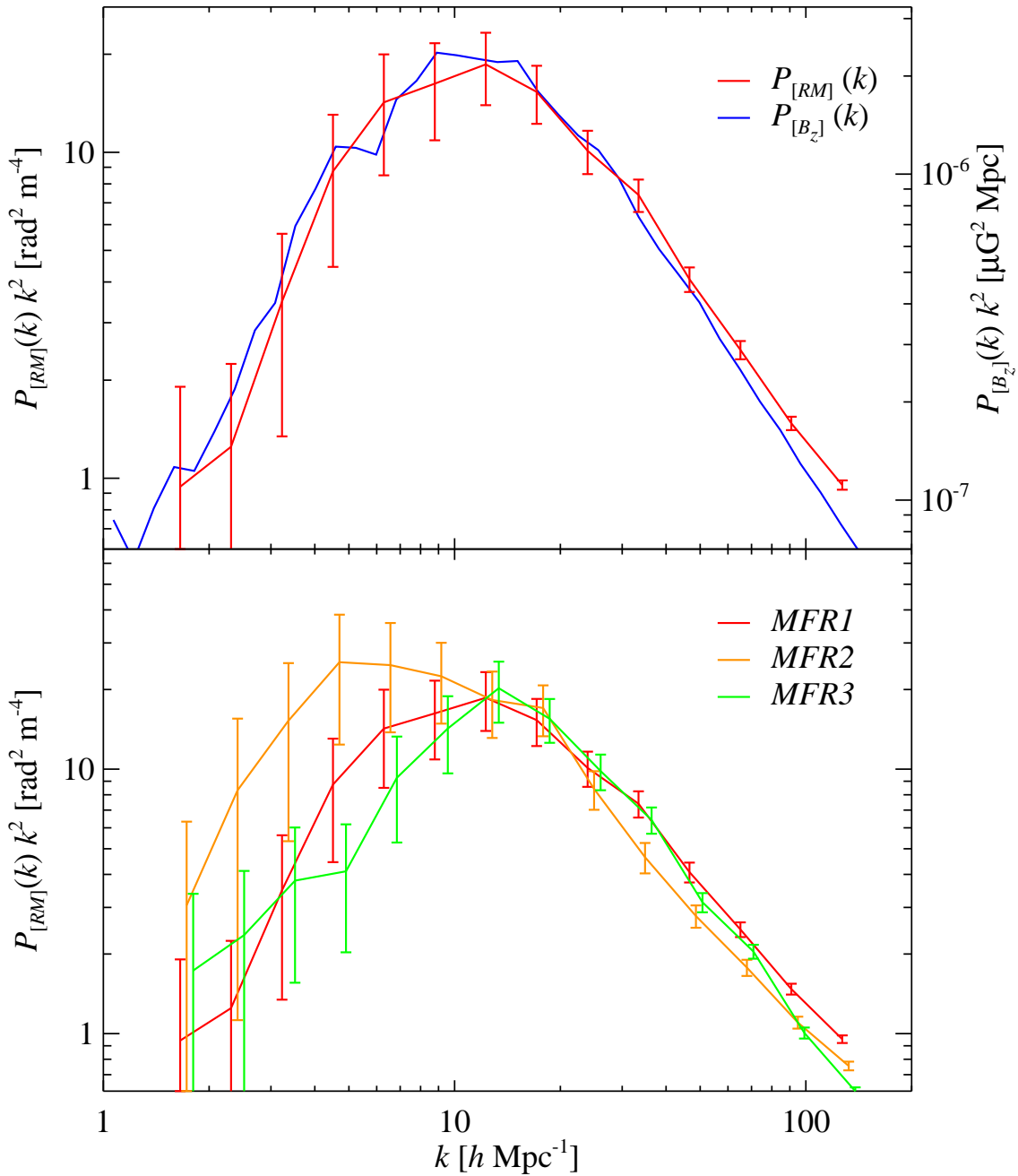


Figure 2.6: Top: power spectrum of the RM map $P_{[RM]}(k)$ and power spectrum of the line-of-sight component of the magnetic field $P_{[B_z]}(k)$ for MFR1, where the error bars represent the 1σ confidence regions. $P_{[RM]}(k)$ attains excess power at large angular scales from fluctuations in n_e . Our RM power spectrum matches the shape and the peak scale of the input power spectrum within the error bars. Bottom: power spectra of RM maps for different magnetic field realizations (cf. Table 2.4.1). All RM power spectra recover the shape and characteristic scale of their magnetic input power spectra.

Table 2.4: Magnetic field realizations (MFR) used in RM maps.

magnetic field realization name	correlation length (λ_B) [h^{-1} kpc]	input slope of power spectra
MFR1	100	-5/3
MFR2	200	-5/3
MFR3	100	-2

relic when calculating the magnetic power spectrum. We define the RM power spectra ($P_{[RM]}$) and the power spectrum of B_z ($P_{[B_z]}$) as follows,

$$\langle RM^2 \rangle = 2\pi \int_0^\infty k P_{[RM]} dk, \quad (2.16)$$

$$\langle B^2 \rangle = 3 \cdot 4\pi \int_0^\infty k^2 P_{[B_z]} dk, \quad (2.17)$$

where the additional factor of three accounts for fluctuations in the total magnetic field while assuming our random Gaussian field. A partial Monte Carlo method was used to determine the 1σ error bars on the power spectrum. Assuming a constant magnetic coherence scale, we construct the envelope function by computing the variance of RM (Eqn. 2.13). We multiply this envelope function with 10^3 realizations of random Gaussian field and measure the power spectrum on each of these maps. The fractional errors are computed from the variance of these power spectra. While the first six power spectrum bins are on average 50 per cent correlated, the correlations drop to be below 20 per cent for the bins on smaller scales.

By construction our parametrization of the magnetic field is correlated with the electron number density n_e which might possibly introduce biases in our RM maps. However, comparing RM power spectrum to the magnetic power spectrum, we find that the RM power spectrum overall resembles the original shape of the magnetic power spectrum and the injection scale corresponds to the scale of maximal power in the RM map. This is true for all our magnetic field realizations. We measure the slope of these power-laws at small scales to an accuracy of ± 0.05 , which is significant to differentiate between Kolmogorov ($k^{-5/3}$) and Burgers (k^{-2}) turbulence spectra. We also find that the measurement of the RM power spectrum slope is independent of the magnetic field parameters α_B and B_0 . The full correlation matrix of the power spectrum bins is used when fitting the power-laws and in the error calculations. We find that our measured slope is flatter than expected and can be attributed to small scale fluctuations in n_e , since $P_{[B_z]}$ has the same slope as the power spectrum of B_z integrated along the line of sight. The small inhomogeneity of n_e in our simulations does not severely affect the intrinsic spectral shape. Thus, it is possible in principle to recover the intrinsic 3D magnetic power spectrum by solving the inverse problem (Vogt & Enßlin, 2003; Enßlin & Vogt, 2003; Vogt & Enßlin, 2005).

Using Eqns. 2.14, 2.16 and 2.17 we estimated the *rms* magnetic field strength from $P_{[RM]}$ and $P_{[B_z]}$ respectively and recover our initial *rms* magnetic field strength. We find that our correlation factor ($\sqrt{C_{n_e B_z}} \simeq 5.3$)⁵ is 20 per cent larger than the correlation factor obtained by fitting a smooth β -model to the spherically averaged profile of n_e and scaling $B \propto n_e^{\alpha_B}$ with the same $\alpha_B = 0.7$ that we used to construct our RM maps (similar to the procedure applied by Enßlin & Vogt 2003 and Murgia et al. 2004). This result suggests that the fairly homogeneous density distribution in our simulations (after removing the galaxy contamination described in Sect. 2.3.4) does not severely bias the average magnetic field strengths estimated by RM studies if one takes into account the overall shape of the profiles of n_e and B .

For convenience, we derive a formula for the *rms* magnetic field strength ($\sqrt{\langle B^2 \rangle}$) as a function of the peak of $P_{[RM]}$ and the *rms* fluctuations of n_e . Multiplying $P_{[RM]}$ with a Heaviside function $\Theta(k)$ and ensuring that the intrinsic spectrum is sufficiently steeper than k^{-2} , Eqn. 2.16 becomes

$$\begin{aligned} \langle RM^2 \rangle &\simeq 2\pi \int_0^\infty k P_{[RM]}(k) \Theta(k - k_{\text{peak}}) dk, \\ &\simeq \pi P_{[RM]}(k_{\text{peak}}) k_{\text{peak}}^2. \end{aligned} \quad (2.18)$$

The value of $P_{[RM]}(k_{\text{peak}}) k_{\text{peak}}^2$ can be read off directly from Fig. 2.6 and combining Eqns. 2.18 and 2.14 yields an approximate value for $\sqrt{\langle B^2 \rangle}$,

$$\begin{aligned} \sqrt{\langle B^2 \rangle} &\simeq \sqrt{\frac{2\pi P_{[RM]}(k_{\text{peak}}) k_{\text{peak}}^2}{a_0^2 \lambda_B L C_{n_e B_z} \langle n_e^2 \rangle}} \\ &\simeq 0.1 \mu\text{G} \left(\frac{P_{[RM]}(k_{\text{peak}}) k_{\text{peak}}^2}{50 \text{ rad m}^{-2}} \right)^{\frac{1}{2}} \left(\frac{\sqrt{\langle n_e^2 \rangle}}{10^{-4} h^2 \text{ cm}^{-3}} \right)^{-1} \\ &\times \left(\frac{\lambda_B}{100 h^{-1} \text{ kpc}} \right)^{-\frac{1}{2}} \left(\frac{L}{4 h^{-1} \text{ Mpc}} \right)^{-\frac{1}{2}} \left(\frac{C_{n_e B_z}}{27} \right)^{-\frac{1}{2}}, \end{aligned} \quad (2.20)$$

where we inserted numerical values from our simulation in the last step.

2.4.2 Existence and properties of the WHIM

In this section, we investigate the potential of radio relic observations to infer the hydrodynamic properties such as density and temperature of the WHIM.

Properties of virializing shocks

Diffusive shock acceleration determines the shape of the CRe spectrum that we model as a power-law momentum spectrum (neglecting non-linear effects). Synchrotron losses cause a steepening of this

⁵We caution the reader that the particular value of $C_{n_e B_z}$ reflects the parametrization of the magnetic field we adopt in our model, and may be realized differently in Nature. We also note that the value of the correlation factor in the non-radiative simulation by Pfrommer et al. (2008) is $\sqrt{C_{n_e B_z}} \simeq 6$. Further work is required to address this question in the context of MHD cluster simulations.

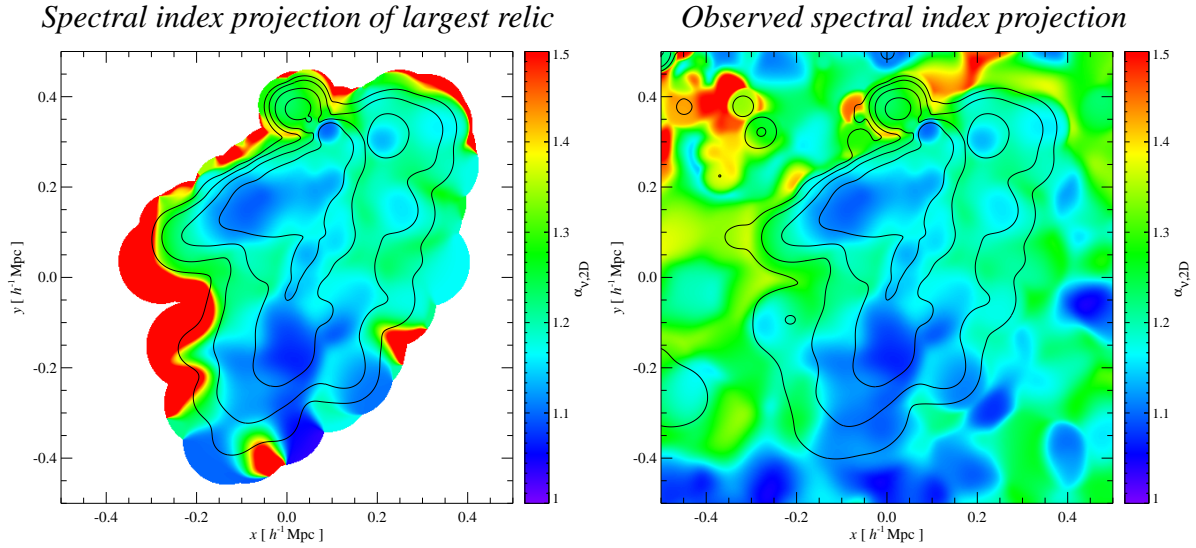


Figure 2.7: Spectral index map, $\alpha_{\nu,2D}$, between 150 MHz and 1.4 GHz for the largest relic in g72a, with only the SPH particles selected by the relic finder projected (left panel) and for the total emission in the same region (right panel). The contours show orders of magnitude in surface brightness in mJy arcmin^{-2} , with the highest contour representing $5 \text{ mJy arcmin}^{-2}$ at $\nu = 1.4 \text{ GHz}$. Notice the edge effects that show up in the projection of the single relic where the emission falls off. These effects are due to the sharp emissivity cutoff of our relic finder and incomplete sampling of SPH relic particles at different frequencies. More importantly, in regions with high synchrotron brightness, the spectral index is almost uniform across the central relic implying that this relic traces a single formation shock wave.

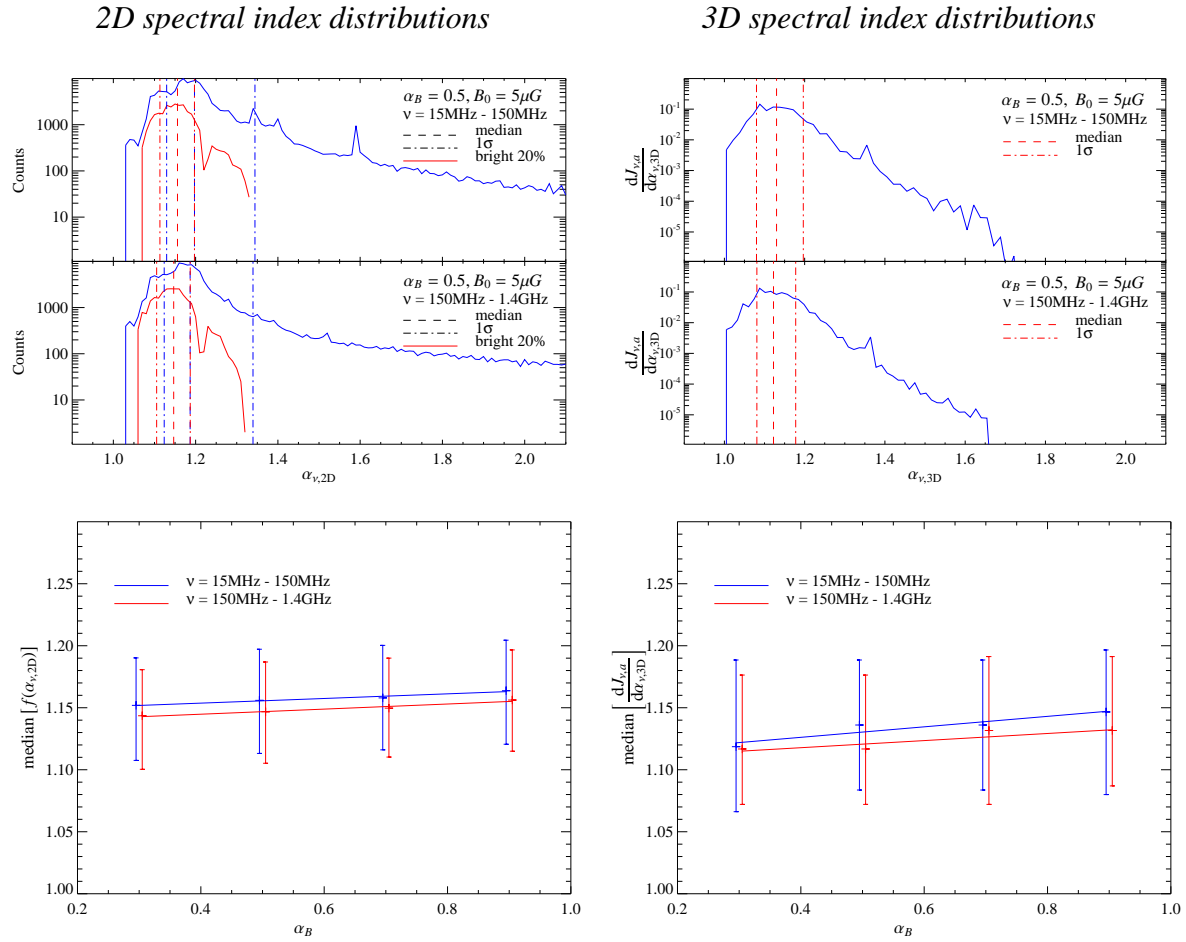


Figure 2.8: Top: spectral index distributions for our largest relic using our standard particular magnetic field parametrization. 2D spectral index distributions, $f(\alpha_{v,2D})$, of the full map and the brightest 20 percent pixels (top left) are contrasted to the radio luminosity weighted distribution of the 3D spectral index, $dJ_{v,a}/d\alpha_{v,3D}$ (top right). Bottom left: the median of $f(\alpha_{v,2D})$ for the brightest 20 percent pixels ($S_\nu \geq 12 \text{ mJy arcmin}^{-2}$ at $\nu = 150 \text{ MHz}$ and $S_\nu \geq 1 \text{ mJy arcmin}^{-2}$ at $\nu = 1.4 \text{ GHz}$) as a function of the magnetic declination α_B with the error bars representing the 1σ percentiles. Bottom right: the median of $dJ_{v,a}/d\alpha_{v,3D}$ as a function of the magnetic declination α_B with the error bars representing the 1σ percentiles. This shows that for the giant radio relic of g72a, the median of the 2D and the 3D spectral indices agree statistically and are almost independent of the magnetic declination α_B .

power-law by one power of momentum. Spatially inhomogeneous virializing shocks with a distribution of shock strengths cause a spatial variation of the spectral index of the cooled CR electron spectrum. This is reflected in an inhomogeneous distribution of synchrotron spectral index that may help to reconstruct the merging geometry by providing a snapshot of the structure formation process in a galaxy cluster.

The spectral indices of the radio surface brightness $\alpha_{\nu,2D}$ and that of the intrinsic 3D emissivity $\alpha_{\nu,3D}$ are defined by,

$$\alpha_{\nu,2D} = -\frac{\log(\frac{S_{\nu}}{S_{\nu_0}})}{\log(\frac{\nu}{\nu_0})}, \quad (2.21)$$

$$\alpha_{\nu,3D} = -\frac{\log(\frac{J_{\nu,a}}{J_{\nu_0,a}})}{\log(\frac{\nu}{\nu_0})}. \quad (2.22)$$

It is unclear ab initio whether the projected spectral index represents the actual deprojected quantity ($\alpha_{\nu,3D}$) due to possible superposition of different radio emitting structures along the line-of-sight. We study how these two quantities relate to each other, and present 2D spectral index maps of both the largest radio relic in g72a and the total emission from the same area (cf. Fig. 2.7). We note that more than 99 per cent of the total radio emission can be attributed to emission within the radio relic. As a result, the $\alpha_{\nu,2D}$ maps are not contaminated by the diffuse spurious emission. Note the edge effects in Fig. 2.7 that show up in the projection of the single relic where the emission falls off. These effects are due to the sharp emissivity cutoff of our relic finder and incomplete sampling of SPH relic particles at different frequencies. In regions with high synchrotron brightness, one can ignore these edge effects, and the resulting distribution of $\alpha_{\nu,2D}$ is fairly uniform ($\langle\alpha_{\nu,2D}\rangle \simeq 1.15$, with $\sigma_{\alpha_{\nu,2D}} \simeq 0.04$) implying that this relic traces a single structure formation shock wave.

We further study the distribution of $\alpha_{\nu,2D}$ and $\alpha_{\nu,3D}$ in our largest individual relic to uncover a connection between them. Probability distribution functions (PDF) are constructed for both $\alpha_{\nu,2D}$ and $\alpha_{\nu,3D}$ for varying parameters of the magnetic field (cf. Fig. 2.8). To avoid contamination from edge effects seen in Fig. 2.7, the $\alpha_{\nu,2D}$ PDF was made for the brightest 20 per cent of the pixels and the $\alpha_{\nu,3D}$ PDF was weighted by particle emissivity. These distributions do not change with our choices for magnetic field parameters implying that the spectral indices are practically independent of the magnetic field and depends mainly on properties of the shock. Another striking result is that the median values for $\alpha_{\nu,2D}$ and $\alpha_{\nu,3D}$ are statistically consistent within $1-\sigma$. Assuming that the line-of-sight integral is dominated by one bright relic and choosing a pixel scale that is smaller than the length scale on which the post-shock density varies, we can easily show that the 2D and intrinsic 3D spectral index are identical. If there are more radio emitting regions contributing to the observed surface brightness, we expect a concave radio spectrum. Synchrotron cooling as well as re-acceleration lead to spectral steepening in particular at high radio frequencies (Schlickeiser et al., 1987). Future work is required to address the associated biases of the relation between $\alpha_{\nu,2D}$ and $\alpha_{\nu,3D}$.

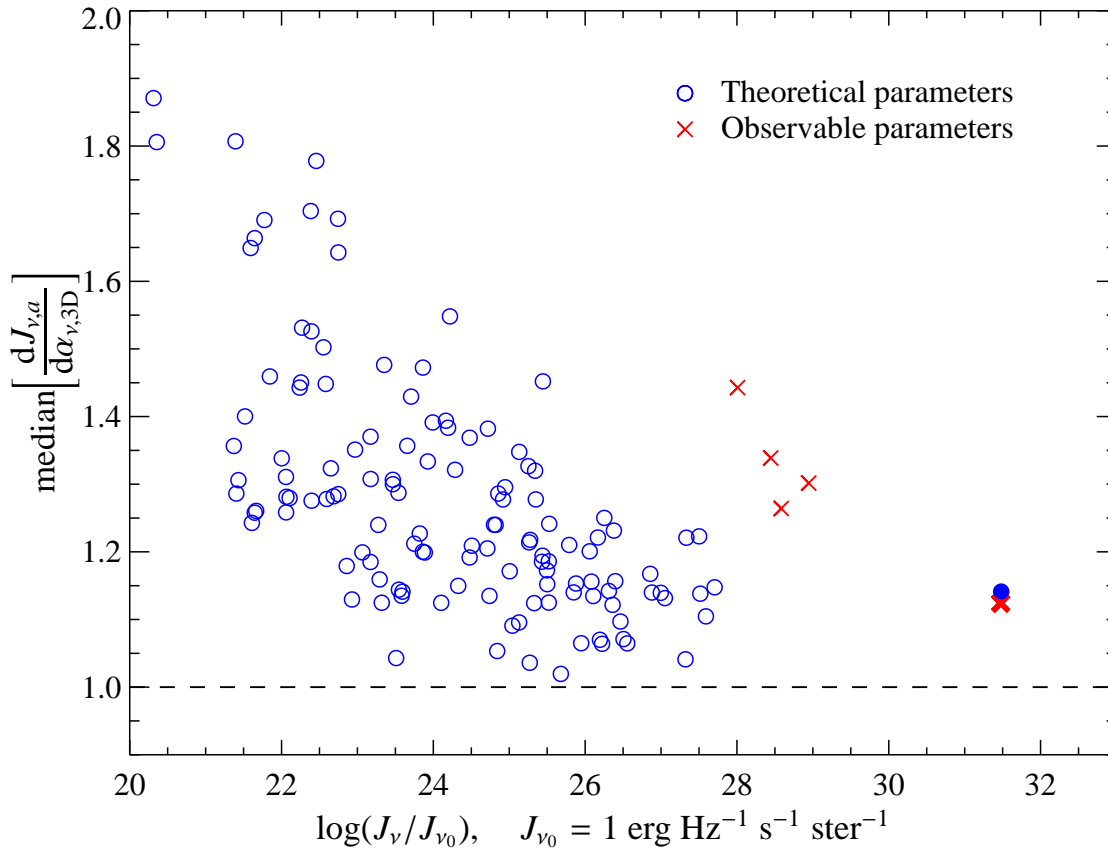


Figure 2.9: Two dimensional observable parameter space for radio relics in galaxy cluster g72a. Each symbol represents a relic within g72a and they are characterized by total luminosity and median of the 3D spectral index. Shown are *observable* relics (red crosses), *theoretical* relics (blue circles) and the large relic is emphasized by the bold cross and the filled circle. There is a trend to high spectral indices and a larger scatter for less luminous relics. As shown in Fig. 2.4, the loss of the less luminous relics from the *observable* to *theoretical* parameters is a result of the brightest relic swallowing up these smaller relics due to a decrease of the emission threshold parameter.

Figure 2.9 shows the observable parameters space of relic luminosity and the median 3D spectral index. This parameter space compares the shocks strength, which is related to the 3D spectral index (cf. Eqn. 2.27) to the energy dissipated at the shock, which is related to the relic luminosity. There is a trend that strong shocks are associated with the more luminous relics. The implications of this trend is that the brightest radio relics should show predominantly flatter spectral indices, which is the current observational status of giant radio relics (Ferrari et al., 2008).

Predicting pre-shock properties

A majority of the hot gas ($> 10^7$ K) found at the centers of galaxy clusters is believed to originate from the WHIM that is shock heated through large-scale virializing structure formation shocks. These structure formation shocks are traced by synchrotron emission in form of radio relics from recently accelerated electrons (cf. Sect. 2.3.3). We have shown that under particular conditions, the observed median 2D spectral index corresponds to the weighted median 3D spectral index $\alpha_{v,3D}$ (cf. Sect. 2.4.2). The 3D spectral index can be related to the Mach number of the shock (cf. Eqn. 2.27) under the assumption that we have an ideal fluid with a given adiabatic index. One can obtain information on the post-shock values for density, pressure and temperature of the ICM through deprojections of deep X-ray or Sunyaev-Zel'dovich observations (Zaroubi et al., 1998). With the knowledge of the Mach numbers combined with post-shock values we calculate the pre-shock conditions of the ICM (the WHIM) using the Rankine-Hugoniot jump conditions (cf. Appendix 2.9).

We take an optimistic approach and assume that the deprojections of the thermal observables can be done ideally such that we use our radial profiles calculated from the solid angle subtended by the largest relic for simplicity (cf. Fig. 2.10). We define the shock region by locating the radial bins that contain the majority of shocked relic particles ($> 85\%$). A small fraction of the relic particles leak into radial bins adjacent to the shock causing slight enhanced values of the radial profile. As mentioned above we insert the calculated average Mach number and the post-shock value into the Rankine-Hugoniot jump conditions for density, pressure and temperature to estimate the upper limits of these WHIM properties. Our predicted upper limits for pressure and temperature of the WHIM are consistent with the simulated pre-shock properties within one standard deviation. We note that the standard deviation of these hydrodynamic properties reflect actual physical variations due to an oblique shock that is not perfect tangential. Additionally, the particular relic chosen is located at $\sim R_{200}/2$, which is within the cluster volume. There are other observationally known relics that reside at the virial radius and beyond (e.g. Bagchi et al., 2006). These relics are better suited to probe the WHIM in combination with future X-ray and multi-frequency SZ data. Thus, this example is to be taken as a demonstration of our concept.

In the following we want to address possible biases with our method and show that the discrepancy between the predicted values and the average radial value of the WHIM can be explained by differences between the calculated Mach numbers and the median of the weighted Mach numbers in the radio relics

(cf. Fig. 2.11). We find that the weighted Mach numbers have systematically lower values compared to the theoretical expectation due to the skewed distribution of the emissivity weighted $\alpha_{v,3D}$. According to the Rankine-Hugoniot jump conditions, systematically higher values of the shock strength should over-estimate the jumps and hence under-predict all the pre-shock quantities, which appears to be the case (Fig. 2.10).

2.4.3 Dependence on dynamical state and cluster mass

We study the distribution of radio relics for the entire galaxy cluster sample, which shows a variety of both dynamical states (ranging from merging to cool core clusters) and masses (a range of almost two orders of magnitude). In Fig. 2.12, we investigate how cluster mass and dynamical state depend on the relic luminosity function. In the case of our theoretical parameter space, more massive galaxy clusters clearly have more radio relics than the lower mass clusters with a power-law scaling of $M_{200}^{0.9}$ (Fig. 2.13). For the current observational capabilities, we predict that only the most massive clusters should have a significant sample of radio relics.

Ideally, one would like to directly compare clusters with the purpose of using relic number statistics as a mass proxy. However, the luminosity functions have another trend, which causes the scatter in the relationship between clusters mass and total number of relics per cluster. This trend relates the cluster's dynamical state to the luminosity of their brighter relics. The clusters g72a and g51 have the same virial mass $1.1 \times 10^{15} M_{\odot}$, but g51 is a relaxed cool core clusters in contrast to the active state of g72a. One can see the two most luminous radio relics of g72a are an order of magnitude brighter than any of g51's relics. Furthermore, the total amount of relics of g72a is greater than that of g51. Merging clusters inherently have more shocks which yields to more high-energy CRes and magnetic field amplification resulting in more radio relics. This trend is even more severe for galaxy clusters of smaller mass (Fig 2.12). Our results show a larger probability of observing a relic in a more massive cluster that is dynamically active. This dependence on mass and dynamical state offers a possible explanation for why all current observed radio relics are in massive merging clusters. They are expected to be the brightest of a dimmer population of radio relics.

2.5 Discussion

2.5.1 Comparison with previous theoretical work

Previously, there has been analytical work (Keshet et al., 2004a) and pioneering cosmological simulations (Miniati et al., 2001, 2000) on studying cluster synchrotron emission from shock-accelerated electrons. The latter authors simulated the non-thermal cluster emission by numerically modelling discretised cosmic ray (CR) energy spectra on top of Eulerian grid-based cosmological simulations. Their

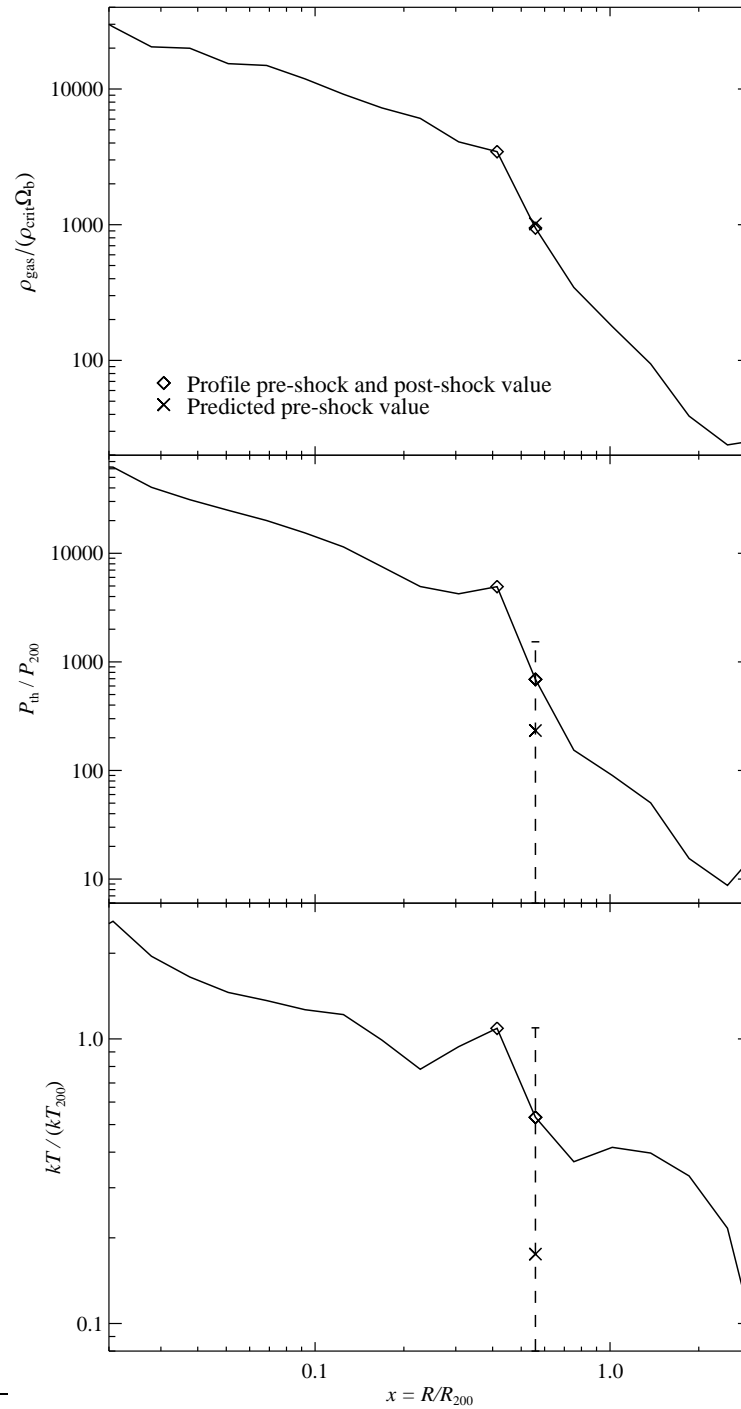


Figure 2.10: Radial profiles of galaxy cluster g72a restricted to the solid angle subtended by the largest relic for the density, pressure and temperature. The shocked region is seen in the profile at roughly $R_{200}/2$ and is marked by the black diamonds with one sigma error bars, except for the density profile where the error bars are too small to show. The predicted pre-shock values (crosses) are $\sim 7\%$, $\sim 67\%$ and $\sim 67\%$ different from the average profile values, but fall within the standard deviation for pressure and temperature. Most of this variation is caused by the shock being oblique and not perfectly tangential.

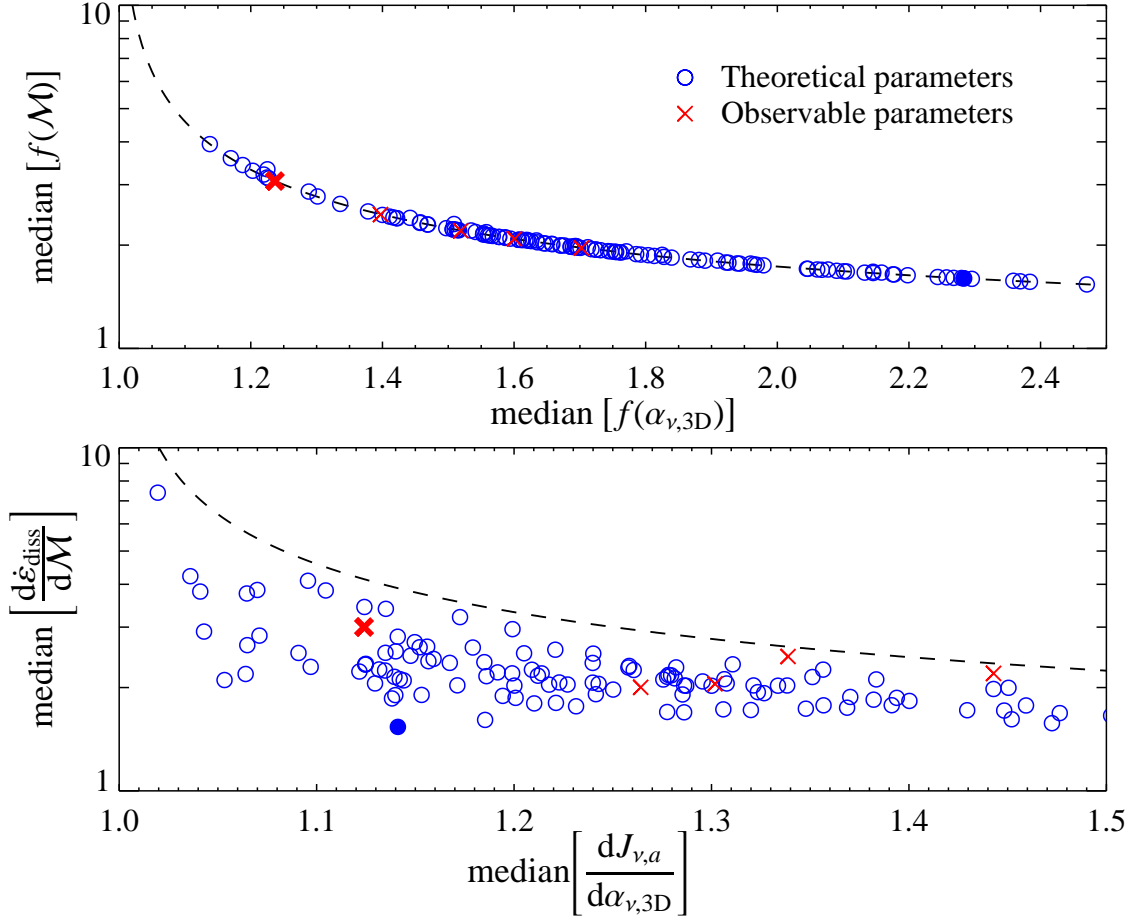


Figure 2.11: Top: median of the Mach number distribution for each relic as a function of the median of the distribution function of $\alpha_{v,3D}$. Bottom: the observationally relevant quantities are the weighted distribution functions. Shown are median of $d\dot{\mathcal{E}}_{\text{diss}}/d\mathcal{M}$ as a function of $dJ_{v,a}/d\alpha_{v,3D}$, where each point represents a radio relic in cluster g72a. Shown are *observable* relics (red crosses), *theoretical* relics (blue circles) and the large relic is emphasized by the bold cross and the filled circle. The dashed line is the theoretical Mach number computed from directly from the $\alpha_{v,3D}$ (cf. Appendix Eqn. 2.27). The theoretical Mach number over-predicts the median of the weighted Mach number, due to the weighting of $\alpha_{v,3D}$ by the skewed distribution function of the radio luminosity.

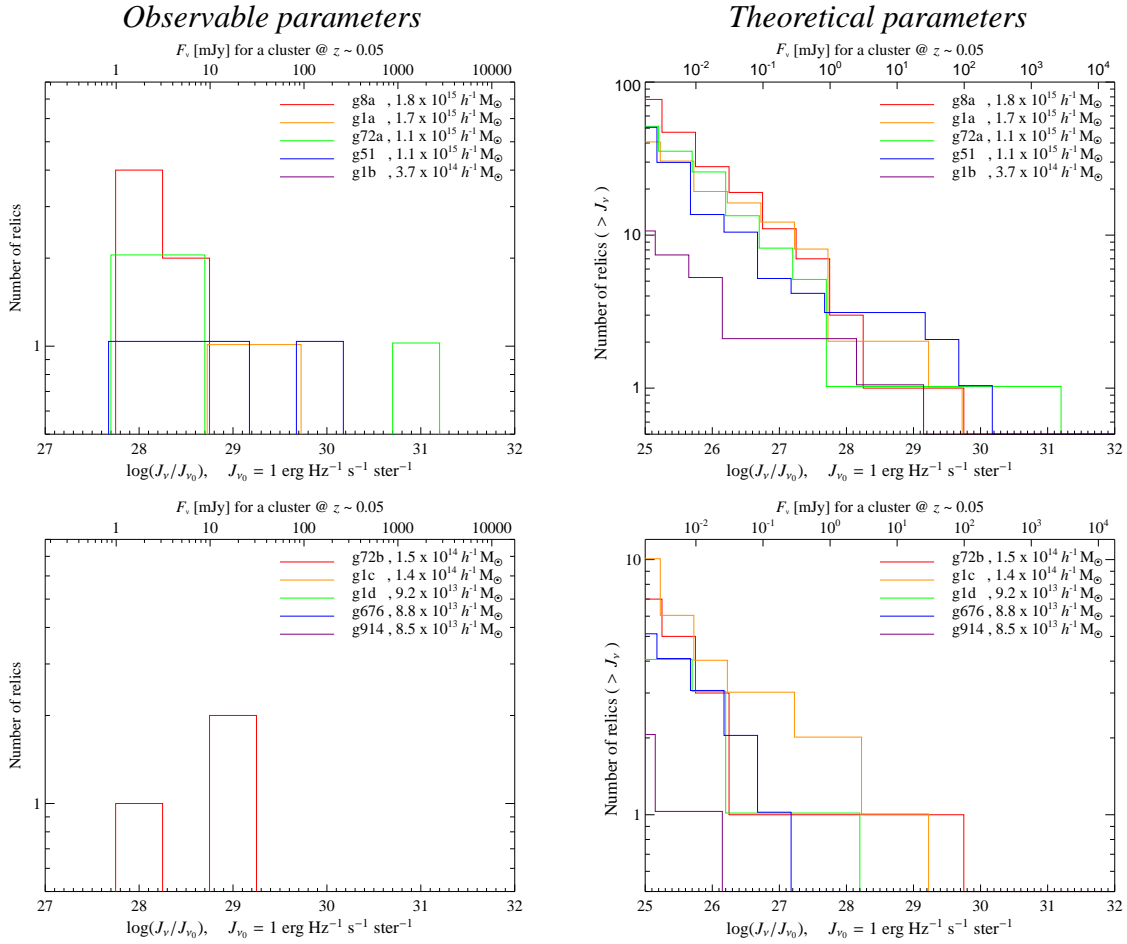


Figure 2.12: Luminosity functions for our sample of 10 clusters with the high mass clusters ($M_{\text{vir}} > 2 \times 10^{14} h^{-1} M_{\odot}$) in the upper panels and the low mass clusters in the lower panels for our standard magnetic model at 150 MHz (see Table 2.3.2). The left panels contain relics found using the observable parameters and the right panels contain the theoretical parameters. The luminosity functions from the observable parameters show that more massive clusters have relics while low mass clusters have no relics (with g1b and g72b being the exceptions in both cases, respectively). The cumulative luminosity functions from the theoretical parameters show the trend for higher mass clusters to contain more relics and dynamical cluster stage modulates this effect notably, especially at low cluster masses. For instance compare the luminosity functions of the equal mass clusters g51 and g72a, the latter of which is a post-merging cluster.

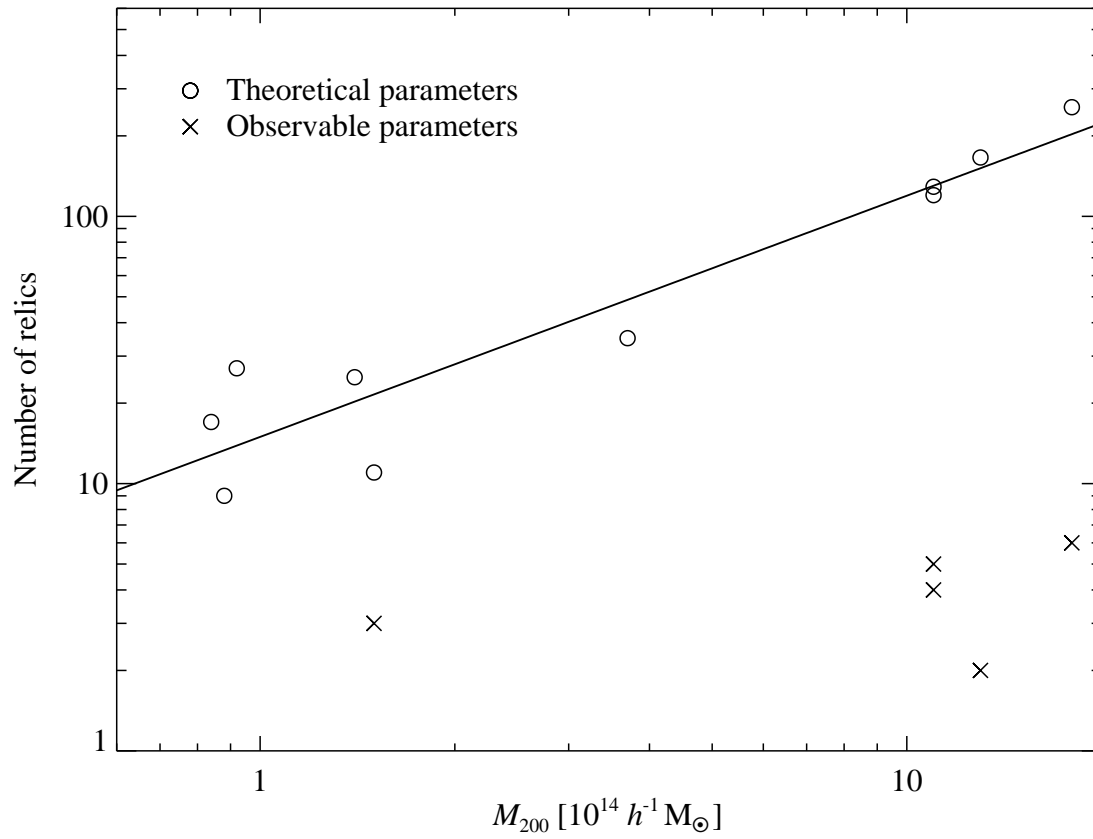


Figure 2.13: Relation between the number of radio relics within a galaxy cluster and the cluster mass, where each point represents one of our simulated clusters and the line represent the best fit power-law that scales as $M_{200}^{0.9}$. There is a trend for higher mass clusters to contain more relics.

approach neglected the hydrodynamic pressure of the CR proton component, was quite limited in its adaptive resolution capability, and neglected dissipative gas physics including radiative cooling, star formation, and supernova feedback. To allow studies of the dynamical effects of CR protons in radiatively cooling galactic and cluster environments, a CR proton formalism was developed that is based on smoothed particle hydrodynamical representation of the equations of motion (Pfrommer et al., 2006; Enßlin et al., 2007; Jubelgas et al., 2008). The emphasis is given to the dynamical impact of CR protons on hydrodynamics, while simultaneously allowing for the important CR proton injection and loss processes in a cosmological setting. Pfrommer et al. (2008) modelled the CR electron components due to shock acceleration as well as those being produced in hadronic CR proton interaction with ambient gas protons. Using this formalism and modelling, Pfrommer et al. (2007, 2008) and Pfrommer (2008) coherently studied the non-thermal cluster emission, the cosmic ray pressure component, and its implications for thermal cluster observables such as the X-ray emission and the Sunyaev-Zel'dovich effect. The focus of Miniati et al. (2001) was on primary CRe synchrotron emission from galaxy clusters as a whole, whereas we focused in this work on the emission from individual relics in detail to study the synchrotron observables and how they are sensitive to the large scale magnetic properties. To summarize, we have improved on past work in the observable predictions, simulations and observational understanding of non-thermal emission from primary accelerated CRe.

Additionally, we point out that IC and γ -ray emission are alternate ways to study structure formation shocks. This was proposed in analytical work by Loeb & Waxman (2000) and in simulations (Miniati, 2003; Keshet et al., 2003; Miniati et al., 2007; Pfrommer et al., 2008; Pfrommer, 2008). We are optimistic that high energy γ -ray experiments, such as the Fermi γ -ray space telescope (formerly GLAST) and future imaging air Čerenkov telescopes, will aid in further developing the picture of non-thermal emission at structure formation shocks.

2.5.2 Assumptions

In our attempt to model diffuse radio relic emission from galaxy clusters, we have made several simplifying assumptions. (1) We assume the modified thermal leakage model fully describes the process of diffusive shock acceleration and did not vary the parameters associated with it. The described observations allow one to test the self-consistency of this hypothesis, and might finally allow improvement of our knowledge about diffusive shock acceleration in high- β plasmas. (2) We neglect at this point the modifications of this simple model due to non-linear shock acceleration, as well as cosmic ray modified shocks, and postpone their study until future work. (3) We also neglect re-acceleration of mildly relativistic electrons that have been injected in the past either by formation shocks or other sources such as AGN. (4) We use a simple parametrization for the magnetic field. There are indications that the main characteristics of this model are realized in clusters on average (Vogt & Enßlin, 2005; Murgia et al., 2004). Future work has to be dedicated to study the distribution of magnetic fields that follow the

magneto-hydrodynamics in radiative simulations. (5) We are solving for a steady-state spectrum of the electron population and are not sensitive to spectral aging processes across the relic as they may have been found recently by Giacintucci et al. (2008). (6) In our model, we assume the thermal reservoir to be the source of electrons. (7) In our analysis, we only consider the rotation measure signal from the line-of-sight integration of the density weighted parallel magnetic field. We explicitly neglect possible contributions from magnetic field amplifications due to post-shock turbulence local to the shock wave (Vladimirov et al., 2006; Ryu et al., 2008). These questions are beyond the scope of this work and will be studied elsewhere. (8) The mass contained within the relics is not a physically relevant quantity and suffers from the finite resolution of the SPH technique at the dilute shocks in the virial regions of clusters and beyond. The radio luminosity, however, is a robust prediction within a given acceleration model since it reflects conserved quantities such as energy and mass across the shock.

2.6 Conclusions

The intermittency and inhomogeneous nature of structure formation shocks are characterized by a highly non-Gaussian distribution function. This requires numerical simulations to study the implied non-universality of the induced radio relic (or gischt) emission. It is hard to conceive of an adequate analytical approach to this problem. Observing the polarized emission of a sample of relics at different frequencies enables us to gain insight into the non-equilibrium processes at work – in particular into the interplay of large scale magnetic fields and structure formation shocks. The relevant observables of the relics include morphology, spectral shape, relic luminosity function and Faraday rotation measure. The theoretical implications of radio relic observables are as follows:

We model the shock acceleration of electrons at formation shocks and find that the *morphology* of radio relics unambiguously characterises the underlying structure of dissipating shock waves (Fig. 2.1). The resulting simulated relics are very similar to the observed relics and thus support our hypothesis. Their positions identify regions that are not in equilibrium and where the electron and ion temperatures are expected to show strong deviations due to the comparatively long Coulomb mean free path that governs their equilibration process.

The *relic luminosity function* is sensitive to the combination of normalization and scaling properties of the magnetic field with thermal energy density as well as the electron acceleration efficiency, the mass and dynamical state of a cluster. Thus, it can provide hints about the processes that generate these large scale fields and can help to disentangle the dominant transport processes which include effects from magnetic flux freezing and growth by turbulent dynamos.

The *rotation measure (RM) map* is sensitive to the line-of-sight integrated magnetic field. From the mean and variance of RM maps, we can infer the location of the formation shock with respect to the cluster center as the variance increases as a function of integration length (Eqn. 2.14). This helps in con-

straining the geometry of the merger. Deprojecting the 2D RM power spectrum enables one to measure the 3D magnetic power spectrum, under the assumption that the behaviour of the electron density along the line of sight can be obtained from X-ray measurements. The peak of the 3D power spectrum yields the total magnetic energy and the magnetic coherence length λ_B . Performing this procedure for different relics or for different regions of one large relic allows us to estimate the variance of λ_B across the cluster and might possibly tell us about the nature of MHD turbulence. We found that the correlation between n_e and B biases the *rms* magnetic field strength derived from RM maps high if this is not taken into account; we note that most works have done so. This correlation should be a natural consequence of MHD effects such as flux freezing. If systematic errors associated with RM studies are smaller than statistical ones, we find that measurements of the small scale slope of the RM power spectrum are accurate enough to differentiate between Kolmogorov ($k^{-5/3}$) and Burgers (k^{-2}) turbulence spectra. The interpretation of these slopes is however not straight forward and needs to account for an additional flattening due to small scale fluctuations in n_e .

The *spectral index* of a power law spectrum of a radio relic is a measure of the shock strength of that relic. The median spectral index of a distribution of relics probes a distribution of virializing shocks and can give an indication of CR proton injection. This is of particular relevance for questions concerning the pressure contribution of non-thermal components and enables comparison with predictions of hydrodynamical simulations. The shape of the spectrum is sensitive to the acceleration mechanism of the relativistic electrons and to their cooling processes. The variation of the spectrum over the relic allows one to infer in situ magnetic field strengths by comparing the synchrotron and IC cooling times to the advection time downstream provided that the magnetic energy density is not much smaller than the CMB energy density. This might constrain models for the magnetic amplification at shocks in high beta plasmas. A radio relic's luminosity is roughly correlated with the shock strength. Thus, it is favourable to look for radio relics in large, dynamically disturbed clusters, or use relic detections as a proxy for dynamical activity of clusters (Schuecker et al., 2001).

We demonstrated that the combination of *the relic spectral index with deprojected X-ray and SZ profiles* allows one to indirectly infer upper limits on the density and temperature of the warm hot intergalactic medium. Simulations show that the WHIM is not uniform, rather it is characterized by highly inhomogeneous structure that shows intermittent accretion events that are channeled mostly through filaments.

We predict that there will be a large sample of polarized radio relics from a considerable number clusters in the near future. This sample should allow one to constrain macroscopic model parameters, which are expected to be highly non-Gaussian, using a joint analysis method on the radio observables. For example, the combination of the relic luminosity function, RM power spectra, X-ray and SZ measurements should constrain the models of diffusive shock acceleration and large scale magnetic fields. Future work will address the details of this procedure.

2.7 Appendix: Interpolating and projecting SPH quantities

In the course of this work we are required to interpolate our Lagrangian energy density distribution as given by SPH on a 3D grid. We remind the reader that the SPH smoothing kernel of an SPH particle a , $W(|\mathbf{r} - \mathbf{r}_a|, h_a)$, is given by Eqn. A.1 of Springel et al. (2001b). It is normalized in the continuum such that $\int W(r, h) d^3\mathbf{r} \equiv 1$. A scalar field $x(\mathbf{r})$ ⁶ is interpolated onto a 3D grid cell at \mathbf{r}_{ijk} by the product of itself with the specific volume M_a/ρ_a of the gas particles over a comoving cube,

$$x(\mathbf{r}_{ijk}) = \frac{1}{L_{\text{pix}}^3} \sum_a x_a \frac{M_a}{\rho_a} \mathcal{W}_{a,ijk}(|\mathbf{r}_{ijk} - \mathbf{r}_a|, h_a), \quad (2.23)$$

where L_{pix}^3 is the comoving volume of the grid cell and we define the normalized 3D smoothing kernel of SPH particle a at the grid position \mathbf{r}_{ijk} by

$$\mathcal{W}(|\mathbf{r}_{ijk} - \mathbf{r}_a|, h_a) = \frac{W(|\mathbf{r}_{ijk} - \mathbf{r}_a|, h_a)}{\sum_{ijk} W(|\mathbf{r}_{ijk} - \mathbf{r}_a|, h_a)}. \quad (2.24)$$

We note that the normalized interpolation conserves the interpolated quantity strictly without any further requirement on the grid size.

Similarly, we employ the method of normalized projection of a three dimensional SPH scalar fields $x(\mathbf{r})$ to perform projection integrals yielding the quantity $X(\mathbf{r}_\perp)$. In analogy to Eqn. 2.23 we obtain

$$X(\mathbf{r}_{\perp,ij}) = \frac{1}{L_{\text{pix}}^2} \sum_a x_a \frac{M_a}{\rho_a} \mathcal{Y}_{a,ij}(|\mathbf{r}_{\perp,ij} - \mathbf{r}_a|, h_a), \quad (2.25)$$

where L_{pix}^2 is the comoving area of the pixel and the normalized 2D projected smoothing kernel of SPH particle a at the grid position $\mathbf{r}_{\perp,ij}$ derives from the projected SPH kernel $Y(|\mathbf{r}_{\perp,ij}|, h_a)$ and is given by

$$\mathcal{Y}(|\mathbf{r}_{\perp,ij} - \mathbf{r}_a|, h_a) = \frac{Y(|\mathbf{r}_{\perp,ij} - \mathbf{r}_a|, h_a)}{\sum_{ijk} Y(|\mathbf{r}_{\perp,ij} - \mathbf{r}_a|, h_a)}. \quad (2.26)$$

2.8 Appendix: Theoretical emission threshold

The emission threshold for the *observable parameters* and *theoretical parameters* differ by 12 orders of magnitude. This dynamic range is beyond the ability of any future telescope on the horizon. Varying the emission threshold of our *theoretical parameters* by six orders of magnitudes only very weakly affects our results. In particular, we show in Fig. 2.14 that such a dramatic variation has only little influence on the high-end of the radio relic luminosity function.

⁶We note that in general, x has to be a thermodynamic extensive volume density such that the product xM/ρ is extensive.

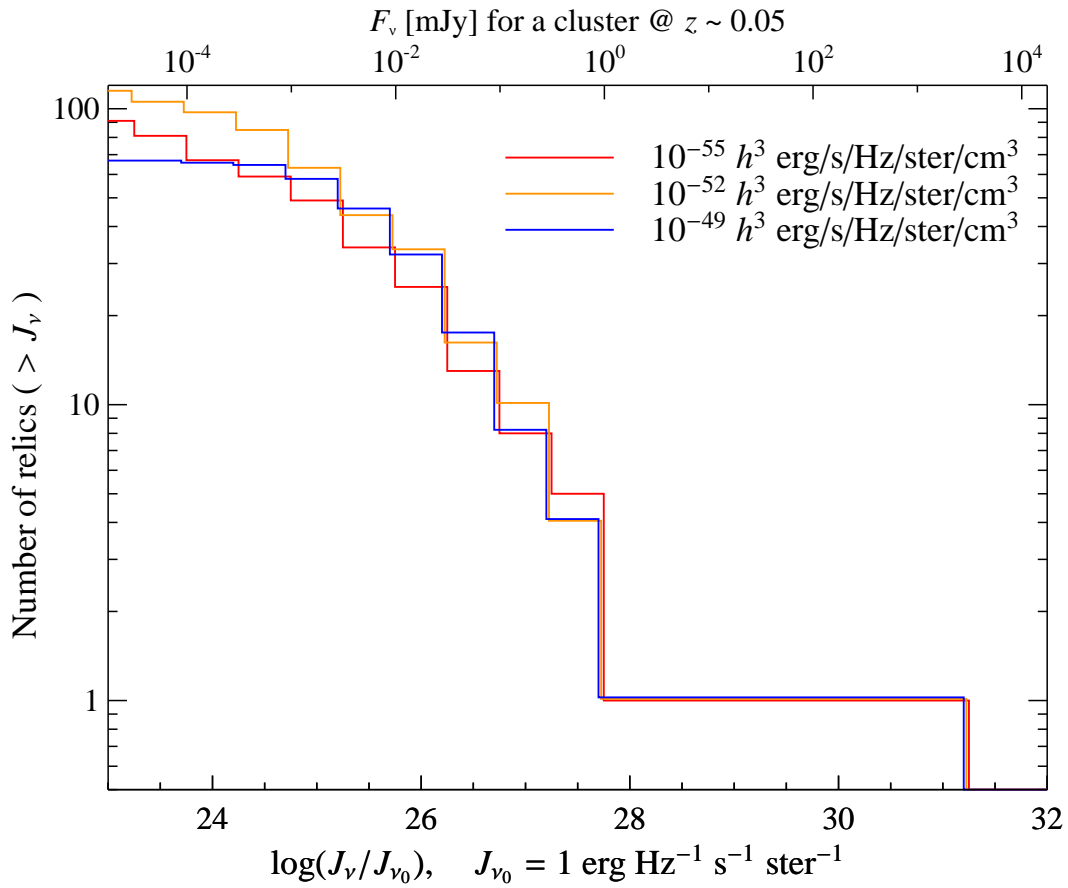


Figure 2.14: Cumulative luminosity functions for different values of the emission cutoff. This shows the robustness of our predictions for future instrument capabilities.

2.9 Appendix: Rankine-Hugoniot conditions

The three dimensional spectral index can be transformed into a Mach number (\mathcal{M}) (EnBlin et al., 2007), if one assumes an ideal fluid that is characterized a a single adiabatic index γ ,

$$\mathcal{M} = \sqrt{\frac{4(1 + \alpha_{v,3D})}{1 + 4\alpha_{v,3D} - 3\gamma}}. \quad (2.27)$$

Under these conditions, the well-known Rankine-Hugoniot jump conditions allow to relate the hydrodynamic post-shock quantities (denoted with a subscript 2) to the pre-shock quantities (denoted with a subscript 1),

$$\frac{\rho_1}{\rho_2} = \frac{(\gamma - 1)\mathcal{M}^2 + 2}{(\gamma + 1)\mathcal{M}^2}, \quad (2.28)$$

$$\frac{T_1}{T_2} = \frac{(\gamma + 1)^2\mathcal{M}^2 + 2}{[2\gamma\mathcal{M}^2 - (\gamma - 1)][(\gamma - 1)\mathcal{M}^2 + 2]}, \quad (2.29)$$

$$\frac{P_1}{P_2} = \frac{\gamma + 1}{2\gamma\mathcal{M}^2 - (\gamma - 1)}. \quad (2.30)$$

Phenomenologically, we show in Fig. 2.11 that Eqn. 2.27 under-predicts the average $\langle \mathcal{M} \rangle$ if one were to infer \mathcal{M} from spectral index maps. This translates into an upper limit for the predicted pre-shock density. In the case of temperature and pressure, the under-prediction of the average $\langle \mathcal{M} \rangle$ leads to an over-estimation of the pre-shock values which translates into lower limits for temperature and pressure (Eqns. 2.29 and 2.30).

Chapter 3

Simulations of the Sunyaev-Zel'dovich Power Spectrum with AGN Feedback

A version of this chapter has been published in the Astrophysical Journal as “Simulations of the Sunyaev-Zel'dovich Power Spectrum with Active Galactic Nucleus Feedback” Battaglia, N., Bond, J. R., Pfrommer, C., Sievers, J. L., & Sijacki, D. 2010, Volume 725, pp. 91-99. Reproduced by permission of ApJ.

3.1 Chapter Overview

We explore how radiative cooling, supernova feedback, cosmic rays and a new model of the energetic feedback from active galactic nuclei (AGN) affect the thermal and kinetic Sunyaev-Zel'dovich (SZ) power spectra. To do this, we use a suite of hydrodynamical TreePM-SPH simulations of the cosmic web in large periodic boxes and tailored higher resolution simulations of individual galaxy clusters. Our AGN feedback simulations match the recent universal pressure profile and cluster mass scaling relations of the REXCESS X-ray cluster sample better than previous analytical or numerical approaches. For multipoles $\ell \lesssim 2000$, our power spectra with and without enhanced feedback are similar, suggesting theoretical uncertainties over that range are relatively small, although current analytic and semi-analytic approaches overestimate this SZ power. We find the power at high 2000 – 10000 multipoles which ACT and SPT probe is sensitive to the feedback prescription, hence can constrain the theory of intracluster gas, in particular for the highly uncertain redshifts > 0.8 . The apparent tension between σ_8 from primary cosmic microwave background power and from analytic SZ spectra inferred using ACT and SPT data is lessened with our AGN feedback spectra.

3.2 SZ Power Templates and the Overcooling Problem

When CMB photons are Compton-scattered by hot electrons, they gain energy, giving a spectral decrement in thermodynamic temperature below $\nu \approx 220$ GHz, and an excess above (Sunyaev & Zeldovich, 1970). The high electron pressures in the intracluster medium (ICM) result in cluster gas dominating the effect. The integrated signal is proportional to the cluster thermal energy and the differential signal probes the pressure profile. The SZ sky is therefore an effective tool for constraining the internal physics of clusters and cosmic parameters associated with the growth of structure, in particular the *rms* amplitude of the (linear) density power spectrum on cluster-mass scales σ_8 (e.g., Birkinshaw, 1999; Carlstrom et al., 2002). Identifying clusters through blind SZ surveys and measuring the SZ power spectrum have been long term goals in CMB research, and are reaching fruition through the South Pole Telescope, SPT (Lueker et al., 2010) and Atacama Cosmology Telescope, ACT (Fowler et al., 2010) experiments. The ability to determine cosmological parameters from these SZ measurements is limited by the systematic uncertainty in theoretical modelling of the underlying cluster physics and hence of the SZ power spectrum. The power contribution due to the kinetic SZ (kSZ) effect that arises from ionized gas motions with respect to the CMB rest frame adds additional uncertainty.

There are two main approaches to theoretical computations of the thermal SZ (tSZ) power spectrum: from hydrodynamical simulations of SZ sky maps or from semi-analytical estimates (Bond et al., 2002, 2005, B0205). Large cosmological simulations providing a astrophysical solution to the pressure distribution should include effects of non-virialized motions, accretion shocks, and deviations from spherical symmetry. Averaging over many realizations of synthetic SZ sky projections yields the power spectrum and its variance (e.g., B0205; da Silva et al., 2000; Springel et al., 2001a; Seljak et al., 2001; Schäfer et al., 2006a). In conjunction with primary anisotropy signals and extragalactic source models, the SZ power spectrum has been used as a template with variable amplitude A_{SZ} for extracting cosmological parameters by the Cosmic Background Imager (CBI) team (B0205; Sievers et al., 2009) and the ACBAR team (Goldstein et al., 2003; Reichardt et al., 2009a). A_{SZ} was used to estimate a $\sigma_{8,\text{SZ}} \propto A_{\text{SZ}}^{1/7}$ as a way to encode tension between the SZ-determined value and the (lower) σ_8 obtained from the primary anisotropy signal. The CBI team also has included an analytic model (Komatsu & Seljak, 2002, KS) which was also the one adopted by the WMAP team (Spergel et al., 2007). The KS template yielded a lower value for $\sigma_{8,\text{SZ}}$ than that obtained with the simulation template, by $\sim 10\%$. The KS model assumes a universal ICM pressure profile in hydrostatic equilibrium with a polytropic (constant Γ) equation of state. The power spectrum is then obtained using an analytic fit to ‘halo model’ abundances. So far the SPT and ACT have only used the KS template and a related semi-analytic one (Ostriker et al., 2005; Bode et al., 2009). This model (Sehgal et al., 2010, S10) allows map generation by painting dark matter halos in N-body simulations with gas. It expands on KS by calculating the gravitational potential from the DM particles, includes an effective infall pressure, adds simplified

Table 3.1: Summary of periodic box simulations

Box size [h^{-1} Mpc]	$N_{\text{DM}} + N_{\text{gas}}$	m_{gas} [$h^{-1} M_{\odot}$]	m_{gas} [$h^{-1} M_{\odot}$]	ε_s [h^{-1} kpc]	Number of simulations		
					Shock heating	Radiative cooling	AGN feedback
165	2×256^3	3.2×10^9	1.54×10^{10}	20	10	10	10
330	2×512^3	3.2×10^9	1.54×10^{10}	20	1	1	1
100	2×64^3	4.6×10^{10}	2.19×10^{11}	52		1	1
100	2×96^3	1.3×10^{10}	6.49×10^{10}	35		1	1
100	2×128^3	5.7×10^9	2.74×10^{10}	26		1	1
100	2×196^3	1.7×10^9	8.12×10^9	18		1	1
100	2×256^3	7.1×10^8	3.42×10^9	13		1	1

models for star formation, non-thermal pressure support and energy feedback which are calibrated to observations. Using these templates, the SPT team derived a $\sigma_{8,\text{SZ}}$ lower than the primary anisotropy σ_8 (e.g., WMAP7, Larson et al., 2010).

Current simulations with *only* radiative cooling and supernova feedback excessively over-cool cluster centers (e.g. Lewis et al., 2000), leading to too many stars in the core, an unphysical rearrangement of the thermal and hydrodynamic structure, and problems when compared to observations, in particular for the entropy and pressure profiles. The average ICM pressure profile found through X-ray observations of a sample of nearby galaxy clusters (Arnaud et al., 2010) is inconsistent the KS analytic model (Komatsu et al., 2010). Adaptive-mesh cluster simulations (Nagai et al., 2007) have been found to be consistent within the observed Arnaud et al. (2010) pressure profile uncertainties, which become large in the cluster core region. Pre-heating (e.g. Bialek et al., 2001) and AGN feedback (e.g. Sijacki et al., 2007, 2008b; Puchwein et al., 2008) help solve the over-cooling problem and improve agreement with observed cluster properties.

Previously, an analytical model by Roychowdhury et al. (2005) has explored the effects of effervescent heating on the SZ power spectrum and Holder et al. (2007) use a semi-analytical model to calculate how an entropy floor affects the SZ power spectrum. There have been several simulations on galaxy and group scales that have studied how ‘quasar’ feedback impacts the total SZ decrement (Thacker et al., 2006; Scannapieco et al., 2008; Bhattacharya et al., 2008; Chatterjee et al., 2008). In this work we explore whether AGN feedback incorporated into hydrodynamical simulations of structure formation can suppress the over-cooling problem and resolve the current inconsistency between theoretical predictions and observations of the SZ power spectrum and X-ray pressure profile.

3.3 Modeled physics in our simulations

3.3.1 Cosmological simulations

We pursue two complementary approaches using smoothed particle hydrodynamic (SPH) simulations: large-scale periodic boxes provide us with the necessary statistics and volume to measure the SZ power spectrum; individual cluster computations allow us to address over-cooling at higher resolution and compare our AGN feedback prescription with previous models. We used a modified version of the GADGET-2 (Springel, 2005) code. Our sequence of periodic boxes had sizes 100, 165, 330 h^{-1} Mpc. The latter two used $N_{\text{DM}} = N_{\text{gas}} = 256^3$ and 512^3 , maintaining the same gas particle mass $m_{\text{gas}} = 3.2 \times 10^9 h^{-1} M_{\odot}$, DM particle mass $m_{\text{DM}} = 1.54 \times 10^{10} h^{-1} M_{\odot}$ and a minimum gravitational smoothing length $\varepsilon_s = 20 h^{-1}$ kpc; our SPH densities were computed with 32 neighbours. For our standard calculations, we adopt a tilted Λ CDM cosmology, with total matter density (in units of the critical) $\Omega_{\text{m}} = \Omega_{\text{DM}} + \Omega_{\text{b}} = 0.25$, baryon density $\Omega_{\text{b}} = 0.043$, cosmological constant $\Omega_{\Lambda} = 0.75$, Hubble parameter $h = 0.72$ in units of $100 \text{ km s}^{-1} \text{ Mpc}^{-1}$, spectral index of the primordial power-spectrum $n_s = 0.96$ and $\sigma_8 = 0.8$. A summary of the box simulations is provided in Table 3.1. For the ‘zoomed’ cases (Katz & White, 1993), we repeatedly simulated the cluster ‘g676’ (with the high resolution $m_{\text{gas}} = 1.7 \times 10^8 h^{-1} M_{\odot}$, $m_{\text{DM}} = 1.13 \times 10^9 h^{-1} M_{\odot}$ and $\varepsilon_s = 5 h^{-1}$ kpc, using 48 neighbours to compute SPH densities, as in Pfrommer et al. 2007).

We show results for three variants of gas heating: (1) the classic non-radiative ‘adiabatic’ case with only formation *shock heating*; (2) an extended *radiative cooling* case with star formation, supernova (SN) feedback and cosmic rays (CRs) from structure formation shocks; (3) *AGN feedback* in addition to radiative cooling, star formation, and SN feedback. Radiative cooling and heating were computed assuming an optically thin gas of a pure hydrogen and helium primordial composition in a time-dependent, spatially uniform ultraviolet background. Star formation and supernovae feedback were modelled using the hybrid multiphase model for the interstellar medium of Springel & Hernquist (2003a). The CR population is modelled as a relativistic population of protons described by an isotropic power-law distribution function in momentum space with a spectral index of $\alpha = 2.3$, following Enßlin et al. (2007). With those parameters, the CR pressure modifies the SZ effect at most at the percent level and causes a reduction of the resulting integrated Compton- y parameter (Pfrommer et al., 2007).

3.3.2 AGN feedback model

Current state-of-the-art cosmological simulations are still unable to span the large range of scales needed to resolve black hole accretion. Hence a compromise treatment for AGN feedback is needed. For example, Sijacki et al. (2007) and Booth & Schaye (2009) adopted estimates of black hole accretion rates based on the Bondi-Hoyle-Lyttleton formula (Bondi & Hoyle, 1944). Here we introduce a sub-grid AGN feedback prescription for clusters that allows for lower resolution still and hence can be applied to large-

scale structure simulations. We couple the black hole accretion rate to the global star formation rate (SFR) of the cluster, as suggested by Thompson et al. (2005) using the following arguments. The typical black hole accretion rates and masses for the inner gravitationally stable AGN disks (of size $\lesssim 1$ pc) are $\sim 1 M_{\odot}/\text{yr}$ and $\sim 10^6 M_{\odot}$. Since AGN lifetimes are much longer than 1 Myr, mass must be transferred from larger radii to the inner disk. However, at much larger radii this outer disk is gravitationally unstable and must be forming stars. Thus, in order to feed the AGN, stability arguments suggest that the rate of accretion must be greater than the SFR. For simplicity we assume that $\dot{M}_{\text{BH}} \propto \dot{M}_{\star}$. We inject energy into the ICM over a spherical region of size R_{AGN} about the AGN, according to

$$E_{\text{inj}}(< R_{\text{AGN}}) = \varepsilon_r \dot{M}_{\star}(< R_{\text{AGN}}) c^2 \Delta t \quad (3.1)$$

if $\dot{M}_{\star}(< R_{\text{AGN}}) > 5 M_{\odot}/\text{yr}$.

The duty cycle over which the AGN outputs energy is Δt and ε_r is an ‘efficiency parameter’. (As we describe below, the calculated efficiency for turning mass into energy is much smaller than ε_r .) We have explored a wide range of our two parameters, but the specific choices made for the figures are $\Delta t = 10^8$ yr and $\varepsilon_r = 2 \times 10^{-4}$. Since feedback and galactic superwinds are ubiquitous when the SFR per unit area is $10^{-1} M_{\odot}/\text{yr kpc}^{-2}$ (Heckman, 2002), we require a minimum SFR of $5 M_{\odot}/\text{yr}$ to activate AGN heating in the housing halo, which corresponds to the value for a typical star forming galaxy.

Given the output AGN energy, we must prescribe how it is to be distributed. Our procedure is motivated by the way Sijacki & Springel (2006) did AGN heating via bubbles. Using an on-the-fly friends-of-friends (FOF) halo finding algorithm in GADGET-2 with a linking length of 0.2, we determine the mass and center of mass of each halo with $M_{\text{halo}} > 1.2 \times 10^{12} h^{-1} M_{\odot}$. We calculate its global SFR within the AGN sphere of influence of radius

$$R_{\text{AGN}} = \max \left\{ 100 h^{-1} \text{kpc} \left[\frac{M_{\text{halo}}}{10^{15} h^{-1} M_{\odot} E(z)^2} \right]^{1/3}, \frac{u_{\text{AGN}}}{1+z} \right\} \quad (3.2)$$

where $u_{\text{AGN}} = \varepsilon_s$ and $E(z)^2 = \Omega_{\text{m}}(1+z)^3 + \Omega_{\Lambda}$. Within the halos we partition E_{inj} onto those gas particles inside of R_{AGN} according to their mass. We have varied the prescription for R_{AGN} and its floor u_{AGN} (chosen here to be the gravitational softening ε_s); the specific numbers given in eq. 3.2 (and for ε_r) match previous successful models that suppress the over-cooling by means of AGN feedback (Sijacki et al., 2008b, see Sect. 3.4.1). Defining R_{Δ} as the radius at which the mean interior density equals Δ times the critical density $\rho_{\text{cr}}(z)$ (e.g., for $\Delta = 200$ or 500), then the ratio of R_{AGN} to R_{200} is a constant ~ 0.05 .

Although we have referred to our feedback mechanism as being caused by AGN outflows, radiation pressure from stellar luminosity acting on dust grains will serve much the same purpose, and could also deliver high efficiencies (e.g. Thompson et al., 2005). In the code, we have so far added E_{inj} as a pure heating component, but it should allow for a mechanical, momentum-driven wind component as well,

which would not be as prone to catastrophic cooling and likely decrease the ε_r needed for useful star formation suppression.

The relevant energy budget is not in fact defined by ε_r , but rather by a redshift-dependent effective feedback efficiency $\varepsilon_{\text{eff}} \equiv \Sigma_i E_{\text{inj},i} / [M_\star(< r) c^2]$, where we sum over every energy injection event (labeled by i) and we calculate the stellar mass $M_\star(< r)$ within a given radius. In all cases, $\varepsilon_{\text{eff}} \ll \varepsilon_r$, because: (i) heating suppresses the stellar mass ΔM_\star created over Δt , making it quite a bit less than the stellar mass $\dot{M}_\star \Delta t$ that would have formed without any feedback; and (ii) E_{inj} is a stochastic variable, which we find to be zero about half of the time because the required SF threshold is not achieved. With our fixed $\varepsilon_r - R_{\text{AGN}}$ prescription, our canonical g676 example has $\varepsilon_{\text{eff}} \sim 5 \times 10^{-6}$ for the entire simulation; if all energy had been released within the final R_{AGN} , ε_{eff} would be 8×10^{-5} , but feedback, especially at early times, is much more widely distributed. Of a total $E_{\text{inj}} = 9 \times 10^{61}$ ergs for g676 we find 58% is delivered in the cluster formation phases at $z > 2$, another 23% is delivered in the redshift range $1 < z < 2$ that can be probed with ACT and SPT resolution, and only 19% comes from the longer period below redshift 1. Feedback prescriptions with smaller E_{inj} which still give the desired star formation suppression need further exploration.

3.4 Pressure Profiles

3.4.1 Testing AGN feedback as resolution varies

AGN feedback self-regulates the star formation and energetics of a cluster. In Fig. 3.1 we compare the fraction of baryons (f_b) and stars (f_{star}) as functions of cluster radius for the high-resolution ‘g676’ simulations. Our radiative simulation produces 1.5 – 2 times more stars than those with AGN feedback. Our sub-grid AGN model nicely reproduces the results in Sijacki et al. (2008b). It should also produce reliable results in the cosmological box simulations in which over-cooling is less severe because of the lower resolution. There is significant sensitivity to the value chosen for the feedback parameter ε_r : doubling it lowers f_b by a factor of 1.5, halving it increases f_{star} by 1.4. The $100 h^{-1}$ Mpc simulations were used to study the resolution dependence of our feedback model by varying $N_{\text{gas}}^{1/3}$ in steps from 64 to 256, with ε_s and hence u_{AGN} (eq. 3.2) decreased accordingly. As u_{AGN} decreased, f_{star} within R_{500} increased almost linearly for radiative cooling, whereas for AGN feedback the increases were less. This can be traced to the hierarchical growth of structure since in low-resolution simulations: the small star forming systems are under-resolved; this decreases the SFR that mediates our AGN feedback; and this lowers the overall number of stars produced in the simulations. This behaviour is seen in other AGN feedback models (Sijacki et al., 2007) and has been extensively studied in non-AGN feedback simulations by Springel & Hernquist (2003b).

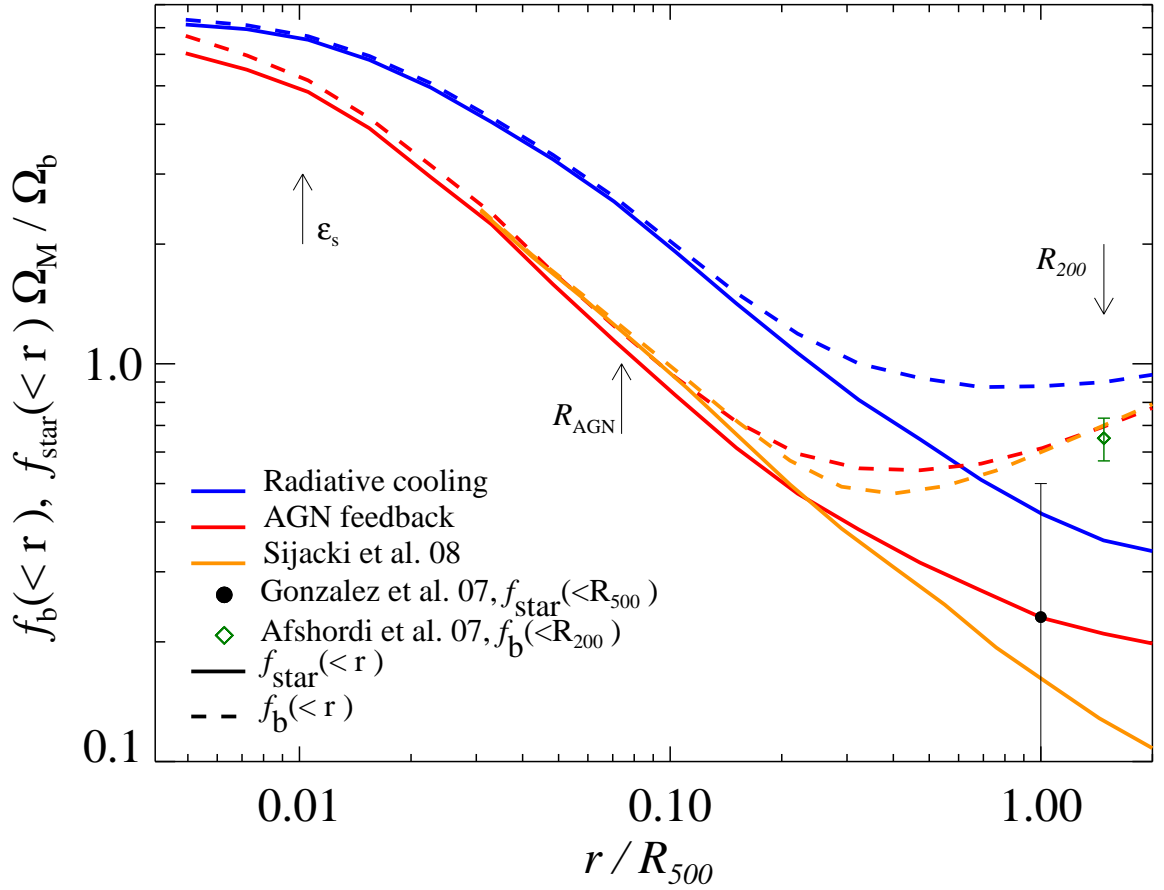


Figure 3.1: Shown are f_b (dashed lines) and f_{star} (solid lines) normalized to the universal value ($f_b = 0.13$) assumed in our simulations of our cluster g676 with $M_{500} = 6.8 \times 10^{13} h^{-1} M_{\odot}$. The blue lines are for the simulation with radiative cooling and star formation while the red and orange lines are for our AGN feedback model ($\epsilon_r = 2 \times 10^{-4}$, $\dot{M}_{\star} \geq 5 M_{\odot}/\text{yr}$) and that by Sijacki et al. (2008b), respectively. The data points are observations by Gonzalez et al. (2007) and Afshordi et al. (2007). $f_{\text{star}}(<R_{500})$ from X-ray measurements also agrees well, but the errors are large. Our sub-grid model matches the results from Sijacki et al. (2008b) in this high resolution simulation well.

3.4.2 Stacked pressure profiles

For every halo identified by our FOF algorithm, we calculate the center of mass, R_Δ , the mass M_Δ within R_Δ and compute the pressure profile (i.e. volume averaged pressure within spherical shells) normalized to $P_\Delta \equiv GM_\Delta \Delta \rho_{\text{cr}}(z) f_b / (2R_\Delta)$, with $f_b = \Omega_b / \Omega_m$ (Voit, 2005) and radii scaled by R_Δ . We then form a weighted average of these profiles for the entire sample of clusters at a given redshift. For Fig. 3.2, we have weighted by the integrated y-parameter,

$$Y_\Delta = \frac{\sigma_T}{(m_e c^2)} \int_0^{R_\Delta} P_e(r) 4\pi r^2 dr \propto E_{\text{th}}(< R_\Delta), \quad (3.3)$$

where σ_T is the Thompson cross-section, m_e is the electron mass and P_e is electron pressure. For a fully ionized medium the thermal pressure $P = P_e(5X_H + 3)/2(X_H + 1) = 1.932P_e$, where $X_H = 0.76$ is the primordial hydrogen mass fraction. Splitting the clusters into a number of mass bins gives similar results to this monolithic Y_Δ weight, as does weighting by Y_Δ^2 . We have found that a simple parametrized model

$$P/P_{500} = A [1 + (x/x_c)^\alpha]^{-\gamma/\alpha}, \quad x \equiv r/R_{500}, \quad (3.4)$$

with core-scale x_c , amplitude A , and two power law indices, α and γ , fits better than with a fixed α . Sample values for our AGN feedback are $A = 44$, $x_c = 1.5$, $\alpha = 0.65$ and $\gamma = 6.2$ at $z = 0$; generally the parameters depend upon cluster mass and redshift, which will be explored in future work. At $z \gtrsim 1$, a more complex parametrization is needed.

In Fig. 3.2, we show average pressure profiles multiplied by x^3 to make them $\propto dE_{\text{th}}/d \ln r$, the thermal energy per logarithmic interval in radius, and hence to $dY_\Delta/d \ln r$. All profiles of $dE_{\text{th}}/d \ln r$ from simulations and observations peak at or before R_{200} , but an integration to at least $4R_{200}$ is required for the total thermal energy to converge. By contrast, the KS profile does not drop over this range due to the constancy of Γ and does not include the outer cluster phenomena of asphericity, accretion shocks, *etc.* Throughout this paper, we have computed the KS model with an updated concentration parameter given by Duffy et al. (2008). We also show a scaled average S10 pressure profile for clusters with $10^{14} M_\odot < M_{500} < 5 \times 10^{14}$ and redshift < 0.2 . The S10 profile has been weighted by Y_Δ and agrees well within R_{500} and with a slight excess pressure beyond R_{500} .

Fig. 3.2 shows our feedback model traces the observed "universal" X-ray profile of Arnaud et al. (2010) shown as a dark-grey band rather well within R_{500} . This fit came out naturally, with no further tuning of our feedback parameters beyond trying to agree with the Sijacki et al. (2008b) simulation. Our models without AGN feedback have larger pressures inside R_{500} . For the light grey band beyond R_{500} , the universal X-ray profile did not use observations, but was fit to an average profile of earlier simulations so the deviation $> R_{500}$ does not represent a conflict of our profiles with the data, rather with the earlier simulations. The band shown for the X-ray profile gives a crude correction for the bias in M_{500} and R_{500} resulting from the Arnaud et al. (2010) assumption of hydrostatic equilibrium. This

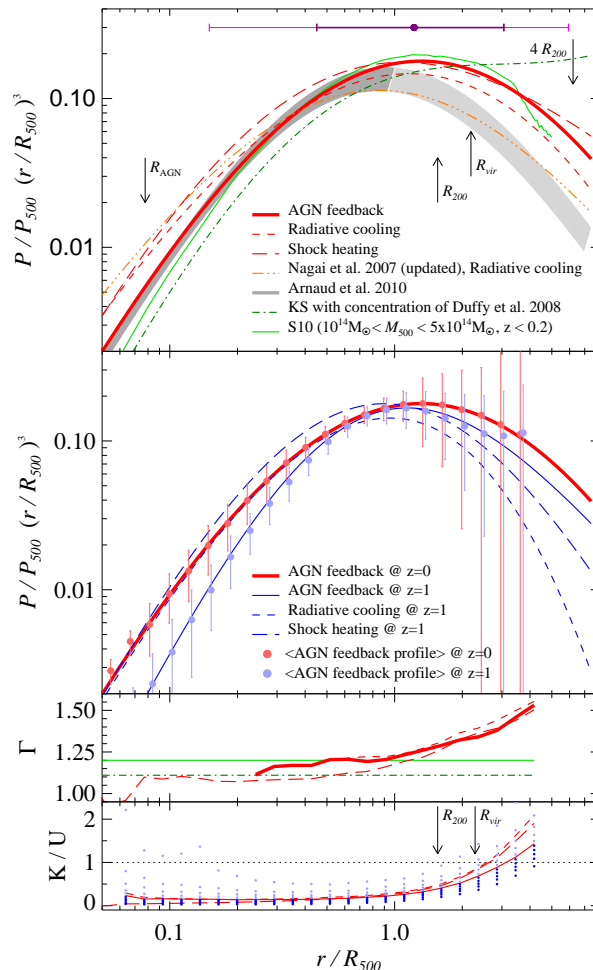


Figure 3.2: *Top*: Comparison of fits to normalized average pressure profiles from analytic calculations, simulations and observations, scaled by $(r/R_{500})^3$. For a cluster of $M_{500} = 2 \times 10^{14} h^{-1} M_{\odot}$, we show fits to our SPH simulations (red), and compare them with the analytic KS profile (green), the semi-analytic S10 average profile (light green), and a fit to AMR simulations (updated profile by Nagai et al., 2007, private communication; orange). Our feedback model matches a fit to X-ray observations (Arnaud et al., 2010, grey bands) within R_{500} well; only the dark grey part is actually a fit to the data, with the light grey their extrapolation using older theory results unrelated to the data. We illustrate the 1 and 2 σ contributions to Y_{Δ} centered on the median for the feedback simulation by horizontal purple and pink error bars. *2nd panel*: We compare fits to our AGN model at redshift $z = 0$ (red solid) to all our three models at redshift $z = 1$ (blue). Shown are the 1σ error bars of the cluster-by-cluster variance of the weighted averages in our AGN models using corresponding lighter colors. *3rd panel*: We show the effective adiabatic index Γ for our simulations, comparing it with KS (dash-dotted) and with a constant 1.2 (light green). *Bottom*: The distribution of kinetic-to-thermal energy in percentile decades is indicated by the dots for the feedback case, with the median shown for all three models; thus, there are significant additions to pressure support even in the cores of simulated clusters, and even more so in the SZ-significant outer parts.

yields mass values which are on average 25% too low (Nagai et al., 2007), so the band represents a 0-25% uncertainty in M_{500} . This change only affects $R_{500} \propto M_{500}^{1/3}$ and $P_{500} R_{500}^3 \propto M_{500}^{5/3}$ but does not affect the shape of the profile. (However, as the bottom panel shows, such a correction from turbulence and un-virialized bulk motions (Kravtsov et al., 2006) will depend upon radius and selection function of the X-ray clusters used to make the fit.)

Another important issue is the relation between the Y_{Δ} and cluster mass. We fit our results for this to the scaling relation

$$Y_{500} = 10^B (M_{500}/3 \times 10^{14} h_{70}^{-1} M_{\odot})^A h_{70}^{-5/2} \text{Mpc}^2, \quad (3.5)$$

where $h_{70} \equiv 0.7 \times 100 \text{ km s}^{-1} \text{ Mpc}^{-1}$. Parameters from our simulation are $B = (-4.73 \pm 0.17, -4.81 \pm 0.18, -4.79 \pm 0.19)$ and $A = (1.64 \pm 0.03, 1.69 \pm 0.03, 1.73 \pm 0.04)$ for the sequence (1) shock heating, (2) radiative cooling and (3) AGN feedback. These values are similar to the $B = -4.739 \pm 0.003$ and $A = 1.790 \pm 0.015$ found by Arnaud et al. (2010), as well as the $B = -4.713 \pm 0.004$ and $A = 1.668 \pm 0.009$ found by S10. We note that Arnaud et al. (2010) actually used a mass proxy in place of M_{500} , so their errors are not representative of the true observational scatter in the $Y - M$ scaling relation. The AGN feedback model of Sijacki et al. (2007) was also able to reconcile the cluster X-ray luminosity and temperature scaling relation (Puchwein et al., 2008).

We find a large variation in the outer pressure profiles beyond R_{vir} , especially at redshift $z \sim 1$ as is shown in the second panel of Fig. 3.2. These regions may have sub-halos, and external but nearby groups on filaments, most of which will eventually be drawn into the clusters. In spite of the large variance of the scaled profiles, the fit to the profiles at $z = 0$ follows the average. At larger redshift, however, our fitting formula will require more degrees of freedom than in eq. 5.9 to reflect the range of behaviour of the highly dynamical outer regions. Additionally, we find the smallest variations in the average scaled profiles are around R_{500} , thus the normalization by $P_{500} \propto M_{500}^{2/3}$ is consistent between our simulations and Arnaud et al. (2010) observational profiles at $z = 0$.

3.5 SZ Power Spectra from Hydrodynamical Simulations

3.5.1 Stacked SZ power spectra of translated-rotated cosmological boxes

We randomly rotate and translate our simulation snapshots at different redshifts (da Silva et al., 2000; Springel et al., 2001a, B0205). To obtain thermal Compton- y maps, we perform a line-of-sight integration of the electron pressure within a given solid angle, i.e. $y = \sigma_T \int n_e k T_e / (m_e c^2) dl$, where k is the Boltzmann constant, n_e and T_e are the number density and temperature, respectively. We construct $1.6^\circ \times 1.6^\circ$ and $3.2^\circ \times 3.2^\circ$ maps for the 256^3 and 512^3 simulations, respectively. Using this method there are large sample variances (White et al., 2002) associated with nearby cluster contamination. We have quantified their influence on the power spectrum for each of our three physics models by averaging over

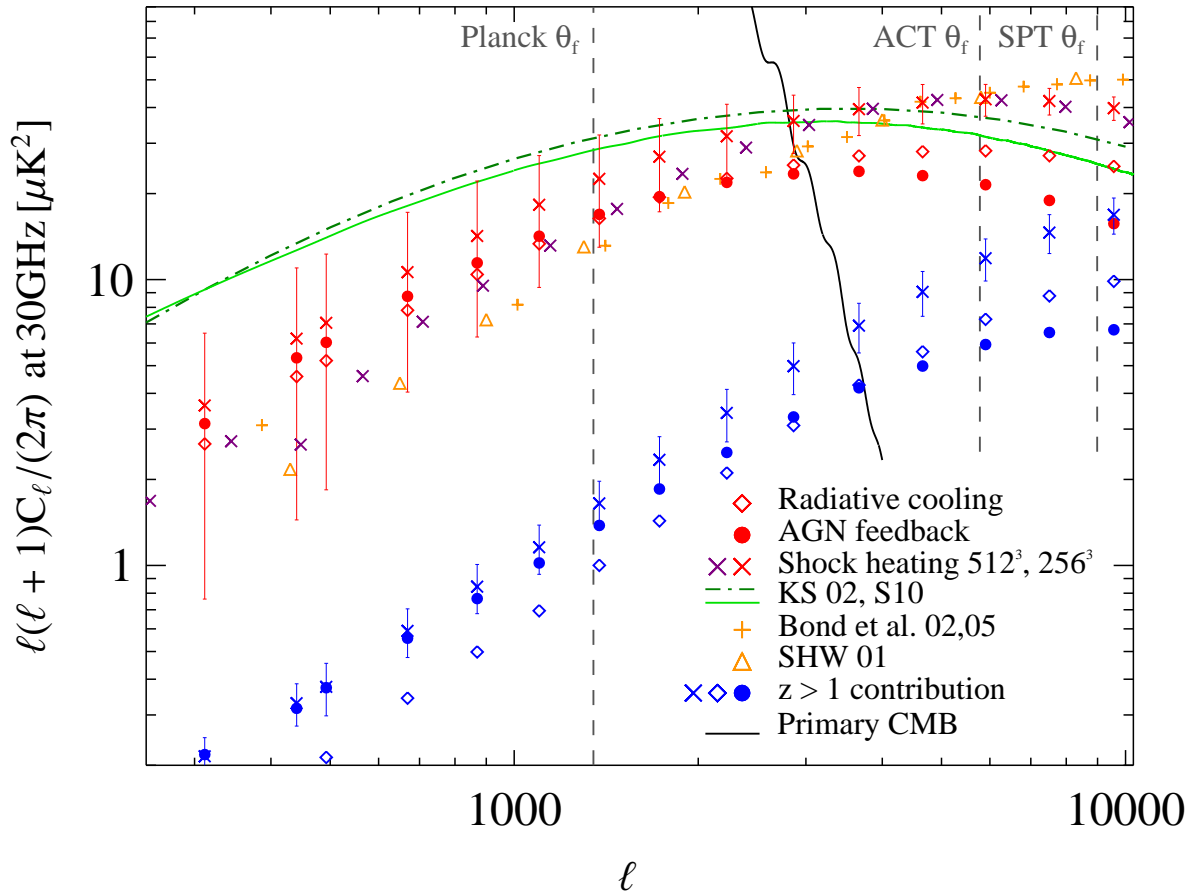


Figure 3.3: Predictions for the tSZ power spectrum at 30 GHz from our simulations (red and purple symbols), simulations by Springel et al. (2001a) (orange triangles), simulations by Bond et al. (2005) (orange pluses), semi-analytical simulations by S10 (dark green) and analytical calculations by KS (light green). The 256^3 power spectra (red symbols) are averages over 12 translate-rotate tSZ maps and 10 separate hydrodynamical simulations for each of the 33 redshift bins, the power spectra of which are then added up to yield the total spectrum; the error bars show the variance among the power in all maps. The full-width half-max values appropriate for Planck, ACT and SPT show which part of the templates these experiments are sensitive to. At low- ℓ , the discrepant higher power in the semi-analytical calculations can be traced to the enhanced pressure structures assumed beyond R_{200} over what we find.

twelve translate-rotate viewing angles each projected from our ten 256^3 full hydrodynamical simulations for each of the 33 redshift outputs back to a redshift $z = 5$; the power spectra of which are then added up to yield the total spectrum. This method of computing the power spectrum has the advantage of taking care of the artificial correlations that occur because any individual simulation follows the time evolution of the same structure. For the shock heating case, we did ten more hydrodynamical simulations to show that our averaged template had converged (within $\sim 10\%$), but note that using only a few boxes can be misleading in terms of rare events.

The computationally more expensive 512^3 SZ spectra have the equivalent of 8 256^3 plus wider coverage, so the 512^3 shock heating result shown gives a reasonable indication of what to expect. The other 2 physics single-box cases at 512^3 are similar to the 256^3 ensemble means. The analytical approach has the great advantage of including an accurate mean cluster density to high halo masses, but to be usable for SZ power estimation, scaled pressure profiles must also be accurate, a subject we turn to in future work. For now, we note that using such profiles from our simulations gives good agreement with the average SZ power shown at the low ℓ where sample variance will be largest. In Fig. 3.4.2, our simulation templates and the KS template shown have excluded structures below $z = 0.07$ to decrease the large sample variance associated with whether a large-ish cluster enters the field-of-view. Such entities would typically be removed from CMB fields and considered separately.

The mean Compton y -parameter found in our AGN feedback simulations is one order of magnitude below the COBE FIRAS upper limit of 15×10^{-6} (Fixsen et al., 1996).

We compare the theoretical predictions for the tSZ power spectrum in Fig. 3.4.2. Our 512^3 and 256^3 shock heating simulations are in agreement with previous SPH simulation power spectra (Springel et al., 2001a, B0205) scaled by $C_\ell \propto (\Omega_b h)^2 \Omega_m \sigma_8^7$, with the factors determined from our simulations of differing cosmologies. The B0205 SZ power shown had a cut at $z = 0.2$, appropriate for CBI fields; using the same cut on a shock heating simulation with the same cosmology that we have done, we get superb agreement.

The KS and S10 semi-analytic SZ power spectra templates differ substantially from our templates, in particular with higher power at low ℓ : as shown in Fig. 3.2, the KS pressure profile beyond R_{500} overestimates the pressure relative to both simulations and observations, leading to the modified shape and larger Y_Δ ; this behaviour is also shown in Komatsu et al. (2010). The spectrum from S10 is very similar to KS possibly because both assume hydrostatic equilibrium, and a polytropic equation of state with a fixed adiabatic index, $\Gamma \sim 1.1 - 1.2$. Inside R_{200} , these assumptions are approximately correct, but they start to fail beyond R_{200} . A demonstration of this is the rising of Γ and of the ratio of kinetic-to-thermal energy K/U shown for our simulations in the bottom panels of Fig. 3.4.2. The present day ($a = 1$) internal kinetic energy of a cluster is given by $K \equiv \sum_i m_{\text{gas},i} |\vec{v}_i - \vec{v} + H_0(\mathbf{x}_i - \bar{\mathbf{x}})|^2 / 2$, where H_0 is the present day Hubble constant, \vec{v}_i and \mathbf{x}_i are the peculiar velocity and comoving position for particle i , and \vec{v} and $\bar{\mathbf{x}}$ are the gas-particle-averaged bulk flow and center of mass of the cluster. The additional

thermal pressure support we find at large radii from AGN feedback results in the slightly slower rate of K/U growth shown. In all cases the large kinetic contribution shown should be properly treated in future semi-analytic models.

Varying the physics over the three cases for energy injection in our simulations leads to relatively minor differences in Fig. 3.4.2 among the power spectra for $\ell \lesssim 2000$. This agreement is due in part to hydrostatic readjustment of the structure so the virial relation holds, which relates the thermal content, hence Y_Δ , to the gravitational energy, which is dominated by the dark matter. Our AGN feedback parameters do not lead to dramatic gas expulsions to upset this simple reasoning. Our radiative cooling template has less power at all scales compared to the shock heating template since baryons are converted into stars predominantly at the cluster centers and the ICM adjusts adiabatically to this change. Thus, at low ℓ where clusters are unresolved, shock heating and radiative simulations give upper and lower limits, bracketing the AGN feedback case. AGN feedback suppresses the core value of the pressure compared to the radiative simulation resulting in less power at $\ell > 2000$, a trend that is more pronounced at $z > 1$ (as shown in Fig. 3.4.2). Thus, at these angular scales, the power spectrum probes the shape of the average pressure profile. It depends sensitively on the physics of star and galaxy formation e.g., Scannapieco et al. (2008). Over the ℓ -range covered by Planck, these effects are sub-dominant, and serve to highlight the importance of the high-resolution reached by ACT and SPT.

3.5.2 Current constraints on SZ template amplitudes and $\sigma_{8,SZ}$

Instead of varying all cosmological parameters on which the thermal and kinetic SZ power spectra, $C_{\ell,tSZ}$ and $C_{\ell,kSZ}$, depend, we freeze the shapes by adopting the parameters for our fiducial $\sigma_8 = 0.8$ (and $\Omega_b h = 0.03096$) model evaluated at 150 GHz, and content ourselves with determining template amplitudes, A_{tSZ} and A_{kSZ} , and a total SZ amplitude A_{SZ} :

$$A_{SZ} C_{\ell,SZ} \equiv \left[\frac{f(\nu)}{f(150 \text{ GHz})} \right]^2 A_{tSZ} C_{\ell,tSZ} + A_{kSZ} C_{\ell,kSZ}. \quad (3.6)$$

The spectral function for the tSZ (Sunyaev & Zeldovich, 1970), $f(\nu)$, crosses 0 at the SZ null (~ 220 GHz) and in the Raleigh-Jeans limit lowers to -2 . Therefore, if we find values of A_{SZ} below unity then either σ_8 is smaller than the fiducial cosmological value as derived from the primary CMB anisotropies, or else the theoretical templates overestimate the SZ signal.

To determine the probability distributions of these amplitudes and other cosmological parameters from current CMB data we adopt Markov Chain Monte Carlo (MCMC) techniques using a modified version of CosmoMC (Lewis & Bridle, 2002). We include WMAP7 (Larson et al., 2010) and, separately, ACT (Fowler et al., 2010) and SPT (Lueker et al., 2010). In all cases, we assume spatial flatness and fit for 6 basic cosmological parameters ($\Omega_b h^2$, $\Omega_{DM} h^2$, n_s , the primordial scalar power spectrum amplitude A_s , the Compton depth to re-ionization τ , and the angular parameter characterizing the sound crossing distance at recombination θ). We also allow for a flat white noise template $C_{\ell,src}$ with amplitude A_{src} ,

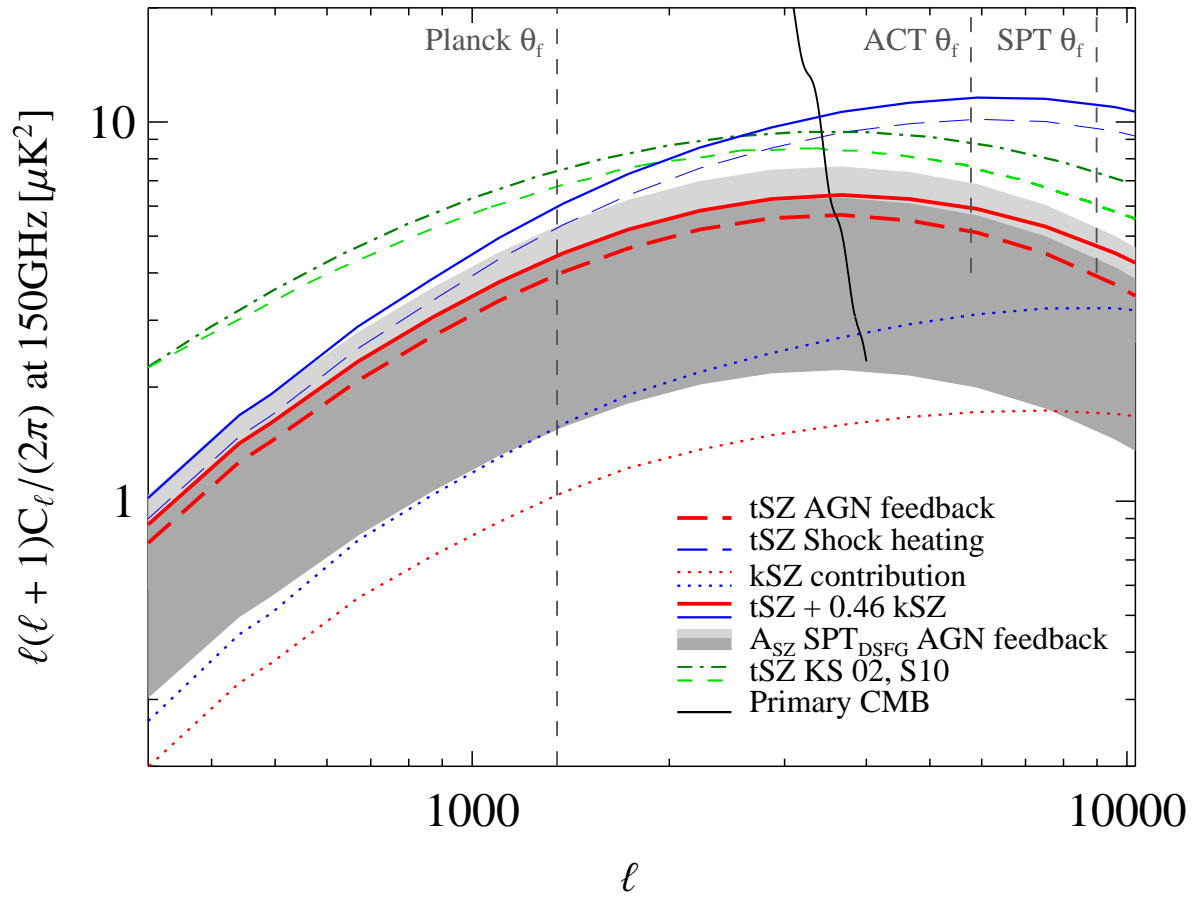


Figure 3.4: Our 150 GHz tSZ adiabatic and feedback ($A_{\text{SZ}} = 1$) power spectra computed with $\sigma_8 = 0.8$ (long dashed lines) are contrasted with the dark grey band indicating the 1σ range in multiplicative amplitude, $A_{\text{SZ}} = 0.75 \pm 0.36$, allowed by the SPT_{DSFG} power spectrum for the feedback template shape. The light grey band is the 2σ upper limit region. The $A_{\text{SZ}} = 1$ S10 tSZ power spectrum (dashed line) and the KS tSZ spectrum (dash dotted line) are shown for contrast; their allowed 1σ band is determined by multiplying these by their A_{SZ} values given in Table 5.8, but cover a similar swath to the grey bands. We also show the averaged kSZ power spectra computed for our simulations by dotted lines. The kSZ spectra were calculated in the same way as the tSZ spectra were, and have similar shapes. However, kSZ is underestimated at low ℓ because of missing bulk velocities in the simulations. There should be an additional (rather uncertain) kSZ template from inhomogeneous re-ionization as well. To show the tension with the CMB data, we plot the tSZ + 0.46 kSZ power (solid lines) since this can be directly compared with the SPT_{DSFG} grey bands.

such as would arise from populations of unresolved point sources. We marginalize over A_{src} , allowing for arbitrary (positive) values, which differs from Lueker et al. (2010) who put a prior on A_{src} . Generally there will also be a spatial clustering component for such sources, and these will have templates that are partially degenerate in shape with that for tSZ, but because of the large uncertainties we ignore such contributions here. Reducing the SZ and unresolved source problems to determinations of overall amplitudes multiplying shapes has a long history, e.g., the CBI sequence of papers, and was adopted as well by the ACT and SPT teams. Our results differ slightly from those reported by the ACT team because they use WMAP5+ACT and a combined tSZ+kSZ S10-template, and by the SPT team who use WMAP5+QUaD+ACBAR+SPT and add constraints on the white noise source amplitude beyond the non-negativity we impose.

We first consider a simplified case with A_{kSZ} constrained to be zero and all other cosmic parameters and the source amplitude marginalized, yielding a probability distribution for A_{SZ} . The means and standard deviations from our MCMC runs are given in the upper rows of Table 5.8 in columns 2, 4 and 6 for a number of data combinations and for our 3 physics simulation cases, contrasting with KS and S10. The ACT data is for 148 GHz. There are two SPT cases given. The first uses just the 153 GHz spectrum so it can be directly compared to ACT. For SPT, Lueker et al. (2010) also report a power spectrum derived from subtracting a fraction x of their 220 GHz data from the 153 GHz data to minimize the contribution from dusty star-forming galaxies (DSFG); since 220 GHz is the SZ null, this does not modify the tSZ contribution, but would diminish the frequency-flat kSZ. However, a normalization factor is chosen to preserve power for primary CMB signals that are flat in frequency like kSZ. This has the effect of boosting the tSZ power by a factor of $(1 - x)^{-2}$. Lueker et al. (2010) find that $x = 0.325$ minimizes the contribution from the DSFGs so the DSFG-subtracted spectrum suppresses the kSZ by a factor of 0.46 relative to the tSZ. A $\sim 25\%$ uncertainty remains in x which should be taken into account statistically, but is not here. The correct approach would be to simultaneously treat the 153 GHz and 220 GHz cases, with full modelling of the different classes of point sources, including their clustering, and to take into account the non-Gaussian nature of the SZ and source signals which impact sample variance.

The ACT data is only giving upper limits with their current published data, whereas SPT has detections at 153 GHz with A_{SZ} compatible with unity. For the SPT 153 GHz-only spectrum, we find S10 gives $A_{\text{SZ}} = 1.39 \pm 0.34$ while the feedback template gives $A_{\text{SZ}} = 1.76 \pm 0.43$, and the comparable 95% upper limits from ACT are 1.95 and 2.93. However, although the white noise shape has been vetoed by marginalization, there could be a residual clustered source contribution from dusty galaxies pushing the derived A_{SZ} high. To the extent that SPT_{DSFG} vetoes this DSFG clustering as well as their Poisson contribution, that A_{SZ} would be a better indicator. It shifts from 0.43 ± 0.21 for KS and 0.50 ± 0.25 for S10 up to 0.75 ± 0.36 for the feedback template, an increase of 50%. The large difference between the 150 and source-subtracted templates, even after marginalizing over a Poisson term, may suggest the power

Table 3.2: Constraints on A_{SZ} and $\sigma_{8,SZ}$

tSZ template	ACT 148 GHz		SPT 153 GHz		SPT _{DSFG}	
	A_{SZ}	A_{tSZ}	A_{SZ}	A_{tSZ}	A_{SZ}	A_{tSZ}
KS	< 1.55	< 1.26	1.01 ± 0.25	0.72 ± 0.25	0.43 ± 0.21	0.30 ± 0.21
S10	< 1.95	< 1.67	1.39 ± 0.34	1.11 ± 0.34	0.50 ± 0.25	0.38 ± 0.25
Shock heating	< 2.13	< 1.84	1.13 ± 0.28	0.84 ± 0.28	0.44 ± 0.22	0.31 ± 0.22
Radiative cooling	< 2.75	< 2.46	1.50 ± 0.37	1.21 ± 0.37	0.59 ± 0.29	0.45 ± 0.29
AGN feedback	< 2.93	< 2.66	1.76 ± 0.43	1.49 ± 0.43	0.75 ± 0.36	0.63 ± 0.36
	$\sigma_{8,SZ}$	$\sigma_{8,tSZ}$	$\sigma_{8,SZ}$	$\sigma_{8,tSZ}$	$\sigma_{8,SZ}$	$\sigma_{8,tSZ}$
KS	< 0.864	< 0.845	$0.792^{+0.029}_{-0.029}$	$0.757^{+0.039}_{-0.037}$	$0.690^{+0.057}_{-0.055}$	$0.622^{+0.105}_{-0.051}$
S10	< 0.891	< 0.874	$0.828^{+0.031}_{-0.030}$	$0.800^{+0.038}_{-0.036}$	$0.705^{+0.060}_{-0.058}$	$0.636^{+0.109}_{-0.054}$
Shock heating	< 0.900	< 0.883	$0.804^{+0.031}_{-0.030}$	$0.768^{+0.040}_{-0.038}$	$0.691^{+0.059}_{-0.057}$	$0.607^{+0.119}_{-0.057}$
Radiative cooling	< 0.935	< 0.922	$0.837^{+0.032}_{-0.031}$	$0.809^{+0.039}_{-0.037}$	$0.721^{+0.060}_{-0.058}$	$0.660^{+0.102}_{-0.053}$
AGN feedback	< 0.944	< 0.932	$0.856^{+0.033}_{-0.032}$	$0.835^{+0.038}_{-0.037}$	$0.746^{+0.061}_{-0.059}$	$0.703^{+0.091}_{-0.055}$

The mean and standard deviation of the thermal SZ power spectrum template amplitude A_{tSZ} and the total SZ, including our computed kSZ contribution. The numbers assume the kSZ template is perfectly degenerate in shape with the tSZ one. $A_{SZ} = A_{tSZ} + A_{kSZ}$ at 150 GHz, with the relative enhancement in our simulations given by $A_{kSZ}/A_{tSZ} = 0.29, 0.29, 0.27$ for the shock heating, radiative cooling and feedback simulations, respectively. We have used the ACT team's 148 GHz power spectrum, the SPT team's 153 GHz spectrum and the SPT DSFG-subtracted (SPT_{DSFG}) spectrum, along with WMAP7. The amplitude of the SZ power is normalized to our fiducial $\sigma_8 = 0.8$ cosmology. A rough guide to the σ_8 tension is obtained in the lower rows, using $\sigma_{8,SZ} \propto A_{SZ}^{1/7} (\Omega_b h)^{-2/7}$, with exponents determined by B0205 and KS. Since kSZ varies more slowly with σ_8 than tSZ, the numbers are just indicative.

in the correlated source component may be similar to the SZ power, emphasizing the work necessary to do a correct treatment.

Any non-zero kSZ contribution will take some of the amplitude from A_{SZ} , leaving even smaller A_{tSZ} values; columns 3, 5 and 7 of the Table 5.8 give estimates of this diminution. The kSZ power spectra that we have computed are broadly similar to the tSZ power shape, with however sufficiently significant differences to allow shape discrimination in addition to the frequency separability, as Fig. 3.4 shows. At 150 GHz and an $\ell = 3000$ pivot, we find the kSZ power is $\sim 29\%$, $\sim 29\%$ and $\sim 27\%$ of the tSZ power for the shock heating, radiative cooling and feedback simulations, respectively. We normalize the kSZ to the tSZ at this pivot of 3000 since it has most of the constraining power in the CosmoMC chains for the ACT and SPT measurements and results in the smallest error bars: on larger scales, the errors are increased by the contribution from primary anisotropies while smaller scales are dominated by the instrumental and galaxy-source shot noise.

We used exactly the same procedure to obtain the kSZ spectrum as we used for the tSZ spectrum. The temperature decrement due to the kSZ effect is $\Delta T/T = \sigma_T \int n_e v_r/c dl$, where v_r is the radial peculiar velocity of the gas relative to the observer. We constructed 12 translate-rotate kSZ maps for each of our 10 separate hydrodynamical simulations and for each of the 41 redshift bins back to $z = 10$ (rather than $z = 5$ for tSZ), computing the average and variance of all of these. Since we use simulations with side length $L = 165 h^{-1}\text{Mpc}$ for our 256^3 cases, with fundamental wavenumber $(26 h^{-1}\text{Mpc})^{-1}$, our spectra are missing a bit of power on the largest scales (affecting low- ℓ) since we do not sample well the long-wavelength tail of the velocity power spectrum in spite of the number of runs done.

We have included the kSZ template by ignoring the relatively small shape difference about the pivot point of the kSZ and tSZ power spectra; i.e., we assume the perfect degeneracy $C_{\ell,\text{kSZ}} \propto C_{\ell,\text{tSZ}}$, as the SPT team did. Thus we only need the ratios $A_{\text{kSZ}}/A_{\text{tSZ}}$ given above for the 150 GHz cases and the further x factors for the mixed frequency DSFG case. For the ratios we use our translate-rotate values of 0.29, 0.29 and 0.27 from our simulations, 0.276 for S10, and used a rough estimate of 0.25 for KS. Apart from ignoring the shape difference, we have also ignored kSZ from patchy re-ionization at high redshift, although it can have a competitive amplitude to the late time fully ionized gas motions with respect to the CMB rest frame that we are modelling (Iliev et al., 2008, 2007). In presenting the results from our analyses of the MC Markov chains, we just subtract A_{kSZ} from A_{SZ} . The Table 5.8 A_{tSZ} that we derive from these assumptions are all on the low side of unity for DSFG, with KS and S10 being more than 2.5σ low, whereas the feedback template is only about 1σ low (and 1σ high for 153 GHz alone). We leave it to future work to include a more complete implementation of the kSZ spectra.

The means and errors on A_{SZ} provide the cleanest way of presenting the tension, or lack thereof, of these SZ models with the primary CMB data which indicates $\sigma_8 \approx 0.8$. However, it has been conventional to translate these numbers into a $\sigma_{8,\text{SZ}}$ using the way A_{SZ} scales with cosmic parameters, roughly as $A_{\text{SZ}} \propto \sigma_8^7 (\Omega_b h)^2$, as given by B0205 and KS. The lower rows in Table 5.8 show $\sigma_{8,\text{SZ}}$ using

this scaling. Although the scaling applies to the tSZ component only, with the kSZ power being less sensitive to σ_8 , we also quote results for the kSZ-corrected cases. Ideally one should use the data to determine the cosmic parameters which uniquely and fully determine the primary spectrum, the A_{tSZ} and A_{kSZ} , and the tSZ and kSZ shape modifications as the parameters vary. This slaved treatment enforcing $\sigma_{8,\text{SZ}} = \sigma_8$ has σ_8 's value being driven by WMAP7 and other primary CMB data rather than by the SZ information. We note that the σ_8 results in Lueker et al. (2010) are determined with A_{SZ} and primary CMB data combined. Therefore, the Lueker et al. (2010) σ_8 results are not comparable to our $\sigma_{8,\text{SZ}}$ results.

3.6 Conclusions and Outlook

Without hydrodynamical simulations in a cosmological framework similar to the ones presented in this paper it is hard to come up with a consistent model of the gas distribution in clusters and the infall regions which both contribute significantly to the SZ power spectrum. In this paper, we identify three main points that a future semi-analytic model of such a pressure distribution has to provide.

(1) In order to arrive at a consistent gas distribution that matches not only the integrated stellar mass fraction but also the X-ray derived pressure profiles within R_{500} , we need self-regulating AGN-type feedback. We emphasize that we tuned our parameters to match a previous single-cluster model that successfully suppressed the over-cooling by means of AGN feedback (Sijacki et al., 2008b). The excellent agreement with current data was a pleasant byproduct: our simulated pressure profiles agree with recently obtained observational ones that have been constructed from X-ray data; the scaling relations between the cluster mass and X-ray based Compton- Y (Arnaud et al., 2010) also agree; as do the integrated stellar and gas mass fractions (Gonzalez et al., 2007; Afshordi et al., 2007).

(2) The amount of non-gravitational energy injection into proto-clusters and groups by AGN and starburst galaxies at intermediate-to-high redshifts $z \gtrsim 0.8$ is poorly understood. Other observables are needed to constrain the physics and to answer this question which seems to be essential in understanding the resulting gas profiles. Our simulations suggest that AGN-type feedback lowers the central pressure values as a hydrodynamic response of the gas distribution to the non-gravitational feedback of energy. This effect inhibits gas from falling into the core regions which causes a flatter and more extended pressure profile and a noticeably reduced power of the SZ power spectrum at small angular scales for $\ell \gtrsim 2000$.

(3) For the SZ flux to be converged, an integration of the pressure profile out to $4R_{200}$ is necessary; half of the SZ flux is contributed from regions outside R_{200} . To compute a reliable SZ power spectrum, it is essential to precisely characterize the state of the gas in these infall regions. In particular, we find that: (i) the pressure support from kinetic energy strongly increases as a function of radius to reach on average equipartition with the thermal energy at $\sim 2R_{200}$ in our AGN model with the exact dependence on cluster

mass to be determined by future work; (ii) the effective adiabatic index $\Gamma = d \ln p / d \ln \rho \sim 1.2$ in the interior, but upturns towards $\Gamma \sim 5/3$ beyond the virial radius; (iii) the inclusion of cluster asphericity at large radii may also become important.

Hence a successful semi-analytic model of the spherical cluster pressure, if that is indeed a viable goal, at the least needs careful calibration using numerical simulations which accurately treat all of the effects. The variance of the average profiles also encodes important information that is manifested in the power spectrum. Our studies also show that simplified analytic models that employ hydrostatic gas models with a constant Γ necessarily overpredict the SZ power on large scales by up to a factor of two and predict an inconsistent shape of the SZ power spectrum. The alternative that we explore in a subsequent paper is to use stacked scaled simulational clusters which are rotated to principal axes to provide the pressure form factors for the semi-analytic approach.

The tSZ power spectrum of our 512^3 simulation agrees well with the average of our ten 256^3 simulations. A large number of simulations are needed to properly sample the high-mass end of the cluster mass function and hence accurately deal with sample (cosmic) variance. Alternatively, larger cosmological volumes can compensate since they contain enough statistics on the large scale modes that are responsible in part for forming the highest-mass clusters which are also the rarest events. This, however, is quite challenging as we require the same (high-)resolution to accurately follow the physics in the cluster cores which is needed to obtain profiles that match current X-ray data. Our 256^3 simulations do not quite sample large enough scales to provide a fully converged kSZ power spectrum at low ℓ since we miss the long-wavelength tail of the velocity power spectrum. We also have ignored the patchy re-ionization kSZ which could be a significant contributor, up to 50% of the total kSZ (e.g., Iliev et al., 2008, 2007).

We have found the $\ell < 2000$ multipole range to be relatively insensitive to cooling and feedback, at least for the range constrained by the X-ray data. We did find the higher multipole range ($\ell \sim 2000 - 10000$) probed by the high-resolution ACT and SPT CMB telescopes is sensitive to the feedback prescription; hence the high- ℓ SZ power spectrum can be used to constrain the theory of intracluster gas, in particular for the highly uncertain redshifts > 0.8 . In addition to the SZ power spectrum probe, our simulations can be used to address the cosmological significance of cluster counts as derived from the SZ effect. Counts provide complementary constraints on parameters that help to break some degeneracies that are present in the power spectrum method. By employing inhomogeneous, localized and self-regulated feedback we are not only able to match recent X-ray reconstructions of cluster core regions, but also decrease the tension in σ_8 estimated from SZ power with σ_8 from other cosmological probes. However, only a detailed confrontation between simulations exploring the vast terrain of feedback options with the rapidly improving high resolution observations of cluster interiors can move the theory of cluster gas physics and its use for precision cosmology forward.

Chapter 4

Scaling Relations, Non-thermal Pressure Support, and Shapes of Galaxy Clusters

4.1 Chapter Overview

The current efforts by large Sunyaev Zel'dovich (SZ) galaxy cluster surveys to constrain cosmological parameters from cluster abundances are limited by the theoretical uncertainty in the SZ flux-to-cluster mass relation, $Y - M$. We explore how the non-thermal pressure support of the intracluster medium (ICM) and the anisotropy of the gas distribution impacts that scaling relation. To this end we use a suite of hydrodynamical TreePM-SPH simulations of the cosmic web in large periodic boxes that employ different variants of simulated physics, including radiative cooling, star formation and supernova feedback, cosmic rays and energetic feedback from active galactic nuclei (AGN). We find that the kinetic pressure support from bulk motions depends on the cluster mass, while the asphericity of the ICM depends less upon the simulated physics and the cluster mass. At large cluster radii, the kinetic pressure support and ICM shapes are dominated by substructure. We find that the intrinsic cluster shapes can on average be inferred from their projected analogues by applying a $\sim 5 - 10\%$ correction to the ellipticity. The radius that contains a mean density of 500 times the critical density of the universe, R_{500} represents the best compromise to study virial properties as it probes a large enough volume which is not dominated by the intricate physics of the cluster core region, has a comparable low non-thermal pressure support of $\sim 20\%$, and shows the smallest variance of ellipticity with cluster mass and redshift. The simulated $Y - M$ relations are consistent with the self-similar predictions for galaxy clusters, with the exception of the relation of our AGN feedback model at low redshift that shows a statistically significant steeper slope due to the feedback-induced deficit of gas inside the lower mass clusters. Including AGN feedback increases the overall scatter in the $Y - M$ relation from $\sim 11\%$ to $\sim 14\%$. If galaxy clusters are selected to have lower kinetic pressure support, we find that the scatter is decreased back to $\sim 11\%$, suggesting that the scatter ultimately originates from the cluster merging history with its redshift and mass dependent

accretion history. This opens an exciting venue of constructing a fundamental plane about the $Y - M$ -relation that minimizes its scatter and allows tighter cosmological constraints.

4.2 Introduction

Galaxy clusters are the largest gravitationally relaxed objects in the universe and form in the highest peaks of the primordial density fluctuations. The interiors are isolated from the cosmic expansion rendering them nearly “closed” systems, so they approximately maintain the universal proportion of baryonic to dark matter (DM). For these reasons galaxy clusters are promising cosmological tools, as they trace the growth of structure in the universe. In galaxy clusters most of the baryons are in the form of a hot diffuse plasma known as the intracluster medium (ICM); the remaining baryons are found in the cluster’s numerous stars and galaxies. Galaxy clusters are therefore in a unique position to probe cosmological parameters as well as to reveal the detailed astrophysical processes of the ICM.

This work will focus on the observational signature from the Sunyaev Zel’dovich (SZ) effect (Sunyaev & Zeldovich, 1970), which describes the Compton up-scattering of cosmic microwave background (CMB) photons by hot electrons. This produces a localized perturbation to the CMB spectrum with a unique spectral shape that is characterized by a decrement in thermodynamic temperature below $\nu \sim 220$ GHz, and an excess above. The SZ signal is proportional to the integrated electron pressure, so the hot gas of the ICM dominates the effect. Furthermore, the SZ surface brightness is independent of redshift. Hence SZ surveys yield a different selection function in redshift and mass in comparison to X-ray and optical cluster surveys, i.e., for a comparable mass limit at low redshifts (as given by the survey sensitivity), SZ surveys will return higher redshift objects than the latter observational techniques. These different selection functions imply complementary degeneracies on cosmological parameters associated with the growth of structure which should yield tighter constraints on these parameters in combination with other cluster surveys and cosmological probes.

In a large cluster survey there is a wealth of information contained about cosmology and structure formation. The abundance of clusters, their distribution in redshift, and their spatial clustering should be determined purely by the geometry of the universe, the power spectrum of initial density fluctuations, and cosmological parameters such as the dark energy equation of state, w , or the *rms* amplitude of the (linear) density power spectrum on cluster-mass scales, σ_8 . In SZ surveys, the number counts as a function of redshift and the power spectrum are two complementary probes of cosmology (e.g., Birkinshaw, 1999; Carlstrom et al., 2002). Identifying clusters through blind SZ surveys and measuring their integrated power spectrum have been long term goals in CMB research, and are reaching fruition through, e.g., the South Pole Telescope, SPT (e.g., Lueker et al., 2010; Shirokoff et al., 2010; Keisler et al., 2011; Vanderlinde et al., 2010), the Atacama Cosmology Telescope, ACT (e.g., Fowler et al., 2010; Dunkley et al., 2010; Marriage et al., 2010; Sehgal et al., 2011), and the Planck satellite (e.g., Planck Collab-

oration et al., 2011a,b,c). However, the ability to precisely determine cosmological parameters from number counts depends on an accurate understanding of the scaling relation between fundamental cluster properties such as the mass, M , and SZ observables, e.g., the total SZ flux, Y , which is proportional to the cluster's thermal energy. Equivalently, the SZ power spectrum probes the average pressure profile of unresolved groups and clusters and depends sensitively on the amplitude of the mass power spectrum on cluster scales. While this allows the study of astrophysical properties of the plasma, it complicates the extraction of the cosmological information which is now degenerate with intrinsic cluster physics. This paper dissects the influence of various physical processes on the $Y - M$ scaling relation while our companion paper (Battaglia et al., Paper II) provides a detailed study of the SZ power spectrum.

Previous work has attempted to calibrate the $Y - M$ scaling relation through observations (e.g., Benson et al., 2004; Bonamente et al., 2008; Marrone et al., 2009; Andersson et al., 2010; Sayers et al., 2011), self-calibration techniques (e.g., Majumdar & Mohr, 2003, 2004; Lima & Hu, 2004; Chaudhuri & Majumdar, 2011; Nath & Majumdar, 2011), simulations (e.g., da Silva et al., 2004; Motl et al., 2005; Schäfer et al., 2006a,b; Bonaldi et al., 2007) and analytical work (Bode et al., 2007; Mroczkowski, 2011). Combining such a $Y - M$ scaling relation with the survey selection function and marginalizing over the associated uncertainties of statistical and systematic nature enables an accurate determination of the mentioned cosmological parameters. SPT (Vanderlinde et al., 2010) and ACT (Sehgal et al., 2011) have published cosmological constraints using a small sample of SZ galaxy clusters. The uncertainties of the constraints on σ_8 are dominated by systematic uncertainties in the underlying cluster physics making this approach less competitive compared to other cosmological probes. Hence in order to improve upon the determination of cosmological parameters, this calls for a better understanding of the mass proxies and their scatter (Nagai, 2006; Stanek et al., 2010; Yang et al., 2010).

Pioneering work by Kaiser (1986) assumed that galaxy clusters are self-similar systems with the mass determining their ICM thermodynamic properties. As shown by X-ray observations, this self-similar description is broken, especially on group scales; low-mass systems are less luminous in comparison to the self-similar expectation (see Voit, 2005, for a review). It is still a field of active research how non-thermal processes such as magnetic fields, cosmic rays, active galactic nuclei (AGN), star formation, radiative cooling and bulk motions contribute to the energy balance and thermodynamic stability within clusters. In particular, it is unclear how these processes vary as a function of radius or dynamical state of the clusters. Thus, state-of-the-art simulations are a valuable tool in building a consistent picture of galaxy clusters. In turn, we provide an overview of the three main processes that influence the $Y - M$ scaling relation. These are the feedback processes that appear to be necessary in explaining the thermodynamic characteristics of the ICM, non-thermal pressure support from bulk motions that accompany the virialization process, and deviations from spherical symmetry; both implications from the relatively recent formation epoch of galaxy groups and clusters.

In many galaxy clusters the ICM cooling times are much shorter than a Hubble time (Fabian, 1994;

Cavagnolo et al., 2009), which should cause extremely high star formation rates that are well beyond what is observed. However, current simulations with *only* radiative cooling and star formation excessively over-cool cluster centers (e.g., Sugihara & Ostriker, 1998; Lewis et al., 2000; Pearce et al., 2000), even with the addition of supernova feedback. This leads to too many stars in the cluster cores, an unphysical rearrangement of the thermal and hydrodynamic structure, and problems when comparing simulations to observations, in particular for the entropy and pressure profiles. Self-regulated, inhomogeneous energy feedback mechanisms by, e.g., AGN are very successful in globally stabilizing the group and cluster atmospheres, and in particular, preventing the cooling catastrophe (Churazov et al., 2001). Observations of cool core galaxy clusters show evidence for an AGN moderating the cooling and potentially able to heat the surrounding ICM from kpc size bubbles to hundreds of kpc size outbursts (McNamara et al., 2005). In hydrodynamical simulations, it has been shown that incorporating a sub-grid for AGN feedback can resolve the over-cooling problem (e.g., Sijacki et al., 2007, 2008a; Battaglia et al., 2010; McCarthy et al., 2011). The effects of AGN feedback on the ICM will mainly alter the cluster cores, where the actual physics is poorly resolved and understood. These effects can be dramatic in X-ray observations (e.g., Fabian et al., 2003), which are proportional to gas density squared. Since the SZ signal is proportional to the gas pressure, these effects are smaller. Hence, AGN feedback should only perturb the integrated thermal SZ signal, with an amplitude that is not yet known.

Studying non-thermal pressure support from bulk motion in galaxy clusters has a long history and was first noticed in simulations by Evrard (1990), which showed that estimates for the binding mass of a cluster using a hydrostatic isothermal β -model in comparison to a fit to the surface brightness profile differ by 15%. They found that inclusion of velocity dispersion in the hydrostatic isothermal β -model reconciled this difference between binding masses. Including the support from residual gas motions in the hydrostatic cluster mass estimator improved the match with the true cluster mass (Rasia et al., 2004), with increasing kinetic pressure at larger cluster radii (Lau et al., 2009). The amount of energy in these bulk motions are of the order of 20% to 30% at radii of interest for cosmology (Battaglia et al., 2010; Burns et al., 2010). However, kinetic pressure support has only recently been included in analytical and semi-analytical templates for the thermal SZ power spectrum (Shaw et al., 2010; Trac et al., 2011)¹. While this is of importance for SZ measurements, X-ray observations of galaxy clusters have been calibrated such that this effect is accounted for when determining mass from the X-ray inferred total thermal energy (e.g., using the Y_X - M relation Kravtsov et al., 2006). In this paper we focus on the effects of bulk motions within galaxy clusters that dominate the total kinetic pressure budget since there is a smaller fraction of energy in a hydrodynamical turbulent cascade compared to the energy on the injection scale. Quantifying the properties of turbulence in galaxy clusters is starting to become possible with simulations beginning to model sub-grid turbulence (e.g., Iapichino & Niemeyer, 2008),

¹Note that full cosmological hydrodynamical simulations by definition account for this contribution and thus, do not require additional modeling of kinetic pressure effects.

which is however not the topic of our work.

DM halo shapes have been studied thoroughly. For SZ observations, the shape of the gas distribution of the ICM is important, especially in the far field of the intracluster medium which contributes substantially to the total integrated SZ flux (Battaglia et al., 2010). The assumption of spherical symmetry is often made when calculating cluster properties from observations and in analytical prescriptions of clusters properties and we would like to assess its validity. Semi-analytic models that employ the full three-dimensional information of a dissipationless simulation use the shape of the resulting gravitational cluster potentials; so an important question in this context is how these shapes compare with those of the dissipational gas distribution. Recent numerical work has already shown the impact of cooling and star-formation on the properties of ICM shape for a sample size of 16 clusters (Lau et al., 2011), however, such a study has not been extended to a larger sample. Furthermore, the question of how energetic feedback in the cluster cores affects ICM shapes has not been addressed.

In this work we explore a large statistical sample of simulated galaxy clusters with identical initial conditions but employing different models for sub-grid physics. We quantify the importance of non-thermal pressure support and ICM shapes on SZ scaling relation. In Section 4.3, we briefly describe the simulations and sub-grid physics used. We present our results for non-thermal pressure support from bulk motions and ICM shapes in Sections 4.4 and 4.5, respectively. The impact of these processes and the simulated physics is presented in Section 4.6. In Section 4.7 we summarize our results and conclude.

4.3 Cosmological simulations and cluster data set

We simulate multiple large-scale boxes of the cosmic web in order to improve our statistics of the number of objects while simultaneously aiming for a sufficiently high mass resolution to map out the core regions of those clusters/groups, which are targeted by current SZ cluster surveys and which dominate the SZ power spectrum signal on scales larger than one arcminute. To this end, we will characterize the average behaviour of the properties of the ICM over a large mass and redshift range. We use a modified version of the GADGET-2 (Springel, 2005) code that employs smoothed particle hydrodynamics (SPH). For each modeled physics, we simulate a sequence of 10 boxes of side length $165 h^{-1}$ Mpc with periodic boundary conditions, encompassing a number of DM and gas particles of $N_{\text{DM}} = N_{\text{gas}} = 256^3$. This yields a gas particle mass of $m_{\text{gas}} = 3.2 \times 10^9 h^{-1} M_{\odot}$, a DM particle mass of $m_{\text{DM}} = 1.54 \times 10^{10} h^{-1} M_{\odot}$ and the minimum gravitational smoothing length $\epsilon_s = 20 h^{-1}$ kpc; our SPH densities are computed with 32 neighbours. For our standard calculations, we adopt a tilted Λ CDM cosmology, with total matter density (in units of the critical) $\Omega_{\text{m}} = \Omega_{\text{DM}} + \Omega_{\text{b}} = 0.25$, baryon density $\Omega_{\text{b}} = 0.043$, cosmological constant $\Omega_{\Lambda} = 0.75$, a present day Hubble constant of $H_0 = 100h$ km s $^{-1}$ Mpc $^{-1}$ with $h = 0.7$, a spectral index of the primordial power-spectrum $n_s = 0.96$ and $\sigma_8 = 0.8$.

We show results for three variants of simulated physics: (1) the classic non-radiative ‘adiabatic’

case with only gravitational formation *shock heating*; (2) an extended *radiative cooling* case with star formation, supernova (SN) feedback and cosmic rays (CRs) from structure formation shocks (for more information on CRs, see Jubelgas et al., 2008; Enßlin et al., 2007; Pfrommer et al., 2007); (3) *AGN feedback* in addition to radiative cooling, star formation, and SN feedback. Radiative cooling and heating were computed assuming an optically thin gas of a pure hydrogen and helium primordial composition in a time-dependent, spatially uniform ultraviolet background. Star formation and supernovae feedback were modelled using the hybrid multiphase model for the interstellar medium of Springel & Hernquist (2003a). The CR population is modelled as a relativistic population of protons described by an isotropic power-law distribution function in momentum space with a spectral index of $\alpha = 2.3$, following Enßlin et al. (2007). With those parameters, the CR pressure modifies the SZ effect at most at the percent level and causes a small reduction of the resulting integrated Compton- γ parameter (Pfrommer et al., 2007). The AGN feedback prescription included in the simulations (for more details see Battaglia et al., 2010) allows for lower resolution and hence can be applied to large-scale structure simulations. It couples the black hole accretion rate to the global star formation rate (SFR) of the cluster, as suggested by Thompson et al. (2005). If the SFR is larger than an observationally motivated threshold, $\dot{M}_* > 5M_\odot \text{yr}^{-1}$, the thermal energy is injected into the ICM at a rate which is proportional to the SFR within a given spherical region.

We define the virial radius of a galaxy cluster, R_Δ , as the radius at which the mean interior density equals Δ times the *critical density*, $\rho_{\text{cr}}(z)$ (e.g., for $\Delta = 200$ or 500). For comparison, we will use an alternative definition of the virial radius, $R_{\Delta, \text{m}}$, where the mean interior density is compared to the *mean matter density*, $\bar{\rho}_{\text{m}}(z)$. For clarity the critical density and the mean matter density are,

$$\rho_{\text{cr}}(z) = \frac{3H_0^2}{8\pi G} [\Omega_{\text{m}}(1+z)^3 + \Omega_\Lambda] \quad (4.1)$$

$$\bar{\rho}_{\text{m}}(z) = \frac{3H_0^2}{8\pi G} \Omega_{\text{m}}(1+z)^3 \quad (4.2)$$

Here we have assumed a flat universe ($\Omega_{\text{m}} + \Omega_\Lambda = 1$) and are only interested in times after the matter-radiation equality, i.e., the radiation term with Ω_{r} is negligible. We chose to define the virial radius with respect to the critical density in continuity with recent galaxy cluster measurements. The merits and utilities of both these definitions are discussed later in the Appendix.

We apply the following two-step algorithm to compute the virial mass of a cluster in our simulations. First, we find all clusters in a given snapshot using a friends-of-friends (FOF) algorithm (Huchra & Geller, 1982). Then, using a spherical overdensity method with the FOF values as starting estimates, we recursively calculate the center of mass, the virial radius, R_Δ , and mass, M_Δ , contained within R_Δ , and compute the radially averaged profiles of a given quantity with radii scaled by R_Δ . We then form a weighted average of these profiles for the entire sample of clusters at a given redshift unless stated

otherwise. We use the integrated Compton y -parameter as our weighting function,

$$Y_{\Delta} = \frac{\sigma_{\text{T}}}{m_e c^2} \int_0^{R_{\Delta}} P_e(r) 4\pi r^2 dr \propto E_{\text{th}}(< R_{\Delta}), \quad (4.3)$$

where σ_{T} is the Thompson cross-section, m_e is the electron mass and P_e is electron pressure. For a fully ionized medium, the thermal pressure $P = P_e(5X_{\text{H}} + 3)/(X_{\text{H}} + 1) = 1.932P_e$, where $X_{\text{H}} = 0.76$ is the primordial hydrogen mass fraction.

4.4 Non-thermal cluster profiles

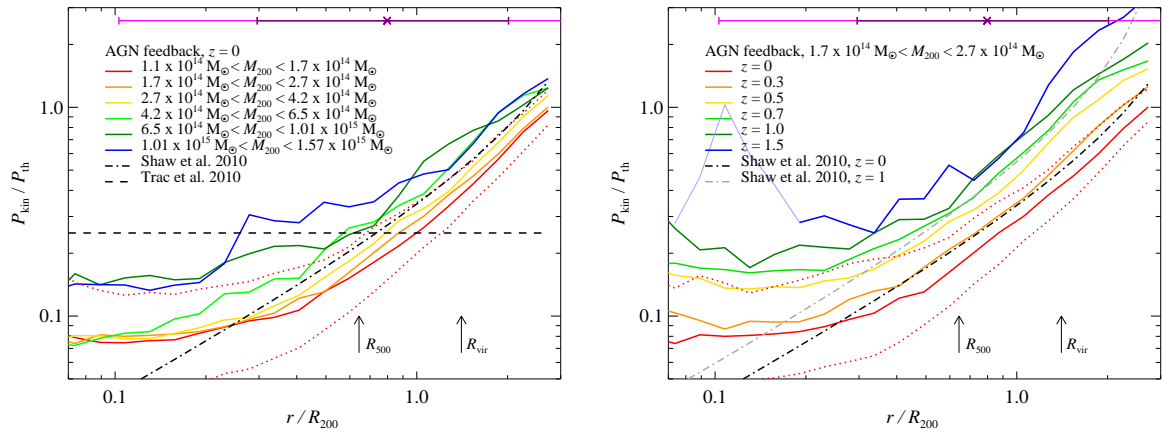


Figure 4.1: The ratio of kinetic and thermal pressure support, $P_{\text{kin}}/P_{\text{th}}$, depends on mass and redshift. We show the median of $P_{\text{kin}}/P_{\text{th}}$ as a function of radius for the AGN feedback simulations for various mass bins at $z = 0$ (left) and as a function of redshift for a fixed mass bin (right). We additionally show the 25th and 75th percentile values for the lowest mass bin at $z = 0$ (dotted). In both panels we illustrate the 1 and 2 σ contributions to Y_{Δ} centered on the median for the feedback simulation by horizontal purple and pink error bars which extends out to $4R_{200}$ (Battaglia et al., 2010). Two analytical models for the P_{kin} by Shaw et al. (2010) and Trac et al. (2011) are shown with the dash dot and dashed lines, respectively. The Shaw et al. (2010) model matches our result in the mass bin $2.7 \times 10^{14} M_{\odot} \leq M_{200} \leq 4.2 \times 10^{14} M_{\odot}$ at intermediate cluster radii (this mass bin best represents the mean mass of their sample at redshift zero), but also illustrates the need for a mass dependence in future analytical models. Note, the mass dependence of this ratio is driven by the mass dependence in P_{kin} (see Fig. 4.2 below).

The thermal pressure profile of clusters has become increasingly important as it is a main component in the analytical thermal SZ power spectrum calculation. Also, the integrated thermal pressure profile is being used as a mass proxy for galaxy clusters, since it is the dominant contribution to the total gas energy of an average cluster. However, several simulations (Evrard, 1990; Rasia et al., 2004; Lau et al.,

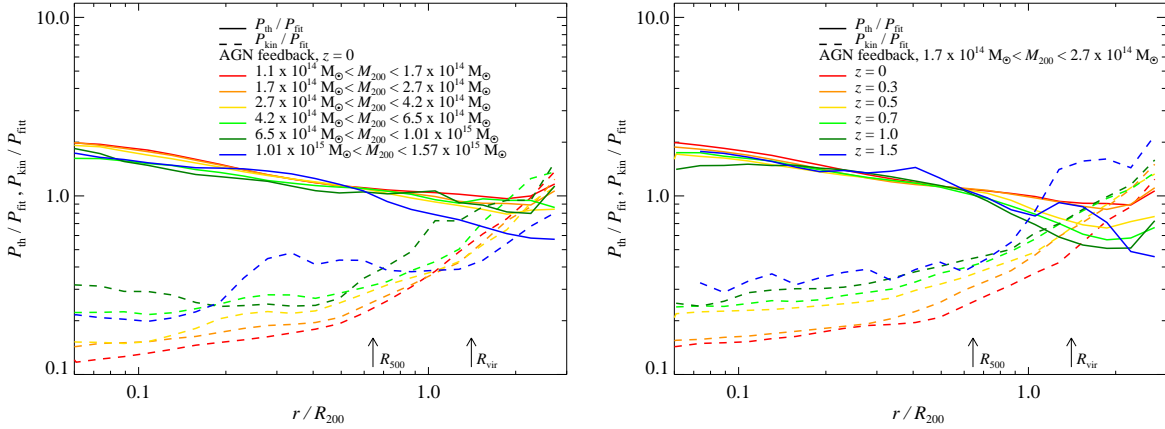


Figure 4.2: Mass and redshift dependence of P_{th} and P_{kin} , normalized to an empirical fit, P_{fit} , to the scaled thermal pressure, P_{th}/P_{Δ} . We show the mean scaled thermal and kinetic pressure profiles at $z = 0$ as a function of radius for the AGN feedback simulations in various mass bins (left), and for various redshifts at fixed mass bin (right).

2009) showed that the kinetic pressure from bulk motions contributes a small but still significant amount of energy within R_{500} and this importance increases for larger cluster radii (Lau et al., 2009; Battaglia et al., 2010; Burns et al., 2010). Hence it is important to accurately quantify the kinetic pressure contribution as it biases the hydrostatic cluster masses. There are two kinetic pressure contributions, namely large-scale, unvirialized bulk motions and subsonic turbulence. For a Kolmogorov power spectrum of turbulence, the energy is dominated by the largest scales which we resolved and characterize in our simulations. Hence we believe that our approach captures the majority of the kinetic pressure contribution.

4.4.1 Kinetic pressure support

We define the kinetic pressure to be one third the trace of the stress tensor,

$$P_{kin} = \rho \delta \vec{v}^2 / 3, \quad (4.4)$$

where the physical velocity of cluster gas is defined as $\delta \vec{v} = a (\vec{v} - \vec{v}) + a H(z) (\mathbf{x} - \bar{\mathbf{x}})$, $H(z)$ is the Hubble function, a is the scale factor, \vec{v} and \mathbf{x} are the peculiar velocity ($d\mathbf{x}/dt$) and comoving position for each particle, and \vec{v} and $\bar{\mathbf{x}}$ are the gas-particle-averaged bulk flow within R_{200} and the center of mass of the cluster, respectively.

We show radial profiles of the kinetic-to-thermal pressure, P_{kin}/P_{th} , for various mass bins in Fig. 4.1. This figure shows that there is an overall mass dependence of this ratio at all cluster radii. This mass dependence is predominately driven by the mass dependence of P_{kin} and not P_{th} as we explicitly show in Fig. 4.2, and reflects the average formation history of galaxy groups and clusters. Scaling P_{kin}

with the virial analogue of the thermal pressure, P_Δ , is not sufficient to account for the mass dependence of P_{kin} . Here, we define $P_\Delta \equiv GM_\Delta \Delta \rho_{\text{cr}}(z) f_b / (2R_\Delta)$, and $f_b = \Omega_b / \Omega_m$ is the universal baryon fraction (Voit, 2005). According to the hierarchical picture of structure formation, galaxy clusters sit atop the mass hierarchy, with the most massive clusters forming and virializing at the present time. In contrast, the median galaxy group ($M_{200} = 10^{13} M_\odot$) has stopped forming today as can be seen by the dramatically decreasing mass accretion rates implying that the associated virializing shocks have dissipated the energy associated with the growth of these objects and hence decreasing the kinetic pressure support (Wechsler et al., 2002; Zhao et al., 2009; Pfrommer et al., 2011). The semi-analytic model for non-thermal pressure support by Shaw et al. (2010) falls in the middle of the mass bins chosen, not surprisingly since this model results from a sample of 16 high resolutions adaptive mesh refinement (AMR) simulations of individual galaxy clusters (Lau et al., 2009) which have a similar mass range. We provide a simple fit for the mass dependence of $P_{\text{kin}}/P_{\text{th}}$ in the Appendix.

We find that the radius at which $P_{\text{kin}} = P_{\text{th}}$ is just beyond the spherical collapse definition for R_{vir} (Bryan & Norman, 1998). Hence, this radius represents a possible physical definition for the virialized boundary of clusters. Additionally, the DM velocity anisotropy of clusters demarcate similar boundaries, even as a function of mass and redshift (cf. Appendix).

The redshift evolution of $P_{\text{kin}}/P_{\text{th}}$ is dramatic. At higher redshift, P_{kin} is increasing faster than P_{th} over all radii (cf. Fig. 4.2), such that at $z = 1$, $P_{\text{kin}}/P_{\text{th}}$ is approximately twice that at $z = 0$. In the picture of hierarchical structure formation, at any given redshift the most massive objects are currently assembled and hence show the largest kinetic pressure contribution in comparison to smaller objects that formed on average earlier. Or equivalently, at fixed cluster mass, the relative contribution from kinetic pressure and the relative amount of substructure increases with redshift. In particular, the relative mass accretion rates increase from $z = 0$ to $z = 2$ by a factor 3 for clusters ($M_{200} = 10^{15} M_\odot$) and 10 for groups ($M_{200} = 10^{13} M_\odot$) (see Pfrommer et al., 2011; Gottlöber et al., 2001). We note that this strong evolution in $P_{\text{kin}}/P_{\text{th}}$ is lessened by a different choice of scaling radius, i.e., if we normalize by $R_{200,m}$ instead of R_{200} (cf. Appendix). Although this ratio cannot be observed, we will use it as an indicator for the dynamical state of clusters in our simulations. Note that results from Lau et al. (2009) find a similar correlation between P_{kin} and the X-ray definition of dynamical state, from a smaller sample of 16 galaxy clusters. At $z = 1$, the Shaw et al. (2010) semi-analytic model for non-thermal pressure support does not match our simulations as well as it does at redshift zero.²

The formation of galaxy clusters and the associated accretion of substructure are driven by the depth

²Our kinetic pressure contribution is larger at the center compared to that in the model by Shaw et al. (2010). This discrepancy is a manifestation of the well-known core entropy problem in numerical simulations, i.e., in (adaptive) grid codes there is a larger level of core entropy generated in comparison to SPH codes implying that the enhanced entropy (which results from dissipating gas motions) is accompanied by a smaller amount of kinetic pressure. This is presumably due to the difference in the amount of mixing in SPH and mesh codes and possibly related to a different treatment of vorticity in the simulations (e.g., Frenk et al., 1999; Mitchell et al., 2009; Vazza et al., 2011).

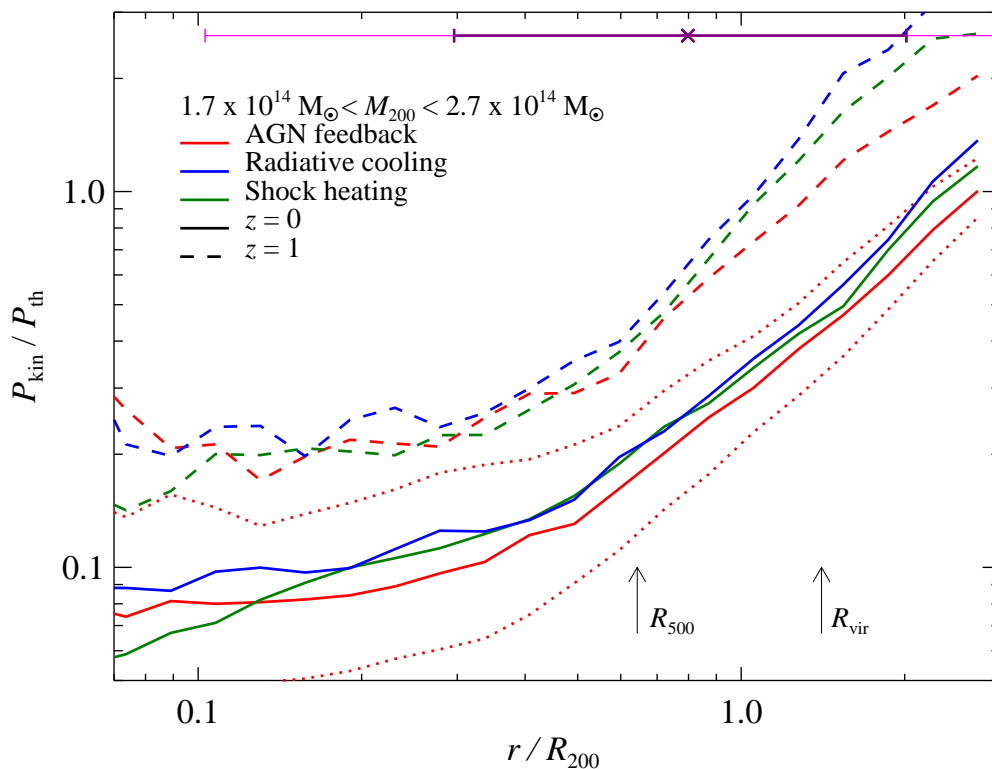


Figure 4.3: The kinetic pressure contribution is similar for our differently simulated physics, suggesting that gravitational processes dictate that contribution (while AGN feedback slightly decreases the kinetic pressure contribution, especially for higher redshifts). Shown is the median of $P_{\text{kin}}/P_{\text{th}}$ as a function of radius for different physics models at $z = 0$ (solid) and $z = 1$ (dashed) with the 25th and 75th percentile values shown for the AGN feedback simulations at $z = 0$ (dotted). Results are shown for the mass bin $1.7 \times 10^{14} M_{\odot} \leq M_{200} \leq 2.7 \times 10^{14} M_{\odot}$ to take out the mass dependence of $P_{\text{kin}}/P_{\text{th}}$. The horizontal purple and pink error bars have the same meaning as in Fig. 4.1.

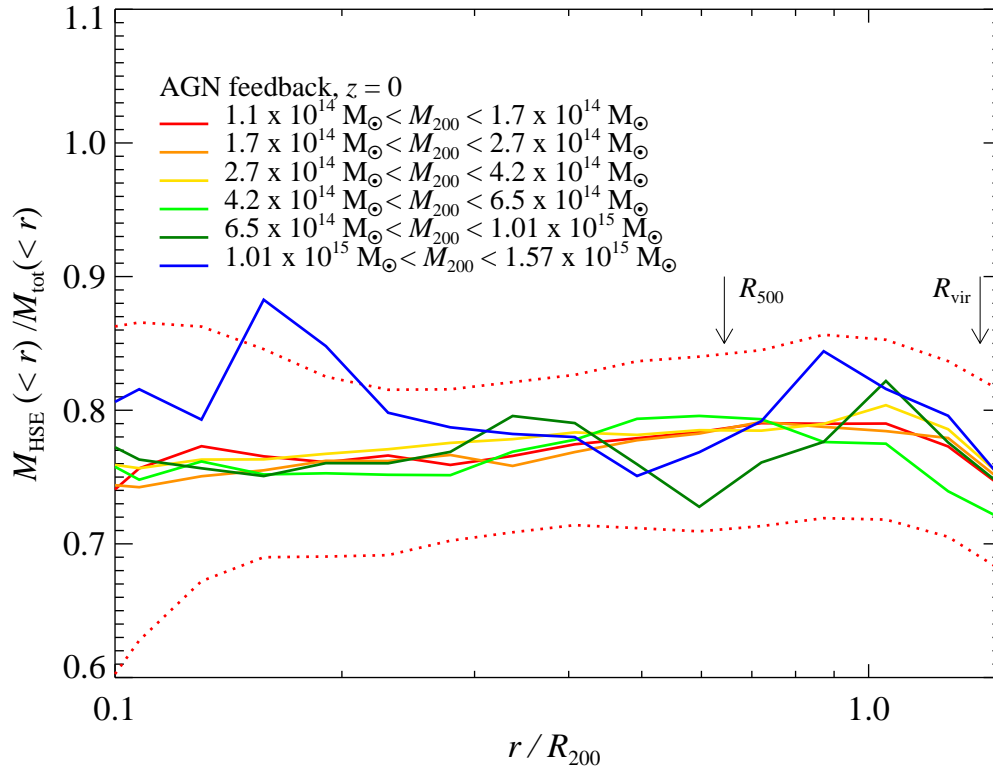


Figure 4.4: The median of $M_{\text{HSE}}/M_{\text{tot}}$ as a function of radius for AGN feedback simulations for various mass bins, with the 25th and 75th percentile values shown for the smallest mass bin (dotted). Assuming hydrostatic equilibrium for all clusters of a given mass will bias the mass values low by 20 to 25%. The scatter about the median amounts to approximately 5%. Note, this bias is not representative for a relaxed cluster sample which will likely evince a smaller bias as the calibration of such a sample against numerical galaxy cluster simulations shows (Kravtsov et al., 2006).

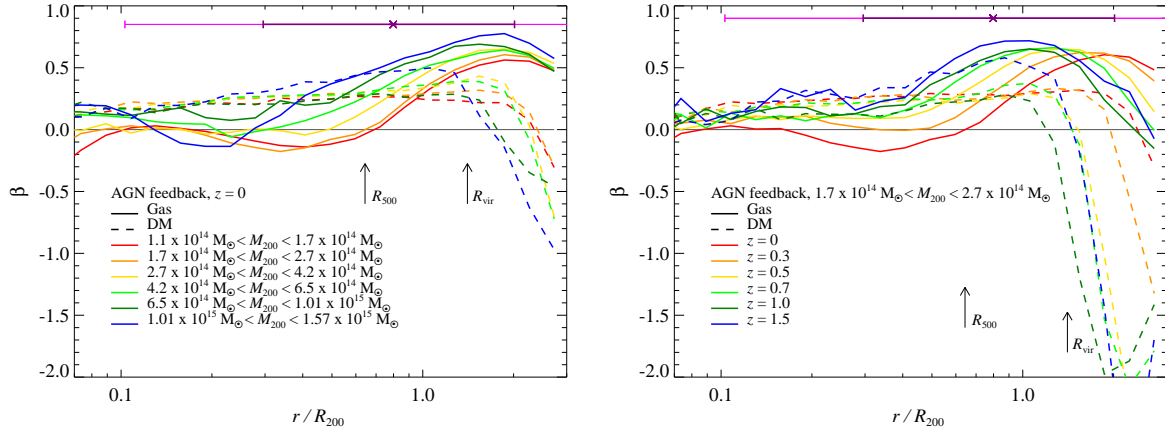


Figure 4.5: The velocity anisotropy, β , for gas (solid) and DM (dashed) is a strong function of cluster mass and redshift. We compare median values for β as a function of radius in different mass bins at $z = 0$ (left) and for different redshifts in a fixed mass bin (right) using our AGN feedback simulations. In the core regions toward the center, the velocity distribution starts to become isotropic for the gas in groups and (to a lesser extent) for the DM and gas in larger clusters. The positive values of β around the virial radius indicate (radial) infall, whereas the strong decrease at even larger radii (very noticeably in the DM) is caused by the turn-around of earlier collapsed shells. This minimizes the radial velocity component such that the tangential components dominate the velocity.

of the cluster gravitational potential. Therefore, it is not surprising that we find kinetic pressure support to be ubiquitous in the three differently simulated physics cases (cf. Fig. 4.3). Looking at the median of this non-thermal pressure support we find similar radial profiles within the 25th and 75th percentiles of the complete distribution of clusters. In the AGN feedback simulations we find marginally lower values for $P_{\text{kin}}/P_{\text{th}}$. These differences are well within the 25th and 75th percentiles implying consistency across differently modeled physics. Thus, our model of AGN feedback does not significantly alter the kinetic pressure support at low redshift although there seems to be a hint that this may be the case at larger radii at redshifts $z \sim 1$ which approach the peak of the AGN luminosity density.

4.4.2 Hydrostatic Masses

Including the kinetic form of non-thermal pressure support becomes important when estimating cluster masses under the assumptions of spherical symmetry,

$$\frac{dP}{dr} = -\frac{GM(< r)\rho}{r^2}. \quad (4.5)$$

As others have shown (Evrard, 1990; Rasia et al., 2004; Lau et al., 2009), assuming that all the pressure in Eq. (5.11) is thermal ($P = P_{\text{th}}$) is incorrect; for clarity we define M_{HSE} to be the mass derived using

$P = P_{\text{th}}$. Comparing M_{HSE} to the true mass inside a given radius, M_{tot} , we find that M_{HSE} on average underestimates M_{tot} by 20–25% depending on the radius (cf. Fig 4.4). This bias is almost independent of cluster mass out to R_{500} , the current maximum radius typically observed by X-ray telescopes. We can understand this weak mass dependence by rewriting the total pressure $P = P(P_{\text{th}}/P + P_{\text{kin}}/P)$. Since $P_{\text{kin}}/P \propto M_{200}^{1/5}$ (see Fig. 4.19), the hydrostatic mass estimates inherit a similarly weak mass dependence. Thus, an overall correction to the hydrostatic mass is reasonable for these measurements.

Individual clusters can stray from this generalization, since each cluster has a unique dynamical state and formation history. These deviations are suggested by the scatter of $\sim 5\%$ between the 25th and 75th percentiles of the complete distribution. For cluster samples that are selected against major mergers (for which the assumption of spherical symmetry will also be questionable), the correction factor will necessarily be smaller, e.g., for quality X-ray data of a Chandra sample, the hydrostatic mass correction was found to be of the order $M_{\text{HSE}} \sim 10\text{--}15\%$ Kravtsov et al. (2006).

4.4.3 Velocity Anisotropy

We decompose the velocity distribution of the gas, $\delta\vec{v}$, into orthogonal components of a spherical coordinate system, $\delta\vec{v}_r$, $\delta\vec{v}_\theta$ and $\delta\vec{v}_\phi$. This is done for each spherical shell within $3R_{200}$ and then normalized by $\vec{v}_{200} = \sqrt{GM_{200}/R_{200}}$. For each of these spherical shells, we also compute the velocity dispersion average, $\sigma^2 \equiv \langle \delta\vec{v}^2 \rangle - \langle \delta\vec{v} \rangle^2$ as well as the anisotropy parameter, β , as defined in Binney & Tremaine (2008),

$$\beta = 1 - \frac{\sigma_t^2}{2\sigma_r^2}, \quad \sigma_t^2 = \sigma_\theta^2 + \sigma_\phi^2, \quad (4.6)$$

to quantify the relevant amount of radial and tangential velocity dispersion. This parameter ranges from 1 for a completely radial flow to $-\infty$ for a completely tangential flow. As shown by Fig. 4.5, galaxy clusters do not have isotropic velocity dispersions in gas and DM (e.g., Cuesta et al., 2008; Wojtak et al., 2008). We find that β does dependent on cluster mass, but does not change much with variations in the simulated physics. In the Appendix, we show that the steep drop in the β parameter of DM at large radii corresponds to the splash-back radius of the galaxy cluster, i.e., is caused by the turn-around of earlier collapsed shells which minimizes the radial velocity component such that the tangential components dominate the velocity. Much like $P_{\text{kin}}/P_{\text{th}}$, this mass dependence of the splash-back radius can also be explained by the formation history of clusters, since more massive clusters are still forming today and are accreting from larger radii. A similar trend in β for a larger range in masses is shown in dissipationless simulations by Cuesta et al. (2008). Focusing on a single mass bin, we found the similar radial redshifts trends as the kinetic pressure support (cf. Fig 4.5). Future SZ experiments may be able to detect these radial motions in galaxy clusters through the kinetic SZ effect.

4.5 Galaxy Cluster Shapes

Generally, we expect galaxy clusters to be triaxial since they grow by accretion and through merging along filamentary structures that impose tidal gravitational forces upon the forming clusters. Following Dubinski & Carlberg (1991), we estimate this non-sphericity of cluster gas and dark matter (DM) by computing several weightings of the inertial tensor,

$$I_{ij}(r < R) = \frac{\sum_{\alpha} w_{\alpha} (x_{i,\alpha} - \bar{x})(x_{j,\alpha} - \bar{x})}{\sum_{\alpha} w_{\alpha}}, \quad (4.7)$$

where α indexes all particles within a given radius R , x_i is the i th coordinate of particle α and w is the weighting. For DM and SPH gas (hereafter gas) particles, a mass weighting, $w_{\alpha} = m_{\alpha}$, results in the inertial tensor of its original form so that a volume rendering provides iso-density surfaces. Hence, this is referred to in the following as gas and DM density weighting. Additionally, we employ a weighting by the product of the gas mass and temperature, $w_{\alpha} = m_{\alpha} T_{\alpha}$, so that a volume rendering of the resulting weighted inertial tensor provides isobaric surfaces. We refer to this as pressure weighting and note that this quantity is of particular importance when considering the effects on the tSZ signal.

We quantify the non-sphericity of cluster gas and DM with two methods, the axis ratios (in particular the ratio of the largest-to-smallest main axis, c/a) and the three-dimensional asymmetric parameters (Bardeen et al., 1986). Both methods use the eigenvalues λ_i which are computed for each inertial tensor at a given radius. These methods differ in the presentation of the λ_i 's. We adopt the convention that $\lambda_1 < \lambda_2 < \lambda_3$. We also calculate the corresponding eigenvectors \mathbf{E}_i and use them later in this work to explore rotation and alignment effects. Here we have chosen to define the axis as $a = \sqrt{\lambda_1}$, $b = \sqrt{\lambda_2}$ and $c = \sqrt{\lambda_3}$, which is different than other definitions, for example the one used by Lau et al. (2011), who use $a' = \lambda_1$, $b' = \lambda_2$, and $c' = \lambda_3$. In the Appendix we explore how an additional r^{-2} -factor in the weightings ($w_{\alpha} = m_{\alpha}/r_{\alpha}^2$ and $w_{\alpha} = m_{\alpha} T_{\alpha}/r_{\alpha}^2$) impacts the results. This makes the inertial tensor more sensitive to the mass/thermal energy in the interiors of clusters and lessens the contributions from larger radii.

The asymmetric parameters are defined as

$$e = \frac{\lambda_1 - \lambda_3}{2\bar{\lambda}}, \quad p = \frac{\lambda_1 - 2\lambda_2 + \lambda_3}{2\bar{\lambda}}, \quad (4.8)$$

where $\bar{\lambda}$ is the mean eigenvalue, e is a measure of ellipticity, and p , is a measure of prolateness/oblateness. When p is positive, the clusters are prolate, and when p is negative, clusters are oblate; and we define the oblateness $o \equiv -p$ for negative p , as in Bardeen et al. (1986). The prolateness and oblateness are morphological classification schemes and a direct measure of the morphological appearance. This is complementary to the ellipticity which quantifies the overall geometry irrespective of morphology.

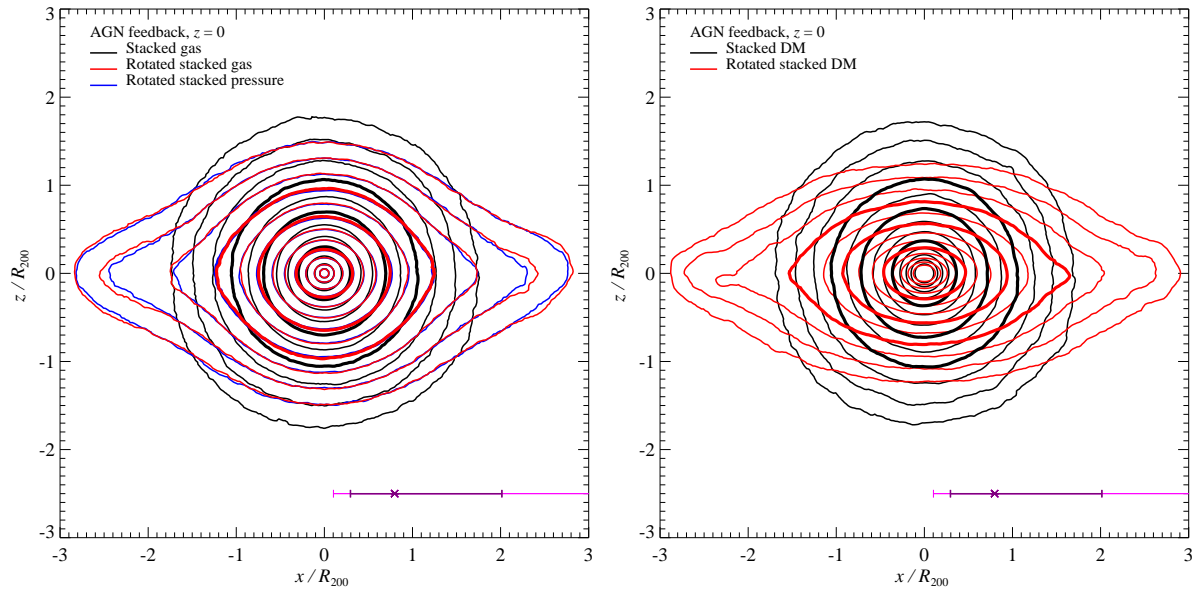


Figure 4.6: Stacked density and pressure distributions with and without rotations into the principle axis frame at $z = 0$. Left: We compare rotated distributions for the gas density (red) and pressure (blue) to the non-rotated stacked gas density (black) at $z = 0$. Right: Shown is the same as on the left for DM. The non-rotated clusters average out to form spherical iso-density contours, while the rotated clusters clearly show elongations along the major axis (defined here as the x -axis). The thicker lines approximately show the radii R_{2500} , R_{500} and R_{200} from the inside out. Note, these contours have been smoothed to a pixel size of $0.09R_{200}$. The horizontal purple and pink error bars have the same meaning as in Fig. 4.1.

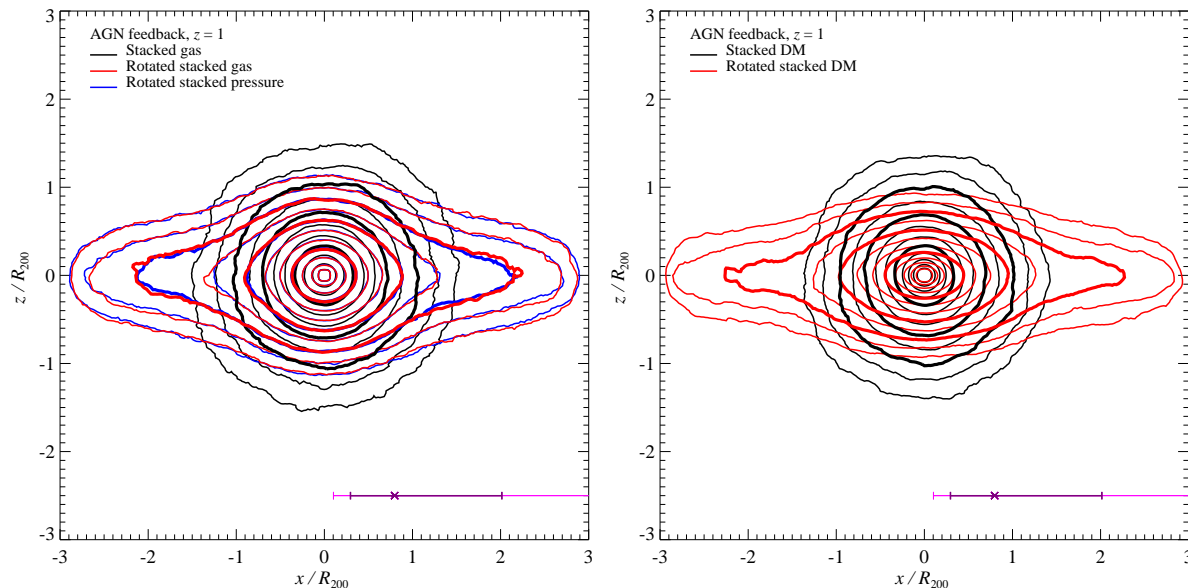


Figure 4.7: Stacked density and pressure with and without rotations into the principle axis frame at $z = 1$. Left: We compare rotated distributions for the gas density (red) and pressure (blue) to the non-rotated stacked gas density (black) at $z = 0$. Right: Shown is the same as on the left for DM. The non-rotated clusters average out to form spherical iso-density contours, while the rotated clusters clearly show elongations along the major axis (defined here as the x -axis). The thicker lines approximately show the radii R_{2500} , R_{500} and R_{200} from the inside out. Note, these contours have been smoothed to a pixel size of $0.09R_{200}$. The horizontal purple and pink error bars have the same meaning as in Fig. 4.1.

4.5.1 Overall shapes and dependence on modeled physics

We rotate all clusters into the inertial tensor frame using the eigenvector matrix \mathbf{E} , so $x' = \mathbf{E}x$. The output ordering is arbitrary; we choose the convention that the major axis is aligned with the x-axis and the minor axis is aligned with the z-axis. In Figs. 4.6 and 4.7 we show stacked DM iso-density contours (black). Those are compared to gas iso-density/pressure contours (red/blue) which have been obtained by computing the inertial tensor within $3R_{200}$, rotating into the inertial tensor frame, and stacking the respective distributions. The rotated contours show obvious elongations along the major axis; with the ellipticity being larger at $z = 1$ in comparison to $z = 0$. The elongation is larger for the DM distribution in comparison to the gas density and pressure which show very similar behaviour. Even in the rotated stacked distributions, the innermost contour lines become more spherical because they are intrinsically less elliptical (see below) and because the main axes of the inner distributions are twisted relative to those at $3R_{200}$ so that their ellipticity partially averages out to become more spherical (see Sect. 4.5.4).

In order to quantify these results, we show the mass dependence and redshift evolution of the ellipticity within R_{200} in Fig. 4.8. Due to the dissipationless nature of DM, its ellipticity is larger (smaller ratio of c/a) in comparison to that of the gas. This is because structure formation shocks dissipate the kinetic energy of the accreted gas at cluster accretion shocks – a process that erases part of the memory of the geometry of the surrounding large scale structures and their tidal force field. Those accretion shocks are typically forming at radii $> R_{200}$ as suggested by numerical simulations (Miniati et al., 2000; Ryu et al., 2003; Pfrommer et al., 2006; Skillman et al., 2008; Vazza et al., 2009) or indirectly by the action of shock waves on radio plasma bubbles, which represents a novel method of finding formation shocks by combining radio observations and analytical insight that is supported by idealized hydrodynamic simulations (e.g., Enßlin et al., 2001; Pfrommer & Jones, 2011). Following these qualitative considerations, it is not surprising that the ellipticity of the gas distribution does not show any mass dependence while the DM distribution of more massive clusters shows a larger ratio of c/a in comparison to smaller systems. However, the ellipticity of the gas and DM distribution are increasing as a function of redshift, at about the same rate. This can be understood by the fact that 1) a given mass range of clusters shows a larger degree of morphological disturbances/merging at higher redshifts which probe on average dynamically younger objects and 2) the redshift evolution of the velocity anisotropy (see Fig. 4.5) which shows that the average location of accretion shocks moves to smaller radii (if scaled by R_{200}). Hence at larger redshifts, also the gas distribution probes the infall/pre-accretion shock region that is shaped by the tides exerted by the far-field of clusters.

We compare the results from our simulations directly with those of Kasun & Evrard (2005) in Figure 4.8 and Table 4.1. Other work (Allgood et al., 2006; Gottlöber & Yepes, 2007; Macciò et al., 2008; Lau et al., 2011) on DM and gas shapes have used varying mass definitions, axis definitions and cosmologies, which differ from our definitions and cosmology. Thus, we do not quantitatively compare with their

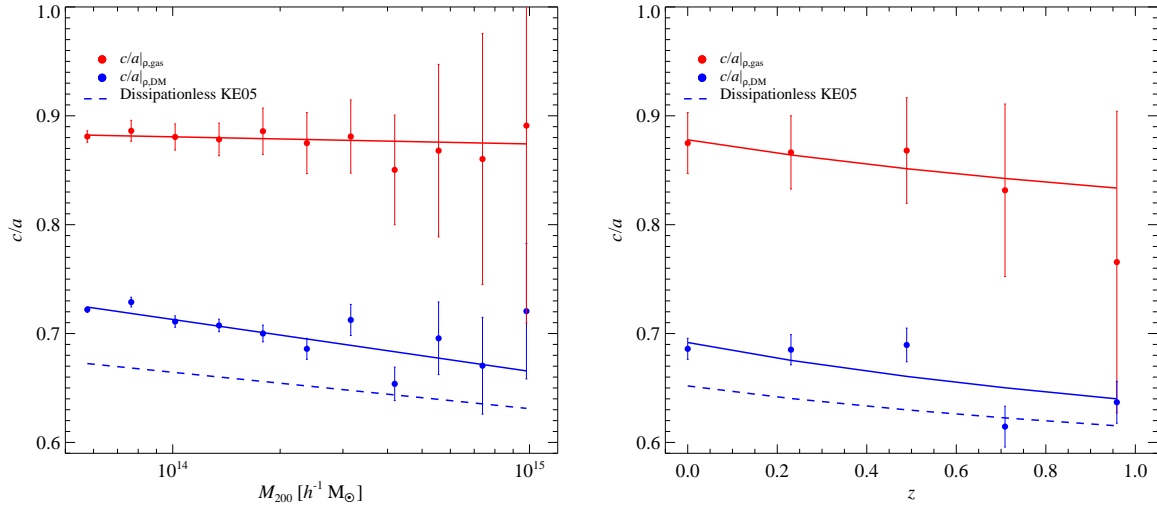


Figure 4.8: We show axis ratios of galaxy clusters that are obtained by computing the inertial tensor of the gas (red) and DM mass distributions (blue) within R_{200} and stacking those in bins of cluster mass and redshift. The resulting mean and standard deviation of the axis ratio c/a is shown as a function of M_{200} at $z = 0$ (left panel) and at fixed average mass bin of $M_{200} = 2.4 \times 10^{14} h^{-1} M_{\odot}$ as a function z (right panel). See Table 4.1 for fit values; here, we have chosen to quote $h^{-1} M_{\odot}$ to compare directly with the dissipationless simulations by Kasun & Evrard (2005, KE05). While shocks dissipate kinetic energy of the gas which causes smaller axis ratios/ellipticities, this couples through gravity to the DM distribution and sphericalize their axis ratios, resulting in smaller ellipticities in comparison to dissipationless simulations alone, e.g., by KE05 (that do not follow the hydrodynamics of the gas).

results, however, we note that their results are consistent with Kasun & Evrard (2005). For the mass and redshift functional fits, Kasun & Evrard (2005) define $c/a(M) = B_M(1 + A_M \ln[M/10^{15} h^{-1} M_{\odot}])$ and $c/a(z) = B_z(1 + z)^{A_z}$, respectively. The axis ratio that we find for the DM mass dependence and redshift evolution have consistent slopes to Kasun & Evrard (2005). However, there is an overall trend that our axis ratios are more spherical than their results. It is possible that the baryons have a noticeable effect on the DM ellipticity, however this difference may also be due to the difference in cosmological parameters used by Kasun & Evrard (2005). We do not explore this question any further since the effects of baryons on the DM have been explored much further by previous work (e.g., Rudd et al., 2008).

In the following, we will show radial profiles of the axis ratios and asymmetric parameters that are obtained by computing the inertial tensor at 30 different radii for each cluster. First, we report on the overall radial distribution of c/a and ellipticity in the gas and DM distributions. Within R_{200} , the ellipticities of gas density and pressure are rather flat at a level of $c/a \simeq 0.85 - 0.9$. As laid out above, this is because dissipation effects at the accretion shocks cause an effective sphericalization and erase

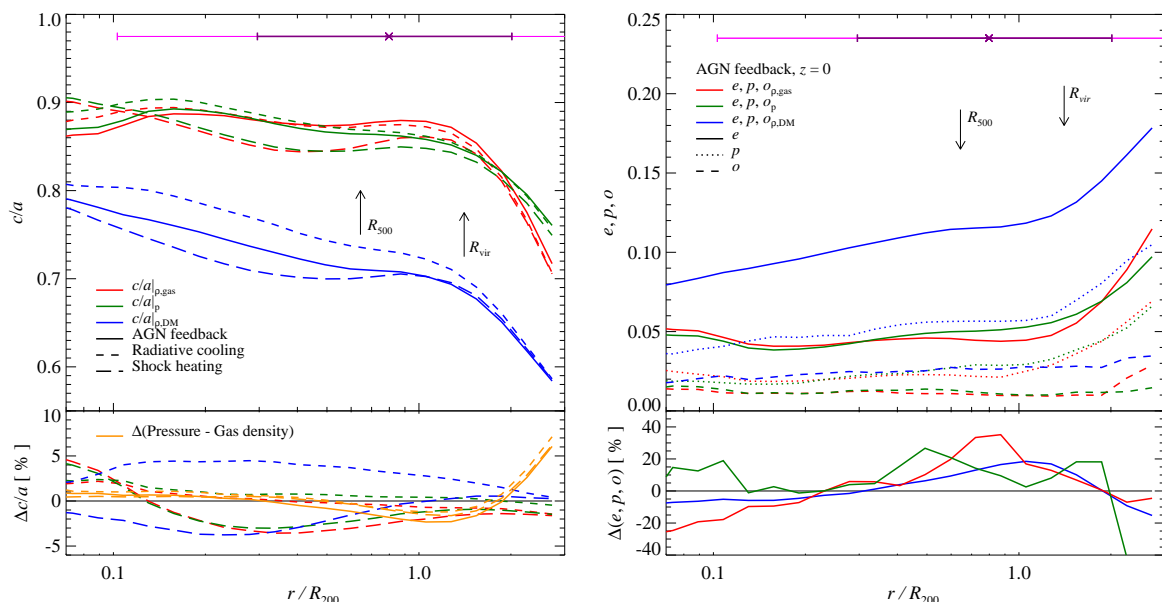


Figure 4.9: Stacked cluster axis ratios and ellipticities for the DM mass (blue), gas mass (red) and pressure (green) distributions within a scaled radius r/R_{200} . Left: Shown is the axis ratio c/a as a function of scaled radius for all simulated physics models. In the bottom panel we show the percent differences from the AGN feedback simulations to the shock heating (long-dashed) and radiative cooling simulations (short-dashed). Right: We show the ellipticity, prolativity and oblativity as a function of scaled radius. The bottom panel shows the percent difference between the pressure and gas density weightings of the inertial tensor. The axis ratio c/a and ellipticity show the same trends. We find clusters to be more prolate than oblate. In the regions beyond R_{vir} the sudden decrease in the axis ratios can be attributed to other nearby clusters (that is also seen as an enhanced density clumping at these radii). The pressure weighted shapes tightly track the density weighted shapes with deviations of less than 5%. The horizontal purple and pink error bars have the same meaning as in Fig. 4.1.

Table 4.1: Axis ratio fits for cluster as a function of mass and redshift.

	B_M	A_M	B_z	A_z
DM	0.665 ± 0.009	-0.031 ± 0.006	0.692 ± 0.009	-0.12 ± 0.04
KE05	0.631 ± 0.001	-0.023 ± 0.002	$0.652^a \pm 0.001$	-0.086 ± 0.004
Gas	0.87 ± 0.02	-0.003 ± 0.01	0.88 ± 0.03	-0.08 ± 0.12

^a We use a re-normalized value from $M_{200} = 1 \times 10^{15} h^{-1} M_{\odot}$ to $M_{200} = 2.4 \times 10^{14} h^{-1} M_{\odot}$.

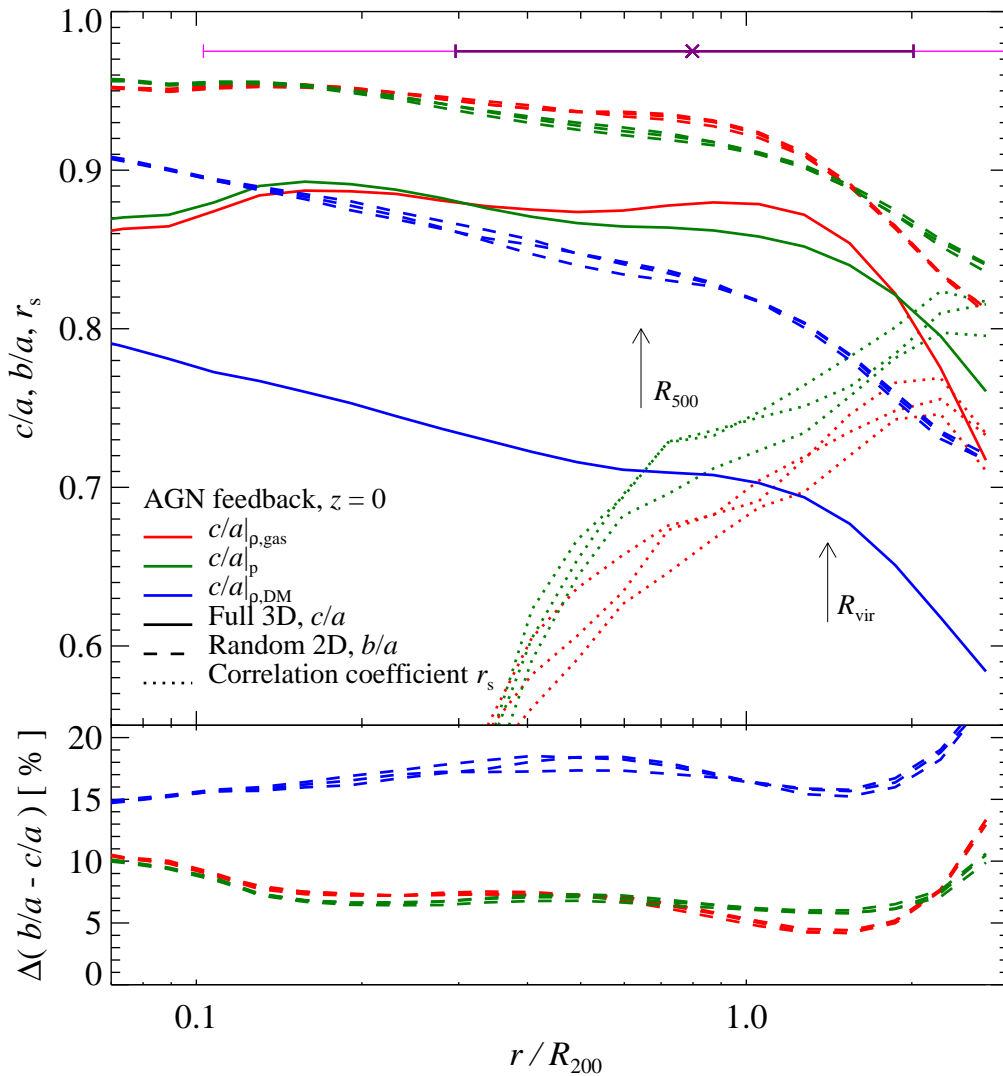


Figure 4.10: Top: We compare the average of the 2D axis ratios (dashed) of three random orthogonal projections to the 3D axis ratios (solid) for the DM mass (blue), gas mass (red) and pressure (green) from the galaxy clusters in the AGN feedback simulations. Additionally, we show the linear correlation coefficient, r_s (dotted line), between the projected 2D and the 3D axis ratios. The horizontal purple and pink error bars have the same meaning as in Fig. 4.1. Bottom: Shown is the percent difference between the projected 2D and the 3D axis ratios. While the relative difference between the projected 2D and the 3D axis ratios vary between 15–20% for the DM mass distribution (with the 2D axis ratios being more spherical), the relative difference is smaller for the mass and pressure distribution of the gas, with values between 5–10%. As expected, the projected 2D and the 3D axis ratios are correlated with an increasing correlation coefficient at larger radii which suggests that the substructure distribution that drives the asphericity also causes this correlation.

the memory of large-scale tidal fields. In contrast, ellipticities are increasing for the DM as a function of radius due to the dissipationless nature of DM, i.e. c/a decreases from values around 0.8 in the center to 0.7 at R_{200} . The radial behaviour may be due to increased tidal effects on DM substructures at small radii which causes a dramatic drop of their central mass density (Springel et al., 2008a,b; Pinzke et al., 2011). Effectively this causes a redistribution of a clumped (elliptical) to a smooth distribution that is able to couple more efficiently to the (more spherical) gas distribution. Studying the asymmetric parameters, we find that if a cluster is prolate, it is on average more elliptical than an oblate one that is always close to spherically symmetric.

We now explore the influence of the simulated physics model on cluster shapes in Fig. 4.9. While the ellipticity of the gas is slightly larger in non-radiative models, it is very similar for the gas distribution in our radiative models (radiative cooling and star formation with and without AGN feedback). Dissipating accretion shocks seem to explain the overall behavior rather well and the different physical models only marginally change the cluster shapes in the gas. In the DM, however, there is still a pronounced difference among our two radiative physics models with the ellipticities of the AGN feedback model being larger than in our pure radiative model. This small ellipticity is a remnant of overcooling that our pure radiative model suffers with an associated star formation rate that is unphysically high. Most of these stars form out of the cold, dense gas in the core region which causes a decreasing central pressure support so that gas at larger radii moves in adiabatically and causes a deeper potential which in turn causes the DM to adiabatically contract. Enhanced dissipation processes in the gas sphericalize the potential which is then communicated to the DM during this central settling. We find that including AGN feedback counteracts the overcooling issue and modifies the DM shapes on the level of 5% in comparison to our pure radiative simulations (cf. Fig 4.9).

Our general trends are similar to those reported by Lau et al. (2011) who also find that the DM distribution is more spherical for radiative simulations in comparison to non-radiative models. However, the differences between radiative and non-radiative simulations are not as extreme as those found in Lau et al. (2011), since our radiative simulations do not suffer from the same catastrophic cooling in the center regions as a result of their higher resolution simulations as well as the inclusion of metal-dependent cooling. Note, however, that AGN feedback stabilizes cooling and hence, softens this behavior in the DM ellipticity.

We find that the average axis ratios and ellipticities have a pronounced break in their slopes at $r \sim 1.5R_{200}$. The break in the ellipticity arises from substructure in the cluster outskirts. Recent X-ray observations of the Perseus cluster find a strong signature of clumping in gas density (Simionescu et al., 2011); qualitatively consistent with the findings in simulations (Nagai & Lau, 2011). This gas density clumping is a direct tracer of substructure and becomes important at roughly the same radius where we find the break in the ellipticity. Interestingly, this effect is not only seen in DM and gas but also in pressure, which suggests that the pressure is clumped in a similar fashion as the gas density. In

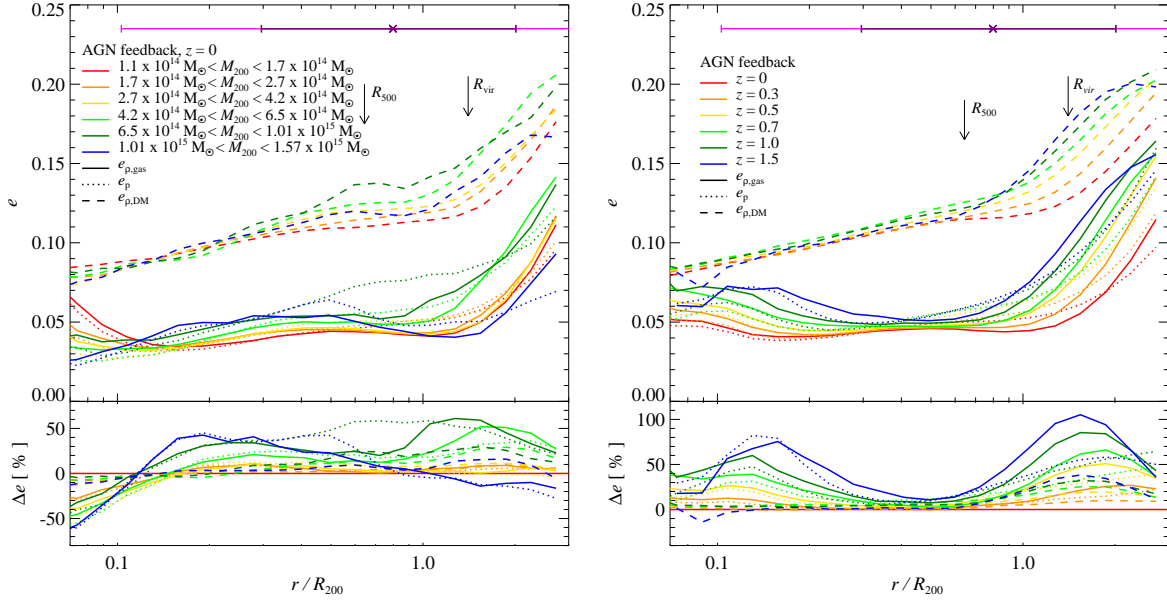


Figure 4.11: Mass dependence and redshift evolution of the cumulative ellipticity profile as a function of r/R_{200} . Left: Shown is the ellipticity profile at $z = 0$ for various mass bins. Bottom left: Shown are the percent differences in ellipticity to the lowest mass bin ($1.1 \times 10^{14} M_{\odot} < M_{200} < 1.7 \times 10^{14} M_{\odot}$). Over this mass range, the cluster ellipticities show a noticeable but not substantial mass dependence within R_{500} , in contrast to the stronger dependence on P_{kin}/P_{th} . Right: Shown is the ellipticity profile for various redshift bins. The horizontal purple and pink error bars have the same meaning as in Fig. 4.1. Bottom right: Shown is the relative difference of ellipticity at a given redshift to $z = 0$. The redshift evolution of the ellipticity (especially at large radii, $r > R_{500}$) is driven by the larger amount of substructures at higher redshifts due to the increased mass accretion rate of group/cluster halos at these redshifts. The pressure weighted ellipticities track the density weighted ones well and show the same trends with redshift.

order to accurately model the outskirts of clusters, semi-analytic models will need to properly deal with the substructure. In the Appendix, we show that one can attempt to counteract or lessen the impact of substructure on the gas, pressure and DM shapes by including an r^{-2} -weighting when calculating the inertial tensor (cf. Eq. (4.7)). In future work, we will further explore the issue of substructure.

4.5.2 Projected and intrinsic shapes

In order to tie the underlying 3-dimensional structure of clusters to observable 2-dimensional projections, we compare the intrinsic 3D axis ratios to axis ratios of random 2D projections, i.e. we project the DM density and gas density/pressure distributions along a randomly chosen direction and then compute the 2D inertial tensor. The results are shown in Figure 4.10. We find that the 2D axis ratios for both, the gas density and pressure are systematically closer to unity than the 3D ratios c/a by $\sim 5\text{--}10\%$ (for the virial region and the central part). In the case of the DM distribution, the projected (2D) axis ratios are on average a $\sim 15\%$ underestimate of the intrinsic (3D) axis ratios. Using the linear correlation coefficient statistic (r_s), we find that the random 2D axis ratios are strongly correlated with the intrinsic 3D axis ratios and the strength of the correlation increases with radius (cf. Fig 4.10). As expected, c/a serves as a limit to the observable 2D projections axis ratio. We find that the mean 2D axis ratio, when given as a function of cluster radius, closely tracks c/a , modulo a roughly constant $\sim 5\text{--}10\%$ bias (for the gas density and pressure).

4.5.3 Mass and redshift dependence of shape profiles

Both the density- and pressure-weighted ellipticities show the same general trends with radius and cluster mass. The ellipticity increases with increasing cluster mass by $\sim 50\%$ over the mass ranges shown (cf. Fig 4.11). On the right-hand side of Fig. 4.11, we show the redshift evolution of the cluster shapes and find that the ellipticity is a stronger function of redshift than the mass. For increasing redshift, the break in the ellipticity profile moves to smaller radii (when scaled to R_{200}). Both behaviors, the mass and redshift dependence can be understood in the hierarchical picture for structure formation, where galaxy clusters show increased mass accretion rates and hence an increased level of substructure for larger clusters (at a given redshift) or, equivalently, for a cluster of given mass at higher redshifts which probe on average systematically younger systems. Similar to the non-thermal pressure support, the redshift evolution found in the ellipticities are lessened by a different choice of scaling radius (cf. Appendix). This result suggests that using a single (constant) ellipticity profile for galaxy clusters is not sufficient for percent level accuracy.

Pressure-weighted ellipticities are marginally more spherical than the density-weighted ellipticities for $r < R_{500}$ (cf. Figs. 4.9 and 4.11). However, between R_{500} and $2R_{500}$ the behavior is reversed. This is because the core region shows a smaller kinetic pressure support implying that hydrostatic forces

had time to act and to smooth out the pressure distribution whereas at larger radii, pressure-weighted ellipticities are affected more by infall caused by a noticeable pressure clumping at these radii (Pfrommer et al. in prep.). We note that the radius of R_{500} appears to be a sweet spot in cluster aperture sizes for the gas, DM and pressure ellipticities, since all ellipticities show only $\sim 10\%$ redshift evolution and mass dependence. Together with the results on the non-thermal pressure support (Sect. 4.4), this is an important result for cluster X-ray observations and theoretically justifies the use of the radial region around R_{500} for characterizing clusters. R_{500} appears to be the best compromise for the criteria small non-thermal pressure support, small ellipticity, and small degree of clumping.

4.5.4 Isophotal twist of cluster structure and semi-analytical models

Semi-analytic models for the baryon distribution in clusters include an underlying assumption that baryons will arrange themselves along equipotential surfaces (or in some cases the DM density-weighted surfaces). Given the importance of this assumption, we test its validity in our simulations. In Figure 4.8, we plot the ratio c/a for both dark matter and gas as function of cluster mass and redshift. While c/a for DM halos decreases with halo mass as expected (Jing & Suto, 2002), we find that c/a is constant for the gas distribution. This is potentially a problem for semi-analytic models of ICM gas (Ostriker et al., 2005; Bode et al., 2009), which use the DM-dominated gravitational potential as the shape on which to paint the baryons. However, the gravitational potential from the DM is more spherical than the underlying matter distribution (e.g. Lau et al., 2011), and so the semi-analytic shape estimates are not as discrepant as one might expect from Figure 4.8.

A more important issue is the alignment of the gas or pressure with respect to the DM. We calculate the angular difference between the major axes of the DM and those of the gas and pressure major axes at a given radius, using the inertial tensor eigenvectors $\mathbf{E}_{1,DM}(r) \cdot \mathbf{E}_{1,gas}(r)$. (Note that we use the DM distribution rather than the potential. However, since the DM dominates the potential, the two alignments are effectively indistinguishable.) When calculating misalignment, the major axes of nearly spherical objects are poorly defined quantities. To avoid this problem we calculate, in each radial bin, a weighted average using $1 - c/a$ as the weight. Furthermore, we exclude the region inside $0.3R_{200}$ since the gas and pressure shapes are nearly spherical, with $c/a|_{DM} > 0.75$. On average at a given radius, the cluster gas and pressure are 20 – 30 degrees misaligned from the major axis of the DM (cf. Fig. 4.12). In the next section we show SZ measurements of the total thermal energy in clusters, Y , strongly depend on the projection axis through the cluster. Thus, misalignment between the semi-analytic baryon distortion and the “true” distribution may cause biases when using semi-analytic models to, e.g., tie weak-lensing and SZ observations together.

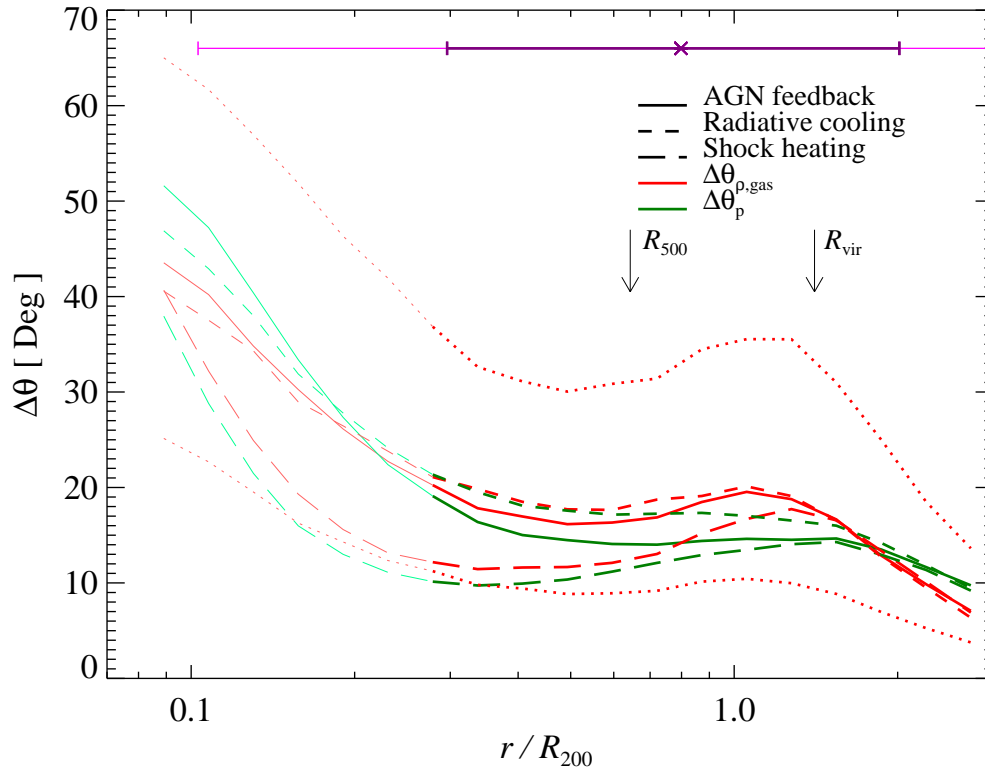


Figure 4.12: The weighted median angles between the DM major axis and gas (red) and pressure (green) axes as a function of radius for all simulated physics models: AGN feedback (solid), radiative cooling (short-dashed), and shock heating-only (long-dashed). The 25th and 75th percentile values are shown for the gas density in the AGN feedback model (dotted). On average the gas and pressure axes are misaligned by 20 to 30 degrees to the DM principle axis, independent of our simulated physics models. However, both simulations with radiative cooling show more misalignment in the inner regions than the non-radiative simulations. The light colors and lines represent the region which the average cluster shape are close to spherical ($c/a_{\text{DM}} > 0.75$) such that the major axes are not well defined and their angles are approaching a random distribution. Note that we have weighted the average angles by $1 - c/a$ to down-weight the angles from the spherical ICM shapes and the cluster interiors. The horizontal purple and pink error bars have the same meaning as in Fig. 4.1.

4.6 SZ Scaling Relation

In this section we explore the impact of AGN feedback, cluster shapes and kinetic pressure support on the SZ scaling relation ($Y - M$ relation) using our large sample of clusters. We compute the SZ flux for all clusters for both, spherical boundaries and cylindrical apertures (Y_{sph} and Y_{cyl}). For the cylindrical aperture calculations the total fluxes are computed along each axis of the moment of inertia frame, measured at R_{200} , and additionally along each axis of another randomly-oriented frame. We choose the line of sight boundaries for the cylindrical integrations to be three times the radius of the aperture. This procedure enables quantifying the importance of substructure, which we have already shown in Sections 4.5 and 4.4 to be significant at radii beyond R_{200} . From the calculated Y_{Δ} values we fit an average scaling relation,

$$Y_{\Delta} = 10^B \left(\frac{M_{\Delta}}{3 \times 10^{14} h_{70}^{-1} M_{\odot}} \right)^A h_{70}^{-1} \text{Mpc}^2, \quad (4.9)$$

where A and B are the fit parameters for the slope and normalization, respectively. We weight each cluster by its Y_{Δ} when fitting for A and B to keep the low-mass clusters from completely dominating the fit.

4.6.1 Self-similar $Y - M$ scaling relation

We review the expectations for Y in the idealized case of a cluster in virial equilibrium to help understand how possible deviations from the self-similar $Y - M$ relation and the scatter about it may arise. Starting with Eq. (5.8), which has been rewritten as,

$$Y = \frac{\sigma_{\text{T}}}{m_e c^2} \int_0^{R_{200}} dV P_e = \frac{(\gamma - 1) \sigma_{\text{T}}}{m_e c^2} x_e X_{\text{H}} \mu E_{\text{gas}}, \quad (4.10)$$

where x_e is the electron fraction defined as the ratio of electron and hydrogen number densities $x_e = n_e/n_{\text{H}} = (X_{\text{H}} + 1)/(2 X_{\text{H}}) = 1.158$, $\gamma = 5/3$ is the adiabatic index, $\mu = 4/(3X_{\text{H}} + 1 + 4X_{\text{H}}x_e) = 0.588$ denotes the mean molecular weight for a fully ionized medium of primordial abundance, and we assume equilibrium between the electron and ion temperatures. Next, we define the characteristic temperature of the halo (Komatsu & Seljak, 2002) as

$$kT_{200} = \frac{GM_{200} \mu m_{\text{p}}}{3R_{200}} = \frac{\mu m_{\text{p}}}{3} [10 G H_0 M_{200} E(z)]^{2/3}, \quad (4.11)$$

so we can write the total thermal energy of the halo with Eq. (4.11) as

$$\begin{aligned} E_{\text{gas}} &= \frac{3}{2} N_{\text{gas}} kT_{200} = (1 - f_*) f_{\text{b}} f_{\text{c}} \frac{GM_{200}^2}{2R_{200}} \\ &= (1 - f_*) f_{\text{b}} f_{\text{c}} \frac{G}{2} [800 \rho_{\text{cr}}(z)]^{1/3} M_{200}^{5/3}. \end{aligned} \quad (4.12)$$

Here $f_* \lesssim M_*/M_{\text{b}}$ is the stellar mass fraction within the halo and f_{c} is the correction factor for fraction of the missing baryons at a given overdensity. Then we insert Eq. (4.12) into Eq. (4.10) to get the integrated

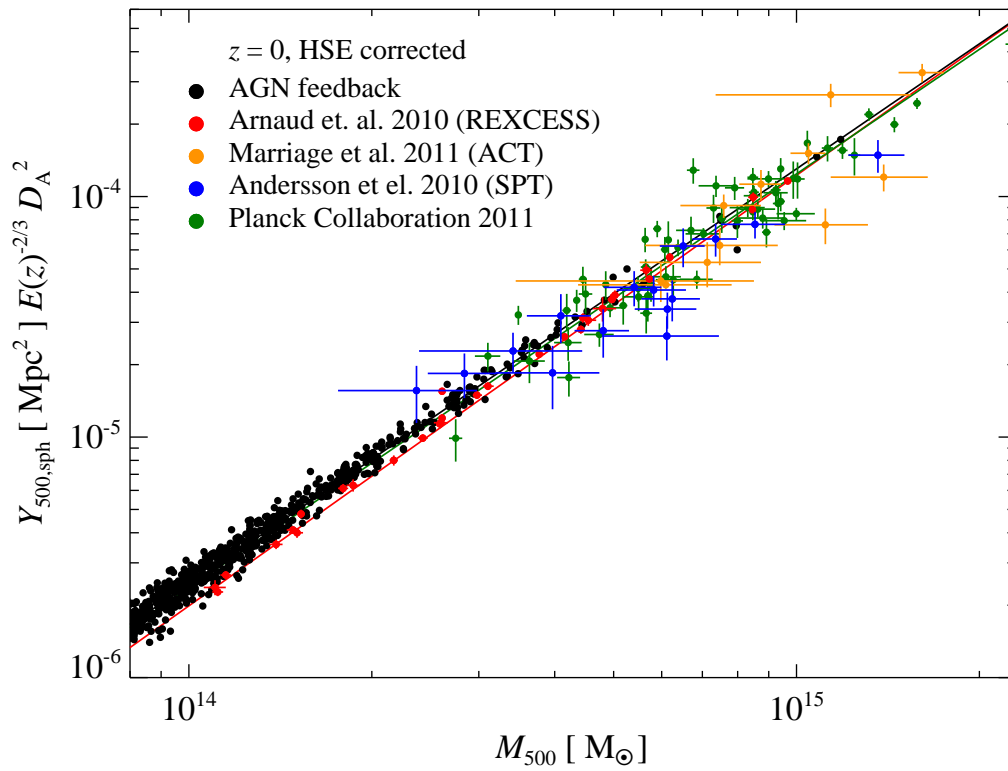


Figure 4.13: The $Y - M$ scaling relation for the AGN feedback simulations compared to recent X-ray results from Arnaud et al. (2010) and SZ results from ACT (Marriage et al., 2010), SPT (Andersson et al., 2010), and Planck (Planck Collaboration et al., 2011a). We have applied the 15% correction to the X-ray M_{HSE} from Kravtsov et al. (2006).

Compton- γ parameter within R_{200} which scales as

$$\begin{aligned}
 Y &= \frac{(\gamma - 1)\sigma_{\text{T}}}{m_{\text{e}}c^2} x_{\text{e}} X_{\text{H}} \mu (1 - f_{*}) f_{\text{b}} f_{\text{c}} G \left[\frac{\pi}{3} 100 \rho_{\text{cr}}(z) \right]^{1/3} M_{200}^{5/3} \\
 &= 97.6 h_{70}^{-1} \text{kpc}^2 E(z)^{2/3} \left(\frac{M_{200}}{10^{15} h_{70}^{-1} M_{\odot}} \right)^{5/3} \frac{\Omega_{\text{b}}}{0.043} \frac{0.25}{\Omega_{\text{m}}} \quad (4.13)
 \end{aligned}$$

For Eq. (4.13), we set $f_{*} = 0$, $f_{\text{c}} = 0.93$ (as calculated from our shock heating simulations at R_{200}) and adopted the cosmological parameters of our simulation. This simple analytical expression for the $Y - M$ scaling relation allows one to explore the assumptions underlying its derivation. More specifically, we test the assumptions of spherical gravitational potential, zero non-thermal pressure support, and constant f_{b} (and for simulation with star formation, constant f_{*}) at R_{Δ} , independent of cluster mass.

4.6.2 Comparison to data

In Figure 4.13, we compare Y_{sph} for our simulated clusters to the X-ray results from Arnaud et al. (2010), and the SZ results from ACT (Marriage et al., 2010), SPT (Andersson et al., 2010), and Planck (Planck Collaboration et al., 2011a). We adopt the 15% correction to the X-ray M_{HSE} estimates from Kravtsov et al. (2006) which is valid for the respective observational sample selection criterion. Our $Y_{\text{sph}} - M$ relation with AGN feedback is consistent with the current data from X-ray and SZ observations. However, at group scales, our simulations slightly overpredict the SZ flux due to the too high gas fractions, f_{gas} , in our simulations compared to X-ray observations (Pfrommer et al. in prep.). Potentially our simulations are missing some of the relevant physics that governs f_{gas} (see, e.g., Pfrommer et al., 2011) or underestimate the action of AGN feedback on these mass scales.

We note that Y_{sph} reported by SZ surveys for known clusters use an X-ray-derived estimate of the aperture size. This is useful because the cluster radii are typically poorly measured in SZ, and so the X-ray aperture fixes the SZ measurement along the otherwise degenerate aperture flux/aperture radius relation. However, this prior introduces correlations between the X-ray and SZ observations, which makes comparisons between these observations difficult to interpret.

4.6.3 Physics dependence of the $Y - M$ relation

In Figure 4.14 we show the dependence of the $Y - M$ relation on our three simulated physics models, i.e., shock heating, radiative cooling and star formation, and AGN feedback. The stark differences between the shock heating simulation and the two other simulations arise from the loss of baryons in the ICM to star formation. The radiative cooling simulations show a constant normalization offset of $\sim 20\%$, which nearly matches the f_{*} values for these simulations. In Table 4.2 we show that the self-similar expectation of Eq. (4.13) almost completely captures the cluster thermodynamics in our simulations when integrated over cluster-sized apertures. Including more physically motivated sub-grid models in

Table 4.2: $Y - M$ scaling relation fits for different simulated physics, subsampling in kinetic-to-thermal energy and ellipticity (of the density and pressure distribution), and along different projected axes yielding Y_{cyl} .

	$z = 0$			$z = 0.5$			$z = 1$		
	B	A	σ_Y	B	A	σ_Y	B	A	σ_Y
Simulated physics									
Theory, Eq. (4.13)	-4.88	1.67	-	-4.81	1.67	-	-4.74	1.67	-
Shock heating	-4.87 ± 0.01	1.64 ± 0.03	0.117 ± 0.003	-4.81 ± 0.02	1.63 ± 0.04	0.126 ± 0.002	-4.76 ± 0.05	1.61 ± 0.07	0.118 ± 0.002
Radiative cooling	-4.94 ± 0.01	1.67 ± 0.03	0.123 ± 0.002	-4.88 ± 0.02	1.67 ± 0.05	0.129 ± 0.002	-4.83 ± 0.05	1.66 ± 0.09	0.121 ± 0.001
AGN feedback	-4.92 ± 0.01	1.71 ± 0.03	0.135 ± 0.001	-4.87 ± 0.02	1.72 ± 0.05	0.140 ± 0.001	-4.82 ± 0.05	1.73 ± 0.09	0.142 ± 0.002
K/U^a									
Lower 3 rd	-4.88 ± 0.04	1.73 ± 0.07	0.108 ± 0.002	-4.83 ± 0.06	1.73 ± 0.11	0.122 ± 0.003	-4.78 ± 0.14	1.76 ± 0.21	0.140 ± 0.005
Middle 3 rd	-4.92 ± 0.02	1.73 ± 0.05	0.114 ± 0.002	-4.87 ± 0.04	1.73 ± 0.08	0.116 ± 0.002	-4.82 ± 0.07	1.73 ± 0.13	0.126 ± 0.004
Upper 3 rd	-4.94 ± 0.02	1.72 ± 0.04	0.123 ± 0.002	-4.89 ± 0.03	1.73 ± 0.07	0.128 ± 0.003	-4.85 ± 0.09	1.72 ± 0.15	0.132 ± 0.004
c/a (gas) ^a									
Lower 3 rd	-4.94 ± 0.02	1.72 ± 0.05	0.133 ± 0.002	-4.89 ± 0.04	1.72 ± 0.08	0.138 ± 0.003	-4.84 ± 0.09	1.73 ± 0.15	0.134 ± 0.003
Middle 3 rd	-4.92 ± 0.02	1.70 ± 0.05	0.124 ± 0.002	-4.86 ± 0.05	1.73 ± 0.09	0.131 ± 0.002	-4.82 ± 0.10	1.72 ± 0.16	0.131 ± 0.002
Upper 3 rd	-4.90 ± 0.02	1.72 ± 0.05	0.120 ± 0.001	-4.86 ± 0.04	1.72 ± 0.08	0.122 ± 0.002	-4.80 ± 0.09	1.73 ± 0.15	0.140 ± 0.003
c/a (pressure) ^a									
Lower 3 rd	-4.94 ± 0.02	1.71 ± 0.05	0.135 ± 0.002	-4.88 ± 0.04	1.73 ± 0.08	0.136 ± 0.003	-4.84 ± 0.08	1.73 ± 0.14	0.148 ± 0.003
Middle 3 rd	-4.92 ± 0.03	1.71 ± 0.05	0.129 ± 0.002	-4.87 ± 0.04	1.72 ± 0.08	0.128 ± 0.002	-4.82 ± 0.08	1.72 ± 0.14	0.134 ± 0.003
Upper 3 rd	-4.90 ± 0.03	1.72 ± 0.05	0.119 ± 0.002	-4.86 ± 0.05	1.71 ± 0.09	0.128 ± 0.002	-4.78 ± 0.12	1.76 ± 0.19	0.137 ± 0.003
Y_{cyl} rotated ^a									
Minor axis	-4.87 ± 0.01	1.69 ± 0.03	0.126 ± 0.001	-4.83 ± 0.02	1.69 ± 0.05	0.134 ± 0.002	-4.79 ± 0.05	1.70 ± 0.09	0.138 ± 0.003
Middle axis	-4.87 ± 0.01	1.69 ± 0.03	0.125 ± 0.001	-4.82 ± 0.02	1.69 ± 0.05	0.134 ± 0.001	-4.78 ± 0.05	1.69 ± 0.09	0.139 ± 0.003
Major axis	-4.84 ± 0.01	1.68 ± 0.03	0.131 ± 0.003	-4.79 ± 0.02	1.67 ± 0.05	0.152 ± 0.005	-4.74 ± 0.05	1.68 ± 0.09	0.171 ± 0.007
Y_{cyl} random ^a									
axis 1	-4.86 ± 0.01	1.69 ± 0.03	0.125 ± 0.002	-4.82 ± 0.02	1.69 ± 0.05	0.139 ± 0.002	-4.77 ± 0.05	1.70 ± 0.09	0.143 ± 0.003
axis 2	-4.86 ± 0.01	1.69 ± 0.03	0.126 ± 0.001	-4.82 ± 0.02	1.69 ± 0.05	0.138 ± 0.003	-4.78 ± 0.05	1.68 ± 0.09	0.147 ± 0.003
axis 3	-4.86 ± 0.01	1.69 ± 0.03	0.128 ± 0.002	-4.82 ± 0.02	1.69 ± 0.05	0.138 ± 0.002	-4.77 ± 0.05	1.70 ± 0.09	0.145 ± 0.004

^a For fits to all subsamples/projections, we use our AGN feedback model. Fit parameters are defined in Eq. (4.9).

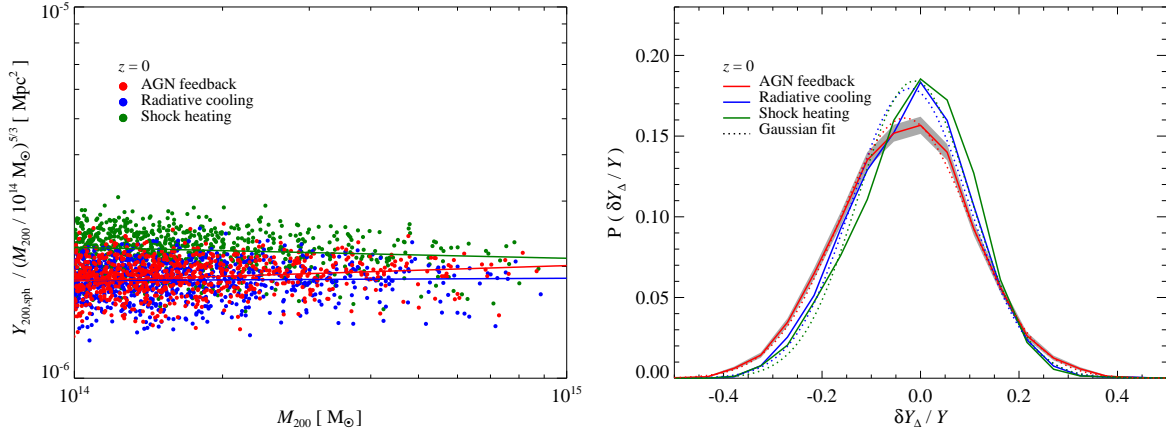


Figure 4.14: The normalization, slope and scatter of the $Y - M$ scaling relations all depend on the simulated physics. Left: The $Y - M$ scaling relations at $z = 0$ for all physics models that we simulate: shock heating (green), radiative cooling (blue), and AGN feedback (red). The y -axis has been scaled by $M^{5/3}$ to highlight the deviations from self-similarity. Right: The probability distributions for the scatter, $\delta Y_{\Delta}/Y$, relative to the best fits to all three physics models. We also show Gaussian fits (dotted lines) and include Poisson deviations for the AGN feedback simulations (grey band). We find that the AGN feedback simulations have the largest scatter and a steeper slope compared to the other simulations.

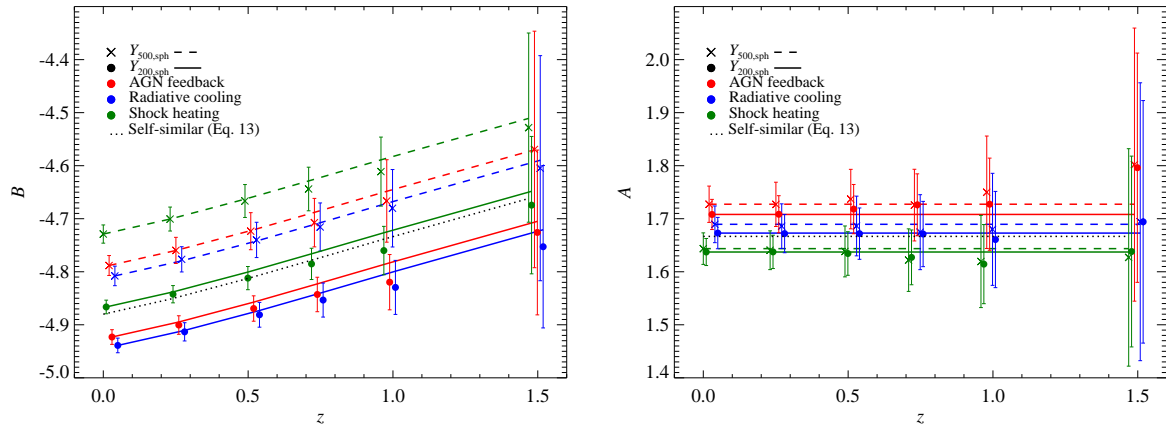


Figure 4.15: The redshift evolution of fit parameters of the $Y - M$ scaling relations for all simulated physics models is consistent with the self-similar prediction (Eq. (4.13)). We show the $Y - M$ scaling relation fits for the normalization, B , (left panel) and slope, A , (right panel) as a function of redshift and for two different virial masses M_{200} and M_{500} , and compare those to the self similar prediction (dotted black). Note that the $Y - M$ relation from AGN feedback simulations has a different slope, but shows no anomalous redshift evolution; hence, it is consistent with the predictions from self-similar redshift evolution.

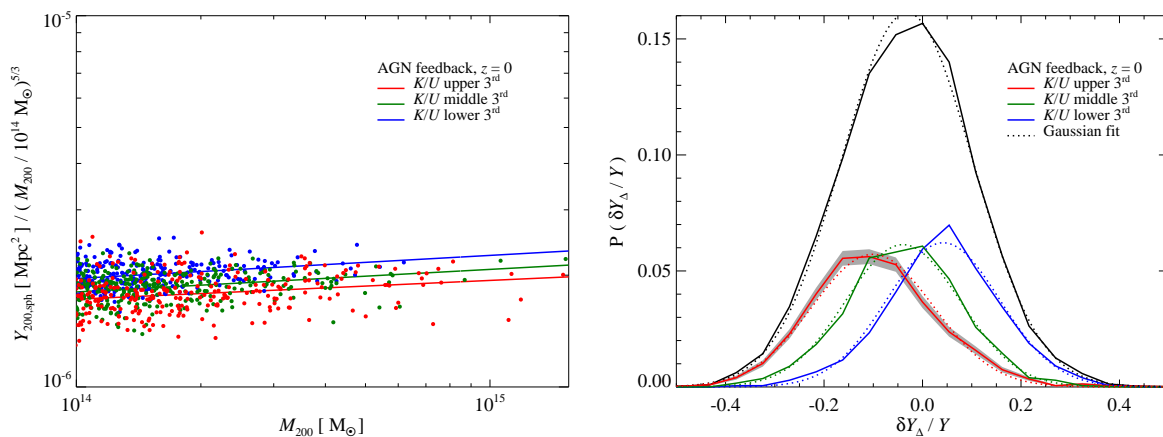


Figure 4.16: The results from sub-sampling the $Y - M$ relations by the kinetic-to-thermal energy ratio (K/U) for the AGN simulations. Left: The $Y - M$ scaling relation for the three K/U sub-samples, upper 3rd (red), middle 3rd (green) and lower 3rd (blue), with the corresponding slope fitted to those points. The y-axis has been scaled by $M^{5/3}$ to highlight the deviations from self-similarity. Right: The probability distributions for the scatter, $\delta Y_{\Delta} / Y$, relative to the best fits to the three sub-samples and the total distribution (black), including the Gaussian fits (dotted lines) and the Poisson deviations for the upper 3rd sub-sample (grey band). The sub-sample of K/U with the largest kinetic pressure support (upper 3rd) shows systematically lower total Y values for a given mass as well as larger scatter, while the lower K/U sub-sample has the lowest scatter of $\sim 10\%$. This is expected because a larger kinetic pressure contribution implies a lower thermal pressure and hence decreases Y .

the simulations, we find that both, the shock heating and radiative cooling slopes are consistent with this self-similar derivation for the $Y - M$ relation, while the AGN feedback simulations has a steeper, mass-dependent slope. This break from self-similarity in the AGN simulations arises from the suppression of star formation in the higher mass clusters and a feedback-induced deficit of gas inside the lower mass clusters. Over the redshift ranges we explore ($z = 0$ to $z = 1.5$) and for all simulated physics models, the $Y - M$ scaling relation normalization changes as predicted by self-similar evolution and the slopes remain essentially constant (cf. Fig. 4.15). So, the $Y - M$ relations from AGN simulations are different at redshift zero, but evolve as predicted by self-similar evolution. Additionally, Fig. 4.15 shows that these results on the redshift evolution are independent of the two aperture sizes chosen, which correspond to over-densities of 200 and 500 times the critical density. As noted in previous sections, within the radii R_{500} and R_{200} galaxy clusters are relatively well behaved, which illustrate that the impact of cluster ellipticities and the kinetic pressure support are small. Furthermore, the volume contained within R_{500} and R_{200} is large enough so that the SZ flux or equivalently the total thermal energy is not significantly dominated by the intricate physics of the cluster core region.

To quantify the scatter, we compute the relative deviation of each cluster from the mean relation, $\delta Y_{\Delta}/Y = (Y_{\Delta} - Y_{\Delta,\text{fit}})/Y_{\Delta,\text{fit}}$, and then fit this distribution with a Gaussian,

$$G(\delta Y_{\Delta}/Y) = A_0 \exp \left[\frac{-(\delta Y_{\Delta}/Y)^2}{2\sigma_Y^2} \right]. \quad (4.14)$$

Here the parameter A_0 is the normalization and σ_Y is the variance, which we will refer to as the scatter. Here we have chosen to model the variation about the mean as a Gaussian, while previous work by Stanek et al. (2010) showed that a log-normal distribution is also a reasonable description of the scatter. In Appendix 4.11, we show that within the (Poisson) uncertainties, the scatter is clearly Gaussian distributed and only approximately log-normal. Forcing a log-normal distribution introduces higher-order moments such as skewness and kurtosis as can be seen by the tails in the distributions and their asymmetric shapes.

We find that the scatter, σ_Y , for the entire sample of clusters is between 11 % and 14 % (cf. Fig. 4.14 and Table 4.2), which is consistent with previous work (Nagai, 2006; Stanek et al., 2010; Yang et al., 2010). In the simplest simulations with only shock heating the source for this scatter in the $Y - M$ relation has been proposed to arise from the formation time, the concentration, and the dynamical state of the cluster (Yang et al., 2010). As our simulations include more sub-grid physics models the scatter increase from $\sim 11\%$ to $\sim 14\%$ at redshift zero and changes further to $\sim 12\%$ to $\sim 14\%$ at redshift one. Of the three different physics models, the simulations with AGN feedback model gives the largest scatter. Note that this model for AGN feedback is self-regulated (Battaglia et al., 2010) and injects $\sim 2/3$ of the energy before redshift one when the average cluster mass is significantly smaller and the associated potentials are shallower so that a fixed energy injection by AGNs may in principle

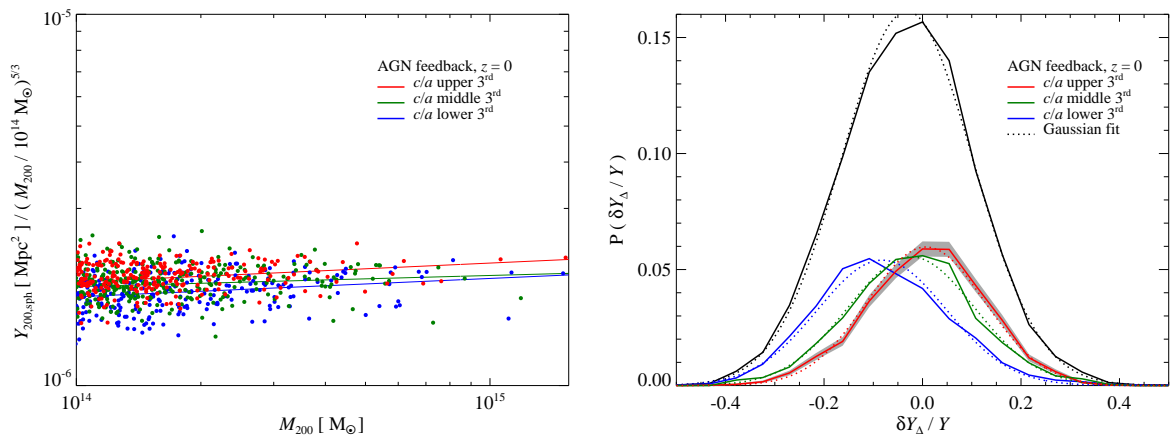


Figure 4.17: The results from sub-sampling the $Y - M$ relations by the gas c/a axis ratio for the AGN simulations. Left: The $Y - M$ scaling relation for the three c/a sub-samples, upper 3rd (red), middle 3rd (green) and lower 3rd (blue), with the corresponding slope fitted to those points. The y-axis has been scaled by $M^{5/3}$ to highlight the deviations from self-similarity. Right: The probability distributions for the scatter, $\delta Y_{\Delta} / Y$, relative to the best fits to the three sub-samples and the total distribution (black), including the Gaussian fits (dotted lines) and the Poisson deviations for the upper 3rd sub-sample (grey band). The sub-sample of c/a containing the lowest values (largest ellipticities) shows systematically lower total Y values for a given mass and larger scatter, while the more spherical high c/a sub-sample shows a lower scatter of $\sim 11\%$. Additionally we find that the pressure c/a axis ratio sub-sample has similar results (cf. Table 4.2).

have a stronger impact³. Thus, the increased scatter in the $Y - M$ relation from the AGN feedback simulations compared to the simulations without feedback is a result of the energy injection, which heats and disturbs the ICM. This statement is in accordance with previous results from Battaglia et al. (2010), where they showed the impact of AGN feedback on the pressure profiles of galaxy clusters and found that simulations with feedback had a shallower asymptotic pressure profile slopes than those without feedback. Thus, the intermittent nature of energy injection results in a larger scatter in the $Y - M$ relation compared to simulations without energetic feedback.

4.6.4 Toward a fundamental plane of $Y - M$

After quantifying the scatter of the entire sample, we aim at understanding its origin. This may enable us to either construct a linear combination of physically motivated observables that minimizes the scatter or to employ subsampling of the full distribution according to some parameter so that the resulting distribution exhibits a smaller intrinsic scatter and potentially allows for tighter cosmological constraints.

In previous sections we explored the average radial trends for kinetic pressure support from bulk motions and gas density/pressure shapes of the ICM. Utilizing this information, we rank order galaxy clusters according to their kinetic pressure support and intrinsic shape information. We follow the same fitting procedure as above for subsets of the lower 3rd, middle 3rd, and upper 3rd of the correspondingly sorted distributions in order to demonstrate the impact of kinetic pressure support and asphericity on the $Y - M$ relation fits and scatter. For the rest of this section we concentrate our analysis on the $Y - M$ relations of the AGN feedback simulations, since they show the greatest amount of scatter (this will provide an upper limit on the scatter) and are most likely our best representation of “real” clusters in comparison to the other physics models in our simulations. We compute the ratio of kinetic-to-thermal energy, K/U , within radial bins and use this ratio as a measure of dynamical state for the galaxy clusters. We define the internal kinetic energy, K , and thermal energy, U , of a cluster as

$$K(< r) \equiv \sum_i \frac{3m_{\text{gas},i}P_{\text{kin},i}}{2\rho_i}, \quad (4.15)$$

$$U(< r) \equiv \sum_i \frac{3m_{\text{gas},i}P_{\text{th},i}}{2\rho_i}, \quad (4.16)$$

where m and ρ are the gas mass and the SPH density, respectively for all particles i less than radius r . Note that K/U is the volume integrated analog to the ratio $P_{\text{kin}}/P_{\text{th}}$, which we show in Sect. 4.4 and will be indicative of the formation history and the substructure for each cluster. For the sub-sample with the highest ratio of K/U , we find a smaller normalization (cf. Fig. 4.16 and Table 4.2) where the difference between this upper 3rd of the distribution and lower 3rd is $\sim 15\%$. Here some of the thermal

³Similar results were found by McCarthy et al. (2011) in simulations with a more detailed feedback prescription.

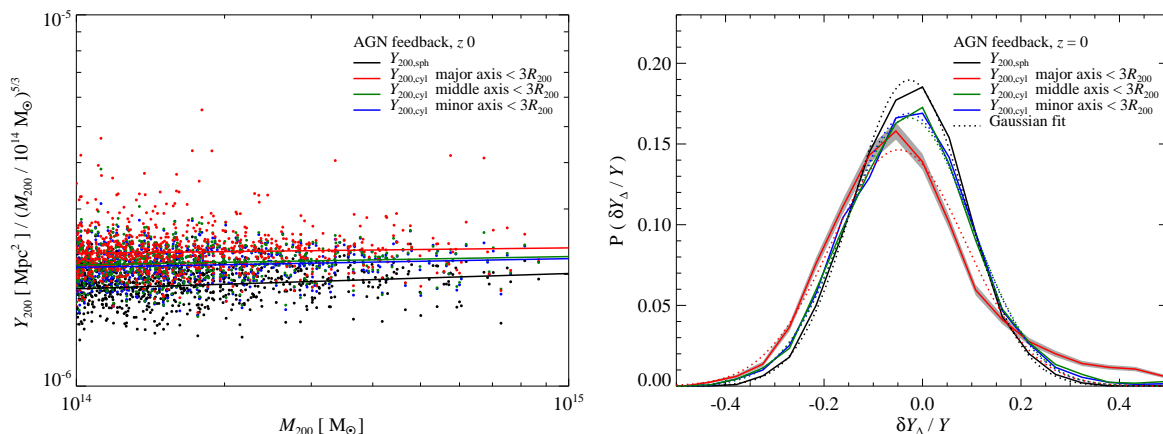


Figure 4.18: Rotating the clusters into their major, middle and minor axes show the effects of sub-structure on the cylindrical $Y - M$ relations. Left: The cylindrical $Y - M$ scaling relations from the AGN simulations for clusters that have been rotated into their major, middle, and minor axes defined by computing the inertial tensor within R_{200} . Right: The probability distributions for the scatter, $\delta Y_{\Delta} / Y$, relative to the best fits to all three distributions, each representing a distinctive rotation as well as the spherical distribution (black). We include the Gaussian fits (dotted lines) and the Poisson deviations for the major axis rotation (grey band). Rotating the clusters such that integration happens along the major axis increases the total Y values, while further distorting and increasing the scatter (due to the large cluster-to-cluster variance in the infall regions). Note that the Y_{cyl} values are integrated along the given axis from $-3R_{200}$ to $3R_{200}$; hence the Y_{cyl} will always be greater than the Y_{sph} values.

pressure support has been compensated for by kinetic pressure support resulting in lower integrated thermal electron pressure, thus, lowering Y -values. Note that more massive galaxy clusters are typically in the high K/U sample rather than the other two samples. We find that the sub-sample with the smallest K/U values shows the lowest scatter, $\sim 10\%$ for the AGN feedback simulations. Further sub-sampling of the smallest K/U values (e.g., the lowest 6th) does not decrease the scatter, which is limited to $\sim 10\%$.

Our sample of galaxy clusters are also sorted by the ratio of minor to major axis c/a as defined in Sec. 4.5. Following the same procedure as for the K/U subsample and concentrating on the AGN feedback simulations, we find that dividing the clusters up by ellipticity, c/a , gives similar results in comparison to K/U subsampling but are not as significant. The galaxy clusters with smaller ellipticities have larger total Y values and less scatter, while the more triaxial clusters have lower total Y and large scatter (cf. Fig. 4.17). These trends are reflected in the fit parameters of the sub-sample $Y - M$ relation shown in Table 4.2, where the differences between the upper 3rd and lower 3rd sub-samples normalization parameters is $\sim 10\%$. Additionally, we found that using the pressure shapes instead of the gas shapes yield almost identical results (cf. Table 4.2). Note that we have used the intrinsic 3D information when

sorting the subsamples; however, these results are applicable to observable projected 2D information, since the 3D and projected 2D axis ratios are highly correlated (cf. Fig 4.10).

The result from sub-sampling clusters according the K/U ratio and axis ratios indicate that there are correlations between these physical properties and the cluster mass. We find that high-mass clusters weakly correlate with larger K/U ratios and larger triaxiality, which appears as an anti-correlation with c/a values. Note, the correlation between mass and c/a is weaker than mass and K/U, as we found previously in the radial profiles. These correlations between kinetic pressure support, ellipticity and mass are the result of the growth of structure being hierarchical, i.e., on average, more massive galaxy clusters are more likely to be forming recently. This supports the argument that kinetic pressure support, ellipticity and sub-structure are all tracers of the dynamical state and the formation history of galaxy clusters which is the ultimate cause of the intrinsic scatter of the $Y - M$ relation. Previous work by Yang et al. (2010) found mass trends in the measured scatter, which is consistent with our findings after including the correlations between K/U, c/a and mass. However, their conclusion is different from ours, since they claim that formation time (and the formation history) does not significantly contribute to the scatter in the $Y - M$ relation and that the scatter is most sensitive to the DM concentration; a finding that may partially be due to the insufficient resolution in their simulations.

For pointed SZ observations of galaxy clusters and SZ surveys, a natural, model-independent observable is the projected flux, Y_{cyl} (Mroczkowski et al., 2009; Sayers et al., 2011). We find $Y_{\text{cyl}} > Y_{\text{sph}}$ in all cases, whether we chose the projection along a principal axis or random axis. This is due to the assumed extension along the line-of-sight integration which we choose to be three times the aperture radius; in observations, structure beyond this scale may additionally contribute in some cases. In fact, a projection integral out to $3R_{200}$ decreases the $Y - M$ slope for the AGN feedback simulations such that it becomes consistent with the self-similar slope (cf. Table 4.2). We find no difference between the random 2D projections and the integration along the middle or minor axes with respect to the normalization and slope (cf. Fig. 4.18 and Table 4.2). The scatter for the random 2D projections is marginally larger than the projections along middle and minor axes. Our results show that the integration along the major axis yields dramatically different results, both, for the normalization and scatter in comparison to projections along the other axes. This has its origin in the more extended tails of the *PDF* (cf. Fig 4.18). The normalization and scatter between the major axis and the other axes differ by $\sim 7\%$ and $\sim 6\%$, respectively; with the scatter being increased. At a higher redshift, these differences are amplified and we find a $\sim 12\%$ difference in the normalization and increase in scatter of $\sim 19\%$. This indicates that substructure is preferentially aligned with major axis and that substructure heavily influences the result from the inertial tensor beyond R_{200} .

4.7 Discussion and Conclusions

In this paper we demonstrate that the spatial distribution of the ICM, kinetic pressure support from bulk motions, and self-regulated thermal energy feedback in clusters cores (that we refer to as AGN feedback) all play very important roles for the thermal properties of galaxy clusters. In particular, the observables for large SZ galaxy cluster surveys, such as ACT, SPT and Planck, will be modified by these processes. Below we highlight and expand on our main results.

Non-thermal pressure support and cluster shapes: The contribution to the overall pressure support in galaxy clusters from bulk motions, P_{kin} , increases substantially for larger radii and is a strong function of both, cluster mass and redshift. Including AGN feedback marginally decreases $P_{\text{kin}}/P_{\text{th}}$ in comparison to the other (more simplified) simulation models, namely our shock heating-only model and that which additionally includes radiative cooling, star formation, supernova feedback, and CRs. However, the difference is not substantial enough to be statistically inconsistent with the variance around the median of $P_{\text{kin}}/P_{\text{th}}$. The mass dependence and redshift evolution of $P_{\text{kin}}/P_{\text{th}}$ is governed by P_{kin} and a direct result of the hierarchical growth of structure. Semi-analytic approaches are just beginning to model P_{kin} . The full dependence on radius, mass and redshift of this component is, by definition, self-consistently included in hydrodynamic simulations.

We find that the distribution of gas density and pressure are weak functions of the simulated physics models within R_{200} (excluding the cluster core) and that AGN feedback mildly modifies the average gas shapes. The cluster mass dependence of the ellipticity is more moderate in comparison to $P_{\text{kin}}/P_{\text{th}}$. The ellipticity is well behaved within R_{500} with little redshift evolution. In combination with the comparably small non-thermal pressure support at these scales (which rises dramatically beyond this characteristic radius), the small clumping factor measured in our simulations, and the small modification of our simulated cluster physics at these radii (in particular of our implementation of AGN feedback), this result is reassuring for X-ray observations of galaxy clusters which use R_{500} to characterize clusters with high-quality *Chandra* and *XMM Newton* observations. Hence, our analysis theoretically supports this choice of radius (which was initially motivated by the simulations in Evrard et al. (1996)) and justifies some of the main assumptions such as spherical symmetry and an almost radius-independent hydrostatic mass bias of $\sim 20 - 25\%$ when using a fair sample of clusters without morphological selection which may be applicable for the future eROSITA sample.

We find substantial redshift evolution in different dynamical quantities, e.g., $P_{\text{kin}}/P_{\text{th}}$, the velocity anisotropy, and anisotropy parameters such as ellipticities. This is in particular the case for the changes in the power-law behaviors of the radial profile of these quantities such as the sudden break in ellipticities which moves to smaller radii as the redshift increases (when scaled to R_{200}). The break and the more pronounced ellipticities and $P_{\text{kin}}/P_{\text{th}}$ outside a characteristic radius are a direct result of increased level of substructure predicted by hierarchical structure formation and the associated higher mass accretion

rate at higher redshift. We explicitly show (in the Appendix) that most of this redshift evolution is somewhat artificial and can be absorbed in a re-definition of the virial radius: scaling with the radius that contains a mean density of 200 times the average mass density rather than the critical density of the universe considerably weakens the observed trends with redshift. This also suggests a physical definition of the virial radius in terms of dynamical quantities (that, however, remain poorly defined observationally), e.g., the equipartition radius of thermal and kinetic pressure, the region where the velocity anisotropy becomes strongly radial, or the radius at which the ellipticity or substructure level increases dramatically. These seemingly different criteria all select a rather similar radius around $R_{200,m}$; almost independent of redshift.

On scales $> R_{500}$, high resolution SZ experiments such as ACT and SPT should be able to perform stacking analyses of projected SZ cluster images and – provided a suitable sample size – may be able to detect projected gas pressure shapes, potentially even in bins of redshift. The results on the randomly projected 2D axis ratios represent the theoretical expectations. Any statistics from the intrinsic 3D distribution is highly correlated with the projected 2D distribution; we find that the (more elliptical) intrinsic cluster shapes can on average be inferred from their projected analogues by applying a $\sim 5 - 10\%$ correction on the ellipticity. Another interesting outcome from our shape analysis is that there is no direct and simple mapping of shapes and alignments for DM spatial distribution to the gas and pressure distributions possible mostly due to the difference in substructure distribution and dissipational nature of the gas. This result is troublesome for semi-analytic models which use dissipationless simulations as a template to paste on gas distributions and pressure shapes. Such a method will produce additional triaxiality and misalignment for such a semi-analytical model of the ICM. The overall magnitude of the shape is reconciled by using the gravitational potential (e.g., Ostriker et al., 2005; Bode et al., 2009; Trac et al., 2011) which has been shown to be less triaxial (Lau et al., 2011) than the DM. However, providing an algorithm to re-alignment these pseudo gas distributions is a non-trivial task.

Y – M scaling relations: Our simulations are in good agreement with the current $Y - M$ scaling relations from both X-ray observations and SZ surveys. However, to properly predict the $Y - M$ scaling relations for an SZ experiment such as ACT, SPT or *Planck* without any prior knowledge of cluster masses, careful mock observations are needed. Those would have to include a simulation of the CMB sky with associated experiment noise and adopt the relevant cluster selection pipelines for the given experiment that employs the same cluster profile used for matched filtering in order to include all the systematics and potential biases that are intrinsic to the data analysis, e.g., X-ray priors on the aperture size.

We find that the inclusion of AGN feedback causes a deviation from the predictions of self-similar evolution for both the normalization and slope of the $Y - M$ relation (as measured within R_{200}). However, we recover the self-similar slope again in our projected $Y - M$ scaling relations (where we integrate along a cylinder of half-height $3R_{200}$), suggesting that AGN feedback pushes a fraction of its gas beyond the

virial radius and a larger aperture/projection radius is able to recover the thermal energy from this larger reservoir of gas.

Including AGN feedback also increases scatter in the $Y - M$ relation compared to simulations that include shock heating alone, from $\sim 11\%$ to $\sim 14\%$. Interestingly, sorting the clusters into subsamples of K/U and c/a will reduce this scatter; e.g., K/U subsampling reduces the scatter from $\sim 14\%$ to $\sim 11\%$. We find that subsampling introduces only a small (predictable) bias in the normalizations on the order of a few percent. This suggests that observational proxies for the dynamical state and ellipticities may be used to construct a fundamental plane of the $Y - M$ relation. The scatter ultimately originates from the merging history with its redshift and mass dependent accretion rates; those determine the non-thermal pressure support, the level of substructure, and the ellipticity. While subsampling on one of these secondary tracers may decrease the scatter, it is unlikely to decrease much more if more tracers are used (as they probe the same underlying process, albeit with a different weighting). Conversely, our sorting analysis on the $Y - M$ relations suggests that large outliers from the mean relations would be interesting candidates for follow up with high resolution SZ observations, since they are more likely to have larger kinetic pressure support and ellipticities.

A fundamental point to take away is that all results at larger radii ($> R_{200}$) for the kinetic pressure support and ICM shapes are dominated by substructure. We also see the impact of substructure on the cylindrical $Y - M$ scaling relation when integrating along the major axis with which substructure is preferentially aligned. Quantifying substructure statistically is difficult because of the problem of double-counting: the large volume contained within the radius that contains 95% of the total SZ flux, $4R_{200}$, necessarily leads to overlapping volumes of neighboring clusters, especially at high-redshift. Thus, this property remains challenging to model phenomenologically or (semi-)analytically.

As discussed previously in the literature (e.g. Battaglia et al., 2010; Sun et al., 2011) SZ galaxy cluster may provide further insight into the interesting astrophysics associated with the ICM of galaxy clusters. This however may significantly complicate cosmological analyses in producing competitive constraints. However, these are exciting prospects for studies of feedback and other energy injection processes within galaxy clusters especially at higher redshift since the selection function of SZ cluster surveys probes galaxy clusters which populate the massive and high redshift end of the distribution.

4.8 Appendix: Fitting function for $P_{\text{kin}}/P_{\text{tot}}$

In Section 4.4 we show that the ratio $P_{\text{kin}}/P_{\text{th}}$ is a function of mass. However, the previous empirical fitting function for $P_{\text{kin}}/P_{\text{tot}}$ (Shaw et al., 2010) does not include a mass dependence,

$$\frac{P_{\text{kin}}}{P_{\text{tot}}}(r, z) = \alpha(z) \left(\frac{r}{R_{500}} \right)^{n_{\text{nt}}} \left(\frac{M_{200}}{3 \times 10^{14} M_{\odot}} \right)^{n_M}, \quad (4.17)$$

where $\alpha(z) \equiv \alpha_0(1+z)^\beta$ for low redshifts ($z \lesssim 1$) and the fit parameters are $\alpha_0 = 0.18 \pm 0.06$, $\beta = 0.5$,

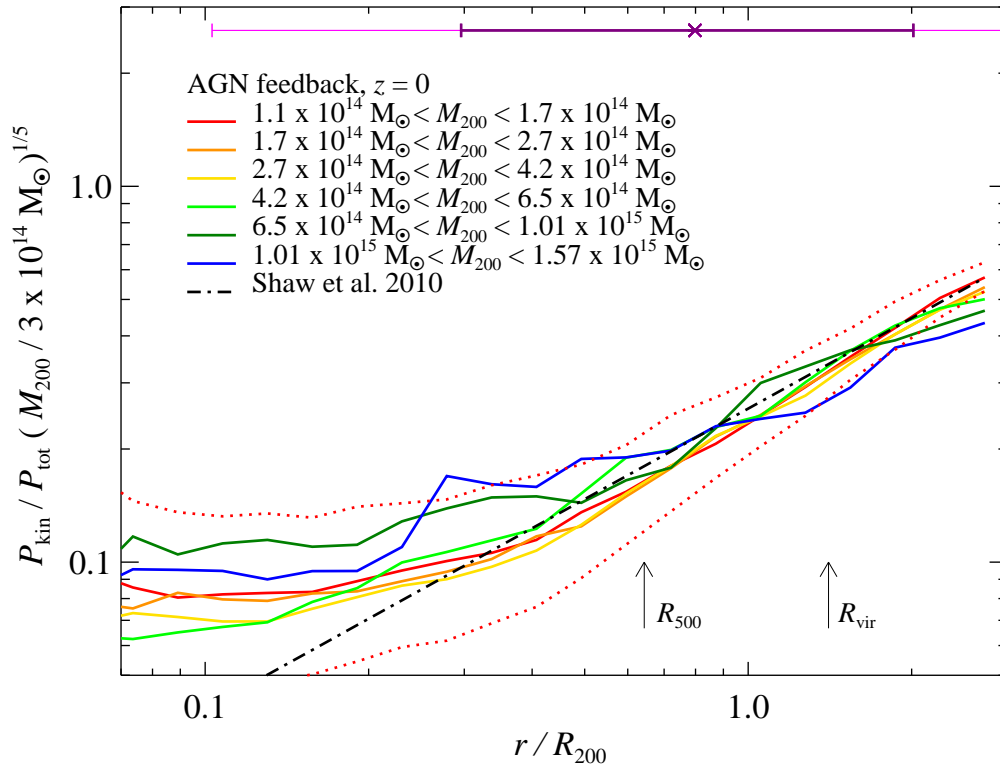


Figure 4.19: The kinetic pressure-to-total pressure is weakly mass-dependent, $P_{\text{kin}}/P_{\text{tot}} \propto M_{200}^{1/5}$. Shown is the median of $P_{\text{kin}}/P_{\text{tot}}$ as a function of radius for the AGN feedback simulations for various mass bins with the 25th and 75th percentile values illustrated by the dotted lines for the lowest mass bin at $z = 0$. For comparison, we also show the model for the $P_{\text{kin}}/P_{\text{tot}}$ by Shaw et al. (2010), which has been calibrated from AMR simulations (dash-dotted). We illustrate the 1 and 2 σ contributions to Y_{Δ} centered on the median for the feedback simulation by horizontal purple and pink error bars. Therefore, ignoring this mass dependence results in a 60 % difference in this ratio for an order of magnitude change in the cluster mass. Note that the median of $P_{\text{kin}}/P_{\text{th}}$ scales as $M_{200}^{1/3}$, which results in a larger difference.

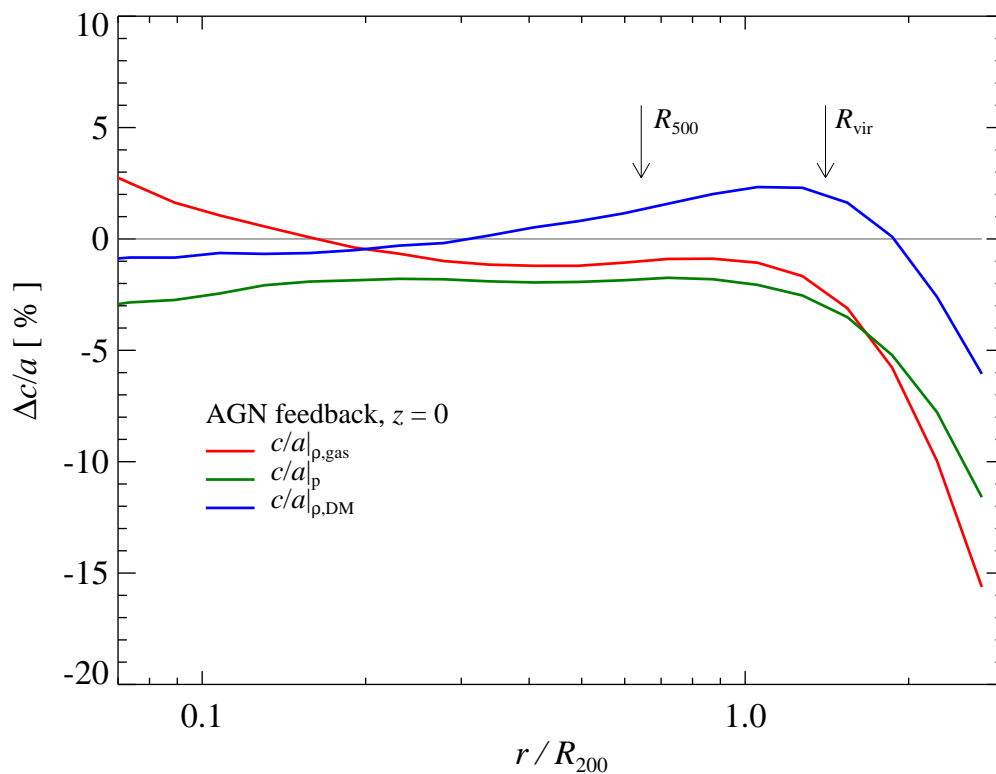


Figure 4.20: Additionally including the r^{-2} weighting in the definition of the inertial tensor decrease the contribution at larger radii by $\sim 15\%$, thus reducing the effect of substructure. Shown is the relative difference between axis ratios with and without the r^{-2} weighting for the gas density (red line), DM density (blue line) and gas pressure (green line) weightings.

$n_{\text{nt}} = 0.8 \pm 0.25$, and by construction, $n_M = 0$. In Fig. 4.19 we compare the fitting function for Eq. (4.17) and the P_{kin} to P_{tot} ratio. We find that including $M_{200}^{1/5}$ scaling accounts for the mass dependence, i.e. $n_M = 1/5$. We chose a normalization of $3 \times 10^{14} M_{\odot}$ to match the fitting function of Shaw et al. (2010). Thus, the median difference between the P_{kin} to P_{tot} ratio for a $10^{15} M_{\odot}$ and a $10^{14} M_{\odot}$ mass cluster is $\sim 60\%$. Note that the ratio in Eq. (4.17) is similar to what is shown Fig. 4.1, however, $P_{\text{kin}}/P_{\text{th}}$ depends more sensitively on mass. We find that the mass dependence for this ratio amounts to $M_{200}^{1/3}$.

4.9 Appendix: Down-weighting the substructure in the inertial tensor

In both the gas density- and pressure-weighting for the inertial tensor, using an additional r^{-2} weighting has minor impact on cluster shapes (cf. Fig. 4.20) and we do not see large differences when comparing the axis ratios at larger radii. Note that the greatest effect of the r^{-2} weighting is in these outer regions of galaxy clusters, where the axis ratios are not as large due to this r^{-2} suppression in comparison to

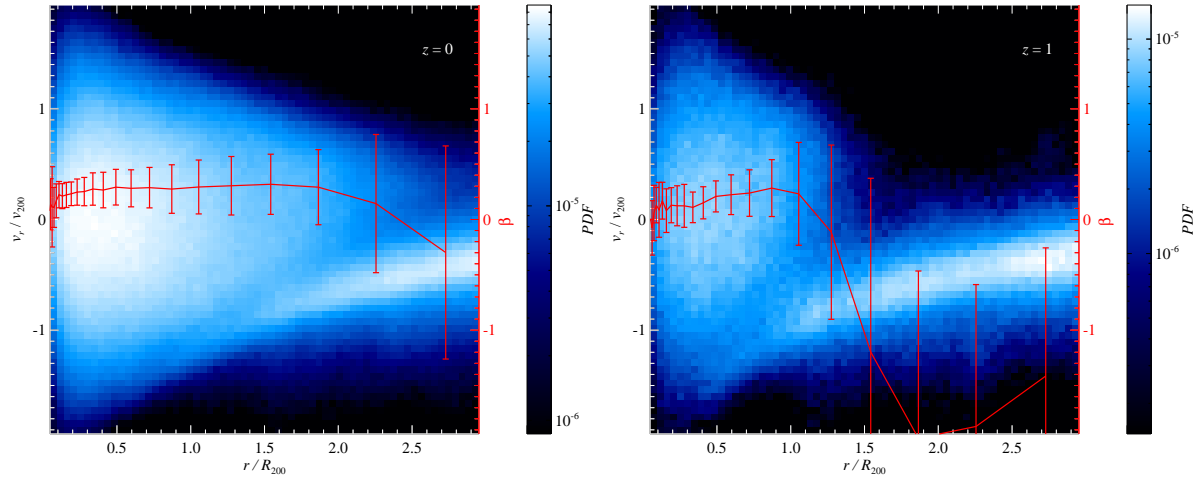


Figure 4.21: We compare the stacked radial velocity PDF (blue colors) and the velocity anisotropy, β , (red line) for all clusters at $z = 0$ (left panel) and $z = 1$ (right panel) for a mass bin $1.7 \times 10^{14} M_{\odot} \leq M_{200} \leq 2.7 \times 10^{14} M_{\odot}$. We choose a particular mass bin due to the strong mass dependence of β , shown in Fig. 4.5. The steep negative slope in the velocity anisotropy clearly matches the region splash-back region, i.e. the turn-around of earlier collapsed shells which minimizes the radial velocity component such that the tangential components dominate the velocity.

the weighting without r^{-2} . So, the purpose of this weighting is to lessen the influence of substructure which has been shown to be important at radii beyond R_{200} . However, this weighting scheme does not completely remove the effect of substructure, which is a non-trivial task in any stacking analysis.

4.10 Appendix: Galaxy cluster in velocity space and dynamical radius definition

We define the velocity and the velocity anisotropy, β , for the gas and DM in Sections 4.4.1 and 4.4.3. In Fig. 4.21 we show the probability distribution function of the radial velocity with the velocity anisotropy over-plotted. We find that the steep drop in the DM β profiles beyond R_{200} marks a distinct region in the cluster dynamics, the splash-back radius. This feature in the velocity anisotropy provides a distinct dynamical marker for a radial boundary in a cluster (though it is not observable). At the splash-back radius we find a tangential flow signifying a decrease in the radial velocity dispersion as a result of the radial velocity approaching zero. Furthermore, we show that this relation between the negative β and the splash-back region of the cluster as a function of redshift is not constant fraction of R_{200} . As noted in the main text, we found similar radial trends as functions of redshift in both the kinetic pressure support and ICM ellipticity when scaled by R_{200} .

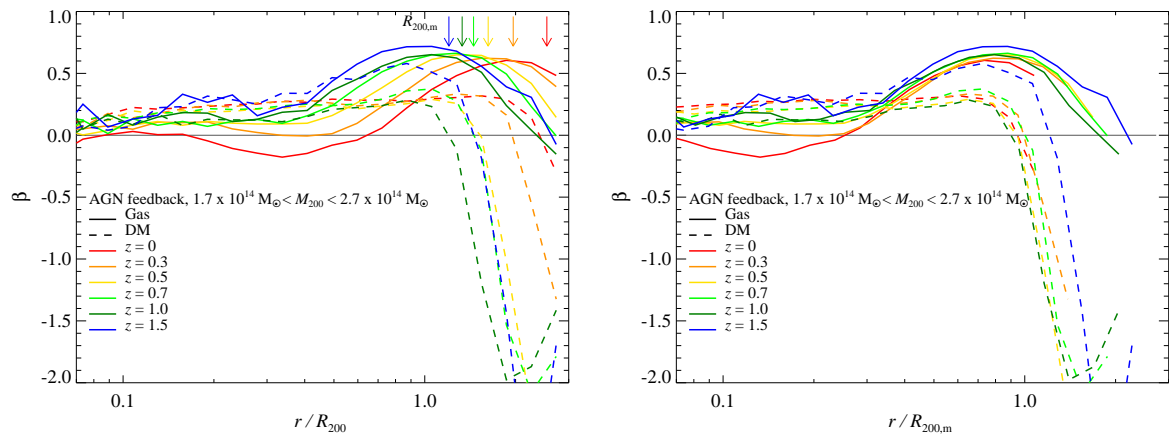


Figure 4.22: The choice for our working definition of virial radius (overdensity relative to the critical density of the universe) has an impact on the redshift evolution of dynamical regions of galaxy clusters. Left: Shown is the velocity anisotropy β at the a given redshift for a mass bin $1.7 \times 10^{14} h^{-1} M_{\odot} \leq M_{200} \leq 2.7 \times 10^{14} h^{-1} M_{\odot}$ scaled by R_{200} . The colored arrows show the location of $R_{200,m}$ and correspond to the same redshift colors in the legend. Right: Same as the left panel, except that the dimensionless radius has been scaled by $R_{200,m}$ instead of R_{200} . With this definition of virial radius (overdensity relative to the mean mass density of the universe), the redshift evolution of β ceases, especially for large radii. We have chosen a particular mass bin due to the strong mass dependence for β shown in Fig. 4.5.

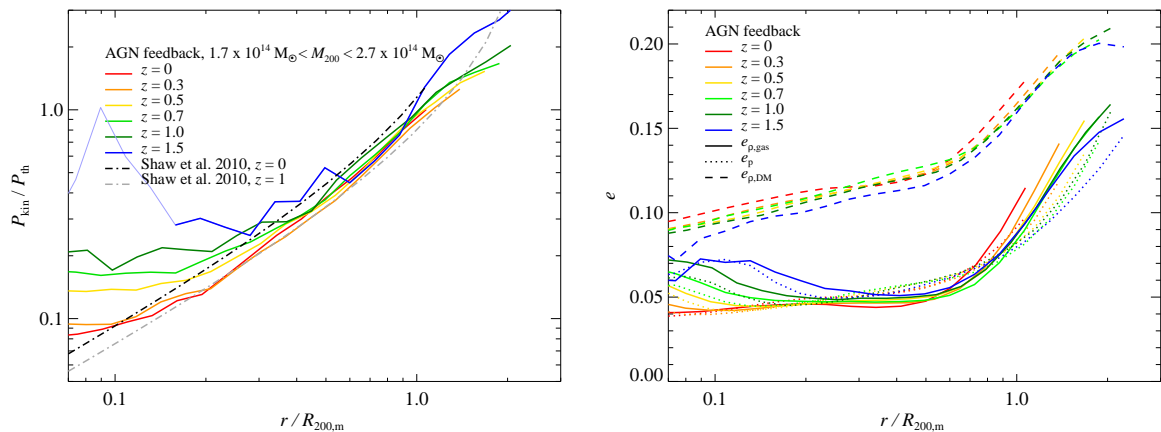


Figure 4.23: The choice for our working definition of virial radius has an impact on the redshift evolution of both, the kinetic pressure support (left) and ellipticity (right) of galaxy clusters. The figures shown here are the same as Fig. 4.1 and Fig. 4.11 except that the dimensionless radius has been scaled by $R_{200,m}$ instead of R_{200} . With this definition of virial radius, the redshift evolution of both, kinetic pressure support and ellipticity is decreased, especially in the outer regions.

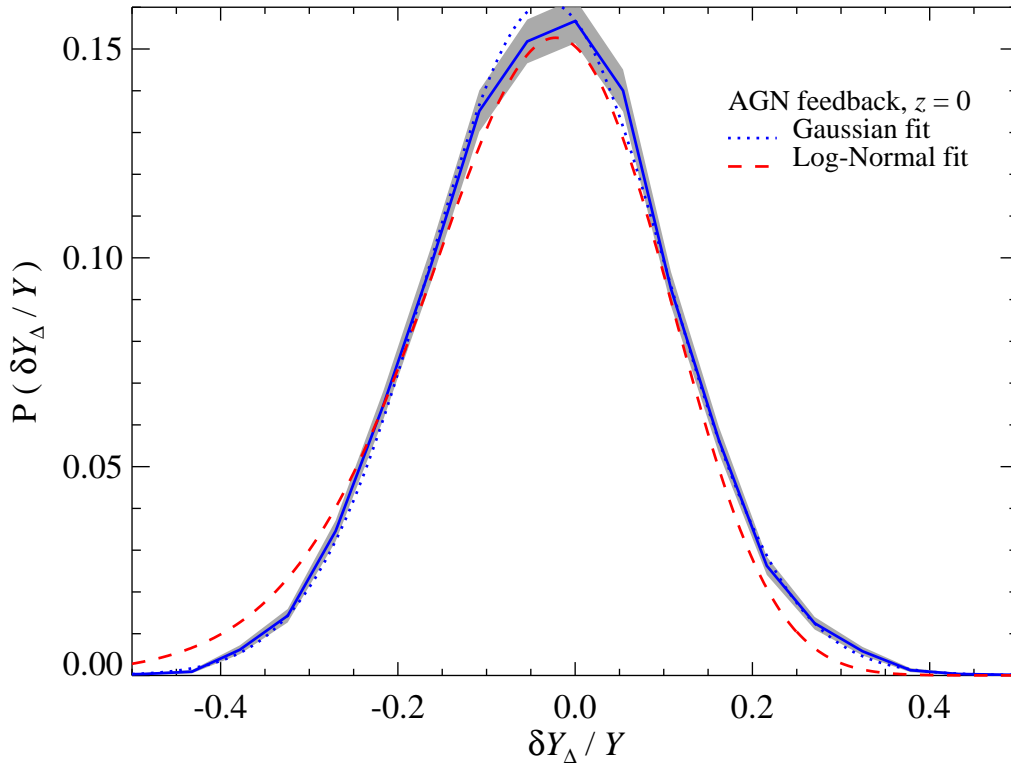


Figure 4.24: Comparison of Gaussian and log-normal scatter relative to the best-fit Y-Mscaling relation at $z = 0$. We show the distribution of the relative *linear* deviation from the mean relation $\delta Y_{\Delta}/Y$ (cf. Eq. 4.14) with the solid blue line and compare it to a Gaussian fit (blue dotted line) and log-normal fit ($\delta \log Y_{\Delta}$, red dashed line). The Poisson deviations are shown with the grey band. Here we transformed the fit to the $\delta \log Y_{\Delta}$ distribution into $\delta Y_{\Delta}/Y$ so they could be shown together. The $\delta Y_{\Delta}/Y$ distribution is fit by a Gaussian better than the $\delta \log Y_{\Delta}$ distribution, with $\chi^2(\delta Y_{\Delta}/Y) \sim 1$ and $\chi^2(\delta \log Y_{\Delta}) \sim 7$. Forcing a log-normal distribution introduces higher-order moments such as skewness and kurtosis as can be seen by the asymmetric shapes of the tails in the log-normal fit.

These radial trends over redshift call for re-examination of the choice for the working definition of radius, which is directly related to the definition of the cluster mass (see White, 2002, for a more thorough discussion of cluster mass definitions in dissipationless simulations). It has been the common choice by both observers and theorists to define the mass within an radii where the average overdensity is greater than a large multiple of a given background density, such as $\rho_{\text{cr}}(z)$ and $\bar{\rho}_m(z)$. For low redshift observations, the more popular definition has been the $\rho_{\text{cr}}(z)$ as the iso-density surface, since no prior knowledge of Ω_m is required. The question remains what definition is physically more intuitive when comparing across various redshifts. At late times ($z < 1$), clearly the inclusion of the dark energy greatly influences the redshift evolution of the critical density compared to the mean matter density. For a hypothetical isolated non-accreting galaxy cluster using the R_Δ definition will result in the cluster radius shrinking as time approaches present day. As shown in Fig. 4.21 using the R_Δ definition clearly selects different dynamical regions of the cluster as a function of redshift. At lower redshifts, R_Δ does not match the position of any dynamical feature (i.e. steep drop in the DM β or the equipartition of kinetic and thermal pressure) in the cluster. For comparison, the $R_{\Delta,m}$ clearly selects the splash-back region at each redshift (cf. Fig. 4.22) and appropriately scales the cluster radius such that an easier comparison can be made across redshifts. Using the $R_{\Delta,m}$ scaling, we find that the drop in the gas and DM anisotropy parameters align at similar radii and removes what apparently looked like a redshift evolution with the original R_Δ scaling of radius. This result is also found in the radius at which kinetic pressure is in equipartition with thermal pressure and the sharp break found in the ICM ellipticity (cf. Fig. 4.23). Thus, for comparison across redshifts it might be better to switch the radial definition to $R_{\Delta,m}$.

4.11 Appendix: Gaussian or Log-normal scatter?

Previous approaches quantified the scatter around the best-fit Y-Mscaling relation with a log-normal distribution, i.e. they characterized the distribution of $\delta \log Y_\Delta = \log Y_\Delta - \log Y_{\Delta,\text{fit}}$ with a Gaussian. Deviations from this log-normal distribution were computed with the Edgeworth expansion, introducing substantial higher order moments, such as skewness and kurtosis (e.g., Yang et al., 2010). Using a non-linear least squares approach we fit a Gaussian to both the $\delta \log Y_\Delta$ and $\delta Y_\Delta/Y$ distributions. In Fig. 4.24 we show that $\delta Y_\Delta/Y$ distribution is a better fit by a Gaussian within the (Poisson) uncertainties than the $\delta \log Y_\Delta$ distribution, with $\chi^2 \sim 1$ compared to $\chi^2 \sim 7$, respectively. Hence we suggest to use relative *linear* deviation instead of log-normal scatter for future characterizations of the scatter in Y-Mrelation.

Chapter 5

Deconstructing the Thermal Sunyaev-Zel'dovich Power Spectrum

5.1 Chapter Overview

Secondary anisotropies in the cosmic microwave background have the potential to be a treasure-trove of cosmological information. However, current experiments are already limited by theoretical uncertainties in interpreting their results rather than by measurement errors. Here, we focus on the secondary anisotropies resulting from the thermal Sunyaev-Zel'dovich (tSZ) effect; the amplitude of which depends critically on the average thermal pressure profile of groups and clusters. To this end, we use a suite of hydrodynamical TreePM-SPH simulations that include radiative cooling, star formation, supernova feedback, and energetic feedback from active galactic nuclei (AGN). We examine in detail how the pressure profile depends on cluster radius, mass, and redshift and provide an empirical fitting function. We employ three different approaches for calculating the tSZ power spectrum: an analytical approach that uses our pressure profile fit, a semi-analytical method of pasting our pressure fit onto simulated clusters, and a direct numerical integration of our simulated volumes. We demonstrate that the detailed structure of the intracluster medium and cosmic web affect the tSZ power spectrum. In particular, the substructure and asphericity of galaxy clusters increase the tSZ power spectrum by 10 – 20% at $\ell \sim 2000 - 8000$, with most of the additional power being contributed by substructures. The contributions to the power spectrum from radii larger than R_{500} is $\sim 20\%$ at $\ell = 3000$, thus galaxy clusters interiors ($r < R_{500}$) dominate the power spectrum amplitude at these angular scales.

5.2 Introduction

As cosmic microwave background (CMB) photons travel through the diffuse hot gas comprising the bulk of baryons in galaxy clusters, a fraction of them are upscattered by the gas in a process called

the thermal Sunyaev-Zel'dovich (tSZ) effect (Sunyaev & Zeldovich, 1970). This scattering produces a unique spectral signature in the CMB, with a decrement in thermodynamic temperature below $\nu \sim 220$ GHz, and an excess above. The tSZ is typically seen on arc-minute scales, and is referred to as a secondary anisotropy, as it originates between us and the surface of last scattering, unlike the primary CMB anisotropies. In the non-relativistic limit, the tSZ is directly proportional to the integrated electron pressure along the line of sight. It typically traces out the spatial distribution of galaxy clusters and galaxy groups, since the hot intracluster medium (ICM) tends to dominate the line-of-sight pressure integral. Thus, the tSZ provides an excellent tool to examine the bulk of cluster baryons. Found at the intersections of filaments in the cosmic web (Bond et al., 1996), galaxy clusters form from the highest peaks of the initial matter density field. They are sign posts for the growth of structure in the Universe, and are a potentially powerful tool for probing underlying cosmological parameters, such as w , the dark energy pressure-to-density ratio.

The angular power spectrum of the tSZ effect is extremely sensitive to cosmological parameters like σ_8 , the RMS amplitude of the (linearized) density fluctuations on $8h^{-1}$ Mpc scales. In fact, the amplitude of the tSZ power spectrum scales at least as steeply as the seventh power of σ_8 (Bond et al., 2002; Komatsu & Seljak, 2002; Bond et al., 2005; Trac et al., 2011) and improving the constraints on σ_8 will aid in breaking the degeneracies found between σ_8 and w when using only primary CMB constraints. An advantage of using the tSZ angular power spectrum over counting galaxy clusters is that no explicit measurement of cluster masses is required. Also, lower mass, and therefore fainter, galaxy clusters that may not be significantly detected as individual objects in SZ still contribute to this statistical signal. However, disadvantages of using the tSZ angular power spectrum include potential contamination from point sources and that no redshift information from the galaxy clusters is used.

Previous observations by the Berkeley-Illinois-Maryland Association (BIMA, Dawson et al., 2006), the Atacama Path-finding Experiment (APEX-SZ, Reichardt et al., 2009b), the Quest at DASI (QUaD, Friedman et al., 2009), Arc-minute Cosmology Bolometer Array Receiver (ACBAR, Reichardt et al., 2009a), and the Cosmic Background Imager (CBI, Sievers et al., 2009) all measured excess power above that expected from primary anisotropies, which have been attributed to some combination of the tSZ effect and point source contamination. The measurements from these experiments provided upper limits to the tSZ power spectrum amplitude. More recently, the Atacama Cosmology Telescope (ACT, Fowler et al., 2010; Dunkley et al., 2010) and the South Pole Telescope (SPT, Lueker et al., 2010; Shirokoff et al., 2010; Keisler et al., 2011) have detected the SZ effect in the CMB power spectrum¹. The results from ACT and SPT emphasize that the “sweet spot” for measuring the tSZ signal is between $\ell \sim 2000 - 4000$. Silk damping (Silk, 1968) and other contributions to the power spectrum are much smaller than at even higher ℓ . At these scales there are important additional contributions to the power

¹The Planck collaboration has released some early SZ science (e.g., Planck Collaboration et al., 2011a,b,c), but to-date there have been no power spectrum results.

spectrum from the kinetic SZ (kSZ) effect, which arises from motions of ionized gas with respect to the CMB rest frame, as well as dusty star-forming galaxies and the radio galaxies, both of which appear as point sources. All these signals increase the uncertainty when determining the tSZ power spectrum, and hence the parameters derived therefrom.

Three main tools have been used to estimate the tSZ power spectrum: Analytic models, semi-analytical models, and numerical simulations. They have been used to derive several different templates for the predicted tSZ power spectrum (e.g., Cole & Kaiser, 1988; Makino & Suto, 1993; da Silva et al., 2000; Refregier et al., 2000; Holder & Carlstrom, 2001; Zhang & Pen, 2001; Springel et al., 2001a; Komatsu & Seljak, 2002; Zhang et al., 2002; Bond et al., 2005; Schäfer et al., 2006a,b; Battaglia et al., 2010; Shaw et al., 2010; Trac et al., 2011; Efstathiou & Migliaccio, 2011). There are both shape and amplitude differences between these three approaches that compute the tSZ power spectrum; comparisons are required to understand these differences (Refregier et al., 2000). At the base of these differences is the galaxy cluster electron pressure profile, since it is a crucial and uncertain component in the analytical thermal SZ power spectrum calculation. The electron pressure profile is directly related to the total thermal energy in a cluster and is sensitive to all the complicated astrophysics of the ICM. For example, some of the ICM processes that should be included are radiative cooling, star-formation, energetic feedback from AGN and massive stars, non-thermal pressure support, magnetic fields, and cosmic rays. Deviations from an average pressure profile, from galaxy clusters substructure and asphericity will also contribute to the tSZ power spectrum. But how much?

The inclusion of AGN feedback is vital to any tSZ power spectrum template (Battaglia et al., 2010). Furthermore, an energetic feedback source (AGN feedback being the most popular) seems to be an important addition to any hydrodynamical simulation, since simulations with *only* radiative cooling and supernova feedback have problems with excessive over-cooling in cluster centers (e.g. Lewis et al., 2000). This over-cooling results in too many stars being produced at the expense of ICM gas, which unphysically alters the thermal and hydrodynamic structure of ICM.

In this paper we present a detailed comparison of the three approaches used to calculate the thermal SZ angular power spectrum. This comparison allows us to identify and quantify the differences between each method. Section 5.3 briefly summarizes the simulations used in this work and Section 5.4 outlines the calculation of the analytical tSZ angular power spectrum. In Sections 5.5 and 5.6 we present our results for numerical average thermal pressure profile and detailed analysis of the tSZ power spectrum, respectively. In Section 5.7 we provide updated constraints on σ_8 using the new ACT and SPT measurements of the CMB power spectrum at high ℓ , and we summarize our results and conclude in Section 5.8.

5.3 Cosmological simulations and cluster data set

We use a modified version of the smoothed particle hydrodynamical (SPH) code GADGET-2 (Springel, 2005) to simulate cosmological volumes. We use a suite of 10 simulations with periodic boundary conditions, box size $165 h^{-1}$ Mpc, and with equal numbers of dark matter and gas particles $N_{\text{DM}} = N_{\text{gas}} = 256^3$. We adopt a flat tilted Λ CDM cosmology, with total matter density (in units of the critical) $\Omega_{\text{m}} = \Omega_{\text{DM}} + \Omega_{\text{b}} = 0.25$, baryon density $\Omega_{\text{b}} = 0.043$, cosmological constant $\Omega_{\Lambda} = 0.75$, a present day Hubble constant of $H_0 = 100h = 72 \text{ km s}^{-1} \text{ Mpc}^{-1}$, a scalar spectral index of the primordial power-spectrum $n_s = 0.96$ and $\sigma_8 = 0.8$. The particle masses are then $m_{\text{gas}} = 3.2 \times 10^9 h^{-1} M_{\odot}$ and $m_{\text{DM}} = 1.54 \times 10^{10} h^{-1} M_{\odot}$. The minimum gravitational smoothing length is $\varepsilon_s = 20 h^{-1}$ kpc; our SPH densities are computed with 32 neighbours.

We include sub-grid models for *AGN feedback*, radiative cooling, star formation, and SN feedback. Throughout this work we will refer to these simulations as *AGN feedback*. The radiative cooling and heating were computed assuming an optically thin hydrogen/helium gas with primordial composition in a time-dependent, spatially uniform ultraviolet background (Katz et al., 1996; Haardt & Madau, 1996). Star formation and supernovae feedback were modelled using the hybrid multiphase model for the interstellar medium of Springel & Hernquist (2003a). The AGN feedback prescription included in the simulations (for more details see Battaglia et al., 2010) allows for lower resolution and hence can be applied to large-scale structure simulations. It couples the black hole accretion rate to the global star formation rate (SFR) of the cluster, as suggested by Thompson et al. (2005). The thermal energy is injected into the ICM such that it is proportional to the star-formation within a given spherical region.

We adopt the standard working definition of cluster radii R_{Δ} as the radius at which the mean interior density equals Δ times the *critical density*, $\rho_{\text{cr}}(z)$ (e.g., for $\Delta = 200$ or 500). For clarity the critical density is

$$\rho_{\text{cr}}(z) = \frac{3H_0^2}{8\pi G} \left[\Omega_{\text{m}}(1+z)^3 + \Omega_{\Lambda} \right]. \quad (5.1)$$

Here we have assumed a flat universe ($\Omega_{\text{m}} + \Omega_{\Lambda} = 1$) and are only interested at times after the matter-radiation equality, i.e., the radiation term with Ω_{r} is negligible. It is important to note that all masses and distances quoted in this work are given relative to $h = 0.7$, since most observations are reported with this value of h .

5.4 The Analytic Calculations of tSZ Angular Power Spectrum

The tSZ can be adequately modelled as a random distributed Poisson process on the sky (Cole & Kaiser, 1988)². There are two components in this model that are required for a statistical representation of the secondary anisotropies: (1) The number density for objects of a given class; and (2) the profile of the same object and class, centered on its position. We focus on galaxy groups and clusters, since they are the dominant source of tSZ anisotropies. This approach is referred to as the halo formalism (e.g., Cole & Kaiser, 1988).

The non-relativistic tSZ signal is the line of sight integrations of the electron pressure,

$$\frac{\Delta T}{T} = f(\nu)y = f(\nu)\frac{\sigma_T}{m_e c^2} \int P_e(l)dl, \quad (5.2)$$

where $f(\nu)$ is the spectral function for the tSZ (Sunyaev & Zeldovich, 1970), y is the Compton- y parameter, σ_T is the Thompson cross-section, m_e is the electron mass and P_e is electron pressure³. For a fully ionized medium, the thermal pressure $P_{\text{th}} = P_e(5X_H + 3)/2(X_H + 1) = 1.932P_e$, where $X_H = 0.76$ is the primordial hydrogen mass fraction, and P_{th} is the thermal pressure.

We adopt the successful analytical *ansatz* for halo number density as a function of mass

$$\frac{dn(M, z)}{dM} = \frac{\bar{\rho}_m}{2M^2} \frac{R(M)}{3\sigma(M, z)^2} \frac{d\sigma(M, z)^2}{dR(M)} f(\sigma(M, z)) \quad (5.3)$$

where $\sigma(M, z)$ is the RMS variance of the linear density field smoothed on the scale of $R(M)$, and $f(\sigma)$ is a functional form determined from N-body simulations (e.g., Jenkins et al., 2001; Warren et al., 2006; Tinker et al., 2008). In this work we use the mass function from Tinker et al. (2008) for the analytic calculations. Note that the tSZ power spectrum is only mildly sensitive to the particulars of the mass function (Komatsu & Seljak, 2002).

The tSZ angular power spectrum at a multipole moment ℓ is

$$C_{\ell, \text{tSZ}} = f(\nu)^2 \int \frac{dV}{dz} dz \int \frac{dn(M, z)}{dM} |\tilde{y}_\ell(M, z)|^2 dM, \quad (5.4)$$

where $\tilde{y}_\ell(M, z)$ is the form factor, which is the Fourier transform of the projected electron pressure profile, P_e . We do not include higher order relativistic corrections to $f(\nu)$ (Nozawa et al., 2006).

The functional form of $\tilde{y}_\ell(M, z)$ can be determined empirically in observations or simulations, or can be determined analytically (Komatsu & Seljak, 2001; Ostriker et al., 2005; Nagai et al., 2007; Arnaud et al., 2010). Following Komatsu & Seljak (2002) we compute $\tilde{y}_\ell(M, z)$, under the assumption of spherical symmetry and using Limber's approximation,

²Note that we are not including the contributions from the clustering of clusters, since this is sub-dominant on scales of $\ell > 300$ (Komatsu & Kitayama, 1999).

³Here we have ignored the temperature of the CMB, T_{CMB} , since $T_{\text{CMB}} \ll T_e$, hence $n_e k_B (T_e - T_{\text{CMB}}) \simeq n_e k_B T_e = P_e$.

$$\tilde{y}_\ell(M, z) = \frac{4\pi r_s}{\ell_s^2} \frac{\sigma_T}{m_e c^2} \int x^2 P_e(x) \frac{\sin(\ell x/\ell_s)}{\ell x/\ell_s} dx, \quad (5.5)$$

where $x \equiv r/r_s$ is a dimensionless radius, $\ell_s \equiv D_A/r_s$ is the corresponding wave number, and D_A is the angular diameter distance. We follow Navarro et al. (1997) in our definition of the scale radius in a cluster with concentration c_{NFW} , $r_s \equiv r_{\text{vir}}/c_{\text{NFW}}$. Here we use the definition for the virial radius from Bryan & Norman (1998).

The dominant source of uncertainty in $C_{\ell, \text{tSZ}}$ comes from $\tilde{y}_\ell(M, z)$, since given a cosmology, one can easily calculate the volume element, and the mass function is known to 5 – 10% (Tinker et al., 2008). Thus, the pressure profile is the critical input into the analytical tSZ angular power spectrum. We would ideally like to know $\tilde{y}_\ell(M, z)$ as well as we know the mass function. This requires an understanding of the detailed physical processes which affect cluster pressure profiles.

The Gaussian and non-Gaussian variance of the power spectrum is also calculated using the halo formalism (Cooray, 2001; Komatsu & Seljak, 2002; Zhang & Sheth, 2007; Shaw et al., 2009), again neglecting the clustering of clusters term. The full-sky variance is

$$\sigma_{\ell\ell', \text{tSZ}}^2 = \left[\frac{2(C_{\ell, \text{tSZ}})^2}{2\ell + 1} \delta_{\ell\ell'} + \frac{T_{\ell\ell'}}{4\pi} \right] \quad (5.6)$$

where $T_{\ell\ell'}$ is the trispectrum (see Equation (5.7)). The variance is proportional to the sky area covered, so for a fraction f_{sky} of the sky covered, $\sigma_{\ell\ell', \text{tSZ}}^2 \propto 1/f_{\text{sky}}$. In this work we will present the diagonal part of the covariance; the diagonal of the trispectrum is

$$T_{\ell\ell, \text{tSZ}} = f(v)^4 \int \frac{dV}{dz} dz \int \frac{dn(M, z)}{dM} |\tilde{y}_\ell(M, z)|^4 dM. \quad (5.7)$$

5.5 The Thermal Pressure Profile

The cluster thermal pressure profile is the most uncertain component of the thermal SZ power spectrum. In this section we use a large sample of clusters from hydrodynamical simulations and explore the mean cluster profile and the subtle differences from self-similar scaling (e.g. Kaiser, 1986; Voit, 2005). Comparisons between the latest pressure profiles from analytics, observations, and simulations have shown that they are in reasonable agreement with one another (Arnaud et al., 2010; Shaw et al., 2010; Trac et al., 2011; Sun et al., 2011). Previous work has shown that AGN feedback can alter the pressure profiles, though the profiles are comparable to previous simulations and observations (Battaglia et al., 2010). We show the dependence of the pressure profile on the cluster mass and redshift and explore deviations from the self-similar scaling.

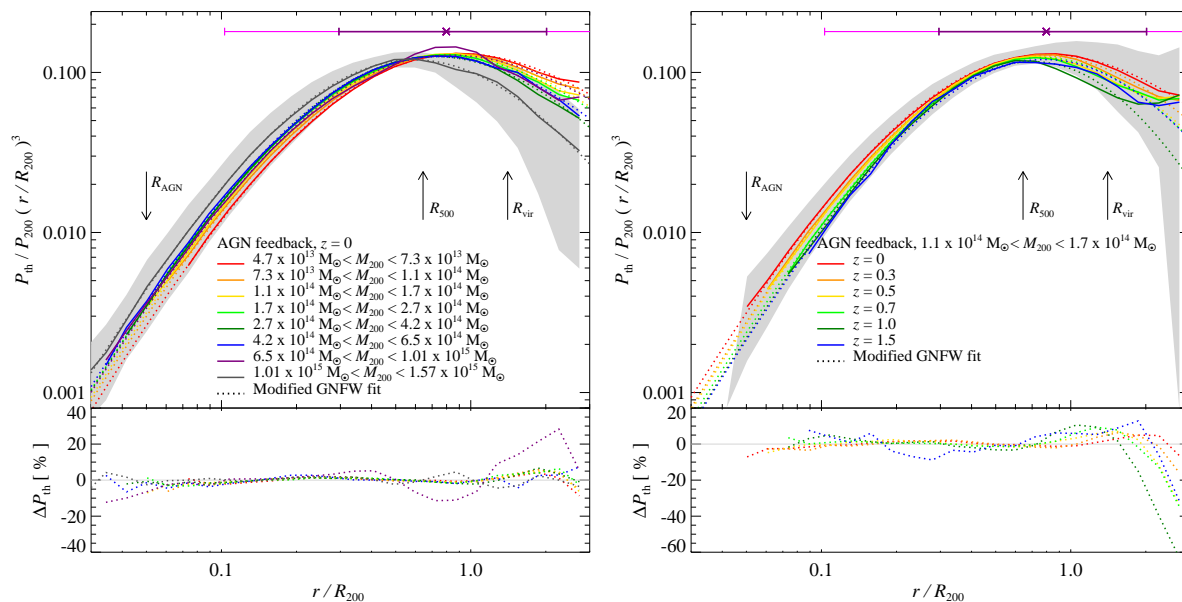


Figure 5.1: The normalized average pressure profiles and *parametrized fits* to these profiles from simulations with AGN feedback scaled by $(r/R_{200})^3$, in mass bins (left panel) and redshift bins (right panel). Here we have independently fit each mass and redshift bin. The grey band shows the standard deviation of the average cluster in the most massive bin (left) and lowest redshift bin (right). In both panels we illustrate the radii that contribute 68% and 95% of the total thermal energy, Y , centered on the median, by horizontal purple and pink error bars. The bottom panels show the percent difference between the fits and the average profiles. The generalized NFW with fixed α and γ fits the average profiles well in the majority of the mass and redshift bins, with deviations within $\sim 5\%$ of the mean. The upturns at large radii are due to contributions from nearby clusters and substructure.

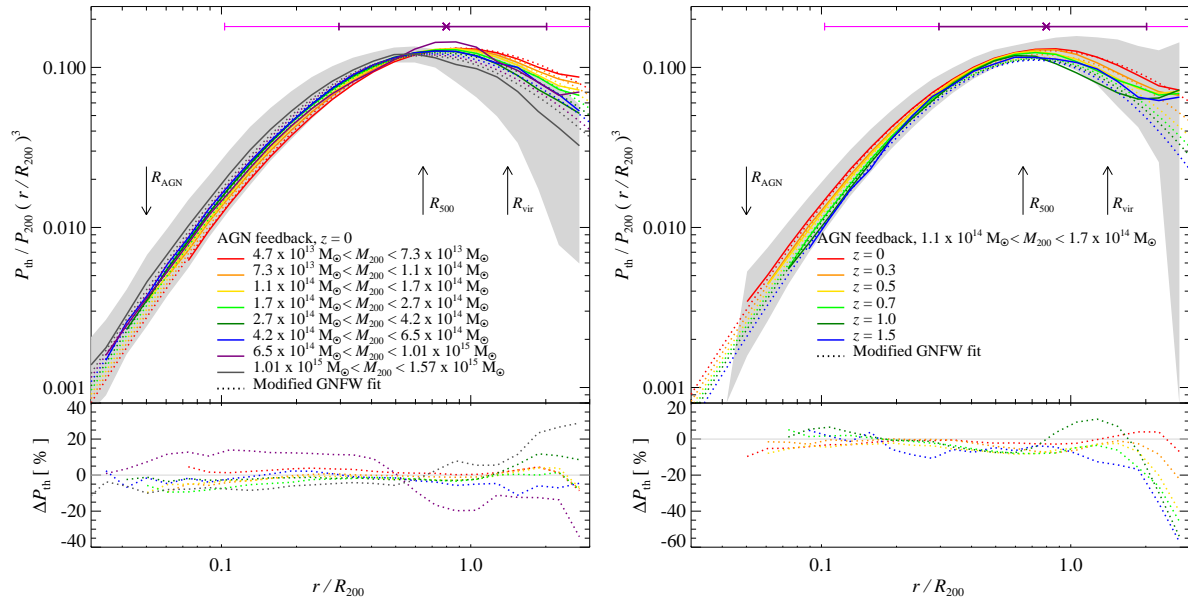


Figure 5.2: The normalized average pressure profiles and *constrained fits* to these profiles from simulations with AGN feedback scaled by $(r/R_{200})^3$, for mass bins (left panel) and redshift bins (right panel). The constrained fit is a global pressure profile, as described in the text, with parameters in Table 5.1. It differs from the fits in Figure 5.1, where each bin was fit independently. The grey band shows the standard deviation of the average cluster in the most massive bin (left) and lowest redshift bin (right). In both panels we illustrate the radii that contribute 68% and 95% of the total thermal energy, Y , centered on the median, by horizontal purple and pink error bars. The bottom panels show the percent difference between the constrained global fit and the average profiles. The constrained fit matches the average profiles well in the majority of the mass and redshift bins and the deviations are within $\sim 10\%$ of the mean. The upturns at large radii are due to contributions from substructure and nearby clusters.

5.5.1 Fitting Pressure Profiles from the Simulations

We apply the following four-step algorithm to compute the average thermal pressure profiles in our simulations. First, we find all clusters in a given snapshot using a friends-of-friends (FOF) algorithm (Huchra & Geller, 1982) using a linking length of 0.2 and an M_{FOF} mass cut of $1.4 \times 10^{13} M_{\odot}$. Second, starting with a position and radius derived from the FOF results, we find the final cluster positions by recursively shrinking the radius of the sphere examined, and re-center on its center of mass. Given the cluster center, we then calculate the spherical-overdensity mass and radius, M_{Δ} and R_{Δ} . Third, we calculate the thermal pressure profile for the entire sample of clusters in spherical shells, with the shells defined relative to R_{Δ} (for the pressure profiles, we use $\Delta = 200$). To facilitate profile comparisons and cluster stacking, we normalize each profile by the self-similar amplitude for pressure $P_{\Delta} \equiv GM_{\Delta}\Delta\rho_{cr}(z)f_b/(2R_{\Delta})$ (Kaiser, 1986; Voit, 2005), with $f_b = \Omega_b/\Omega_m$. Finally, we form a weighted average of these profiles by stacking clusters in a given redshift and mass bins. We use the integrated Compton y -parameter as our weighting function,

$$Y_{\Delta} = \frac{\sigma_T}{m_e c^2} \int_0^{R_{\Delta}} P_e(r) 4\pi r^2 dr \propto E_{th}(< R_{\Delta}), \quad (5.8)$$

The stacked average profiles $\bar{P}_{th} = \langle P_{th}/P_{\Delta} \rangle$ are then fit to a restricted version of the Generalized NFW profile,

$$\bar{P}_{fit} = P_0 (x/x_c)^{\gamma} [1 + (x/x_c)^{\alpha}]^{-\beta}, \quad x \equiv r/R_{\Delta}, \quad (5.9)$$

where the fit parameters are a core-scale x_c , an amplitude P_0 and a power law index β for the asymptotic fall off of the profile. There is substantial degeneracy between fit parameters, so we fix $\alpha = 1.0$ and $\gamma = -0.3$ (as suggested by Nagai et al., 2007; Arnaud et al., 2010). We find that fitting for all parameters did not provide a significantly better fit than when α and γ were fixed. However, without fixing α and γ , a direct comparison of fit parameters between different mass and redshift slices was not meaningful. We find the best-fit parameters using a non-linear least squares Levenberg-Marquardt approach (Levenberg, 1944; Marquardt, 1963). We weight each radial bin by the internal variance of the cluster profiles within that bin.

In Figure 5.1, we show the mass and redshift dependence of the average cluster thermal pressure profile and the corresponding parametrized fits to these profiles. We scale the pressure profiles by x^3 , such that the height corresponds to the contribution per logarithmic radial interval to the total thermal energy content of the cluster (cf. horizontal purple and pink error bars for the radii that contribute 68% and 95% of the cluster thermal energy). In the bottom panels of Figure 5.1, we highlight the residuals from the smoothed fitting function by showing the relative difference, $\Delta P_{th} = 100 (P_{fit} - \bar{P}_{th}) / \bar{P}_{th}$. The fitting function, Equation 5.9, provides an accurate fit over all mass and redshift ranges, with a majority of the deviations from the average profile being $< 5\%$.

We find that there are subtle dependencies on the cluster mass and redshift (cf. Table 5.1), which suggests that excluding these dependencies would not yield the required 5 – 10% precision needed for calculations of tSZ power spectrum. We also find that there are contributions to the average pressure profile at larger radii from substructure and nearby clusters, which cause deviation from the mean profile to be greater than 5%. In a companion paper, we also show that substructure affects the kinetic support in cluster outskirts and the shape of the ICM shape at similar radii (Battaglia et al., 2011). In these regions (redshift dependent, but typically $\gtrsim 2R_{200}$) P_{fit} often deviates from \bar{P}_{th} by more than 5%. We chose not to model this behavior because of two reasons. First, the problem of double-counting SZ flux: the large volume contained within the radius that contains 95% of the total SZ flux, $r < 4R_{200}$, necessarily leads to overlapping volumes of neighboring clusters, especially at high-redshift. Second, the total SZ flux of an increasing pressure profile, scaled by x^3 , does not converge and an arbitrarily chosen radial cutoff would substantially contribute to the resulting power of the tSZ power spectrum. Because we weight by the variance within radial bins, these contaminated regions are naturally down-weighted in the profile fits.

5.5.2 Constrained Thermal Pressure Profile Fits

In this section we derive a global fit to our pressure profiles as a function of mass and redshift. We find treating each parameter as a separable function of mass and redshift gives good results, with the fit parameters constrained to be of the following form: For generic parameter A , we have

$$A = A_0 \left(\frac{M_{200}}{10^{14} M_{\odot}} \right)^{\alpha_m} (1+z)^{\alpha_z}. \quad (5.10)$$

For each of P_0 , β , and x_c , we find α_m by fitting to the $z = 0$ snapshot, and we find α_z by fitting to clusters with $1.1 \times 10^{14} M_{\odot} < M_{200} < 1.7 \times 10^{14} M_{\odot}$. The weights used in the fits were the inverse variance of the fit parameters when fitting each individual cluster in that mass/redshift bin. With these fit parameters, presented in Table 5.1, and using Equations (5.9) and (5.10), we now have a global model for the average electron pressure as a function of cluster radius, redshift, and mass. Hereafter we refer to this global empirical description as the constrained pressure profile. In Figure 5.2 we compare the constrained fits to the stacked averages. With fewer degrees of freedom, the constrained fits will naturally not be as accurate as fitting each mass/redshift bin completely independently, but we do find that the mean recovered profile is accurate to the 5 – 10% accuracy with which we wish to measure the tSZ power spectrum.

In Figure 5.3, we present projected 30 GHz temperature maps of 4 sample clusters (cut at a spherical radius of $6R_{500}$), their expected maps from the global constrained fit, and the errors in the predicted temperature. A quantitative comparison of the tSZ power spectrum is deferred until Section 5.6.1. Hereafter, we refer to the predicted temperature maps as pasted profile maps. Note that this is not a representative sample of the difference between the pasted profiles and the simulations. Instead, we

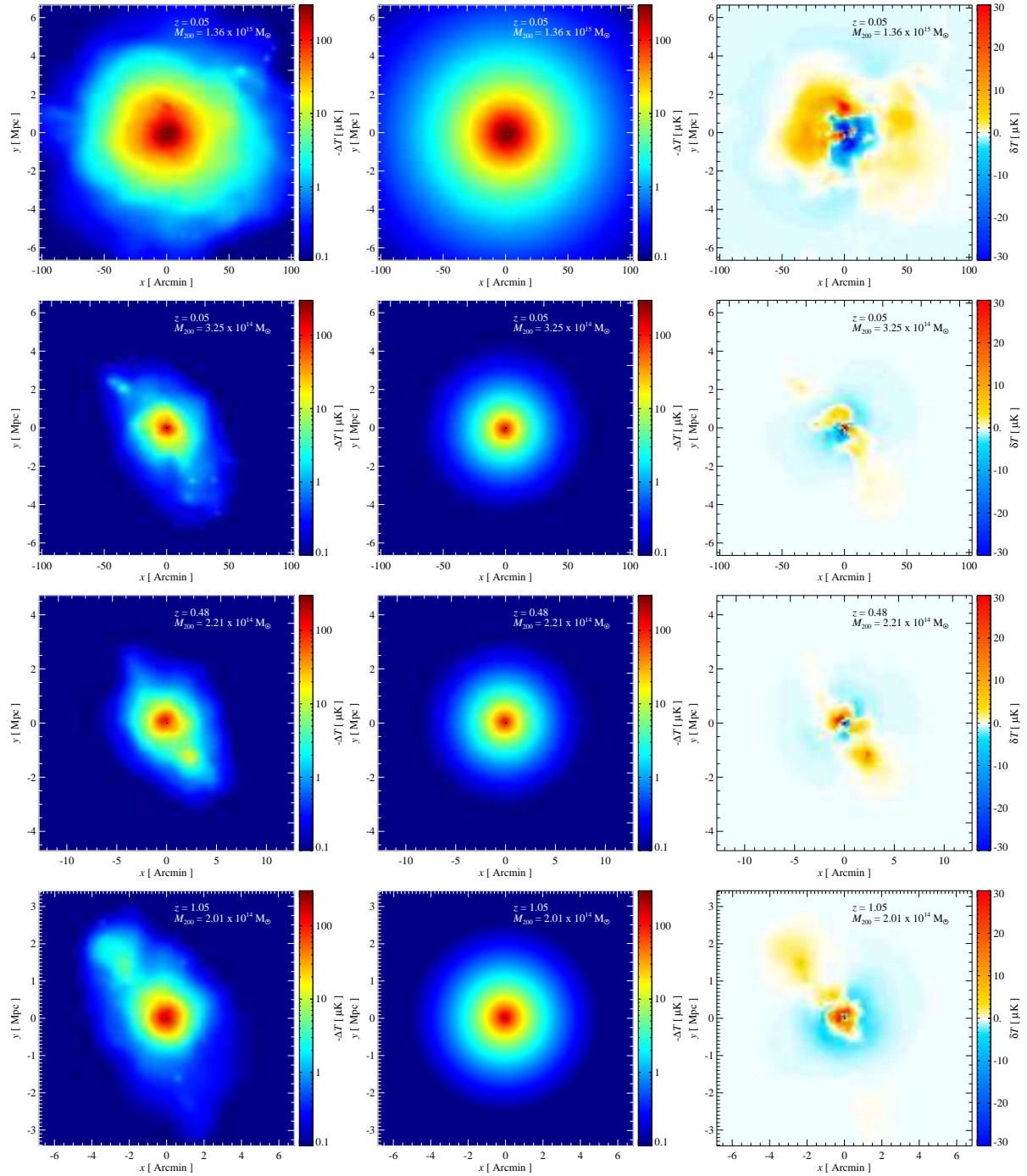


Figure 5.3: A comparison of four projected pressure maps of simulated galaxy clusters to the projected pasted-profile maps. From left to right, the panels show the simulated clusters (cut at a spherical radius of $6R_{500}$), the projected pasted profiles from the constrained fit, and the difference map between the two. The maps show the temperature decrement $-\Delta T$ in units of μK , at a frequency of 30 GHz. The difference maps, δT , illustrate the scales and amplitudes of the residuals between the simulated clusters and the projected pasted profiles. Note the color scale is logarithmic for the left two panels (from $-0.1 \mu\text{K}$ to $-100 \mu\text{K}$), while it is linear for the difference map (from $-30 \mu\text{K}$ to $30 \mu\text{K}$). For all panels the left and top axes are in units of Mpc and the bottom and right axes are in units of arc-minutes.

Table 5.1: Mass and Redshift Fit Parameters from Eqns. (5.9) and (5.10).

Parameter	$A_m = A_z$	α_m	α_z
P_0	18.1	0.154	-0.758
x_c	0.497	-0.00865	0.731
β	4.35	0.0393	0.415

The input weights are chosen to be the inverse variances of fit parameter values from the individual pressure fits for each cluster within the bin.

attempt to show different size clusters across different redshifts and illustrate the scales of the deviations from the constrained fit, primarily resulting from substructure⁴. In the rightmost panel of Figure 5.3, we show the residuals amplitudes between the simulated cluster projections and the pasted profile from the constrained fits. We find that these profiles are within $\sim 10\%$ of the actual simulated cluster, which is similar to the differences found in the bottom panels of Figure 5.2. These substructures are significant on scales of tens of arc minutes for nearby massive clusters and scales of arc minutes for higher redshift clusters, corresponding to $\ell \sim 1000 - 10000$.

5.5.3 Analytic Assumptions in the Thermal Pressure Profile

Analytic and semi-analytic models typically rely on assuming an equation of state and some form of hydrostatic equilibrium (HSE), possibly including non-thermal support terms. Fully analytic models, (e.g., Komatsu & Seljak, 2002; Shaw et al., 2010), apply HSE to theoretical, spherically symmetric dark matter potentials. Semi-analytic models, (e.g., Sehgal et al., 2010; Trac et al., 2011), take dark matter simulations, and paste baryons on top of the dark matter potential wells, again using (possibly corrected) HSE and an equation of state. The results from both classes of models, then, rely critically on the input equation of state and are sensitive to departures from HSE. In contrast, empirical fits to the average cluster pressure profile derived from simulations have a key advantage over analytical models because the simulations naturally deal with kinetic pressure support from non-thermalized bulk flows which provide substantial support in the outer parts of clusters, but do not contribute to the tSZ. They also make no assumptions about HSE (which is grossly violated during, for instance, mergers), and rather than force an equation of state onto the gas, they track the flow of energy into and out of the ICM.

The (semi-)analytic calculations cast the equation of state in terms of a pressure law $P \propto \rho^\Gamma$, and usually assume a constant Γ , where P can be either the thermal pressure P_{th} which is the source for the tSZ effect, or the total pressure, $P_{\text{tot}} \equiv P_{\text{th}} + P_{\text{nt}}$, where P_{nt} is any non-thermal support, principally

⁴There is also some mis-centering, since the cluster center of mass does not necessarily line up with the peak of the projected pressure.

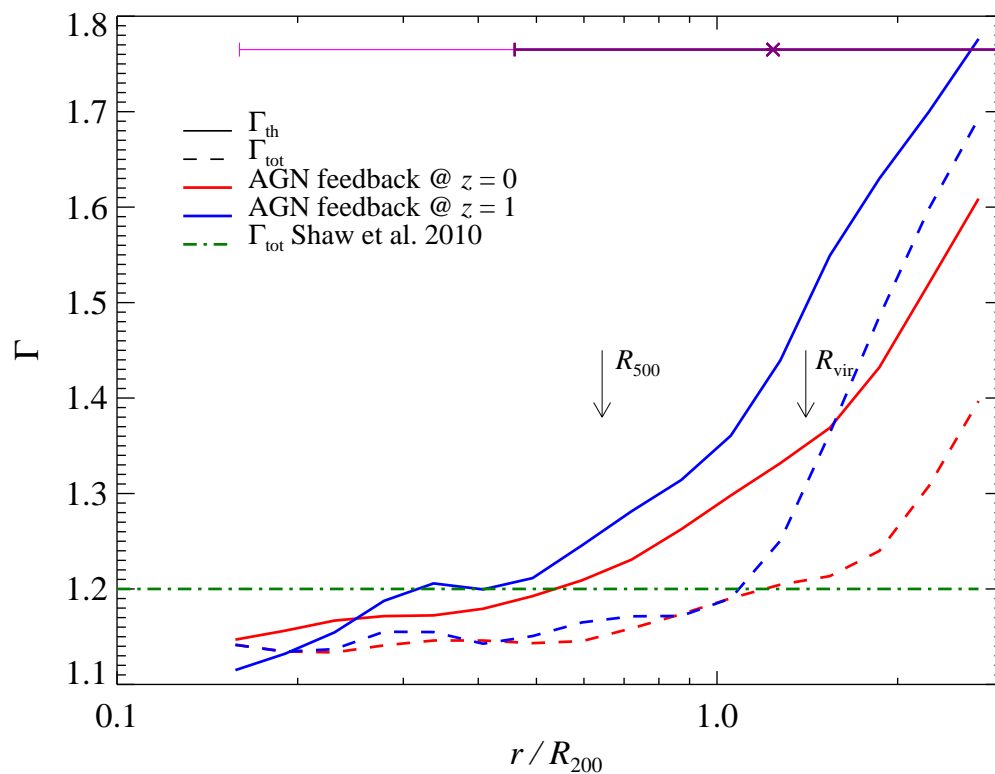


Figure 5.4: The assumption of a constant thermal or total adiabatic index, as most analytic models assume, is not consistent with the results from our simulations. The thermal (Γ_{th} solid line) and total adiabatic indexes (Γ_{tot} dashed line) are shown as functions of radius at $z = 0$ and $z = 1$ from simulations with AGN feedback. For comparison, we show the total adiabatic index used by Shaw et al. (2010), and we find that the differences increase at larger radii, especially at high redshifts.

kinetic motion of the ICM⁵. The total pressure is the input to the equation of hydrostatic equilibrium:

$$dP_{\text{tot}} / dr = -GM(< r)\rho / r^2. \quad (5.11)$$

We present the effective adiabatic index, $\Gamma = d \log P / d \log \rho$, as a function of cluster radius in Figure 5.4. We find that the assumption of constant Γ is grossly violated, particularly in the outer parts of clusters, and for P_{th} . These results stress the importance of deriving pressure profiles from observations and hydrodynamical simulations, particularly as good-quality observational data from cluster outskirts is in short supply.

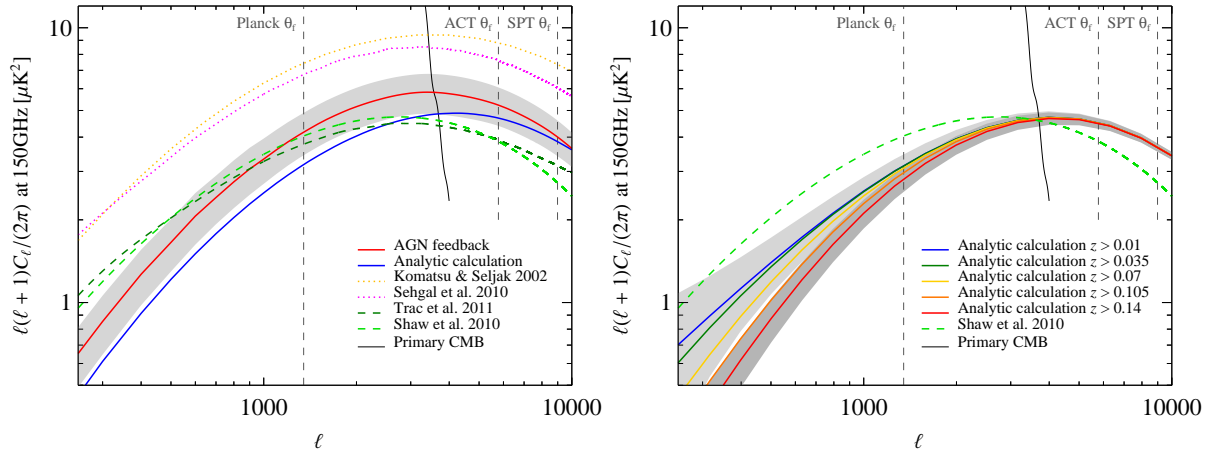


Figure 5.5: In the left panel, we show a comparison of the current predictions for the tSZ power spectra at 150 GHz from our simulations with AGN feedback (red line) and the analytical calculations using the constrained pressure profiles in this work (blue line). The standard deviation among our 10 simulations is shown with a light grey band. We also include the semi-analytical simulations by Sehgal et al. (2010) (pink dotted line) and Trac et al. (2011) which includes enhanced non-thermal pressure support (dark green dashed line) and the fully analytical calculations by Komatsu & Seljak (2002) (orange dotted line) and Shaw et al. (2010) (light green dashed line). The full-width half-max values appropriate for the Planck, ACT and SPT beams are also plotted. At low- ℓ , our two methods of calculating the tSZ diverge because our simulations happen to contain a large number of high mass objects driving the power up, though the excess is consistent with expected Poisson fluctuations. At high- ℓ the discrepancy is the result of substructure and asphericity, as demonstrated in Sections 5.6.1 and 5.6.2. The right panel shows a comparison between the current analytic calculations for the tSZ power spectra and how the power spectrum changes with the variation of the lower redshift limit of integration. The variance of the full-sky power spectrum (cf. Equation (5.6)) is illustrated by the grey bands for the highest and the lowest redshift limits of integration.

5.6 The tSZ power spectrum in detail

In this section we compare three different ways of calculating the tSZ power spectrum: directly projecting the electron pressure in the simulations, taking the simulation cluster catalogs and projecting our constrained global pressure profile onto the cluster locations (the “pasted profile” maps), and using a completely analytical halo calculation. For the analytic calculation, we use the formalism described in Section 5.4 and the constrained pressure profile from Section 5.5. For the simulation and pasted profile, the thermal Compton- γ maps are obtained by performing a line-of-sight integration of the electron pressure through the entire simulation box at each redshift output, covering $z = 0.07$ to $z = 5$. For each redshift-output map we compute the average power spectrum for our ten simulations and add these differential power spectra up⁶. This procedure uses all the information within the simulation volume and decreases the variance of the power spectrum, especially at low redshifts. One benefit of this technique is that by summing over redshift slices *after* taking the power spectra, we ignore any correlations between different redshift slices, as effectively happens in nature. With more traditional methods that stack redshift slices (such as were used in Battaglia et al. (2010)), care must be taken that different redshift slices do not project the same objects to the same locations, as that induces artificial correlations, potentially altering the tSZ power spectrum.

In the left panel in Figure 5.5, we plot the tSZ power from our analytical halo calculation and that from the AGN simulations. For reference, we include other tSZ power spectrum templates (Komatsu & Seljak, 2002; Sehgal et al., 2010; Shaw et al., 2010; Trac et al., 2011). We choose the cosmological parameters for the halo calculation to match the simulations and integrate from $z = 0.07$ to $z = 5$, so that the only possible sources of differences are the mass function and the pressure profile. There are clear differences between the analytical halo calculation and the complete simulation maps. The main difference at low ℓ s results from shot noise within the sample of simulated boxes, where we had more (though consistent within the expected error) high-mass clusters than expected, but this is only a 6% effect in the total power spectrum (cf. Appendix). The differences at higher ℓ s arise from deviations about the average pressure profile, including from cluster substructure and asphericity. We see these variations in the residual maps of individual simulated cluster projections and pasted profile projections (cf. Fig. 5.3). We further explore these differences in the power spectrum between the analytic calculation and the simulations in the following Sections 5.6.1 and 5.6.2. It is challenging to determine the causes for all the differences between our calculations and other calculations for the tSZ power spectrum (Komatsu & Seljak, 2002; Sehgal et al., 2010; Shaw et al., 2010; Trac et al., 2011), since the thermal pressure profile we use is different from the ones used by the other calculations. However, the reasons for the differences we find between our three methods, will be generally applicable to the

⁵Some older models have ignored kinetic support entirely, in which case $P_{\text{tot}} = P_{\text{th}}$.

⁶We have selected the redshifts at which we write out the simulation snapshots to be the light crossing time of the simulation; hence, the total power spectrum is the sum of the differential power spectra.

other methods of calculating the tSZ power spectra.

The right panel of Figure 5.5 shows a direct comparison between our analytical model and the Shaw et al. (2010) model. In both calculations, the same cluster mass function was used and the power spectra are scaled to the same cosmological parameters, so the differences are related to the model for the thermal pressure profile. We investigate the redshift integration limits⁷, but find they do not significantly affect the differences at $\ell \gtrsim 1000$. We present the expected mean and standard deviation of a full-sky tSZ measurement as a function of lower redshift cutoff, and find that the low- ℓ variance is substantially suppressed by raising the low- z cutoff. On the scales where the tSZ peaks, we find both the mean spectrum and the variance are only weakly affected by varying the redshift limit from $z=0.01$ to $z=0.14$. Similar results have been found when making intensity cuts on sky maps (Shaw et al., 2009).

We now present power spectra calculated directly from the simulations. In addition to projecting the full electron pressure from all particles, we also take advantage of the information from the simulation cluster catalogs. By doing this, we can employ mass, redshift, and radius cuts to explore the dependence of the full tSZ power spectrum. By pasting our global pressure profile to locations and redshifts of simulated clusters, we can also explore, without having to worry about sample variance, the effects of using our profile instead of the full simulation results.

We use the cluster catalogs described in Section 5.5.1, and remind the reader that M_{FOF} is roughly equal to M_{200} , though with large scatter.⁸ Our cluster mass function becomes incomplete below $M_{200} \sim 4 \times 10^{13} M_{\odot}$ (cf. Appendix) primarily due to our M_{FOF} cutoff in the original cluster finding of $1.4 \times 10^{13} M_{\odot}$, but partially due to the linking length merging some clusters/groups into nearby larger clusters at the 10 – 15% level (e.g., Davis et al., 1985; Bertschinger & Gelb, 1991; Cole & Lacey, 1996; Cohn & White, 2008). For these reasons we examine only cluster with $M_{500} > 4.2 \times 10^{13} M_{\odot}$ when we bin clusters in mass.

In Figure 5.6 we show the cumulative distribution function (CDF) for the tSZ power for a $CDF(M >, z <)$ at $\ell = 3000$. The CDF illustrates where the relative amount of power originates at the 25%, 50% and 75% percentile levels. Half the power at $\ell = 3000$ comes from clusters with $z > 0.6$ and half originates from clusters with mass $M_{500} < 2 \times 10^{14} M_{\odot}$. This result is in general agreement with other work (Komatsu & Seljak, 2002; Trac et al., 2011). We note that the particulars of these mass and redshift ranges are sensitive to the input modeling of the ICM. The comparatively low mass and high redshift of the clusters and groups that make up the bulk of the tSZ signal mean that they have not been as well studied as more massive and nearby objects. Thus, the tSZ angular power spectrum can provide a statistical constraint on the astrophysical processes of importance at high redshift and in low-mass clusters.

⁷For the remainder of this paper, we use a low redshift cutoff of $z = 0.07$, so that we can directly compare our analytic calculation to the simulations.

⁸For detailed work on comparing the mass definitions of M_{FOF} to M_{Δ} and the resulting halo mass catalogs from these definitions see More et al. (2011) and the references therein.

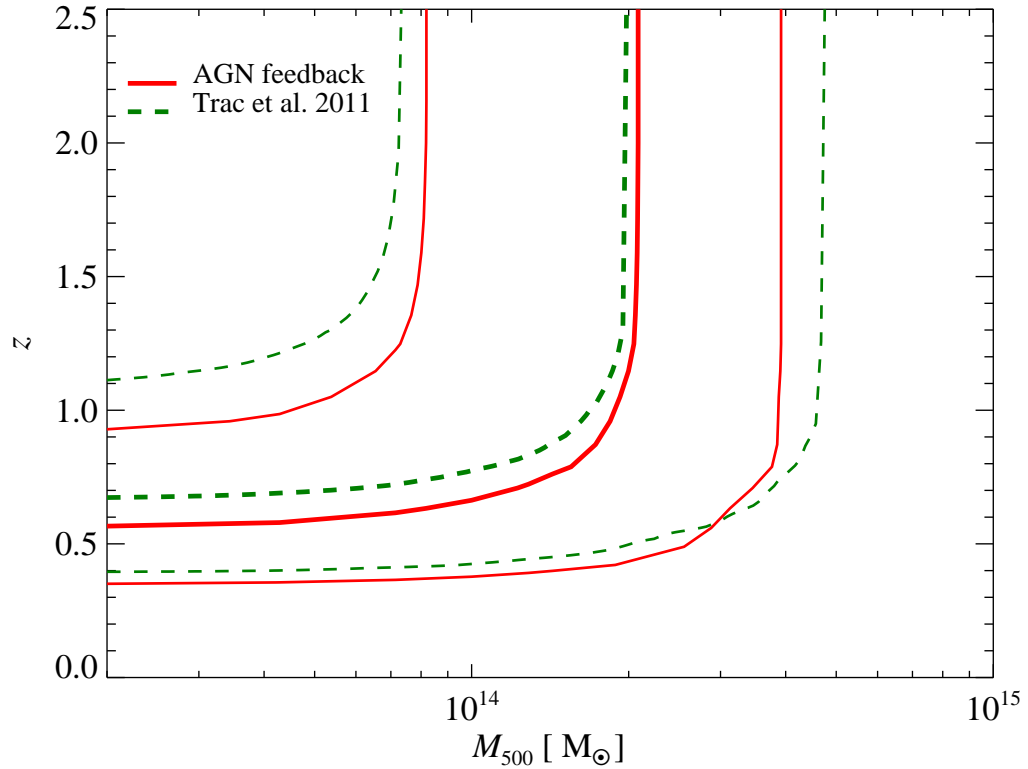


Figure 5.6: Shown is the cumulative distribution function for the thermal SZ power spectrum as a function of mass and redshift at $\ell = 3000$. The curves show the lower mass and upper redshift cutoffs that contribute [25, 50, 75]% to the tSZ power spectrum. At $\ell = 3000$, half the power of tSZ power spectrum comes from galaxy clusters with $z > 0.6$, and half comes from clusters with $M_{500} < 2 \times 10^{14} M_{\odot}$. For comparison, the dashed green lines show the semi-analytical results of Trac et al. (2011), which include enhanced non-thermal pressure support.

5.6.1 Contribution to the tSZ Power Spectrum in Cluster Mass Bins

In this subsection, we calculate the power spectrum in mass bins. This allows us to isolate the differences between the simulations, the pasted profile maps, and the analytic calculation, as functions of cluster mass, integrating in redshift between $z = 0.07$ and $z = 5$. We explore both, cumulative and differential mass bins. We consider all gas particles (or radii) within $6R_{500}$ when projecting the thermal pressure of the simulations. In Figure 5.7, we show the power spectrum broken down into cumulative (left panel) and differential (right panel) mass bins. The bottom panels show the relative differences, where $\Delta C_\ell = 100(C_{\ell, sim} - C_{\ell, i})/C_{\ell, sim}$, with $C_{\ell, sim}$ denoting the power spectra from the simulations and the $C_{\ell, i}$ are the power spectra from either the projected pasted profile maps or the analytic calculation.

The largest deviations between our analytic/pasted profile spectra and the full simulations are for the highest mass ($M_{500} \gtrsim 7 \times 10^{14} M_\odot$) clusters, particularly on small angular scales. The deviations between the pasted profiles and the simulations in this mass range arise from the increased level of substructure and asphericity in massive clusters in comparison to smaller objects due to the more recent formation epoch of large systems in a hierarchical structure formation (Wechsler et al., 2002; Zhao et al., 2009; Pfrommer et al., 2011; Battaglia et al., 2011). The high-mass difference between the fully analytic tSZ spectrum and the simulation results reflects our overabundance of high-mass clusters due to shot noise relative to the mass function used in the analytic calculation. The agreement between all three methods is excellent for masses below $7 \times 10^{14} M_\odot$ until our cluster catalog becomes incomplete at low masses. In the most massive cluster bin, the relative differences between the power spectra are $\sim 30 - 60\%$ for $\ell \sim 2000 - 9000$ (cf. Fig 5.7). For the lower mass bins the differences fluctuate between $\pm 10\%$, with the pasted profiles generally agreeing better with the full simulation results.

5.6.2 Contribution to the tSZ Power Spectrum in Redshift Bins

In this subsection we calculate the power spectrum in redshift bins and compare the results from the simulation, the pasted profile maps, and the analytical calculation to aid in understanding the differences between these approaches. In Figure 5.7, we show the power spectrum broken down into cumulative (left panel) and differential (right panel) redshift bins. Here we fix the mass range to be $M_{500} > 4.2 \times 10^{13} M_\odot$ and set the lower redshift integration bound for the cumulative spectra to be $z = 0.07$. We use the same definition for ΔC_ℓ to show the differences between power spectrum calculations. In contrast to the mass cuts, the differences between the projected simulated maps and the pasted profile maps are similar across all the redshift slices (cf. Fig. 5.8). For $\ell < 5000$, there is a $\sim 5 - 10\%$ difference between the pasted profiles and the simulations, rising to $\sim 20\%$ at $\ell = 10,000$. This results suggests that the contributions from substructure and asphericity to the power spectrum are similar across the redshift range explored, with the exception of one redshift bin $z \sim 0.4$ which contains a rare merger event. The large deviations between the analytic and simulation/profile-paste spectra in the highest redshift bin are likely due to the

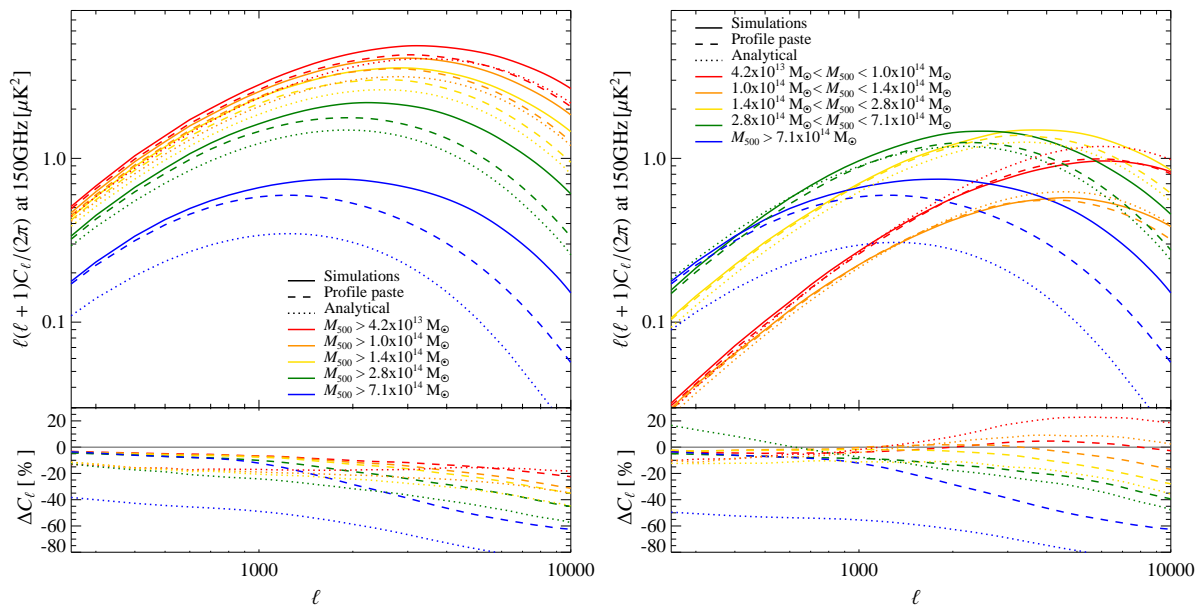


Figure 5.7: The tSZ power spectrum sorted into bins of cluster mass. Left: we show the cumulative tSZ power spectrum in mass bins ($C_{\ell,\text{tSZ}}(M_{500} > M_{\text{cut}})$) from the AGN feedback simulations, the pasted profile maps and the analytical calculation. Right: we show the differential tSZ power spectrum $C_{\ell,\text{tSZ}}(M_{\text{cut,low}} < M_{500} < M_{\text{cut,high}})$ for the same power spectrum calculations. In the bottom of both panels we show the relative difference, $\Delta C_{\ell} = 100(C_{\ell,\text{sim}} - C_{\ell,i})/C_{\ell,\text{sim}}$, where $C_{\ell,\text{sim}}$ is the power spectrum of the simulated maps and $C_{\ell,i}$ is that from the pasted profile maps and the analytical calculation. The differences between the simulations and the pasted profile maps result from the absence of substructure and asphericity in the pasted profile maps, which is larger for more massive clusters. The larger differences found between the analytical calculation and the simulations are the result of the mass catalog of the simulations having an excess of high mass clusters and deficit of lower mass cluster compared to the analytic mass function (cf. Fig. 5.11).

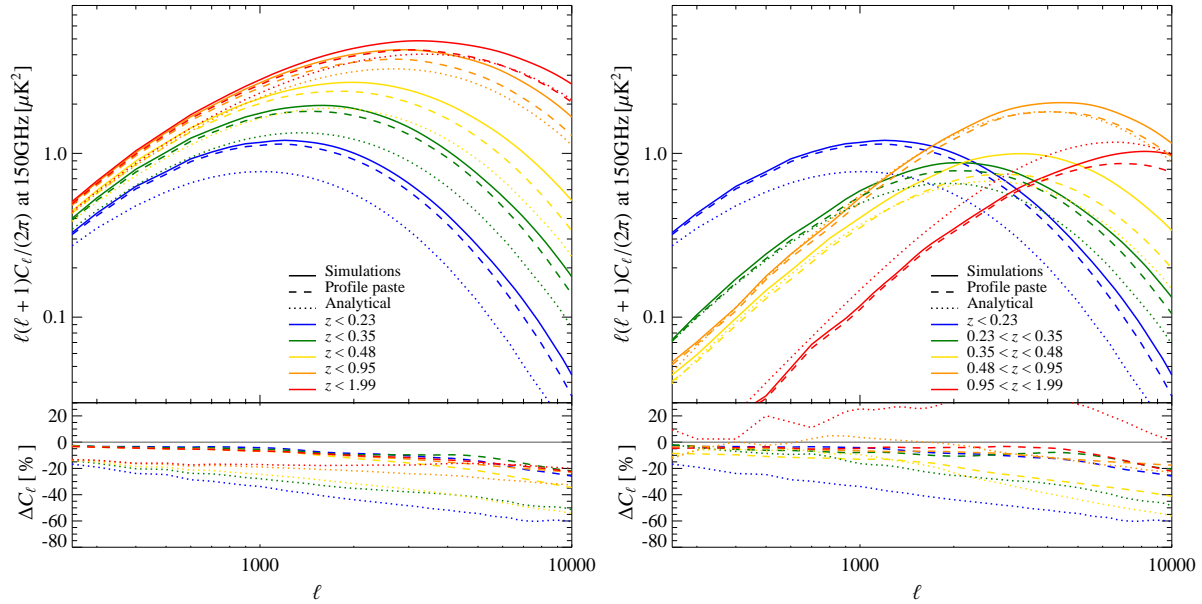


Figure 5.8: The same as Figure 5.7, however for redshift slices. Left: we show the cumulative tSZ power spectrum in redshift bins $C_{\ell,tSZ}(z < z_{\text{cut}})$ from the AGN feedback simulations, the pasted profile maps and the analytical calculation. Right: we show the differential tSZ power spectrum $C_{\ell,tSZ}(z_{\text{cut,low}} < z < z_{\text{cut,high}})$ for the same power spectrum calculations. In the bottom of both panels we show the relative difference, $\Delta C_{\ell} = 100(C_{\ell,\text{sim}} - C_{\ell,i})/C_{\ell,\text{sim}}$, where $C_{\ell,\text{sim}}$ is the power spectrum of the simulated maps and $C_{\ell,i}$ is that from the pasted-profile maps and the analytical calculation. The agreement between the pasted profile and simulation spectra is excellent below $\ell \sim 5000$ for all redshifts. On smaller scales, cluster substructure contributes similarly across all redshift bins examined.

incompleteness of the cluster catalogs at the lowest masses, which are preferentially more important at high redshift. At low redshift, we attribute the difference between the analytic and the profile-paste power spectra to the shot noise in the most massive clusters.

5.6.3 Contribution to the tSZ Power Spectrum within given Cluster Radii

In this subsection we apply radial truncations to the full simulated pressure maps, using clusters with $M_{500} > 4.2 \times 10^{13} M_{\odot}$ at $0.07 < z < 5$. The procedures for making real space radius cuts in maps or analytical calculations are not trivial, since any sharp cut in real space produces ringing in Fourier space, potentially transferring power from large to small angular scales. To reduce ringing and the potential to artificially increase the high- ℓ power spectrum, we use a Gaussian taper when truncating the pressure profile. We place radial tapers at $r = R_{500}, 2R_{500}, 3R_{500}$, and $6R_{500}$ in the maps, adopting $6R_{500}$ as the reference radial taper⁹. The form of the taper is

$$\mathcal{T}(r) = \exp \left[- \left(\frac{r - r_t}{80 \times R_{500}} \right)^2 \right] \quad (5.12)$$

for r greater than the taper radius r_t , and unity otherwise. In the bottom panel of Figure 5.9 we show the relative difference, $\Delta C_{\ell} = 100(C_{\ell,6R_{500}} - C_{\ell,i})/C_{\ell,6R_{500}}$, where $C_{\ell,6R_{500}}$ is the power spectrum from the $6R_{500}$ radial cut and $C_{\ell,i}$ are power spectra from the other radial cuts. The trend we find is that the large radii of clusters are only important for the low ℓ s, for example the contributions to the tSZ power spectrum when only integrating out to R_{500} yields $\sim 30 - 65\%$ of the total power from $\ell = 100 - 1000$, respectively. At $\ell = 3000$ only about 10% of the total tSZ power comes from beyond R_{500} . This number is consistent with previously quoted values (Sun et al., 2011). We note that there is some small residual Fourier ringing, as the tapered spectra rise above the fiducial at ℓ s of many thousand. Nevertheless, at higher ℓ , the cluster centers begin to be resolved and become the dominant contributors to the tSZ spectrum since their surface brightnesses are so much larger than any emission in the cluster outskirts.

5.7 Constraints of σ_8 from Current ACT and SPT Data

Using tSZ power spectrum and ignoring any template uncertainty, the constraints on σ_8 are competitive with other cosmological measurements. After accounting for template uncertainty, there is no statistically significant discrepancy between σ_8 determined from the tSZ power and that derived from primary CMB anisotropies, or other the measurements (Dunkley et al., 2010; Shirokoff et al., 2010). Here we use our $C_{\ell,\text{tSZ}}$ templates at the fiducial parameters $\sigma_8 = 0.8$ (and $\Omega_b h = 0.03096$) to define the shape of the tSZ power spectrum, and content ourselves with determining only the template amplitude, A_{tSZ} ,

⁹We avoid double counting gas particles when we project them into maps. If a particle lies in the overlap region between two clusters, we taper the particle with the larger of the two possible taper values, i.e. those particles with a smaller radius R/R_{500} , to avoid artificially suppressing power in the overlap region.

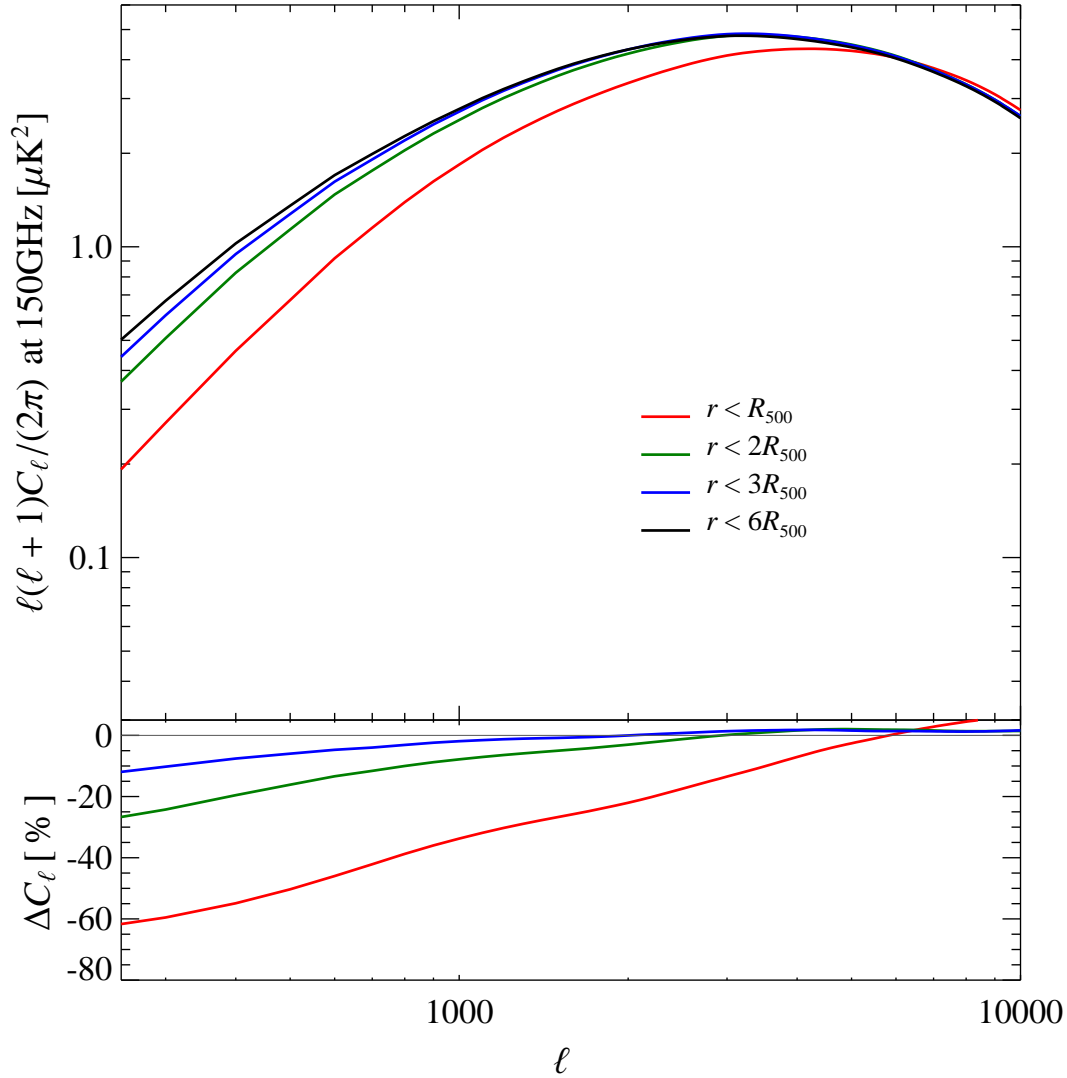


Figure 5.9: $C_{\ell,\text{tSZ}}(r < R_{\text{cut}})$ for the AGN feedback simulations. The thermal pressure distribution has been tapered as in Equation (5.12) at varying cluster-centric radii before projection. On small scales, virtually all of the power at $\ell > 2000$ comes from $r < 2R_{500}$. About 80% of the tSZ power is recovered at $\ell = 3000$ when tapering at R_{500} , though the deviations become substantially larger at smaller ℓ . These results emphasize the importance of understanding cluster pressure profiles well past R_{500} in order to do high-precision work with the tSZ power spectrum.

relative to that expected from the background cosmology (e.g., Battaglia et al., 2010; Dunkley et al., 2010). The amplitude of A_{tSZ} is proportional to a large power of σ_8 ($A_{\text{tSZ}} \propto \sigma_8^{7...9}$ Bond et al., 2002; Komatsu & Seljak, 2002; Bond et al., 2005; Trac et al., 2011). It follows that values of A_{tSZ} below unity imply that theoretical templates overestimate the SZ signal, or else points to a smaller value of σ_8 than the value derived from primary CMB anisotropies.

The probability distributions of the amplitude, A_{tSZ} , and other cosmological parameters are determined from current CMB data using a modified version of CosmoMC (Lewis & Bridle, 2002), which uses Markov-Chain Monte Carlo techniques. We include data from WMAP7 (Larson et al., 2010) and, separately, ACT (Das et al., 2011) and the dusty star-forming galaxy subtracted data from SPT (Shirokoff et al., 2010). We fit for 6 basic cosmological parameters with the assumption of spatial flatness ($\Omega_{\text{b}}h^2$, $\Omega_{\text{DM}}h^2$, n_{s} , the primordial scalar power spectrum amplitude A_{s} , the Compton depth to re-ionization τ , and the angular parameter characterizing the sound crossing distance at recombination θ) with the assumption of spatial flatness. We also include a white noise template for point sources $C_{\ell,\text{src}}$ with amplitude A_{src} . The primary difference between our analysis and the analysis by SPT Shirokoff et al. (2010) is that we marginalize over A_{src} , allowing for arbitrary (positive) values, and ignore the spatial clustering component of point sources. We assume a perfect degeneracy $C_{\ell,\text{kSZ}} \propto C_{\ell,\text{tSZ}}$ for the kinetic SZ (kSZ) component, so we only need the relative amplitude of $A_{\text{kSZ}}/A_{\text{tSZ}}$ at a given frequency and use the kSZ amplitudes from Battaglia et al. (2010), where the ratio of kSZ to tSZ at $\ell = 3000$ and 150 GHz is 0.44. As mentioned in Battaglia et al. (2010), these simulations do not fully sample the long wavelength tail of the velocity power spectrum and do not include any contributions from patchy re-ionization (Iliev et al., 2007, 2008). Hence this kSZ power spectrum template is a lower limit to the total power.

In Figure 5.10 we illustrate the 68% allowed confidence intervals for the tSZ power spectrum, given the shape of our AGN feedback template, our predicted tSZ to kSZ power spectrum ratio, and the current data from ACT and SPT. We scale our template using the best-fit σ_8 value from Keisler et al. (2011) of 0.814 and scale our template (which was calculated at $\sigma_8 = 0.8$) by $(0.814/0.8)^8$, about 15%. We find that our template is within the 68% confidence interval region for both ACT and SPT, after correcting for our predicted kSZ to tSZ power spectrum ratio of 0.44. Note that the semi-analytic and analytic models without substructure have lower tSZ amplitudes, which would result in higher values of A_{tSZ} and higher σ_8 .

5.8 Discussion and Conclusion

In this work, we found a global fitting function for galaxy cluster thermal pressure profiles using the simulations presented in Battaglia et al. (2010). We find that this global fit matches the mean pressure profiles across mass and redshift generally to an accuracy of better than 10%. We have used the profile to

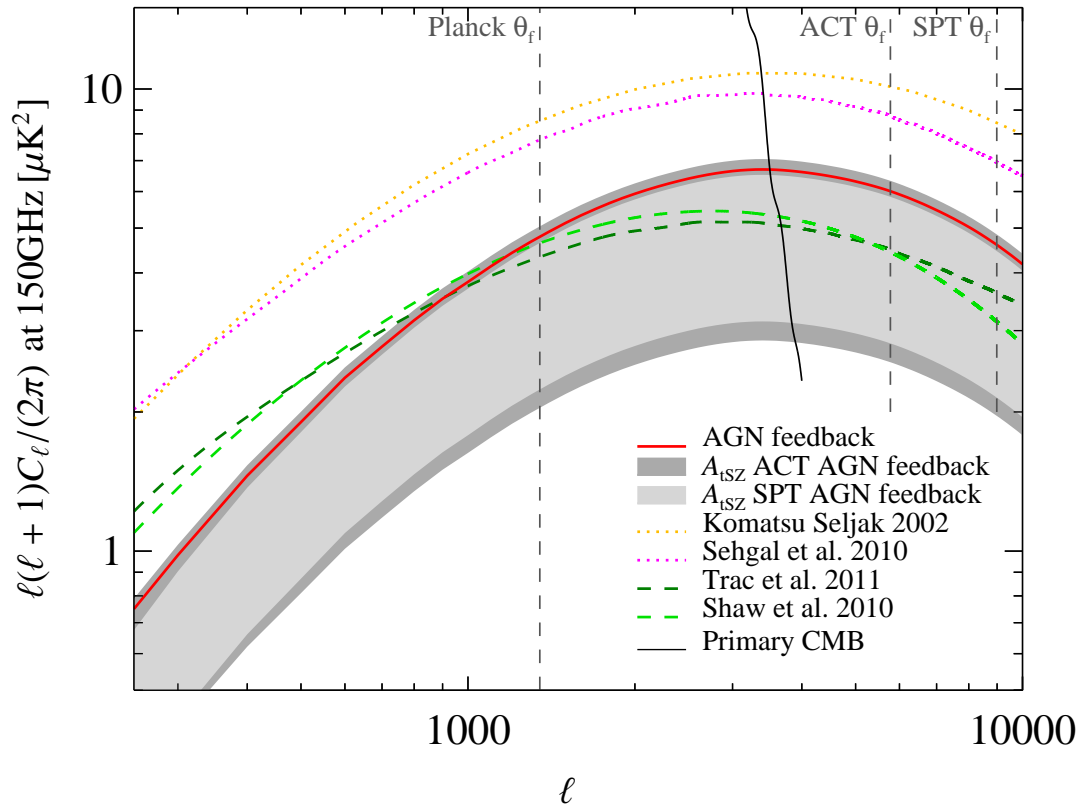


Figure 5.10: Our 150 GHz tSZ power spectrum of our AGN feedback model, rescaled to the Keisler et al. (2011) best-fit σ_8 value of 0.814 (red line) is contrasted with the bands indicating the 68% range in tSZ amplitude from ACT (Das et al., 2011, dark grey) and SPT (Shirokoff et al., 2010, light grey). For comparison, we plot several other models for the tSZ power spectrum, also shifted to the fiducial $\sigma_8 = 0.814$. These are Sehgal et al. (2010) (pink dotted line), Trac et al. (2011) (dark green dashed line), Komatsu & Seljak (2002) (orange dotted line), and Shaw et al. (2010) (light green dashed line). We include the estimated beam FWHM for ACT, SPT, and Planck.

Table 5.2: Cosmological constraints on A_{tSZ} and σ_8 from ACT and SPT using the AGN feedback tSZ power spectrum template

Data	A_{tSZ}	σ_8
ACT (Das et al., 2011)	0.85 ± 0.36	$0.784^{+0.036}_{-0.053}$
SPT (Shirokoff et al., 2010)	0.69 ± 0.29	$0.764^{+0.035}_{-0.051}$

reconstruct the thermal Sunyaev-Zel’dovich power spectrum using both fully analytic and semi-analytic pasted profiles onto cluster position in the simulations, and find we recover the tSZ power spectrum to $\sim 15\%$ at $\ell = 3000$ (cf. Figure 5.5). Other analytic and semi-analytic models for the tSZ effect commonly assume constant adiabatic indices when solving the equation of hydrostatic equilibrium. The assumption is not borne out in our simulations, where both the thermal adiabatic index and the effective pressure adiabatic index (which includes non-thermal support from bulk flows in clusters) break substantially in cluster outskirts (cf. Figure 5.6). Using both the simulations and the global pressure profile, we examined the contributions to the tSZ spectrum as functions of cluster mass, redshift, and truncation radius. We found that the contributions from substructure and asphericity are most important for the highest mass clusters ($M_{500} \gtrsim 7 \times 10^{14} M_{\odot}$), but remain significant at the 10 – 15% level across all mass bins. We find that half the power of the tSZ power spectrum at $\ell = 3000$ is contributed by clusters with $z > 0.6$ and half the power originates from clusters with $M_{500} < 2 \times 10^{14} M_{\odot}$.

We have compared our tSZ prediction to results from the Atacama Cosmology Telescope and the South Pole Telescope. We found that there is no statistically significant difference between our model and the data, after accounting for a simplistic correction from the kinetic SZ effect. More complete component separation should be possible with better frequency coverage (Millea et al., 2011). We note that our analysis differs from that in Shirokoff et al. (2010) in that we make no prior assumption about the amplitude of the point source power spectrum, other than that it is non-negative.

The pressure profile presented in this work is derived from the *mean* electron pressure in our simulations and we defer the derivation of a mean profile designed to include the effects of substructure and asphericity in the power spectrum to a future work (Battaglia et al., in prep). This profile will not be expected to match individual cluster observations, but we hope will allow analytic calculations of the tSZ power spectrum to an accuracy of significantly better than 10%. With future data sets, such as those expected from Planck, ACTpol, and SPTpol, it may be possible to constrain not just the amplitude but the shape of the tSZ spectrum. In this case, analytic calculations may be usable to constrain not just cosmology but the important astrophysical processes in clusters with the tSZ effect. Doing so through the power spectrum has the advantage that it is sensitive to lower mass and higher redshift clusters as well as cluster outskirts in ways that are complementary to other data sets.

5.9 Appendix: Comparing the Cluster Mass Catalog to the Mass function

In this appendix we compare the mass function from our simulations with that of Tinker et al. (2008). Our cluster mass catalogs were made with spherical overdensity mass with respect to the critical density and the mass function is with respect to the mean matter density. So, we converted the M_{200} from the simulations to $M_{200,m}$ assuming the mass profile is dominated by dark matter and use the concentration-mass relations from Duffy et al. (2008). We show in Figure 5.11 that there is a clear deficit of low mass clusters due to the chosen linking length of 0.2 in our FOF finder. At this length, it is well known that neighboring clusters are sometimes artificially merged together (e.g., Davis et al., 1985). We also instituted a firm lower limit mass cutoff in the initial FOF catalogs of $M_{\text{FOF}} > 1.4 \times 10^{13} M_{\odot}$, and so our mass function is also expected to be incomplete near that mass.

There is a clear excess of high-mass clusters in our simulations, but it is consistent with shot noise (we only have 6 clusters with $M_{500} > 7.1 \times 10^{14} M_{\odot}$). We now estimate the excess power in our full simulation power spectrum due to this upwards fluctuation in the highest mass bin. Where the cluster catalogs are complete, we expect that over an enormous number of simulations, the paste profile and analytic calculation of the tSZ power spectrum would converge, and indeed see the agreement is excellent between the two in the right panel of Figure 5.7 for all but the lowest (due to catalog incompleteness) and highest (due to shot noise) mass bins. We therefore adopt the ratio of the the pasted profile spectrum to the analytic spectrum as a quantitative estimate of the over-representation of high mass clusters in our finite number of realizations. At $\ell = 3000$ this value is 2.0, though as can be seen in Figure 5.7 the specific value is insensitive to the reference ℓ . Since the high-mass contribution to the tSZ spectrum from the full simulation projections is $0.67 \mu\text{K}^2$ at $\ell = 3000$, in the limit of an infinite number of simulations, we would expect the average contribution from clusters with $M_{500} > 7.1 \times 10^{14} M_{\odot}$ to be $0.34 \mu\text{K}^2$ lower. The total power spectrum at $\ell = 3000$ is $5.78 \mu\text{K}^2$, so this shot noise correction amounts to just less than a 6% shift in the total power spectrum.

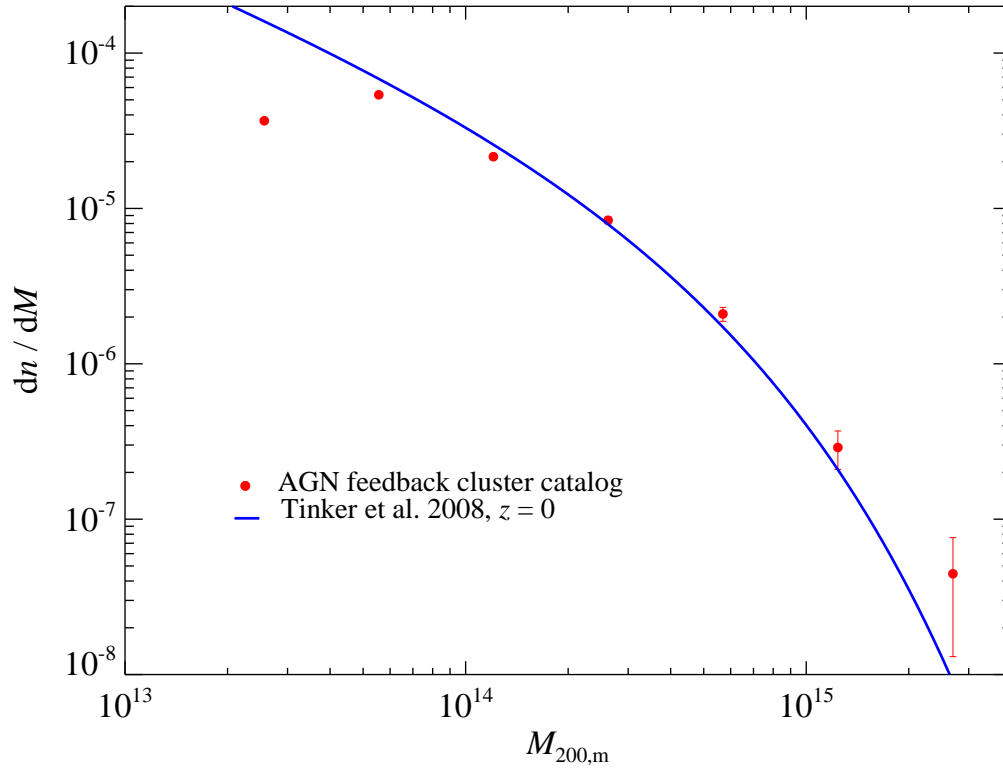


Figure 5.11: We compare the mass function, dn/dM , for the cluster catalog from AGN feedback simulations to the mass function from Tinker et al. (2008). The differences at high masses indicates that in the 10 independent simulations we happen to have more high-mass clusters than is expected on average (though with only 6 with $M_{500} > 7.1 \times 10^{14} M_{\text{sun}}$ this is consistent with shot noise). At low masses, our catalog is incomplete due to our FOF halo finding (see text).

Chapter 6

Conclusions and Outlook

Galaxy clusters have been and will remain among the most interesting of astronomical objects. The growing appreciation of their complexity continues to foster interest and excitement as astrophysical laboratories and cosmological probes in the cluster community.

The detailed conclusions of this thesis are given at the ends of, chapters 2, 3, 4 and 5, and will only be briefly summarized here.

- Using radio relics as observational probes we can study the magnetic fields in the galaxy clusters through relic luminosity functions and rotation measure statistics.
- We can determine the Mach numbers of structure formation shocks from the spectral index of the radio relics.
- A coarse grained stochastic model of AGN feedback in galaxy clusters affects the thermal pressure profiles of galaxy clusters and the Sunyaev-Zel'dovich angular power spectrum.
- The SZ scaling relations are affected at the 15% level by non-thermal pressure support in clusters and by the anisotropic shape of the ICM.
- A constrained fit to the thermal pressure profile provided as a function of cluster mass, redshift and radius, is accurate to the level of precision required by current high precision observations.
- We quantified the contribution of sub-structure and asphericity to the SZ angular power spectrum by comparing three different methods for calculating the power spectrum.
- We constrained the density power spectrum amplitude, σ_8 , from the latest ACT and SPT measurements of tSZ angular power spectrum.

Understanding the ICM at the level of detail, in this work and even more so, will be extremely important to interpret results from upcoming cluster missions, such as the imminent X-ray satellite mission, E-Rosita, ACTpol, SPTpol, Planck, and the optical Dark Energy Survey.

6.1 Future Work

We are already working on several avenues of clusters astrophysics and cosmology that flow naturally from this thesis. We plan to explore the vast parameter space of energetic feedback possibilities, including momentum injection and relativistic energy injection, as well as further exploration of the thermal energy injection like the type used in this thesis. The crucial question to answer is how do these particular forms of feedback impact the thermal SZ power spectrum and other cluster observables. An urgent project driven by data already available or coming soon from ACT, SPT, and Planck, is to develop a fast analytic calculation that properly accounts for sub-structure, bulk motions, and asphericity. One of the subjects related to substructure is density and pressure clumping. We have shown in chapter 5 that the ICM is decidedly non-uniform. The clumping must be included to interpret observations correctly (Simionescu et al., 2011; Nagai & Lau, 2011). We are in the process of characterizing the sizes of these density and pressure clumps, and will incorporate these results into semi-analytical models of the ICM. Another project is to study the growth of clusters from their proto-cluster precursors, focusing on the build up of entropy in their formation, using high resolution simulations of individual clusters. How is the information stored in the proto-cluster state encoded into its final cluster configuration? This is hardly an exhaustive list of projects, only those on the front burner which should reach fruition within the near future. There is still so much to explore beyond these projects and so many questions to be addressed and answered in the tight interplay between theory and observations that is cluster science. And there is an entire Universe of gravitationally collapsed clustered objects of lower mass at higher redshifts to explore with the sort of hydrodynamical/N-body simulations used here.

Bibliography

Abell, G. O. 1958, *ApJS*, 3, 211

Afshordi, N., Lin, Y., Nagai, D., & Sanderson, A. J. R. 2007, *MNRAS*, 378, 293

Allen, S. W., Rapetti, D. A., Schmidt, R. W., Ebeling, H., Morris, R. G., & Fabian, A. C. 2008, *MNRAS*, 383, 879

Allgood, B., Flores, R. A., Primack, J. R., Kravtsov, A. V., Wechsler, R. H., Faltenbacher, A., & Bullock, J. S. 2006, *MNRAS*, 367, 1781

Ananthakrishnan, S. 1995, *Journal of Astrophysics and Astronomy Supplement*, 16, 427

Andersson, K., Benson, B. A., Ade, P. A. R., Aird, K. A., Armstrong, B., Bautz, M., Bleem, L. E., Brodwin, M., Carlstrom, J. E., Chang, C. L., Crawford, T. M., Crites, A. T., de Haan, T., Desai, S., Dobbs, M. A., Dudley, J. P., Foley, R. J., Forman, W. R., Garmire, G., George, E. M., Gladders, M. D., Halverson, N. W., High, F. W., Holder, G. P., Holzzapfel, W. L., Hrubes, J. D., Jones, C., Joy, M., Keisler, R., Knox, L., Lee, A. T., Leitch, E. M., Lueker, M., Marrone, D. P., McMahon, J. J., Mehl, J., Meyer, S. S., Mohr, J. J., Montroy, T. E., Murray, S. S., Padin, S., Plagge, T., Pryke, C., Reichardt, C. L., Rest, A., Ruel, J., Ruhl, J. E., Schaffer, K. K., Shaw, L., Shirokoff, E., Song, J., Spieler, H. G., Stalder, B., Staniszewski, Z., Stark, A. A., Stubbs, C. W., Vanderlinde, K., Vieira, J. D., Vikhlinin, A., Williamson, R., Yang, Y., & Zahn, O. 2010, *ArXiv:1006.3068*

Arnaud, M., Pratt, G. W., Piffaretti, R., Böhringer, H., Croston, J. H., & Pointecouteau, E. 2010, *A&A*, 517, A92+

Bagchi, J., Durret, F., Neto, G. B. L., & Paul, S. 2006, *Science*, 314, 791

Balsara, D. S. 1998, *ApJS*, 116, 133

Bardeen, J. M., Bond, J. R., Kaiser, N., & Szalay, A. S. 1986, *ApJ*, 304, 15

Battaglia, N., Bond, J. R., Pfrommer, C., & Sievers, J. L. 2011, in prep.

Battaglia, N., Bond, J. R., Pfrommer, C., Sievers, J. L., & Sijacki, D. 2010, *ApJ*, 725, 91

- Beck, R. 2001, *Space Science Reviews*, 99, 243
- Beck, R., Brandenburg, A., Moss, D., Shukurov, A., & Sokoloff, D. 1996, *ARA&A*, 34, 155
- Benson, B. A., Church, S. E., Ade, P. A. R., Bock, J. J., Ganga, K. M., Henson, C. N., & Thompson, K. L. 2004, *ApJ*, 617, 829
- Bertschinger, E. & Gelb, J. M. 1991, *Computers in Physics*, 5, 164
- Bhattacharya, S., Di Matteo, T., & Kosowsky, A. 2008, *MNRAS*, 389, 34
- Bialek, J. J., Evrard, A. E., & Mohr, J. J. 2001, *ApJ*, 555, 597
- Binney, J. & Tremaine, S. 2008, *Galactic Dynamics: Second Edition*, ed. Binney, J. & Tremaine, S. (Princeton University Press)
- Birkinshaw, M. 1999, *Phys. Rept.*, 310, 97
- Blandford, R. & Eichler, D. 1987, *Phys. Rept.*, 154, 1
- Bode, P., Ostriker, J. P., & Vikhlinin, A. 2009, *ApJ*, 700, 989
- Bode, P., Ostriker, J. P., Weller, J., & Shaw, L. 2007, *ApJ*, 663, 139
- Bonaldi, A., Tormen, G., Dolag, K., & Moscardini, L. 2007, *MNRAS*, 378, 1248
- Bonamente, M., Joy, M., LaRoque, S. J., Carlstrom, J. E., Nagai, D., & Marrone, D. P. 2008, *ApJ*, 675, 106
- Bond, J. R. Probing cosmic density fluctuation spectra, ed. Rubin, V. C. & Coyne, G. V., 419–435
- Bond, J. R. 1996, in *Cosmology and Large Scale Structure*, ed. R. Schaeffer, J. Silk, M. Spiro, & J. Zinn-Justin, 469–+
- Bond, J. R., Cole, S., Efstathiou, G., & Kaiser, N. 1991, *ApJ*, 379, 440
- Bond, J. R., Contaldi, C. R., Pen, U., Pogosyan, D., Prunet, S., Ruetalo, M. I., Wadsley, J. W., Zhang, P., Mason, B. S., Myers, S. T., Pearson, T. J., Readhead, A. C. S., Sievers, J. L., & Udomprasert, P. S. 2005, *ApJ*, 626, 12
- Bond, J. R., Kofman, L., & Pogosyan, D. 1996, *Nature*, 380, 603
- Bond, J. R. & Myers, S. T. 1996a, *ApJS*, 103, 1
- . 1996b, *ApJS*, 103, 41

—. 1996c, *ApJS*, 103, 63

Bond, J. R., Ruetalo, M. I., Wadsley, J. W., & Gladders, M. D. 2002, in *Astronomical Society of the Pacific Conference Series*, Vol. 257, *AMiBA 2001: High-Z Clusters, Missing Baryons, and CMB Polarization*, ed. L.-W. Chen, C.-P. Ma, K.-W. Ng, & U.-L. Pen, 15

Bondi, H. & Hoyle, F. 1944, *MNRAS*, 104, 273

Booth, C. M. & Schaye, J. 2009, *MNRAS*, 398, 53

Borgani, S. & Kravtsov, A. 2009, *ArXiv:0906.4370*

Bridle, A. H. & Fomalont, E. B. 1976, *A&A*, 52, 107

Bridle, A. H., Fomalont, E. B., Miley, G. K., & Valentijn, E. A. 1979, *A&A*, 80, 201

Bryan, G. L., Cen, R., Norman, M. L., Ostriker, J. P., & Stone, J. M. 1994, *ApJ*, 428, 405

Bryan, G. L. & Norman, M. L. 1998, *ApJ*, 495, 80

Burns, J. O., Skillman, S. W., & O'Shea, B. W. 2010, *ApJ*, 721, 1105

Carilli, C. L. & Taylor, G. B. 2002, *ARA&A*, 40, 319

Carlstrom, J. E., Holder, G. P., & Reese, E. D. 2002, *ARA&A*, 40, 643

Cavagnolo, K. W., Donahue, M., Voit, G. M., & Sun, M. 2009, *ApJS*, 182, 12

Cavaliere, A. & Fusco-Femiano, R. 1978, *A&A*, 70, 677

Cen, R. & Ostriker, J. P. 1999, *ApJ*, 514, 1

Chatterjee, S., Di Matteo, T., Kosowsky, A., & Pelupessy, I. 2008, *MNRAS*, 390, 535

Chaudhuri, A. & Majumdar, S. 2011, *ApJ*, 728, L41+

Churazov, E., Brüggén, M., Kaiser, C. R., Böhringer, H., & Forman, W. 2001, *ApJ*, 554, 261

Clarke, T. E. & Enßlin, T. 2006, *Astronomische Nachrichten*, 327, 553

Cohn, J. D. & White, M. 2008, *MNRAS*, 385, 2025

Cole, S. & Kaiser, N. 1988, *MNRAS*, 233, 637

Cole, S. & Lacey, C. 1996, *MNRAS*, 281, 716

Cooray, A. 2001, *Phys.Rev.D*, 64, 063514

- Cuesta, A. J., Prada, F., Klypin, A., & Moles, M. 2008, MNRAS, 389, 385
- da Silva, A. C., Barbosa, D., Liddle, A. R., & Thomas, P. A. 2000, MNRAS, 317, 37
- da Silva, A. C., Kay, S. T., Liddle, A. R., & Thomas, P. A. 2004, MNRAS, 348, 1401
- Dalal, N., Doré, O., Huterer, D., & Shirokov, A. 2008, Phys.Rev.D, 77, 123514
- Danforth, C. W. & Shull, J. M. 2005, ApJ, 624, 555
- Das, S., Marriage, T. A., Ade, P. A. R., Aguirre, P., Amiri, M., Appel, J. W., Barrientos, L. F., Battistelli, E. S., Bond, J. R., Brown, B., Burger, B., Chervenak, J., Devlin, M. J., Dicker, S. R., Bertrand Doriese, W., Dunkley, J., Dünner, R., Essinger-Hileman, T., Fisher, R. P., Fowler, J. W., Hajian, A., Halpern, M., Hasselfield, M., Hernández-Monteagudo, C., Hilton, G. C., Hilton, M., Hincks, A. D., Hlozek, R., Huffenberger, K. M., Hughes, D. H., Hughes, J. P., Infante, L., Irwin, K. D., Baptiste Juin, J., Kaul, M., Klein, J., Kosowsky, A., Lau, J. M., Limon, M., Lin, Y.-T., Lupton, R. H., Marsden, D., Martocci, K., Mauskopf, P., Menanteau, F., Moodley, K., Moseley, H., Netterfield, C. B., Niemack, M. D., Nolta, M. R., Page, L. A., Parker, L., Partridge, B., Reid, B., Sehgal, N., Sherwin, B. D., Sievers, J., Spergel, D. N., Staggs, S. T., Swetz, D. S., Switzer, E. R., Thornton, R., Trac, H., Tucker, C., Warne, R., Wollack, E., & Zhao, Y. 2011, ApJ, 729, 62
- Davé, R., Cen, R., Ostriker, J. P., Bryan, G. L., Hernquist, L., Katz, N., Weinberg, D. H., Norman, M. L., & O'Shea, B. 2001, ApJ, 552, 473
- Davis, M., Efstathiou, G., Frenk, C. S., & White, S. D. M. 1985, ApJ, 292, 371
- Dawson, K. S., Holzapfel, W. L., Carlstrom, J. E., Joy, M., & LaRoque, S. J. 2006, ApJ, 647, 13
- Dolag, K., Bartelmann, M., & Lesch, H. 1999, A&A, 348, 351
- Dolag, K., Grasso, D., Springel, V., & Tkachev, I. 2005, Journal of Cosmology and Astro-Particle Physics, 1, 9
- Drury, L. O. 1983, Reports of Progress in Physics, 46, 973
- Dubinski, J. & Carlberg, R. G. 1991, ApJ, 378, 496
- Dubois, Y. & Teyssier, R. 2008, A&A, 482, L13
- Duffy, A. R., Schaye, J., Kay, S. T., & Dalla Vecchia, C. 2008, MNRAS, 390, L64
- Dunkley, J., Hlozek, R., Sievers, J., Acquaviva, V., Ade, P. A. R., Aguirre, P., Amiri, M., Appel, J. W., Barrientos, L. F., Battistelli, E. S., Bond, J. R., Brown, B., Burger, B., Chervenak, J., Das, S., Devlin, M. J., Dicker, S. R., Bertrand Doriese, W., Dunner, R., Essinger-Hileman, T., Fisher, R. P., Fowler,

- J. W., Hajian, A., Halpern, M., Hasselfield, M., Hernandez-Monteagudo, C., Hilton, G. C., Hilton, M., Hincks, A. D., Huffenberger, K. M., Hughes, D. H., Hughes, J. P., Infante, L., Irwin, K. D., Juin, J. B., Kaul, M., Klein, J., Kosowsky, A., Lau, J. M., Limon, M., Lin, Y., Lupton, R. H., Marriage, T. A., Marsden, D., Mauskopf, P., Menanteau, F., Moodley, K., Moseley, H., Netterfield, C. B., Niemack, M. D., Nolte, M. R., Page, L. A., Parker, L., Partridge, B., Reid, B., Sehgal, N., Sherwin, B., Spergel, D. N., Staggs, S. T., Swetz, D. S., Switzer, E. R., Thornton, R., Trac, H., Tucker, C., Warne, R., Wollack, E., & Zhao, Y. 2010, ArXiv:1009.0866
- Efstathiou, G. & Migliaccio, M. 2011, ArXiv e-prints
- Eisenstein, D. J. & Hu, W. 1998, ApJ, 496, 605
- Ellison, D. C., Jones, F. C., & Eichler, D. 1981, Journal of Geophysics Zeitschrift Geophysik, 50, 110
- Enßlin, T. A., Biermann, P. L., Klein, U., & Kohle, S. 1998, A&A, 332, 395
- Enßlin, T. A. & Gopal-Krishna. 2001, A&A, 366, 26
- Enßlin, T. A., Pfrommer, C., Springel, V., & Jubelgas, M. 2007, A&A, 473, 41
- Enßlin, T. A., Simon, P., Biermann, P. L., Klein, U., Kohle, S., Kronberg, P. P., & Mack, K.-H. 2001, ApJ, 549, L39
- Enßlin, T. A. & Vogt, C. 2003, A&A, 401, 835
- Evrard, A. E. 1988, MNRAS, 235, 911
- . 1990, ApJ, 363, 349
- Evrard, A. E., MacFarland, T. J., Couchman, H. M. P., Colberg, J. M., Yoshida, N., White, S. D. M., Jenkins, A., Frenk, C. S., Pearce, F. R., Peacock, J. A., & Thomas, P. A. 2002, ApJ, 573, 7
- Evrard, A. E., Metzler, C. A., & Navarro, J. F. 1996, ApJ, 469, 494
- Fabian, A. C. 1994, ARA&A, 32, 277
- Fabian, A. C., Sanders, J. S., Allen, S. W., Crawford, C. S., Iwasawa, K., Johnstone, R. M., Schmidt, R. W., & Taylor, G. B. 2003, MNRAS, 344, L43
- Felten, J. E., Gould, R. J., Stein, W. A., & Woolf, N. J. 1966, ApJ, 146, 955
- Feretti, L., Burigana, C., & Enßlin, T. A. 2004, New Astronomy Review, 48, 1137
- Ferrari, C., Govoni, F., Schindler, S., Bykov, A. M., & Rephaeli, Y. 2008, Space Science Reviews, 134, 93

- Fixsen, D. J., Cheng, E. S., Gales, J. M., Mather, J. C., Shafer, R. A., & Wright, E. L. 1996, *ApJ*, 473, 576
- Fowler, J. W., Acquaviva, V., Ade, P. A. R., Aguirre, P., Amiri, M., Appel, J. W., Barrientos, L. F., Battistelli, E. S., Bond, J. R., Brown, B., Burger, B., Chervenak, J., Das, S., Devlin, M. J., Dicker, S. R., Doriese, W. B., Dunkley, J., Dünner, R., Essinger-Hileman, T., Fisher, R. P., Hajian, A., Halpern, M., Hasselfield, M., Hernández-Monteagudo, C., Hilton, G. C., Hilton, M., Hincks, A. D., Hlozek, R., Huffenberger, K. M., Hughes, D. H., Hughes, J. P., Infante, L., Irwin, K. D., Jimenez, R., Juin, J. B., Kaul, M., Klein, J., Kosowsky, A., Lau, J. M., Limon, M., Lin, Y., Lupton, R. H., Marriage, T. A., Marsden, D., Martocci, K., Maukopf, P., Menanteau, F., Moodley, K., Moseley, H., Netterfield, C. B., Niemack, M. D., Nolta, M. R., Page, L. A., Parker, L., Partridge, B., Quintana, H., Reid, B., Sehgal, N., Sievers, J., Spergel, D. N., Staggs, S. T., Swetz, D. S., Switzer, E. R., Thornton, R., Trac, H., Tucker, C., Verde, L., Warne, R., Wilson, G., Wollack, E., & Zhao, Y. 2010, *ApJ*, 722, 1148
- Frenk, C. S., White, S. D. M., Bode, P., Bond, J. R., Bryan, G. L., Cen, R., Couchman, H. M. P., Evrard, A. E., Gnedin, N., Jenkins, A., Khokhlov, A. M., Klypin, A., Navarro, J. F., Norman, M. L., Ostriker, J. P., Owen, J. M., Pearce, F. R., Pen, U.-L., Steinmetz, M., Thomas, P. A., Villumsen, J. V., Wadsley, J. W., Warren, M. S., Xu, G., & Yepes, G. 1999, *ApJ*, 525, 554
- Friedman, R. B., Ade, P., Bock, J., Bowden, M., Brown, M. L., Cahill, G., Castro, P. G., Church, S., Culverhouse, T., Ganga, K., Gear, W. K., Gupta, S., Hinderks, J., Kovac, J., Lange, A. E., Leitch, E., Melhuish, S. J., Memari, Y., Murphy, J. A., Orlando, A., O'Sullivan, C., Piccirillo, L., Pryke, C., Rajguru, N., Rusholme, B., Schwarz, R., Taylor, A. N., Thompson, K. L., Turner, A. H., Wu, E. Y. S., Zemcov, M., & QUaD collaboration. 2009, *ApJ*, 700, L187
- Fukugita, M. 2004, in *IAU Symposium*, Vol. 220, *Dark Matter in Galaxies*, ed. S. Ryder, D. Pisano, M. Walker, & K. Freeman, 227
- Furlanetto, S. R. & Loeb, A. 2004, *ApJ*, 611, 642
- Gardner, F. F. & Whiteoak, J. B. 1966, *ARA&A*, 4, 245
- Geller, M. J. & Huchra, J. P. 1983, *ApJS*, 52, 61
- Giacintucci, S., Venturi, T., Macario, G., Dallacasa, D., Brunetti, G., Markevitch, M., Cassano, R., Bardelli, S., & Athreya, R. 2008, *A&A*, 486, 347
- Gladders, M. D. & Yee, H. K. C. 2000, *AJ*, 120, 2148
- Gladders, M. D., Yee, H. K. C., Majumdar, S., Barrientos, L. F., Hoekstra, H., Hall, P. B., & Infante, L. 2007, *ApJ*, 655, 128

- Goldstein, J. H., Ade, P. A. R., Bock, J. J., Bond, J. R., Cantalupo, C., Contaldi, C. R., Daub, M. D., Holzappel, W. L., Kuo, C., Lange, A. E., Lueker, M., Newcomb, M., Peterson, J. B., Pogosyan, D., Ruhl, J. E., Runyan, M. C., & Torbet, E. 2003, *ApJ*, 599, 773
- Gonzalez, A. H., Zaritsky, D., & Zabludoff, A. I. 2007, *ApJ*, 666, 147
- Gottlöber, S., Klypin, A., & Kravtsov, A. V. 2001, *ApJ*, 546, 223
- Gottlöber, S. & Yepes, G. 2007, *ApJ*, 664, 117
- Govoni, F., Murgia, M., Feretti, L., Giovannini, G., Dolag, K., & Taylor, G. B. 2006, *A&A*, 460, 425
- Grasso, D. & Rubinstein, H. R. 2001, *Phys. Rept.*, 348, 163
- Guidetti, D., Murgia, M., Govoni, F., Parma, P., Gregorini, L., de Ruiter, H. R., Cameron, R. A., & Fanti, R. 2008, *A&A*, 483, 699
- Gursky, H., Kellogg, E., Murray, S., Leong, C., Tananbaum, H., & Giacconi, R. 1971, *ApJ*, 167, L81+
- Haardt, F. & Madau, P. 1996, *ApJ*, 461, 20
- Heckman, T. M. 2002, in *Astronomical Society of the Pacific Conference Series*, Vol. 254, *Extragalactic Gas at Low Redshift*, ed. J. S. Mulchaey & J. T. Stocke, 292–+
- Hellsten, U., Gnedin, N. Y., & Miralda-Escudé, J. 1998, *ApJ*, 509, 56
- Hernquist, L. & Springel, V. 2003, *MNRAS*, 341, 1253
- Holder, G. P. & Carlstrom, J. E. 2001, *ApJ*, 558, 515
- Holder, G. P., McCarthy, I. G., & Babul, A. 2007, *MNRAS*, 382, 1697
- Hubble, E. P. 1926, *ApJ*, 64, 321
- Huchra, J. P. & Geller, M. J. 1982, *ApJ*, 257, 423
- Iapichino, L. & Niemeyer, J. C. 2008, *MNRAS*, 388, 1089
- Iliev, I. T., Mellema, G., Pen, U., Bond, J. R., & Shapiro, P. R. 2008, *MNRAS*, 384, 863
- Iliev, I. T., Pen, U., Bond, J. R., Mellema, G., & Shapiro, P. R. 2007, *ApJ*, 660, 933
- Jenkins, A., Frenk, C. S., White, S. D. M., Colberg, J. M., Cole, S., Evrard, A. E., Couchman, H. M. P., & Yoshida, N. 2001, *MNRAS*, 321, 372
- Jing, Y. P. & Suto, Y. 2002, *ApJ*, 574, 538

- Jubelgas, M., Springel, V., Enßlin, T., & Pfrommer, C. 2008, *A&A*, 481, 33
- Kaiser, N. 1986, *MNRAS*, 222, 323
- . 1992, *ApJ*, 388, 272
- Kang, H., Cen, R., Ostriker, J. P., & Ryu, D. 1994, *ApJ*, 428, 1
- Kang, H., Ryu, D., Cen, R., & Song, D. 2005, *ApJ*, 620, 21
- Kassim, N. E., Polisensky, E. J., Clarke, T. E., Hicks, B. C., Crane, P. C., Stewart, K. P., Ray, P. S., Weiler, K. W., Rickard, L. J., Lazio, T. J. W., Lane, W. M., Cohen, A. S., Nord, M. E., Erickson, W. C., & Perley, R. A. 2005, in *Astronomical Society of the Pacific Conference Series*, Vol. 345, *Astronomical Society of the Pacific Conference Series*, ed. N. Kassim, M. Perez, W. Junor, & P. Henning, 392
- Kasun, S. F. & Evrard, A. E. 2005, *ApJ*, 629, 781
- Katz, N., Weinberg, D. H., & Hernquist, L. 1996, *ApJS*, 105, 19
- Katz, N. & White, S. D. M. 1993, *ApJ*, 412, 455
- Keisler, R., Reichardt, C. L., Aird, K. A., Benson, B. A., Bleem, L. E., Carlstrom, J. E., Chang, C. L., Cho, H. M., Crawford, T. M., Crites, A. T., de Haan, T., Dobbs, M. A., Dudley, J., George, E. M., Halverson, N. W., Holder, G. P., Holzzapfel, W. L., Hoover, S., Hou, Z., Hrubes, J. D., Joy, M., Knox, L., Lee, A. T., Leitch, E. M., Lueker, M., Luong-Van, D., McMahon, J. J., Mehl, J., Meyer, S. S., Millea, M., Mohr, J. J., Montroy, T. E., Natoli, T., Padin, S., Plagge, T., Pryke, C., Ruhl, J. E., Schaffer, K. K., Shaw, L., Shirokoff, E., Spieler, H. G., Staniszewski, Z., Stark, A. A., Story, K., van Engelen, A., Vanderlinde, K., Vieira, J. D., Williamson, R., & Zahn, O. 2011, *ArXiv:1105.3182*
- Kempner, J. C., Blanton, E. L., Clarke, T. E., Enßlin, T. A., Johnston-Hollitt, M., & Rudnick, L. 2004, in *The Riddle of Cooling Flows in Galaxies and Clusters of galaxies*, ed. T. Reiprich, J. Kempner, & N. Soker, 335
- Keshet, U., Waxman, E., & Loeb, A. 2004a, *ApJ*, 617, 281
- . 2004b, *New Astronomy Review*, 48, 1119
- Keshet, U., Waxman, E., Loeb, A., Springel, V., & Hernquist, L. 2003, *ApJ*, 585, 128
- Komatsu, E., Dunkley, J., Nolta, M. R., Bennett, C. L., Gold, B., Hinshaw, G., Jarosik, N., Larson, D., Limon, M., Page, L., Spergel, D. N., Halpern, M., Hill, R. S., Kogut, A., Meyer, S. S., Tucker, G. S., Weiland, J. L., Wollack, E., & Wright, E. L. 2008, *ApJS* submitted, *arXiv:0803.0547*

- Komatsu, E. & Kitayama, T. 1999, *ApJ*, 526, L1
- Komatsu, E. & Seljak, U. 2001, *MNRAS*, 327, 1353
- . 2002, *MNRAS*, 336, 1256
- Komatsu, E., Smith, K. M., Dunkley, J., Bennett, C. L., Gold, B., Hinshaw, G., Jarosik, N., Larson, D., Nolta, M. R., Page, L., Spergel, D. N., Halpern, M., Hill, R. S., Kogut, A., Limon, M., Meyer, S. S., Odegard, N., Tucker, G. S., Weiland, J. L., Wollack, E., & Wright, E. L. 2010, arXiv:1001.4538
- Kravtsov, A. V., Vikhlinin, A., & Nagai, D. 2006, *ApJ*, 650, 128
- Kronberg, P. P. 1994, *Reports of Progress in Physics*, 57, 325
- Kulsrud, R. M. 1999, *ARA&A*, 37, 37
- Large, M. I., Mathewson, D. S., & Haslam, C. G. T. 1959, *Nature*, 183, 1663
- Larson, D., Dunkley, J., Hinshaw, G., Komatsu, E., Nolta, M. R., Bennett, C. L., Gold, B., Halpern, M., Hill, R. S., Jarosik, N., Kogut, A., Limon, M., Meyer, S. S., Odegard, N., Page, L., Smith, K. M., Spergel, D. N., Tucker, G. S., Weiland, J. L., Wollack, E., & Wright, E. L. 2011, *ApJS*, 192, 16
- . 2010, arXiv:1001.4635
- Lau, E. T., Kravtsov, A. V., & Nagai, D. 2009, *ApJ*, 705, 1129
- Lau, E. T., Nagai, D., Kravtsov, A. V., & Zentner, A. R. 2011, *ApJ*, 734, 93
- Levenberg, K. 1944, *Quarterly Journal of Applied Mathematics*, II, 164
- Lewis, A. & Bridle, S. 2002, *Phys.Rev.D*, 66, 103511
- Lewis, G. F., Babul, A., Katz, N., Quinn, T., Hernquist, L., & Weinberg, D. H. 2000, *ApJ*, 536, 623
- Lima, M. & Hu, W. 2004, *Phys.Rev.D*, 70, 043504
- Loeb, A. & Waxman, E. 2000, *Nature*, 405, 156
- Lueker, M., Reichardt, C. L., Schaffer, K. K., Zahn, O., Ade, P. A. R., Aird, K. A., Benson, B. A., Bleem, L. E., Carlstrom, J. E., Chang, C. L., Cho, H., Crawford, T. M., Crites, A. T., de Haan, T., Dobbs, M. A., George, E. M., Hall, N. R., Halverson, N. W., Holder, G. P., Holzappel, W. L., Hrubes, J. D., Joy, M., Keisler, R., Knox, L., Lee, A. T., Leitch, E. M., McMahon, J. J., Mehl, J., Meyer, S. S., Mohr, J. J., Montroy, T. E., Padin, S., Plagge, T., Pryke, C., Ruhl, J. E., Shaw, L., Shirokoff, E., Spieler, H. G., Stalder, B., Staniszewski, Z., Stark, A. A., Vanderlinde, K., Vieira, J. D., & Williamson, R. 2010, *ApJ*, 719, 1045

- Macciò, A. V., Dutton, A. A., & van den Bosch, F. C. 2008, *MNRAS*, 391, 1940
- Majumdar, S. & Mohr, J. J. 2003, *ApJ*, 585, 603
- . 2004, *ApJ*, 613, 41
- Makino, N. & Suto, Y. 1993, *ApJ*, 405, 1
- Malkov, M. A. & O’C Drury, L. 2001, *Reports of Progress in Physics*, 64, 429
- Marquardt, D. W. 1963, *SIAM Journal on Applied Mathematics*, 11, 431
- Marriage, T. A., Acquaviva, V., Ade, P. A. R., Aguirre, P., Amiri, M., Appel, J. W., Barrientos, L. F., Battistelli, E. S., Bond, J. R., Brown, B., Burger, B., Chervenak, J., Das, S., Devlin, M. J., Dicker, S. R., Doriese, W. B., Dunkley, J., Dunner, R., Essinger-Hileman, T., Fisher, R. P., Fowler, J. W., Hajian, A., Halpern, M., Hasselfield, M., Hern’andez-Monteaquedo, C., Hilton, G. C., Hilton, M., Hincks, A. D., Hlozek, R., Huffenberger, K. M., Hughes, D. H., Hughes, J. P., Infante, L., Irwin, K. D., Juin, J. B., Kaul, M., Klein, J., Kosowsky, A., Lau, J. M., Limon, M., Lin, Y., Lupton, R. H., Marsden, D., Martocci, K., Mauskopf, P., Menanteau, F., Moodley, K., Moseley, H., Netterfield, C. B., Niemack, M. D., Nolta, M. R., Page, L. A., Parker, L., Partridge, B., Quintana, H., Reese, E. D., Reid, B., Sehgal, N., Sherwin, B. D., Sievers, J., Spergel, D. N., Staggs, S. T., Swetz, D. S., Switzer, E. R., Thornton, R., Trac, H., Tucker, C., Warne, R., Wilson, G., Wollack, E., & Zhao, Y. 2010, *ArXiv:1010.1065*
- Marrone, D. P., Smith, G. P., Richard, J., Joy, M., Bonamente, M., Hasler, N., Hamilton-Morris, V., Kneib, J., Culverhouse, T., Carlstrom, J. E., Greer, C., Hawkins, D., Hennessy, R., Lamb, J. W., Leitch, E. M., Loh, M., Miller, A., Mroczkowski, T., Muchovej, S., Pryke, C., Sharp, M. K., & Woody, D. 2009, *ApJ*, 701, L114
- Masson, C. R. & Mayer, C. J. 1978, *MNRAS*, 185, 607
- McCarthy, I. G., Schaye, J., Bower, R. G., Ponman, T. J., Booth, C. M., Vecchia, C. D., & Springel, V. 2011, *MNRAS*, 412, 1965
- McNamara, B. R., Nulsen, P. E. J., Wise, M. W., Rafferty, D. A., Carilli, C., Sarazin, C. L., & Blanton, E. L. 2005, *Nature*, 433, 45
- Millea, M., Doré, O., Dudley, J., Holder, G., Knox, L., Shaw, L., Song, Y.-S., & Zahn, O. 2011, *ArXiv e-prints*
- Miniati, F. 2003, *MNRAS*, 342, 1009
- Miniati, F., Jones, T. W., Kang, H., & Ryu, D. 2001, *ApJ*, 562, 233

- Miniati, F., Koushiappas, S. M., & Di Matteo, T. 2007, *ApJ*, 667, L1
- Miniati, F., Ryu, D., Kang, H., Jones, T. W., Cen, R., & Ostriker, J. P. 2000, *ApJ*, 542, 608
- Mitchell, N. L., McCarthy, I. G., Bower, R. G., Theuns, T., & Crain, R. A. 2009, *MNRAS*, 395, 180
- Morales, M. F., Bowman, J. D., Cappallo, R., Hewitt, J. N., & Lonsdale, C. J. 2006, *New Astronomy Review*, 50, 173
- More, S., Kravtsov, A. V., Dalal, N., & Gottlöber, S. 2011, *ApJS*, 195, 4
- Motl, P. M., Hallman, E. J., Burns, J. O., & Norman, M. L. 2005, *ApJ*, 623, L63
- Mroczkowski, T. 2011, *ApJ*, 728, L35+
- Mroczkowski, T., Bonamente, M., Carlstrom, J. E., Culverhouse, T. L., Greer, C., Hawkins, D., Hennessy, R., Joy, M., Lamb, J. W., Leitch, E. M., Loh, M., Maughan, B., Marrone, D. P., Miller, A., Muchovej, S., Nagai, D., Pryke, C., Sharp, M., & Woody, D. 2009, *ApJ*, 694, 1034
- Murgia, M., Govoni, F., Feretti, L., Giovannini, G., Dallacasa, D., Fanti, R., Taylor, G. B., & Dolag, K. 2004, *A&A*, 424, 429
- Nagai, D. 2006, *ApJ*, 650, 538
- Nagai, D., Kravtsov, A. V., & Vikhlinin, A. 2007, *ApJ*, 668, 1
- Nagai, D. & Lau, E. T. 2011, *ApJ*, 731, L10+
- Nath, B. B. & Majumdar, S. 2011, *ArXiv:1105.2826*
- Navarro, J. F., Frenk, C. S., & White, S. D. M. 1997, *ApJ*, 490, 493
- Nozawa, S., Itoh, N., Suda, Y., & Ohhata, Y. 2006, *Nuovo Cimento B Serie*, 121, 487
- Ostriker, J. P., Bode, P., & Babul, A. 2005, *ApJ*, 634, 964
- Pearce, F. R., Thomas, P. A., Couchman, H. M. P., & Edge, A. C. 2000, *MNRAS*, 317, 1029
- Peebles, P. J. E. 1970, *AJ*, 75, 13
- . 1993, *Principles of Physical Cosmology*, ed. Peebles, P. J. E.
- Pfrommer, C. 2008, *MNRAS*, 278
- Pfrommer, C., Chang, P., & Broderick, A. E. 2011, *ArXiv:1106.5505*
- Pfrommer, C., Enßlin, T. A., & Springel, V. 2008, *MNRAS*, 277

- Pfrommer, C., Enßlin, T. A., Springel, V., Jubelgas, M., & Dolag, K. 2007, *MNRAS*, 378, 385
- Pfrommer, C. & Jones, T. W. 2011, *ApJ*, 730, 22
- Pfrommer, C., Springel, V., Enßlin, T. A., & Jubelgas, M. 2006, *MNRAS*, 367, 113
- Pinzke, A., Pfrommer, C., & Bergstrom, L. 2011, *ArXiv:1105.3240*
- Pizzo, R. F., de Bruyn, A. G., Feretti, L., & Govoni, F. 2008, *A&A*, 481, L91
- Planck Collaboration, Ade, P. A. R., Aghanim, N., Arnaud, M., Ashdown, M., Aumont, J., Baccigalupi, C., Balbi, A., Banday, A. J., Barreiro, R. B., & et al. 2011a, *ArXiv:1101.2026*
- . 2011b, *ArXiv:1101.2024*
- Planck Collaboration, Aghanim, N., Arnaud, M., Ashdown, M., Aumont, J., Baccigalupi, C., Balbi, A., Banday, A. J., Barreiro, R. B., Bartelmann, M., & et al. 2011c, *ArXiv:1101.2043*
- Press, W. H. & Schechter, P. 1974, *ApJ*, 187, 425
- Price, D. J. & Monaghan, J. J. 2004, *MNRAS*, 348, 139
- . 2005, *MNRAS*, 364, 384
- Puchwein, E., Sijacki, D., & Springel, V. 2008, *ApJ*, 687, L53
- Rasia, E., Tormen, G., & Moscardini, L. 2004, *MNRAS*, 351, 237
- Rees, M. J. 1987, *QJRAS*, 28, 197
- Refregier, A., Komatsu, E., Spergel, D. N., & Pen, U.-L. 2000, *Phys.Rev.D*, 61, 123001
- Reichardt, C. L., Ade, P. A. R., Bock, J. J., Bond, J. R., Brevik, J. A., Contaldi, C. R., Daub, M. D., Dempsey, J. T., Goldstein, J. H., Holzzapfel, W. L., Kuo, C. L., Lange, A. E., Lueker, M., Newcomb, M., Peterson, J. B., Ruhl, J., Runyan, M. C., & Staniszewski, Z. 2009a, *ApJ*, 694, 1200
- Reichardt, C. L., Zahn, O., Ade, P. A. R., Basu, K., Bender, A. N., Bertoldi, F., Cho, H.-M., Chon, G., Dobbs, M., Ferrusca, D., Halverson, N. W., Holzzapfel, W. L., Horellou, C., Johansson, D., Johnson, B. R., Kennedy, J., Kneissl, R., Lanting, T., Lee, A. T., Lueker, M., Mehl, J., Menten, K. M., Nord, M., Pacaud, F., Richards, P. L., Schaaf, R., Schwan, D., Spieler, H., Weiss, A., & Westbrook, B. 2009b, *ApJ*, 701, 1958
- Riess, A. G., Macri, L., Casertano, S., Sosey, M., Lampeitl, H., Ferguson, H. C., Filippenko, A. V., Jha, S. W., Li, W., Chornock, R., & Sarkar, D. 2009, *ApJ*, 699, 539

- Röttgering, H. 2003, *New Astronomy Review*, 47, 405
- Röttgering, H., Snellen, I., Miley, G., de Jong, J. P., Hanisch, R. J., & Perley, R. 1994, *ApJ*, 436, 654
- Röttgering, H. J. A., Wieringa, M. H., Hunstead, R. W., & Ekers, R. D. 1997, *MNRAS*, 290, 577
- Roychowdhury, S., Ruszkowski, M., & Nath, B. B. 2005, *ApJ*, 634, 90
- Rozo, E., Wechsler, R. H., Rykoff, E. S., Annis, J. T., Becker, M. R., Evrard, A. E., Frieman, J. A., Hansen, S. M., Hao, J., Johnston, D. E., Koester, B. P., McKay, T. A., Sheldon, E. S., & Weinberg, D. H. 2010, *ApJ*, 708, 645
- Rudd, D. H., Zentner, A. R., & Kravtsov, A. V. 2008, *ApJ*, 672, 19
- Ryu, D., Kang, H., Cho, J., & Das, S. 2008, *Science*, 320, 909
- Ryu, D., Kang, H., Hallman, E., & Jones, T. W. 2003, *ApJ*, 593, 599
- Sayers, J., Golwala, S. R., Ameglio, S., & Pierpaoli, E. 2011, *ApJ*, 728, 39
- Scannapieco, E., Thacker, R. J., & Couchman, H. M. P. 2008, *ApJ*, 678, 674
- Schäfer, B. M., Pfrommer, C., Bartelmann, M., Springel, V., & Hernquist, L. 2006a, *MNRAS*, 370, 1309
- Schäfer, B. M., Pfrommer, C., Hell, R. M., & Bartelmann, M. 2006b, *MNRAS*, 370, 1713
- Schekochihin, A. A. & Cowley, S. C. 2006, *Physics of Plasmas*, 13, 6501
- Schlickeiser, R., Sievers, A., & Thiemann, H. 1987, *A&A*, 182, 21
- Schuecker, P., Böhringer, H., Reiprich, T. H., & Feretti, L. 2001, *A&A*, 378, 408
- Schuecker, P., Finoguenov, A., Miniati, F., Böhringer, H., & Briel, U. G. 2004, *A&A*, 426, 387
- Sehgal, N., Bode, P., Das, S., Hernandez-Monteagudo, C., Huffenberger, K., Lin, Y., Ostriker, J. P., & Trac, H. 2010, *ApJ*, 709, 920
- Sehgal, N., Trac, H., Acquaviva, V., Ade, P. A. R., Aguirre, P., Amiri, M., Appel, J. W., Barrientos, L. F., Battistelli, E. S., Bond, J. R., Brown, B., Burger, B., Chervenak, J., Das, S., Devlin, M. J., Dicker, S. R., Bertrand Doriese, W., Dunkley, J., Dünner, R., Essinger-Hileman, T., Fisher, R. P., Fowler, J. W., Hajian, A., Halpern, M., Hasselfield, M., Hernández-Monteagudo, C., Hilton, G. C., Hilton, M., Hincks, A. D., Hlozek, R., Holtz, D., Huffenberger, K. M., Hughes, D. H., Hughes, J. P., Infante, L., Irwin, K. D., Jones, A., Baptiste Juin, J., Klein, J., Kosowsky, A., Lau, J. M., Limon, M., Lin, Y.-T., Lupton, R. H., Marriage, T. A., Marsden, D., Martocci, K., Mauskopf, P., Menanteau,

- F., Moodley, K., Moseley, H., Netterfield, C. B., Niemack, M. D., Nolta, M. R., Page, L. A., Parker, L., Partridge, B., Reid, B., Sherwin, B. D., Sievers, J., Spergel, D. N., Staggs, S. T., Swetz, D. S., Switzer, E. R., Thornton, R., Tucker, C., Warne, R., Wollack, E., & Zhao, Y. 2011, *ApJ*, 732, 44
- Seljak, U., Burwell, J., & Pen, U. 2001, *Phys.Rev.D*, 63, 063001
- Shaw, L. D., Nagai, D., Bhattacharya, S., & Lau, E. T. 2010, *ApJ*, 725, 1452
- Shaw, L. D., Zahn, O., Holder, G. P., & Doré, O. 2009, *ApJ*, 702, 368
- Shirokoff, E., Reichardt, C. L., Shaw, L., Millea, M., Ade, P. A. R., Aird, K. A., Benson, B. A., Bleem, L. E., Carlstrom, J. E., Chang, C. L., Cho, H. M., Crawford, T. M., Crites, A. T., de Haan, T., Dobbs, M. A., Dudley, J., George, E. M., Halverson, N. W., Holder, G. P., Holzappel, W. L., Hrubes, J. D., Joy, M., Keisler, R., Knox, L., Lee, A. T., Leitch, E. M., Lueker, M., Luong-Van, D., McMahon, J. J., Mehl, J., Meyer, S. S., Mohr, J. J., Montroy, T. E., Padin, S., Plagge, T., Pryke, C., Ruhl, J. E., Schaffer, K. K., Spieler, H. G., Staniszewski, Z., Stark, A. A., Story, K., Vanderlinde, K., Vieira, J. D., Williamson, R., & Zahn, O. 2010, *ArXiv:1012.4788*
- Sievers, J. L., Mason, B. S., Weintraub, L., Achermann, C., Altamirano, P., Bond, J. R., Bronfman, L., Bustos, R., Contaldi, C., Dickinson, C., Jones, M. E., May, J., Myers, S. T., Oyarce, N., Padin, S., Pearson, T. J., Pospieszalski, M., Readhead, A. C. S., Reeves, R., Shepherd, M. C., Taylor, A. C., & Torres, S. 2009, *arXiv:0901.4540*
- Sijacki, D., Pfrommer, C., Springel, V., & Enßlin, T. A. 2008a, *MNRAS*, 695
- . 2008b, *MNRAS*, 387, 1403
- Sijacki, D. & Springel, V. 2006, *MNRAS*, 366, 397
- Sijacki, D., Springel, V., Di Matteo, T., & Hernquist, L. 2007, *MNRAS*, 380, 877
- Silk, J. 1968, *ApJ*, 151, 459
- Simard-Normandin, M., Kronberg, P. P., & Button, S. 1981, *ApJS*, 45, 97
- Simionescu, A., Allen, S. W., Mantz, A., Werner, N., Takei, Y., Morris, R. G., Fabian, A. C., Sanders, J. S., Nulsen, P. E. J., George, M. R., & Taylor, G. B. 2011, *Science*, 331, 1576
- Skillman, S. W., O'Shea, B. W., Hallman, E. J., Burns, J. O., & Norman, M. L. 2008, *ApJ*, 689, 1063
- Spergel, D. N., Bean, R., Doré, O., Nolta, M. R., Bennett, C. L., Dunkley, J., Hinshaw, G., Jarosik, N., Komatsu, E., Page, L., Peiris, H. V., Verde, L., Halpern, M., Hill, R. S., Kogut, A., Limon, M., Meyer, S. S., Odegard, N., Tucker, G. S., Weiland, J. L., Wollack, E., & Wright, E. L. 2007, *ApJS*, 170, 377

- Springel, V. 2005, MNRAS, 364, 1105
- Springel, V. & Hernquist, L. 2003a, MNRAS, 339, 289
- . 2003b, MNRAS, 339, 312
- Springel, V., Wang, J., Vogelsberger, M., Ludlow, A., Jenkins, A., Helmi, A., Navarro, J. F., Frenk, C. S., & White, S. D. M. 2008a, MNRAS, 391, 1685
- Springel, V., White, M., & Hernquist, L. 2001a, ApJ, 549, 681
- Springel, V., White, S. D. M., Frenk, C. S., Navarro, J. F., Jenkins, A., Vogelsberger, M., Wang, J., Ludlow, A., & Helmi, A. 2008b, Nature, 456, 73
- Springel, V., Yoshida, N., & White, S. D. M. 2001b, New Astronomy, 6, 79
- Stanek, R., Rasia, E., Evrard, A. E., Pearce, F., & Gazzola, L. 2010, ApJ, 715, 1508
- Subramanian, K. 2003, Physical Review Letters, 90, 245003
- Suginohara, T. & Ostriker, J. P. 1998, ApJ, 507, 16
- Sun, M., Sehgal, N., Voit, G. M., Donahue, M., Jones, C., Forman, W., Vikhlinin, A., & Sarazin, C. 2011, ApJ, 727, L49+
- Sunyaev, R. A. & Zeldovich, Y. B. 1970, Ap&SS, 7, 3
- Taylor, G. B., Fabian, A. C., Gentile, G., Allen, S. W., Crawford, C., & Sanders, J. S. 2007, MNRAS, 382, 67
- Thacker, R. J., Scannapieco, E., & Couchman, H. M. P. 2006, ApJ, 653, 86
- Thomas, P. A. & Couchman, H. M. P. 1992, MNRAS, 257, 11
- Thompson, T. A., Quataert, E., & Murray, N. 2005, ApJ, 630, 167
- Tinker, J., Kravtsov, A. V., Klypin, A., Abazajian, K., Warren, M., Yepes, G., Gottlöber, S., & Holz, D. E. 2008, ApJ, 688, 709
- Trac, H., Bode, P., & Ostriker, J. P. 2011, ApJ, 727, 94
- Tribble, P. C. 1991, MNRAS, 253, 147
- Vanderlinde, K., Crawford, T. M., de Haan, T., Dudley, J. P., Shaw, L., Ade, P. A. R., Aird, K. A., Benson, B. A., Bleem, L. E., Brodwin, M., Carlstrom, J. E., Chang, C. L., Crites, A. T., Desai, S., Dobbs, M. A., Foley, R. J., George, E. M., Gladders, M. D., Hall, N. R., Halverson, N. W., High,

- F. W., Holder, G. P., Holzapfel, W. L., Hrubes, J. D., Joy, M., Keisler, R., Knox, L., Lee, A. T., Leitch, E. M., Loehr, A., Lueker, M., Marrone, D. P., McMahon, J. J., Mehl, J., Meyer, S. S., Mohr, J. J., Montroy, T. E., Ngeow, C., Padin, S., Plagge, T., Pryke, C., Reichardt, C. L., Rest, A., Ruel, J., Ruhl, J. E., Schaffer, K. K., Shirokoff, E., Song, J., Spieler, H. G., Stalder, B., Staniszewski, Z., Stark, A. A., Stubbs, C. W., van Engelen, A., Vieira, J. D., Williamson, R., Yang, Y., Zahn, O., & Zenteno, A. 2010, *ApJ*, 722, 1180
- Vazza, F., Brunetti, G., & Gheller, C. 2009, *MNRAS*, 395, 1333
- Vazza, F., Dolag, K., Ryu, D., Brunetti, G., Gheller, C., Kang, H., & Pfrommer, C. 2011, *ArXiv:1106.2159*
- Vikhlinin, A., Kravtsov, A. V., Burenin, R. A., Ebeling, H., Forman, W. R., Hornstrup, A., Jones, C., Murray, S. S., Nagai, D., Quintana, H., & Voevodkin, A. 2009, *ApJ*, 692, 1060
- Vladimirov, A., Ellison, D. C., & Bykov, A. 2006, *ApJ*, 652, 1246
- Vogt, C. & Enßlin, T. A. 2003, *A&A*, 412, 373
- . 2005, *A&A*, 434, 67
- Voit, G. M. 2005, *Reviews of Modern Physics*, 77, 207
- Warren, M. S., Abazajian, K., Holz, D. E., & Teodoro, L. 2006, *ApJ*, 646, 881
- Wechsler, R. H., Bullock, J. S., Primack, J. R., Kravtsov, A. V., & Dekel, A. 2002, *ApJ*, 568, 52
- White, M. 2002, *ApJS*, 143, 241
- White, M., Hernquist, L., & Springel, V. 2002, *ApJ*, 579, 16
- White, S. D. M. 1976, *MNRAS*, 177, 717
- Widrow, L. M. 2002, *Reviews of Modern Physics*, 74, 775
- Wielebinski, R. & Krause, F. 1993, *A&A Rev.*, 4, 449
- Wojtak, R., Łokas, E. L., Mamon, G. A., Gottlöber, S., Klypin, A., & Hoffman, Y. 2008, *MNRAS*, 388, 815
- Yang, H., Bhattacharya, S., & Ricker, P. M. 2010, *ApJ*, 725, 1124
- Yoshida, N., Sheth, R. K., & Diaferio, A. 2001, *MNRAS*, 328, 669
- Zaroubi, S., Squires, G., Hoffman, Y., & Silk, J. 1998, *ApJ*, 500, L87

Zel'dovich, Y. B. 1970, *A&A*, 5, 84

Zhang, P. & Pen, U.-L. 2001, *ApJ*, 549, 18

Zhang, P., Pen, U.-L., & Wang, B. 2002, *ApJ*, 577, 555

Zhang, P. & Sheth, R. K. 2007, *ApJ*, 671, 14

Zhao, D. H., Jing, Y. P., Mo, H. J., & Börner, G. 2009, *ApJ*, 707, 354

Zwicky, F. 1937, *ApJ*, 86, 217